

Photophysical Properties of Protonated Aromatic Hydrocarbons

Thesis by

Vadym A. Kapinus

In Partial Fulfillment of the Requirements

for the Degree of

Doctor of Philosophy



California Institute of Technology

Pasadena, California

2005

(Defended December 14, 2004)

© 2005

Vadym A. Kapinus

All Rights Reserved

Acknowledgements

I have greatly enjoyed the years I have spent at Caltech and it will be hard to express my thanks to the many people to whom I am indebted to for such unforgettable experiences.

First, I was fortunate to have Professor Geoffrey Blake as my research advisor. I appreciate the energy, enthusiasm and support that Geoff provided during my graduate career. The door of his office was always open for students, he always welcomed new ideas, and would have a few suggestions when the experiment did not work. Most of all, I value the freedom that Geoff gave me in conducting research. I would also like to thank Professors Jack Beauchamp and Mitchio Okumura for some of the discussions I had with them.

When I joined the Blake group, I was working closely on the experiments with Sheng Wu and Zulfikar Morbi. I learned many things about non-linear optical devices from Sheng, and later I had a long collaboration with him on a number of tunable solid state light sources. Zulf and I worked on the carbon chain project, and from him I learned many useful things about lab management and experimental techniques. He was also the one who started me on programming the remote control of digital oscilloscopes, which later became the main part of my data collection software. Susanna Widicus-Weaver helped me in my attempt to record the microwave spectrum of protonated benzene. Michael Morton was the beta tester for the BGSpecT software.

The Blake group was an interesting place to work and I would like to thank some of its

former and current members for providing a friendly working environment, and for lending a hand or a good word when I needed them: Susanna, Mike, Zulf, Sheng, Hui Zhang, Zifu Wang, François Jeanneret, Rogier Braakman and Daniel Holland.

Administrative assistants, Janis Haskell and Leticia Calderon from GPS division were very helpful with placing orders and solving some organizational questions. I would also like to acknowledge the help of the people from the Chemistry machine shop for their quality work on the parts for my experiment: Mike Roy, Guy Duremburg, Ray Garcia and Steven Olson. Tom Dunn from the Chemistry electronics shop was helpful with circuit designs and was generous with borrowing his high voltage probe. Tony Solyom from the Biology Division fixed a few chillers and vacuum pumps for me. I also enjoyed our long conversations on various topics. My thanks go to the Thaddeus group from Harvard for sharing their designs of the discharge source and the electronic circuitry for it.

With Andrei Deev, a longtime friend and roommate since my undergraduate years, I had many discussions about science and life in general. Ironically, we both ended up at Caltech, in the same department, and conducting research in related areas – even having our thesis defense scheduled on the same day!

Many other people at Caltech contributed to the quality of my non-academic life, and became my friends. Julia Lyubovitsky taught me quite a few subtle things about american culture, first when doing homework together and later, during our long lunch chats. Leo Eisner used my weakness for good food to introduce me to the sport of orienteering. Together, we had many unforgettable moments, especially at Mt. Piños, Redwoods, Lake Tahoe and the Sierras.

Ulyana Dyudina, Andrei Khodakovsky, Andrey Bereznyak and Dmitry Novikov were my buddies on hiking trips – from going up to the local mountains, to going down to the Grand

Canyon. They, and some other members of russian-speaking community (Andy Greenberg and Galina Lokshina, George Shapovalov and Kira Kostenko, Alexander Putilin, Vadim Borokhov, Alexei Dvoretzkii, Ivan Mokhnal and Dmitry Kossakovski) did not allow me to lose the cultural connection with my homeland.

I would like to thank my soccer teammates from the Red Square and Kicking Buck teams, especially Jim Kempf, Lou Madsen and Gabriel Brandt.

I became a fan and a participant of another sport at Caltech: dancesport. Derrick Bass, the legendary guru of the Caltech Ballroom Dance Club, taught me my first steps. His thorough teaching style (what else can you expect from a theoretical physicist?) sparked my competitive spirit and interest in good technique. Our activities were not only limited to the dance floor with many other members of the ‘old’ team, including my first partner Meina Xu, Andreea Boca, Kok Win Goh, Joseph Chen, Christina Lam, Andrej Zlatos, Tammy Lam, Helen Claudio, Ania Kashina, Ulyana, Galka, Sasha. I also enjoyed working closely with the members of the CBDC organizing committee, especially Michael Fleming, Megan Ferguson and Keith Brown.

My dancing hobby profoundly changed my life by leading me to cross paths with my wife, Vanessa, who from just being a friend and dance partner became my best friend and partner in life. Her friendly words and warm smile gave me a lot of energy during the past two years. I express my great appreciation for her love, encouragement, patience and faith in me.

Finally, I would like to thank my family, especially my parents, Alexander and Nelya. They always provided me with freedom of choice and supported my interest in science, even when that interest led me to distant shores.

Abstract

Diffuse interstellar bands (DIBs) were first observed in the visible region of the electromagnetic spectrum in the 1920s, with over a hundred features now discovered out to near-IR wavelengths. Since their initial discovery, many attempts have been made to identify the species that are responsible for the DIBs. Polycyclic aromatic hydrocarbons (PAHs) and their derivatives are among the likely candidates for DIB carriers, as demonstrated by the intense unidentified IR emission bands from 3.3 – 11.3 μm that strongly point to their presence of aromatic species in the interstellar medium (ISM). The $S_1 \leftarrow S_0$ electronic transitions for small PAHs lie in the near-UV, however, so only large neutral PAHs with 30+ carbon atoms can absorb at the visible wavelengths characteristic of the DIBs. In diffuse clouds and dense cloud envelopes that are exposed to the harsh interstellar radiation field, molecules are expected to be ionized. Positively charged PAHs are predicted to acquire a hydrogen atom to form thermodynamically stable protonated PAHs in diffuse clouds. These are closed-shell molecular ions with electronic transitions that are red-shifted compared to neutral PAHs, so even small protonated PAHs can, in principle, produce absorption bands in the visible.

Little is known about the photophysical properties of these compounds, however, so this thesis presents an experimental and theoretical analysis of two-, three-, and four-ring protonated PAHs. Theoretically, density functional theory calculations using the B3LYP

functional were used to study protonated PAHs in their ground electronic state. In particular, the energetics of the various potential protonated PAH isomers were calculated along with the proton tunneling or hopping barriers between them. The relative energies of the lowest lying photodissociation pathways were also calculated. It was found that the different isomers of protonated PAHs likely exist in thermodynamic equilibrium under interstellar conditions, thanks to the moderate ($\sim 15 - 20$ kcal/mol) barriers to proton migration. Photochemically, the loss of an H atom or H₂ molecule from a protonation site were identified as the most favorable dissociation channels for protonated PAHs. The H and H₂ loss channels were found to be within a few kcal/mol of each other in energy, and about 45 – 60 kcal/mol above the ground state, depending on the parent molecule and isomer.

Following the ground state geometry optimizations and energy calculations, the Configuration Interaction Singles (CIS) method was used to estimate the positions of the electronic transitions for protonated PAHs. Depending on the PAH and isomer, red shifts up to 150 nm were predicted even for small systems, i.e., protonated naphthalene, anthracene, phenanthrene and pyrene. This places the $S_1 \leftarrow S_0$ transitions of essentially all protonated PAHs well into the DIB wavelength region.

In order to investigate these predictions experimentally, a robust hydrogen discharge source was designed to produce protonated PAHs. Laser photodissociation of protonated PAHs was first studied with an excimer laser/reflectron time-of-flight mass spectrometer under ultrahigh vacuum conditions that mimic those in the ISM. Small protonated PAHs were found to be very photostable. Indeed, it was determined that nanosecond pulse length photodissociation is multiphoton even at short wavelengths (193 nm). For protonated anthracene, the dissociation limit was estimated to be 13 – 15 eV, which is much higher than the predicted thermodynamic threshold of 2.5 – 3.0 eV. This was attributed to the onset of

rapid intramolecular vibrational relaxation (IVR) upon electronic excitation.

Thanks to the excellent photostability of protonated PAHs, a cluster photodissociation approach was used to locate the electronic transitions of protonated anthracene between 420 and 540 nm. Clusters with water molecules were produced in a two-valve mixing discharge source. Visible photodissociation spectrum of these clusters was recorded using a novel optical parametric oscillator (OPO) with low beam divergence. The OPO utilizes a hybrid matching scheme involving BBO type I and II crystals in a rotated prism cavity. The observed protonated anthracene absorption bands are very wide (20 nm FWHM) – too wide to account for the DIBs. Again, this spectral broadening most likely results from rapid IVR induced by the high density of states in protonated PAHs. Such strong, wide bands may be important contributors to the overall visual extinction in the diffuse ISM and should efficiently produce infrared emission such as that seen in the Unidentified Infrared emission features, or UIRs.

Contents

| | |
|--|------------|
| Acknowledgements | iii |
| Abstract | vi |
| 1 Protonated Polycyclic Aromatic Hydrocarbons and the Interstellar Medium | 1 |
| 1.1 Interstellar Molecules | 1 |
| 1.2 PAHs and the Unidentified IR Emission Bands | 3 |
| 1.3 The Diffuse Interstellar Bands | 4 |
| 1.3.1 Carbon Chains and the DIBs | 6 |
| 1.3.2 PAHs and the DIBs | 6 |
| 1.4 Protonated PAHs | 9 |
| 1.4.1 Protonated PAHs in ISM | 9 |
| 1.4.2 Protonated PAHs and the DIBs | 10 |
| 1.4.3 Other Applications of Protonated Aromatics | 11 |
| 1.4.4 Previous Studies of Protonated Aromatics | 11 |
| 1.5 Research Goals | 13 |
| 2 Ground State Calculations for Protonated PAHs | 15 |
| 2.1 Introduction | 15 |
| 2.2 Methodology | 16 |

| | | |
|-------|--|----|
| 2.2.1 | Naming Conventions | 16 |
| 2.2.2 | Software | 17 |
| 2.2.3 | Choice of the Computer System | 18 |
| 2.2.4 | Theory Level and Basis Set | 19 |
| 2.3 | Geometries | 21 |
| 2.3.1 | Protonated Benzene, Naphthalene, Anthracene and Pyrene | 21 |
| 2.3.2 | Typical Geometry Changes Upon Protonation | 27 |
| 2.3.3 | Geometries of Dehydrogenated PAH Cations | 28 |
| 2.3.4 | Geometries of Hydrogenated and Dehydrogenated PAHs | 28 |
| 2.4 | Calculated Values | 29 |
| 2.4.1 | Vibrational Frequencies | 29 |
| 2.4.2 | Proton Affinities | 30 |
| 2.4.3 | Ionization Energies | 31 |
| 2.5 | Energy Landscapes | 32 |
| 2.5.1 | Protonated Benzene | 33 |
| 2.5.2 | Protonated Naphthalene | 34 |
| 2.5.3 | Protonated Anthracene | 36 |
| 2.5.4 | Protonated Phenanthrene | 38 |
| 2.5.5 | Protonated Pyrene | 40 |
| 2.5.6 | Hydrogenated PAHs | 41 |
| 2.6 | Discussion | 44 |
| 2.6.1 | Changes in the Vibrational Spectrum | 45 |
| 2.6.2 | Proton Mobility | 46 |
| 2.6.3 | Dissociation Channels | 47 |

| | | |
|----------|--|-----------|
| 2.6.4 | Interstellar H ₂ Formation | 48 |
| 2.7 | Summary | 50 |
| 3 | Excited States Calculations for Protonated PAHs | 52 |
| 3.1 | Introduction | 52 |
| 3.2 | Methodology | 53 |
| 3.2.1 | Theory Level and Basis Set | 53 |
| 3.2.2 | Convergence Tests | 54 |
| 3.2.3 | Scaling Factors | 56 |
| 3.3 | Valence Molecular Orbitals | 57 |
| 3.3.1 | Protonated Benzene | 57 |
| 3.3.2 | Other Protonated Aromatics | 58 |
| 3.3.3 | Electronic States Assignment | 59 |
| 3.4 | Excited States Energies | 61 |
| 3.4.1 | Comparison with DIB spectrum | 64 |
| 3.5 | Summary | 65 |
| 4 | Experimental Setup | 67 |
| 4.1 | Introduction | 67 |
| 4.2 | Pulsed Discharge Source | 69 |
| 4.2.1 | Design | 69 |
| 4.2.2 | Voltage and Current Profiles | 72 |
| 4.2.3 | Protonation Mechanism and Efficiency | 73 |
| 4.3 | Cluster Source | 77 |
| 4.3.1 | Design | 77 |

| | | |
|----------|--|------------|
| 4.3.2 | Operation | 78 |
| 4.4 | Mass Spectrometer | 79 |
| 4.4.1 | Ion Shielding | 80 |
| 4.4.2 | Ion Extraction | 81 |
| 4.4.3 | Reflectron Mode | 82 |
| 4.4.4 | Detectors | 83 |
| 4.4.5 | Vacuum System | 83 |
| 4.5 | Laser Systems | 84 |
| 4.5.1 | Excimer Laser | 84 |
| 4.5.2 | Nd:YAG Lasers | 85 |
| 4.5.3 | BBO Type II OPO | 85 |
| 4.6 | Hybrid BBO OPO with a Rotated Prism Cavity | 87 |
| 4.6.1 | New Cavity Design | 88 |
| 4.6.2 | Phase Matching | 88 |
| 4.6.3 | The Choice of Crystals | 90 |
| 4.6.4 | Hybrid Cavity Performance | 92 |
| 4.7 | Other Hardware | 94 |
| 4.8 | Data Acquisition | 95 |
| 4.8.1 | Blake Group Spectroscopy Tools Software | 95 |
| 4.8.2 | Choice of Delay Times | 96 |
| 4.8.3 | Data Analysis | 99 |
| 5 | Laser Dissociation of Protonated PAHs | 100 |
| 5.1 | Experiments | 100 |

| | | |
|----------|--|------------|
| 5.1.1 | The Type II BBO OPO as a Laser Photodissociation Source | 101 |
| 5.1.2 | Two-color Dissociation – OPO and Excimer Laser | 102 |
| 5.1.3 | Dissociation Yield with Excimer Laser | 103 |
| 5.2 | Observed Results | 106 |
| 5.2.1 | Photodissociation Products | 106 |
| 5.2.2 | Yield Dependence on the Pulse Energy | 108 |
| 5.3 | Discussion | 111 |
| 5.3.1 | Multiphoton Nature of the Photodissociation | 111 |
| 5.3.2 | Photostability and Implications for ISM | 113 |
| 5.4 | Summary | 114 |
| 6 | Cluster Predissociation Spectroscopy of Protonated Anthracene | 116 |
| 6.1 | Introduction | 116 |
| 6.2 | Experiment | 117 |
| 6.3 | Results and Discussion | 119 |
| 6.3.1 | Cluster Geometry | 119 |
| 6.3.2 | Measured Spectrum | 121 |
| 6.3.3 | Band Positions and Widths | 123 |
| 6.3.4 | Comparison with Spectra of Other Clusters | 124 |
| 6.3.5 | Effect of Proton Mobility on the Spectral Width | 125 |
| 6.3.6 | Other Factors | 126 |
| 6.3.7 | Comparison with the DIBs | 127 |
| 6.4 | Summary | 128 |
| 7 | Summary | 130 |

| | | |
|----------|---|------------|
| 7.1 | Structures and Reaction Pathways | 130 |
| 7.2 | Molecular Orbitals and Electronic Transitions | 131 |
| 7.3 | Photostability of Protonated PAHs | 133 |
| 7.4 | Visible Spectrum of Protonated Anthracene | 134 |
| 7.5 | Conclusions | 135 |
| 7.6 | Future Research Directions | 135 |
| A | GAUSSIAN 98 Results | 138 |
| A.1 | Geometries | 138 |
| A.1.1 | Z-Matrices | 139 |
| A.2 | Vibrational Frequencies | 156 |
| A.3 | Vibrational Spectra | 169 |
| A.4 | Energy Landscapes for Protonated PAHs | 179 |
| A.5 | Energy Landscapes for Hydrogenated PAHs | 181 |
| A.6 | Ionization Energies | 183 |
| A.7 | Excited States | 184 |
| B | Experimental Setup Descriptions | 191 |
| B.1 | Discharge | 191 |
| B.1.1 | Pulsed Discharge Source | 191 |
| B.1.2 | Pulsed Discharge Cluster Source | 198 |
| B.2 | Circuits | 201 |
| B.2.1 | TTL Pulse Width Selector | 201 |
| B.2.2 | Pulsed Valve Driver | 202 |
| B.2.3 | TOF MS High Voltage Pulser | 204 |

| | | |
|----------|--|------------|
| B.2.4 | Frequency Divider | 206 |
| C | Blake Group Spectroscopy Tools Software | 208 |
| C.1 | Main Panel | 208 |
| C.1.1 | Instruments | 209 |
| C.1.2 | Tools | 210 |
| C.1.3 | Menus | 210 |
| C.1.4 | System Tray Icon | 211 |
| C.1.5 | Other | 212 |
| C.2 | Lambda Tune Panel | 212 |
| C.2.1 | Remote Parameters Setup | 213 |
| C.2.2 | Lambda Tune Parameters | 214 |
| C.2.2.1 | Calibration File | 214 |
| C.2.2.2 | Wavelength Conversions | 218 |
| C.2.2.3 | Other Lambda Tune Parameters | 220 |
| C.2.3 | Changing Lambda Tune Wavelength | 221 |
| C.3 | Wavemeter Panel | 221 |
| C.3.1 | Remote Parameters Setup | 222 |
| C.3.2 | Wavemeter Parameters | 223 |
| C.3.3 | Reading Wavelength | 223 |
| C.4 | Motion Control Panel | 223 |
| C.4.1 | Remote Parameters Setup | 224 |
| C.4.2 | Motion Axes Parameters | 225 |
| C.4.3 | Moving Axes | 226 |

| | | |
|---------|---|-----|
| C.4.4 | Positions File | 227 |
| C.5 | Oscilloscope Panel | 227 |
| C.5.1 | Remote Parameters Setup | 227 |
| C.5.2 | Waveform Acquisition and Manipulation | 230 |
| C.5.2.1 | Reading Waveforms | 230 |
| C.5.2.2 | Viewing Waveforms | 231 |
| C.5.2.3 | Saving Waveforms | 232 |
| C.5.3 | Oscilloscope Parameters Setup | 233 |
| C.5.3.1 | Panel Parameters | 234 |
| C.5.3.2 | Common Scope Parameters | 234 |
| C.5.3.3 | Channel Parameters | 236 |
| C.5.3.4 | Channel Task Parameters | 238 |
| C.5.3.5 | Save and Load Configuration | 240 |
| C.6 | Delay Generator Panel | 241 |
| C.6.1 | Remote Parameters Setup | 241 |
| C.6.2 | Delay Generator Parameters | 242 |
| C.6.2.1 | Trigger Parameters | 243 |
| C.6.2.2 | Output Line Parameters | 243 |
| C.6.2.3 | Delay Line Parameters | 244 |
| C.6.2.4 | Save and Load Settings | 245 |
| C.6.3 | Visualize Output Delay Pulses | 245 |
| C.7 | Photon Counter Panel | 246 |
| C.7.1 | Remote Parameters Setup | 247 |
| C.7.2 | Photon Counter Parameters | 248 |

| | | |
|---------|--|-----|
| C.7.2.1 | Panel Parameters | 248 |
| C.7.2.2 | Common Photon Counter Parameters | 249 |
| C.7.2.3 | Counter Channel Parameters | 249 |
| C.7.2.4 | Save and Load Settings | 250 |
| C.7.3 | Reading Counts | 251 |
| C.8 | Spectrum Scan Panel | 251 |
| C.8.1 | Sources and Detectors | 252 |
| C.8.2 | Sources Setup | 252 |
| C.8.3 | Detectors Setup | 256 |
| C.8.4 | Spectrum View | 258 |
| C.8.5 | Other Features | 260 |
| C.8.6 | Performing the Scan | 262 |
| C.9 | Device Talk Panel | 263 |
| C.9.1 | COM Port Settings | 264 |
| C.9.2 | Talking to Devices | 264 |
| C.10 | Devices | 266 |
| C.11 | Device Setup | 266 |
| C.11.1 | Create Device | 267 |
| C.11.2 | Device Type | 267 |
| C.11.3 | Device Communication Type | 268 |
| C.11.4 | Device Communication Address | 268 |
| C.11.5 | Turning Device On/Off | 270 |
| C.11.6 | Panel Configuration Backup | 270 |
| C.11.7 | Help | 271 |

| | |
|----------------------------------|------------|
| C.12 Readme | 271 |
| C.13 License Agreement | 274 |
| Bibliography | 277 |

List of Figures

| | | |
|------|--|----|
| 1.1 | A synthetic spectrum of the diffuse interstellar bands, based on the DIB compilation in [1]. The image is from [2]. | 5 |
| 2.1 | Structures for protonated benzene PES stationary points. Adapted from [3]. | 15 |
| 2.2 | Carbon atom numbering conventions for neutral PAHs. | 17 |
| 2.3 | Structures of protonated benzene $C_6H_7^+$ and its isomerization transition state 1-2 $C_6H_7^+$ | 22 |
| 2.4 | Structures of the protonated naphthalene $C_{10}H_9^+$ isomers 1,2 and 9, along with three of the isomerization transition states that connect them. | 23 |
| 2.5 | Structures of the protonated anthracene $C_{14}H_{11}^+$ isomers 1, 2, 9 and 11, along with two of the lowest barrier isomerization transition states. | 24 |
| 2.6 | Structures of the protonated phenanthrene $C_{14}H_{11}^+$ isomers 1, 2, 3, 4 and 9. . | 25 |
| 2.7 | Structures of the protonated pyrene $C_{16}H_{11}^+$ isomers 1, 2 and 4. | 26 |
| 2.8 | Benzene geometry changes (dashed line). 1 – during protonation, 2 – during cation dehydrogenation. | 27 |
| 2.9 | The energy landscape for protonated benzene. | 33 |
| 2.10 | The energy landscape of protonated naphthalene. | 35 |
| 2.11 | Protonated anthracene energy landscape. | 37 |
| 2.12 | A simplified version of the protonated phenanthrene energy landscape. . . . | 39 |

| | | |
|------|---|----|
| 2.13 | The energy landscape of protonated pyrene (not complete). | 40 |
| 2.14 | Hydrogenated benzene energy landscape. | 41 |
| 2.15 | Hydrogenated naphthalene energy landscape. | 42 |
| 2.16 | Hydrogenated anthracene energy landscape. | 43 |
| 3.1 | The π molecular orbitals of benzene. | 58 |
| 3.2 | The π molecular orbitals of protonated benzene. | 59 |
| 3.3 | Orthogonal axis selection for molecules with different symmetry. | 60 |
| 3.4 | Diffuse interstellar bands and calculated $S_1 \leftarrow S_0$ wavelengths for protonated PAHs. | 64 |
| 4.1 | The pulsed discharge source design. | 70 |
| 4.2 | Pulsed nozzle discharge voltage and current profiles. | 72 |
| 4.3 | Mass spectra of anthracene and protonated anthracene in He <i>vs.</i> H ₂ discharges. | 74 |
| 4.4 | H ₃ ⁺ formation and the protonation of different aromatic molecules (benzene, anthracene and pyrene) in hydrogen discharges. | 75 |
| 4.5 | Pulsed discharge cluster source with two pulsed valves. | 77 |
| 4.6 | The time-of-flight mass spectrometer setup for photodissociation experiments (top view). | 80 |
| 4.7 | A top view of the BBO type II OPO. | 86 |
| 4.8 | A top view of the BBO type I and II hybrid OPO with rotated prism cavity. | 88 |
| 4.9 | A rotated right angle prism. | 89 |
| 4.10 | The additional phase delay caused by an Al-coated BK-7 right angle prism. Calculated by Foreal Spectrum Co. | 90 |
| 4.11 | Light polarizations in a birefringent nonlinear crystal. | 91 |

| | | |
|------|--|-----|
| 4.12 | Beam shape for the mixed BBO type I and II prism cavity OPO. | 93 |
| 4.13 | Hybrid cavity OPO wavemeter reading at $\lambda_{\text{idler}} = 719$ nm. | 93 |
| 5.1 | An ion channel mass spectrum of protonated anthracene photodissociation with $\lambda = 193$ nm excimer laser pulses. | 104 |
| 5.2 | An ion channel mass spectrum of protonated pyrene photodissociation with $\lambda = 193$ nm excimer laser pulses. | 104 |
| 5.3 | Mass spectrum of the neutral products from protonated anthracene photodis- sociation. | 105 |
| 5.4 | Comparison of the linear mode mass spectra for protonated anthracene and its neutral photodissociation products. | 105 |
| 5.5 | Protonated anthracene photodissociation with $\lambda = 193$ nm excimer laser pulses. The dependence of neutral products yield on the pulse energy is indi- cated by the linear fits in this and subsequent log-log plots. | 108 |
| 5.6 | Protonated anthracene photodissociation with $\lambda = 248$ nm excimer laser pulses. | 109 |
| 5.7 | Protonated pyrene photodissociation with $\lambda = 193$ nm excimer laser pulses. . | 110 |
| 5.8 | Estimates of dissociation energy for protonated anthracene by multiphoton nanosecond laser excitation. | 111 |
| 6.1 | A mass spectrum of the two-nozzle source of protonated anthracene–water clusters. | 118 |
| 6.2 | The benzene–water ($\text{C}_6\text{H}_6 \cdot \text{H}_2\text{O}$) dimer geometry. | 119 |
| 6.3 | Protonated anthracene–water ($1\text{-C}_{14}\text{H}_{11}^+ \cdot \text{H}_2\text{O}$) cluster geometry. | 120 |

| | | |
|------|---|-----|
| 6.4 | Protonated anthracene–water ($C_{14}H_{11}^+ \cdot H_2O$) cluster photodissociation spectrum. Top: The recorded spectrum and exponential+Lorentzian fit. Bottom: Data with the exponential rise to short wavelengths removed. | 122 |
| 6.5 | The expected protonated anthracene–water cluster photodissociation spectrum from comparisons with PAH and PAH^+ clusters. | 125 |
| A.1 | Calculated benzene C_6H_6 IR vibrational spectrum. | 169 |
| A.2 | Calculated protonated benzene $C_6H_7^+$ IR vibrational spectrum. | 169 |
| A.3 | Calculated naphthalene $C_{10}H_8$ IR vibrational spectrum. | 170 |
| A.4 | Calculated protonated naphthalene 1- $C_{10}H_9^+$ IR vibrational spectrum. | 170 |
| A.5 | Calculated protonated naphthalene 2- $C_{10}H_9^+$ IR vibrational spectrum. | 171 |
| A.6 | Calculated anthracene $C_{14}H_{10}$ IR vibrational spectrum. | 172 |
| A.7 | Calculated protonated anthracene 1- $C_{14}H_{11}^+$ IR vibrational spectrum. | 172 |
| A.8 | Calculated protonated anthracene 2- $C_{14}H_{11}^+$ IR vibrational spectrum. | 173 |
| A.9 | Calculated protonated anthracene 9- $C_{14}H_{11}^+$ IR vibrational spectrum. | 173 |
| A.10 | Calculated phenanthrene $C_{14}H_{10}$ IR vibrational spectrum. | 174 |
| A.11 | Calculated protonated phenanthrene 1- $C_{14}H_{11}^+$ IR vibrational spectrum. | 174 |
| A.12 | Calculated protonated phenanthrene 2- $C_{14}H_{11}^+$ IR vibrational spectrum. | 175 |
| A.13 | Calculated protonated phenanthrene 3- $C_{14}H_{11}^+$ IR vibrational spectrum. | 175 |
| A.14 | Calculated protonated phenanthrene 4- $C_{14}H_{11}^+$ IR vibrational spectrum. | 176 |
| A.15 | Calculated protonated phenanthrene 9- $C_{14}H_{11}^+$ IR vibrational spectrum. | 176 |
| A.16 | Calculated pyrene $C_{16}H_{10}$ IR vibrational spectrum. | 177 |
| A.17 | Calculated protonated pyrene 1- $C_{16}H_{11}^+$ IR vibrational spectrum. | 177 |
| A.18 | Calculated protonated pyrene 2- $C_{16}H_{11}^+$ IR vibrational spectrum. | 178 |
| A.19 | Calculated protonated pyrene 4- $C_{16}H_{11}^+$ IR vibrational spectrum. | 178 |

| | | |
|------|--|-----|
| B.1 | Pulsed discharge source. | 191 |
| B.2 | Ground (outside) pulsed discharge electrode. | 192 |
| B.3 | High voltage (inside) pulsed discharge electrode. | 193 |
| B.4 | Teflon insulating spacer between discharge electrodes. | 194 |
| B.5 | PEEK insulating spacer between inside electrode and pulsed valve. | 195 |
| B.6 | Electrode inserts for screw insulation. | 196 |
| B.7 | Screw washer for insulation form outside electrode. | 197 |
| B.8 | Pulsed discharge cluster source with two pulsed valves. | 198 |
| B.9 | Ground (outside) discharge electrode for cluster production. | 199 |
| B.10 | Non-discharge pulsed valve faceplate flange for cluster production. | 200 |
| B.11 | TTL pulse width selector circuit, triggered by a TTL pulse rising front. . . . | 201 |
| B.12 | Pulsed valve driver circuit. | 203 |
| B.13 | One channel of the TOF MS high voltage pulser. | 204 |
| B.14 | TOF MS pulser high voltage pulse profile (full). | 205 |
| B.15 | TOF MS pulser high voltage pulse profile (front). | 205 |
| B.16 | TTL triggering frequency divider. | 207 |

List of Tables

| | | |
|-----|---|-----|
| 1.1 | Abundance of the more common chemical elements in the solar system [4]. | 1 |
| 1.2 | Identified interstellar and circumstellar molecules and molecular ions (as of Dec. 2004). | 2 |
| 2.1 | PC performance tests with GAUSSIAN 98. | 19 |
| 2.2 | Experimental and calculated proton affinities of neutral aromatics. | 31 |
| 2.3 | Experimental and calculated ionization energies of neutral aromatics. | 31 |
| 3.1 | Convergence dependence on the basis set for the $S_1 \leftarrow S_0$ transition wavelength (nm) calculations in neutral and protonated naphthalene. | 55 |
| 3.2 | Scaling factors for the $S_1 \leftarrow S_0$ transitions in neutral aromatic hydrocarbons. | 56 |
| 3.3 | Scaled calculated $S_1 \leftarrow S_0$ wavelengths for neutral and protonated PAHs. | 62 |
| 3.4 | Comparison of the calculated $S_1 \leftarrow S_0$ wavelengths and ground state dissociation energies for protonated PAHs, in kcal/mol. | 63 |
| 4.1 | OPO wave polarizations for BBO type I and II crystals. | 91 |
| A.1 | Symmetry Groups, Dipole Moments, Rotational Constants. | 138 |
| A.2 | Benzene (C_6H_6) Z-Matrix. | 139 |
| A.3 | Protonated benzene ($C_6H_7^+$) Z-Matrix. | 139 |
| A.4 | Naphthalene ($C_{10}H_8$) Z-Matrix. | 140 |

| | | |
|------|--|-----|
| A.5 | Protonated naphthalene ($1\text{-C}_{10}\text{H}_9^+$) Z-Matrix. | 140 |
| A.6 | Protonated naphthalene ($2\text{-C}_{10}\text{H}_9^+$) Z-Matrix. | 141 |
| A.7 | Anthracene ($\text{C}_{14}\text{H}_{10}$) Z-Matrix. | 142 |
| A.8 | Protonated anthracene ($1\text{-C}_{14}\text{H}_{11}^+$) Z-Matrix. | 143 |
| A.9 | Protonated anthracene ($2\text{-C}_{14}\text{H}_{11}^+$) Z-Matrix. | 144 |
| A.10 | Protonated anthracene ($9\text{-C}_{14}\text{H}_{11}^+$) Z-Matrix. | 145 |
| A.11 | Phenanthrene ($\text{C}_{14}\text{H}_{10}$) Z-Matrix. | 146 |
| A.12 | Protonated phenanthrene ($1\text{-C}_{14}\text{H}_{11}^+$) Z-Matrix. | 147 |
| A.13 | Protonated phenanthrene ($2\text{-C}_{14}\text{H}_{11}^+$) Z-Matrix. | 148 |
| A.14 | Protonated phenanthrene ($3\text{-C}_{14}\text{H}_{11}^+$) Z-Matrix. | 149 |
| A.15 | Protonated phenanthrene ($4\text{-C}_{14}\text{H}_{11}^+$) Z-Matrix. | 150 |
| A.16 | Protonated phenanthrene ($9\text{-C}_{14}\text{H}_{11}^+$) Z-Matrix. | 151 |
| A.17 | Pyrene ($\text{C}_{16}\text{H}_{10}$) Z-Matrix. | 152 |
| A.18 | Protonated pyrene ($1\text{-C}_{16}\text{H}_{11}^+$) Z-Matrix. | 153 |
| A.19 | Protonated pyrene ($2\text{-C}_{16}\text{H}_{11}^+$) Z-Matrix. | 154 |
| A.20 | Protonated pyrene ($4\text{-C}_{16}\text{H}_{11}^+$) Z-Matrix. | 155 |
| A.21 | Scaling of the benzene molecule vibrational frequencies. | 156 |
| A.22 | Scaling of the anthracene molecule vibrational frequencies. | 157 |
| A.23 | Benzene and protonated benzene: scaled vibrational frequencies and IR intensities. | 158 |
| A.24 | Naphthalene and protonated naphthalene: scaled vibrational frequencies and IR intensities. | 159 |
| A.25 | Anthracene and protonated anthracene: scaled vibrational frequencies and IR intensities. | 161 |

| | | |
|------|--|-----|
| A.26 | Phenanthrene and protonated phenanthrene: scaled vibrational frequencies and IR intensities. | 163 |
| A.27 | Pyrene and protonated pyrene: scaled vibrational frequencies and IR intensities. | 167 |
| A.28 | Protonated benzene energy landscape. | 179 |
| A.29 | Protonated naphthalene energy landscape. | 179 |
| A.30 | Protonated anthracene energy landscape. | 180 |
| A.31 | Protonated phenanthrene energy landscape. | 180 |
| A.32 | Protonated pyrene energy landscape. | 180 |
| A.33 | Hydrogenated benzene energy landscape. | 181 |
| A.34 | Hydrogenated naphthalene energy landscape. | 181 |
| A.35 | Hydrogenated anthracene energy landscape. | 182 |
| A.36 | Ionization energies for PAHs, hydrogenated and dehydrogenated PAHs. . . . | 183 |
| A.37 | Calculated first singlet excited states of neutral and protonated PAHs. S_1 state energies, $S_1 \leftarrow S_0$ wavelengths, red shifts, oscillator strengths. | 184 |
| A.38 | Symmetry and S_0 , S_1 electronic states assignment for neutral and protonated PAHs. | 185 |
| A.39 | Highest occupied (HOMO) and lowest unoccupied (LUMO) molecular orbitals of neutral and protonated PAHs. | 186 |

Chapter 1

Protonated Polycyclic Aromatic Hydrocarbons and the Interstellar Medium

1.1 Interstellar Molecules

Although hydrogen is the most abundant element in the universe, it is other elements that determine the complexity of interstellar chemistry. Besides hydrogen and helium which account for 98% of the mass of a gas of ‘solar composition,’ the next most abundant elements are oxygen, carbon, and nitrogen (Table 1.1). Together with hydrogen, these elements form the main building blocks for molecules detected in the interstellar medium, or ISM.

Table 1.1: Abundance of the more common chemical elements in the solar system [4].

| Element | | Abundance Atoms / 10^6 Si |
|---------|-----------|--------------------------------|
| H | Hydrogen | $2.72 \cdot 10^{10}$ |
| He | Helium | $2.15 \cdot 10^9$ |
| O | Oxygen | $2.01 \cdot 10^7$ |
| C | Carbon | $1.21 \cdot 10^7$ |
| Ne | Neon | $3.76 \cdot 10^6$ |
| N | Nitrogen | $2.48 \cdot 10^6$ |
| Mg | Magnesium | $1.08 \cdot 10^6$ |
| Si | Silicon | $1.00 \cdot 10^6$ |
| Fe | Iron | $9.00 \cdot 10^5$ |
| S | Sulfur | $5.15 \cdot 10^5$ |

Table 1.2: Identified interstellar and circumstellar molecules and molecular ions (as of Dec. 2004).

| Number of atoms | | | | | | | | | |
|-----------------|-------------------------------|--------------------------------|---------------------------------|---------------------------------|-----------------------------------|-----------------------------------|-----------------------------------|-------------------------------------|--|
| 2 | 3 | 4 | 5 | 6 | 7 | 8 | 9 | 10+ | |
| H ₂ | H ₂ O | NH ₃ | CH ₄ | CH ₃ OH | HCCCCH ₃ | CH ₃ COOH | (CH ₃) ₂ O | (CH ₃) ₂ CO | |
| CO | H ₂ S | H ₂ CO | SiH ₄ | CH ₃ SH | HC(O)CH ₃ | HC(O)OCH ₃ | C ₂ H ₅ OH | (CH ₂ OH) ₂ | |
| CSi | HCN | H ₂ CS | CH ₂ NH | C ₂ H ₄ | CH ₃ NH ₂ | H ₃ C ₃ -CN | C ₂ H ₅ CN | | |
| CP | HNC | C ₂ H ₂ | NH ₂ CN | HC ₄ H | CH ₂ CH(CN) | HOCH ₂ C(O)H | CH ₃ C ₄ H | HC ₈ CN | |
| CS | CO ₂ | HNCO | CH ₂ CO | CH ₃ CN | HC ₄ -CN | C ₆ H ₂ | HC ₆ CN | | |
| NO | SO ₂ | HNCS | HCOOH | CH ₃ NC | C ₆ H | C ₆ H ₂ | C ₈ H | C ₆ H ₆ | |
| NS | MgCN | H ₃ O ⁺ | HCC-CN | HC(O)NH ₂ | c-C ₂ H ₄ O | C ₂ H ₆ | | OC(CH ₂ OH) ₂ | |
| SO | MgNC | HOCO ⁺ | HCC-NC | HCCC(O)H | CH ₂ CH(OH) | C ₇ H | | | |
| HCl | NaCN | C ₃ S | c-C ₃ H ₂ | C ₅ H | | H ₂ CCHC(O)H | | HC ₁₁ N | |
| NaCl | N ₂ O | H ₂ CN | l-C ₃ H ₂ | HC ₃ NH ⁺ | | | | | |
| KCl | NH ₂ | c-C ₃ H | CH ₂ CN | C ₅ O | | | | | |
| AlCl | OCS | l-C ₃ H | C ₄ H | C ₅ N | | | | | |
| AlF | HCO | HCCN | C ₄ Si | | | | | | |
| PN | C ₃ | H ₂ CO ⁺ | C ₅ | | | | | | |
| SiN | C ₂ H | C ₂ CN | HNCCC | | | | | | |
| SiO | HCO ⁺ | C ₃ O | H ₂ COH ⁺ | | | | | | |
| SiS | HOC ⁺ | HCNH ⁺ | | | | | | | |
| NH | N ₂ H ⁺ | CH ₂ D ⁺ | | | | | | | |
| OH | HNO | CH ₃ | | | | | | | |
| C ₂ | HCS ⁺ | SiC ₃ | | | | | | | |
| CN | H ₃ ⁺ | ND ₃ | | | | | | | |
| HF | C ₂ O | | | | | | | | |
| CO ⁺ | C ₂ S | | | | | | | | |
| SO ⁺ | SiC ₂ | | | | | | | | |
| CH | AlNC | | | | | | | | |
| CH ⁺ | CH ₂ | | | | | | | | |
| SH | SiCN | | | | | | | | |
| LiH | | | | | | | | | |
| FeO | | | | | | | | | |

Nearly 150 molecules and molecular ions have been detected in interstellar and circumstellar environments to date [5,6] (Table 1.2). Most of them are small, 2 – 4 atom molecules. Many of the larger molecules are linear or highly symmetric and have large dipole moments which facilitate their detection. There must be many more less abundant or not as strongly absorbing/emitting molecules in the ISM that have not yet been detected or positively identified. One such suite of molecules involves polycyclic aromatic hydrocarbons (PAHs) and their derivatives. While PAHs are believed to be present in the ISM in large quantities, benzene is the only aromatic molecule for which a possible detection has been reported using high resolution spectroscopy such as that used to assemble Table 1.2 [7].

1.2 PAHs and the Unidentified IR Emission Bands

In 1973, an Unidentified Infrared Emission band (UIR) was observed at $11.3\ \mu\text{m}$ from a planetary nebulae [8]. A few other observations of a variety of objects added 3.3, 6.2, 7.7, 8.6, 12.7, 14.2, and $16.2\ \mu\text{m}$ bands to the UIR list [9–13]. The strongest emission was observed from dusty regions bathed in the intense UV radiation from nearby young stars. The emitting species could not be identified exactly, although some conclusions were made about their nature.

Associated with these UIR bands is a pseudo-continuum component whose color temperature is independent of the distance from the exciting star [14]. Thus, both the continuum and bands must be produced by the ‘heating’ associated with the absorption of a single photon [15,16]. This requires the species responsible for the emission to be intermediate in size, between small molecules and macroscopic dust grains ($\sim 20 - 50$ atoms). It has been noted that some of the vibrations of aromatic hydrocarbons are close in wavelength to many of the UIR features [17]. Based on intensity ratios and the correlation observed among different

UIRs, it has been suggested that the PAHs which generate these IR bands are peripherally hydrogenated, should have pericondensed structures, and may be ionized [16, 18].

Numerous laboratory experiments have been conducted to measure the IR and visible spectra of neutral and ionic PAHs, and the results have been compared to astronomical observations [19–21]. From laboratory measurements, it was established that both neutral and cationic PAHs may be UIR carriers [22], but that ionized PAHs provide a better match to the general characteristics observed in the interstellar spectra. Density functional calculations added protonated PAHs to that list [23]. Although no single PAH species can account for the full suite of UIR features alone, it is possible to approximate the observed astronomical spectra by a mixture of many different PAHs [24].

PAHs are believed to be ubiquitous in the ISM, for the UIR features are observed throughout the galaxy. As a class, they may be the most abundant organic species in the ISM, and may account for up to 20% of total interstellar carbon [25]. They may also be responsible for other astronomical features, such as the Diffuse Interstellar Bands, discussed next.

1.3 The Diffuse Interstellar Bands

The Diffuse Interstellar Bands, or DIBs, present the longest-standing puzzle in astronomical spectroscopy [26]. The DIBs are $1 - 200 \text{ cm}^{-1}$ wide features in seen visible and near infrared spectra of reddened stars, produced by the absorption of star light by species in diffuse or translucent interstellar clouds. They were originally discovered in 1922 [27], but their interstellar nature was only established some twelve years later [28, 29]. By 1975, 39 DIBs had been discovered [30]. Thanks to ongoing improvements in astronomical spectrographs and especially in CCD arrays, a large number of weaker DIBs have now been

discovered. Based on more recent surveys [31–33], for example, there are more than 150 known DIBs that span the wavelength interval from 380 to 950 nm (Figure 1.1).

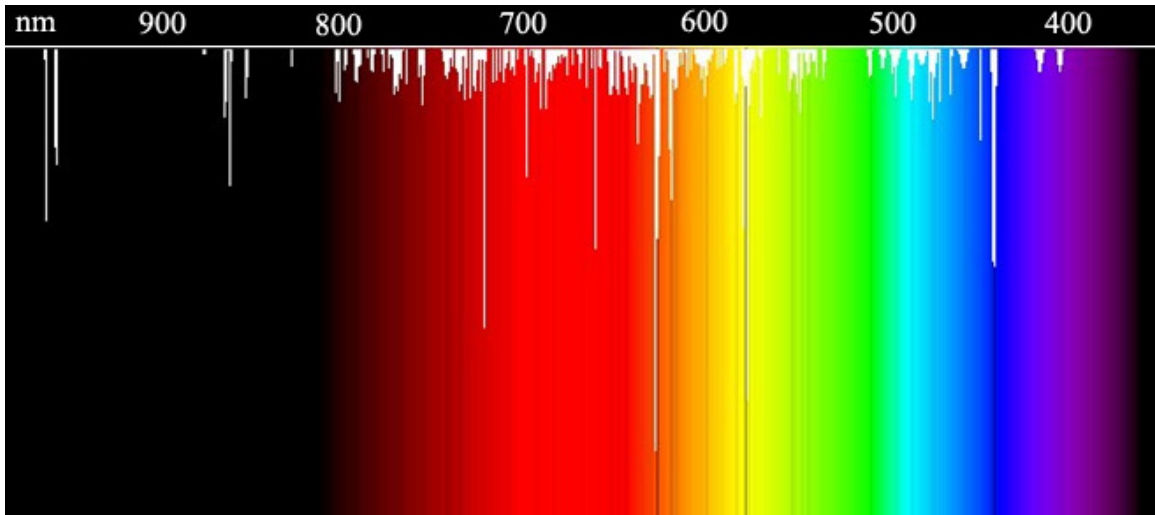


Figure 1.1: A synthetic spectrum of the diffuse interstellar bands, based on the DIB compilation in [1]. The image is from [2].

Many different theories have been proposed to account for the DIBs. The wide range of DIB widths and the fact that a few of the DIBs are seen in emission toward unusual objects points to the molecular nature of the species responsible. Carriers cannot reside on or within dust particles or grains because particle size, shape and composition influence the peak positions and profiles, which have not been observed astronomically. Since a wide variety of carbon-containing species are found in space and since the overall strength of the DIBs is well correlated with the $[C]/[H]$ ratio, carbonaceous molecules or radicals are the most attractive candidates. Among them are [34, 35]:

1. Highly unsaturated hydrocarbons (carbon chains)
2. Polycyclic aromatic hydrocarbons (PAHs)
3. Fullerenes and their derivatives

4. Porphyrins
5. Other unspecified organics

The first two classes have been studied extensively in the laboratory setting, and therefore, will be reviewed here.

1.3.1 Carbon Chains and the DIBs

Carbon chains have been cited as promising candidates for DIB carriers for many years [36,37]. Their conjugated systems of electrons produce intense $\pi - \pi^*$ transitions at visible and UV wavelengths. Both the electronic oscillator strengths and dipole moments of (apolar) carbon chains increase with chain length, a fact that has enabled the detection of quite long chains – up to HC_{11}N and C_8H – in dark molecular clouds by radio astronomy methods [38,39]. Laboratory spectra of carbon chains have been measured in microwave [40–42], visible, and UV [43–47] wavelength ranges. Such studies culminated in measurements of the electronic absorption spectra of carbon chain anions C_6^- , C_7^- , C_8^- and C_9^- , whose $\pi - \pi^*$ transitions were found to be very close to a number of DIBs [48,49]. More detailed astronomical spectroscopy failed to yield a definite assignment of any DIBs to carbon chain anions [50–52], but even so, it is not possible to completely rule out carbon chains as potential DIB carriers – especially large chains where very strong excited state (S_n , $n \geq 2$) bands move into the visible [53].

1.3.2 PAHs and the DIBs

PAHs are good candidates for DIB carriers. They are thought to be present in a large number of environments in the ISM from the widespread detection of the UIRs. While the UIRs provide important constraints on the *type* of material responsible for the emission, they

are sufficiently broad and entangled that the identification of specific molecular species is not possible. These bands are believed to be emitted by large, internally excited molecules, and the only way to efficiently generate such excitation is through the absorption of visible or UV photons. The first electronic transitions of small, multi-ring neutral PAHs lie in the near-UV. For example, the $S_1 \leftarrow S_0$ transition for anthracene occurs at 361.17 nm, and that for pyrene at 367.43 nm. A PAH molecule needs to have at least 25 – 30 carbon atoms to absorb strongly in the visible range, and the number of carbon atoms must be significantly larger in order to achieve absorption in the red and near IR parts of the spectrum where many DIBs are located.

On the other hand, even small PAH cations absorb visible and near-IR photons. For example, the $D_2 \leftarrow D_0$ transitions of the naphthalene and phenanthrene cations lie at 670.65 nm and 891.90 nm, respectively; the $D_3 \leftarrow D_0$ transition of the naphthalene cation has been measured to be 454.85 nm. The ionization energies of PAHs are below 9.3 eV, and for PAHs with more than two aromatic rings they are less than 7.9 eV. Neutral PAHs should therefore be ionized rapidly in the regions of the ISM exposed to UV radiation, i.e., close to stars or in diffuse interstellar clouds.

A few attempts have been made to compare PAH electronic spectra with the DIBs [54–56], but while there are some close coincidences, no DIBs have been found to have an exact match with the measured electronic transitions of neutral PAHs or their cations. In general, if PAHs are indeed DIB carriers, one might expect them to be responsible for the wider DIB features due to their large sizes as compared to the molecules detected by high resolution spectroscopy.

In the past, the lack of laboratory data for PAHs led to a suite of extensive studies in matrices [56–59], helium droplets [60, 61] and the gas phase (both isolated [61–69] and in

clusters [69–74]). There are, however, several experimental challenges that make it difficult to obtain the spectra of cold, isolated, multi-ring PAHs which could be directly compared with the DIBs.

In the gas phase, it is hard to achieve high PAH concentrations due to the low vapor pressure of the solid. For example, most PAH samples have to be heated to high temperatures, sometimes in excess of 300 – 500 °C, in order to carry out direct absorption studies or to efficiently seed them into molecular beams. The heated vapor is vibrationally hot, which in turn, leads to significant spectral broadening. Furthermore, PAH cations are usually created in some form of a discharge which leads to even broader spectra, thanks to the high electron temperature in such sources.

To alleviate some of these concerns, the spectra of clusters of small PAHs with argon atoms have been recorded [69–74]. Cluster dissociation has been especially useful in obtaining the spectra of cold PAH cations with rare gases [71–74]. Here, neutral PAH clusters were threshold photoionized to yield the $\text{PAH}^+\text{-Rg}$ species. In principle, both vibrational and electronic spectra of PAH cations can be obtained in this fashion, but the spectra acquired are shifted from that of bare chromophore, sometimes by 100 – 200 cm^{-1} – thus, precluding a direct comparison to the DIBs or the UIR features.

Similar studies of PAHs in argon and neon matrices conducted at cryogenic temperatures suffer from similar limitations. The PAH concentration can be varied as they are deposited into a matrix and as a result, very good signal-to-noise ratios can be obtained with a relatively simple apparatus. The main problems with PAH spectra in matrices are the spectral shift and the broadening due to interactions with matrix atoms, but such data sets form an excellent overview from which to select candidate molecules for more detailed study.

1.4 Protonated PAHs

1.4.1 Protonated PAHs in ISM

Neutral PAHs in the ISM may be ionized by UV radiation. The PAH cations created may react with highly abundant hydrogen to form protonated PAHs. In order to pursue quantitative chemical modeling, the reaction rates between hydrogen and PAH cations, dehydrogenated cations, and protonated PAHs were measured in flowing afterglow-selected ion flow tube experiments for benzene, naphthalene and pyrene [75]. No significant reactions were observed between PAH cations or protonated PAHs with H_2 molecules, but PAH cations reacted with atomic hydrogen at nearly the Langevin rate ($\sim 10^{-10} \text{ cm}^3/\text{s}$) to form protonated PAHs. Dehydrogenated PAH cations associated with H atoms at almost the same rate. On the other hand, the association of protonated PAHs with atomic hydrogen was found to be ≥ 100 times slower. This led authors to conclude that protonated PAHs would be a dominant form of PAHs in ISM regions with a high ionization rate and hydrogen atom abundance such as diffuse or translucent clouds.

Based on these experiments, the interstellar chemistry involving benzene/naphthalene cations and hydrogen atoms have been considered [76]. It was concluded that even at low densities, the radiative association with H is very efficient, and that the H_2 molecule loss dissociation channel for protonated species is not likely to be important in these reactions.

Another source of protonated PAHs in the denser regions of the ISM may be the proton transfer from known protonated species such as H_3^+ , HCO^+ , H_3O^+ [77–81], to neutral PAHs. Reaction rate studies of proton transfer to a range of organic compounds in a recent flowing afterglow-selected ion flow tube experiment [82] found that the proton transfer to alkanes, alkenes and alkynes was dissociative, non-dissociative or both, depending on whether the

proton donor was H_3^+ , H_3O^+ or N_2H^+ , respectively. Aromatic hydrocarbons, on the other hand, underwent only non-dissociative proton transfer, forming protonated PAHs.

To extend such laboratory results on a few selected species to the more general population of potential DIB and UIR carriers in the ISM, a statistical theory has been developed to consider the hydrogenation and charge states of PAHs in diffuse interstellar clouds [83,84]. The main result was that small PAHs, specifically those with less than 20 carbon atoms, would be destroyed by the interstellar UV radiation field; intermediate size PAHs with 20 – 30 carbon atoms would be highly dehydrogenated but stable; and large PAHs would be nearly fully hydrogenated, and even protonated. In terms of the overall charge balance, large PAHs were predicted to be essentially 100% ionized, with 60 – 80% of intermediate size PAHs estimated to be in their cationic or protonated forms.

Both of the experiments outlined above indicate that protonated PAHs should exist in the ISM, especially for large, multi-ring PAHs. Smaller PAHs should exist in a wide range of hydrogenation and charge states that depend sensitively on the H/H_2 ratio and the UV radiation flux. In particular, the photostability of each type of PAH will play an important role in the overall chemical speciation of the important suite of compounds.

1.4.2 Protonated PAHs and the DIBs

Protonated PAHs are closed-shell ions. Their electronic structure is closely related to that of neutral PAHs in that protonated PAHs retain a system of conjugated electrons which is responsible for the lowest energy $\pi - \pi^*$ electronic transitions. As described in Chapter 3, such transitions are expected to be red-shifted with respect to the same transition in the corresponding neutral PAH. The amount of this shift is not known, but from simple energetic considerations, it is expected to be on the order of a few tens of nanometers. Thus,

even small PAHs with only 3 – 4 aromatic rings may absorb in the DIB wavelength range.

1.4.3 Other Applications of Protonated Aromatics

Aromatic electrophilic substitution reactions are an important class of reactions in organic chemistry. Such substitution reactions occur in two steps:



where AH is a neutral aromatic molecule and E is an electrophilic reagent (Cl, Br, NO₃, SO₃H, etc.). Protonated aromatic molecules are believed to be intermediates in these aromatic electrophilic substitution reactions [85].

In living organisms, many molecules form hydrogen bonds. UV radiation may break some of these bonds and lead to the formation of protonated aromatic species. The study of protonated aromatics may help lead to a better understanding of the radiation damage processes that occur in biological cells.

1.4.4 Previous Studies of Protonated Aromatics

UV spectra of protonated aromatic compounds (carbonium ions) were studied in anhydrous solution with HF and BF₃ [86]. These spectra consisted of broad absorption bands and were located at visible wavelengths. To re-examine these results, solution spectra for the complexes of aromatic compounds with Al₂Br₆ and Al₂Cl₆ have been recorded [87]. When the C₆H₆·Al₂Br₆ complex was stabilized with HBr, protonated benzene was created. The UV spectrum of this solution displayed a broad structureless band with a maximum near 330 – 340 nm and another broad absorption feature at wavelengths shorter than 275 nm. A systematic study of UV, IR and NMR spectra of protonated aromatic compounds performed in similar solutions [88] found UV absorption band maxima at 332 nm for pro-

tonated benzene, 390 nm for protonated naphthalene, 408 nm for protonated anthracene, 510 nm for protonated phenanthrene, and 476 nm for protonated pyrene.

More directly relevant to the results presented in this thesis are the gas phase photodissociation spectra of organic compounds obtained in an ion cyclotron resonance mass spectrometer [89,90]. Among the experiments carried out was the UV photodissociation of protonated benzene. The recorded spectrum had two broad featureless absorption bands with maxima at 330 and 240 nm. These bands corresponded to the $S_1 \leftarrow S_0$ and $S_2 \leftarrow S_0$ electronic transitions of protonated benzene. The protonation led to relatively large redshifts: ~ 80 nm for the S_1 electronic state and $\sim 40 - 50$ nm for the S_2 state; the widths of the bands measured were $\sim 25 - 35$ nm FWHM. The spectrum was recorded with 10 nm resolution and most likely, the dissociation was multiphoton [91].

The structure of protonated benzene has been the subject of a number of theoretical studies [92–95]. Originally, σ - and π -complexes were considered as two possible structures. The proton binds to a carbon atom in the σ -complex forming a CH_2 site, while in the π -complex, the proton binds to the system of aromatic electrons. Later, the bridged structure in which the proton binds to the C–C bond was added for consideration. These studies have established that the σ -complex is a stable isomer of protonated benzene, the bridged structure is a first order transition state, and the π -complex is a second order transition state.

For larger systems, the structures and vibrational frequencies of protonated naphthalene, protonated pyrene, protonated coronene and protonated circumcoronene have been calculated using density functional theory [23]. All stable isomers were found to have σ -complex structures. Reactions of H atoms with PAH cations to form the protonated σ -complexes were found to be exothermic by 55 – 62 kcal/mol. The energies for both isomers and the

barrier height for 1–2 isomerization of protonated naphthalene have been calculated as well. The main goal of this study was to investigate vibrational spectra of protonated PAHs and, possibly, compare them with the UIRs.

Symmetric and asymmetric C–H stretching vibrations of the CH₂ site of protonated PAHs are characteristic of the σ -complex structure. The spectrum of these vibrations has been measured in gas phase IR dissociation experiments with clusters of protonated benzene with Ar, N₂, CH₄ and H₂O [3,96], an experiment that provided solid experimental proof that the σ -complex is the stable, lowest energy isomer of protonated benzene. The cluster experiment was promptly followed by the IR multiphoton dissociation spectroscopy of protonated benzene using free electron laser in the 6.2 – 9.3 μ m wavelength region [97].

1.5 Research Goals

The goal of this thesis is to study the gas phase properties of protonated PAHs and their interaction with visible and UV radiation. The purpose is to assess whether small protonated PAHs are an important component of ‘molecular grains’ in the ISM, and to investigate the relationship between protonated PAHs and the DIBs. Another outcome of the study would be a better understanding of intrinsic properties of protonated PAHs. There are two main questions addressed by the research presented here:

1. Do protonated PAHs exist in the interstellar medium?
2. Are protonated PAHs the carriers of the diffuse interstellar bands?

To date, only the low resolution spectrum of protonated benzene has been recorded in the gas phase. Electronic spectra of protonated polycyclic aromatic molecules with a few aromatic rings need to be recorded, and data obtained should be compared with the

observed DIBs. Photodissociation has been chosen as the method to record the spectra of protonated PAHs in this thesis, whose structure is described below.

Density functional theory calculations are performed in Chapter 2 in order to analyze the possible dissociation channels of protonated PAHs. In addition, the fate of protonated PAHs upon their recombination with electrons is investigated. Chapter 3 concentrates on the electronic structure of protonated PAHs and on predictions for the $S_1 \leftarrow S_0$ electronic transition wavelengths. A full compendium of the results from Chapters 2 and 3 is presented in Appendix A. The photostability of protonated PAHs is investigated in Chapter 5 via their photodissociation by visible and UV nanosecond lasers. The visible photodissociation spectrum of clusters of protonated anthracene with water is discussed in Chapter 6. The results are summarized in Chapter 7. Chapter 4 contains a detailed description of the experimental setup and some of its most important components. Draft drawings of the discharge parts and critical electric circuit diagrams are located in Appendix B. Appendix C contains the documentation for the data acquisition software developed in this thesis.

Chapter 2

Ground State Calculations for Protonated PAHs

2.1 Introduction

Ab initio ground electronic state calculations can be used to determine geometries and energies of all possible protonated PAH isomers and thereby examine whether there are common properties and general trends among this class of compounds. In addition, the stability and allowed dissociation channels need to be investigated to guide the interpretation of the spectroscopic data presented later in this thesis, while the geometries serve as the starting point for calculation of the energies of excited electronic states.

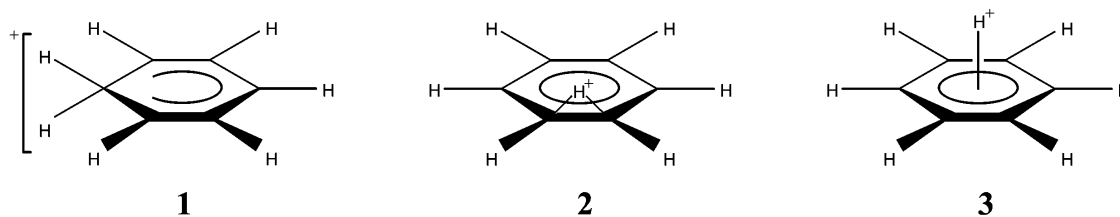


Figure 2.1: Structures for protonated benzene PES stationary points. Adapted from [3].

There have been a number of quantum chemical calculations performed on the structures of protonated benzene [92–95]. Three stationary points on its potential energy surface were

identified (Figure 2.1). They are the σ complex structure (1), the H^+ bridged structure (2), and a π complex of benzene and H^+ (3). Structure (1) is the global minimum (the most stable form) and the other two are first and second order transition states, respectively. Their relative energies were calculated to be 0, 6.4 and 49.3 kcal/mol [3].

Fairly low level results on the structures of stable isomers for selected protonated PAHs (naphthalene, pyrene, coronene, circumcoronene) and their vibrational spectra have also been calculated [23]. An extensive suite of quantum chemical calculations for benzene, naphthalene, anthracene, phenanthrene and pyrene is presented in this chapter. Although benzene is technically not a PAH molecule, it was considered here as a well-studied aromatic test system. Before turning to the results themselves, the nomenclature of protonated PAHs and the computational approach will be covered first.

2.2 Methodology

2.2.1 Naming Conventions

The naming of different isomers of protonated PAHs is based on the IUPAC nomenclature of neutral PAHs. Figure 2.2 outlines the conventional numbering of carbon atoms in neutral PAHs. The numbers in **bold** depict the stable isomers of protonated PAHs. Fusion carbon atoms at the juncture of two aromatic rings are usually not numbered, but they are referenced in certain calculations, especially for protonated naphthalene and anthracene. These atoms are therefore labeled with numbers in *italics*.

For protonated PAHs, the naming system is illustrated by the following example: when H^+ is attached to C atom number 1 of naphthalene or C atom number 9 of anthracene, for example, the 1-hydronaphthalene and 9-hydroanthracene cations are formed, respectively.

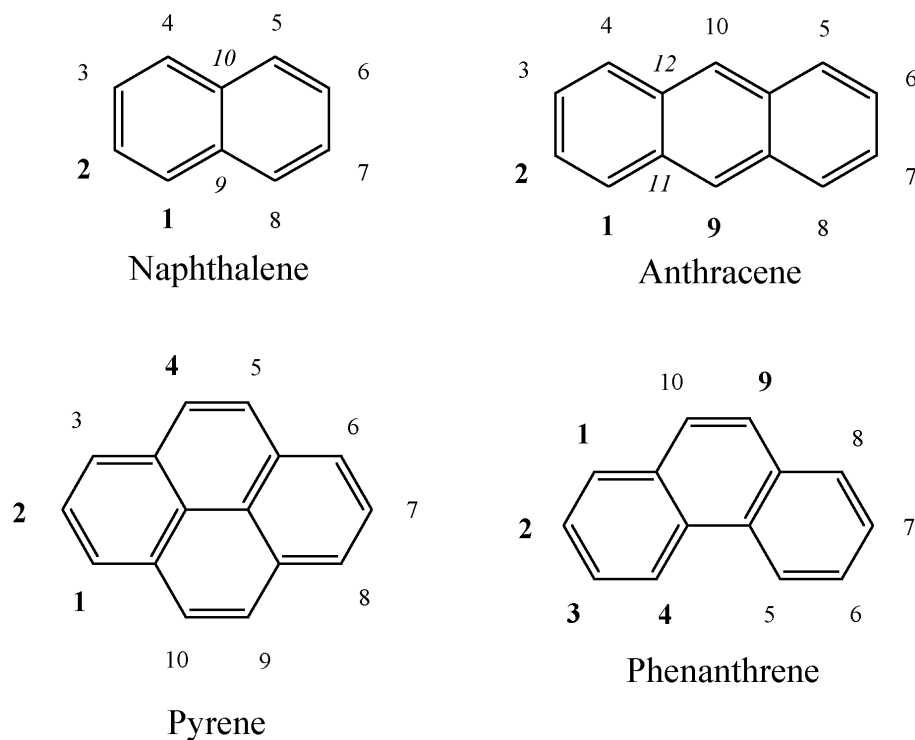


Figure 2.2: Carbon atom numbering conventions for neutral PAHs.

For simplicity, in this thesis the notation isomer 1 of protonated naphthalene and isomer 9 of protonated anthracene, or $1\text{-C}_{10}\text{H}_9^+$ and $9\text{-C}_{14}\text{H}_{11}^+$ will be used. The notation $1\text{-}2\text{-C}_{10}\text{H}_9^+$ thus designates a transition state between $1\text{-C}_{10}\text{H}_9^+$ and $2\text{-C}_{10}\text{H}_9^+$, while $6\rightarrow 1\text{-C}_{10}\text{H}_8^+$ describes $1\text{-C}_{10}\text{H}_9^+$ with a hydrogen atom removed from carbon number 6 of naphthalene. This is an isomer of naphthalene cation, where a hydrogen atom has been moved from carbon atom 6 to carbon atom 1. Similarly, $1\text{-C}_{10}\text{H}_7^+$ designates the naphthalene cation with a hydrogen atom removed from the carbon 1 position.

2.2.2 Software

Contemporary desktop personal computer (PC) systems are now sufficiently powerful to perform *ab initio* calculations on moderately complex systems in reasonable times. Although

they are not as powerful as mainframe systems, they are very attractive from the price and availability perspective. GAUSSIAN 98, Revision A.9 [98] (the most widely used version) for Microsoft Windows was used to carry out all calculations mentioned below.

2.2.3 Choice of the Computer System

Most central processing units (CPUs) on the PC market are manufactured by Intel and Advanced Microdevices (AMD). Software performance depends strongly on the computer hardware, the most important of which is the CPU (specifically its architecture and clock speed). A few tests were therefore performed to determine the best performing PC for GAUSSIAN calculations and consisted of two different calculations (italics below correspond to commands within GAUSSIAN 98):

The first test was to optimize the geometry of isomer 1 of protonated anthracene:

Opt=(CalcAll,Tight,GDIIS) rB3LYP/6-311++G(d,p) Guess=Mix

This calculation is performed mostly in memory and takes about 24 hours.

The second calculation was to optimize the geometry of protonated benzene:

Opt rMP2/6-311+G(d,p) Guess=Mix

This calculation takes only about 1.5 hours, but carries out substantial read/write operations with the hard drive.

The following PC systems, differing mostly by CPU type, were tested:

P4-3.6 – CPU Intel Pentium 4, 3.4 GHz running at 3.67 GHz (8% overclock), RAM 1 Gb Dual DDR 433 (2×433 MHz), Hard drive ATA-5 (133Mb/s), Windows XP SP1.

P4-2.7 – CPU Intel Pentium 4, 2.66 GHz running at 2.72 GHz (2.26% overclock), RAM 1 Gb RDRAM (1066 MHz), Hard drive ATA-5 (133 Mb/s), Windows XP SP1.

A-XP – CPU AMD Athlon XP, 2800+ running at 2.11 GHz (0% overclock), RAM 1 Gb

Dual DDR 333 (2×333 MHz), Hard drive SATA (150 Mb/s), Windows 2000 SP4.

A-64 – CPU AMD Athlon 64, 3000+ running at 2.10 GHz (5% overclock), RAM 1 Gb DDR 433 (433 MHz), Hard drive ATA-5 (133 Mb/s), Windows XP SP1.

Results for each system are presented in Table 2.1 from which it is clear that at present, PCs with Intel Pentium 4 CPUs run GAUSSIAN 98 calculations faster than AMD Athlon CPUs, rated for approximately the same equivalent clock speed. Almost all calculations described in this thesis were performed on the P4-2.7 and P4-3.6 systems.

Table 2.1: PC performance tests with GAUSSIAN 98.

| PC System | P4-3.6 | P4-2.7 | A-XP | A-64 |
|----------------------------------|--------|--------|--------|------|
| CPU Clock, MHz | 3638 | 2720 | 2112 | 2100 |
| Equivalent CPU Clock Rating, MHz | 3638 | 2720 | 2800 | 3150 |
| In-memory job, s | 63900 | 86286 | 106568 | – |
| High disk swap job, s | 4536 | 5484 | 7102 | 5665 |

2.2.4 Theory Level and Basis Set

Density functional theory (DFT) [99,100] has proven to be a good alternative to Linear Combination of Atomic Orbitals-Molecular Orbital (LCAO-MO) *ab initio* methods, especially for aromatic hydrocarbons. The advantages of DFT calculations are in their speed and smaller computer resource requirements. One such method denoted B3LYP (Becke three-parameter functional [101] with Lee-Yang-Parr correlation functional [102]) was used in previous calculations of protonated PAH structures [23] and has been selected here to optimize the geometries and calculate vibrational frequencies of several systems.

The basis set was constrained to be the same for all molecules studied, with a calculation limit of no more than 1 week chosen to define the basis set size. For the largest molecule studied – protonated pyrene – the biggest basis set is 6-311++G** (McLean-Chandler 6-311G basis set [103,104] with polarization functions (d,p) [105] and diffuse functions

++ [106]).

In addition to being faster, DFT performs most integral calculations in memory and requires little swap space on the computer hard drive. For comparison, the Møller-Plesset MP2 6-311++G(d,p) method on protonated benzene uses about 10 Gb of the swap space. For protonated naphthalene at the same theory level and basis set, the required amount of the swap space would exceed 16 Gb which is the maximum allowed by 32-bit versions of GAUSSIAN 98.

Geometry optimization was performed in a few steps, where the basis set size was slowly increased to speed convergence. At the largest basis set, the vibrational frequencies were calculated as a part of the optimization process. The total calculational procedure was as follows:

1. A model of the molecule was built in the GAUSSIAN 98 visualization package GaussView, version 2.1 [107].
2. The geometry was optimized with the 6-31G basis set.
3. The geometry was optimized with the 6-31+G(d) basis set.
4. The geometry was optimized with the 6-311G(d,p) basis set.
5. The geometry was optimized with the 6-311++G(d,p) basis set.

In step 5, the specific calculation call was:

Opt=(CalcAll,Tight,GDIIS) B3LYP/6-311++G(d,p) NoSymm Guess=Mix

Options *CalcAll*, *Tight* and *GDIIS* were used to assure better convergence, while *CalcAll* was used to predict the frequencies and intensities of IR-active vibrational modes. The *NoSymm* switch proved important in stabilizing the convergence criteria for molecules with rotational symmetry, especially neutral PAHs and their cations.

2.3 Geometries

2.3.1 Protonated Benzene, Naphthalene, Anthracene and Pyrene

Appendix A (Tables A.2 – A.20) contains GAUSSIAN Z-matrices for the optimized geometries of neutral benzene, naphthalene, anthracene and pyrene, as well as stable isomers of their protonated forms. The calculated dipole moments, A, B and C rotational constants, and derived molecular symmetry groups are also listed there (Table A.1).

Protonated benzene $C_6H_7^+$ has only one isomer, while the transition state for isomerization (1–2 $C_6H_7^+$) is that of the bridged structure (2) from Figure 2.1. Molecular models of these structures are shown in Figure 2.3.

Protonated naphthalene has two principal isomers: 1– and 2– $C_{10}H_9^+$ (Figure 2.4). An additional isomer 9– $C_{10}H_9^+$ is much higher in energy and has a very low barrier for isomerization into 1– $C_{10}H_9^+$. Thanks to the increasing number of isomers, there are now several isomerization transition states: 1–2, 2–3 (not shown), 1–9 and 9–10.

Protonated anthracene has three main principal isomers: 1–, 2– and 9– $C_{14}H_{11}^+$. Again, the 11– $C_{14}H_{11}^+$ isomer is much higher in energy and has a very low barrier for isomerization into 9– $C_{14}H_{11}^+$. Figure 2.5 presents a number of molecular models of these isomers and the 1–2, 2–3 (not shown), 1–11 (not shown), 9–11 and 11–12(not shown) transition states accessed by proton tunneling or hopping.

Protonated phenanthrene has five stable isomers: 1–, 2–, 3–, 4– and 9– $C_{14}H_{11}^+$ (Figure 2.6). Thanks to the much more complex potential energy surface, higher energy isomers and transition states are not considered here.

Protonated pyrene has three main isomers: 1–, 2– and 4– $C_{16}H_{11}^+$ (Figure 2.7). Less stable isomers and transition states are not considered here.

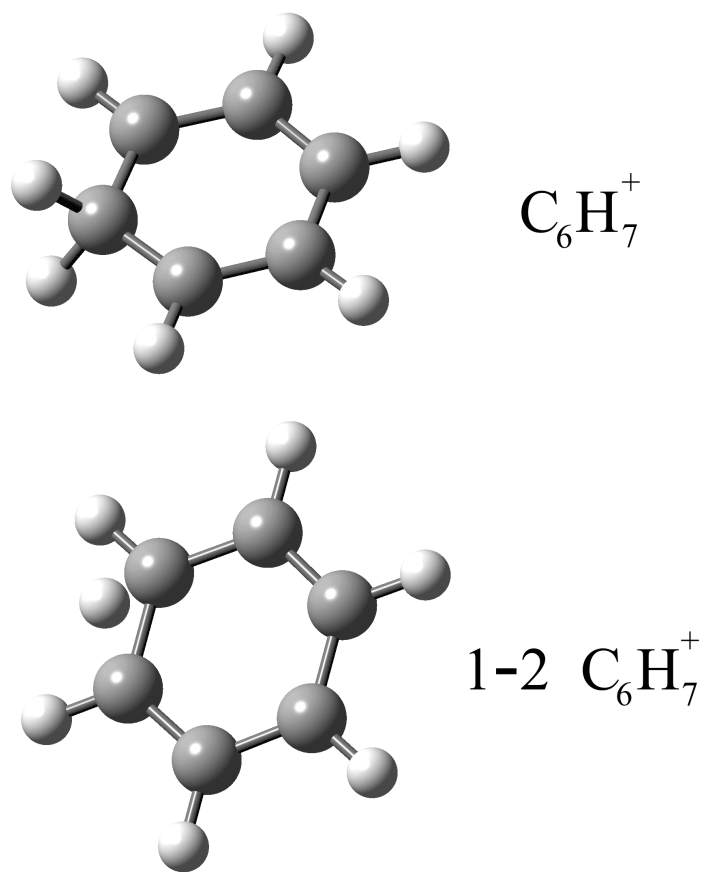


Figure 2.3: Structures of protonated benzene C_6H_7^+ and its isomerization transition state 1-2 C_6H_7^+ .

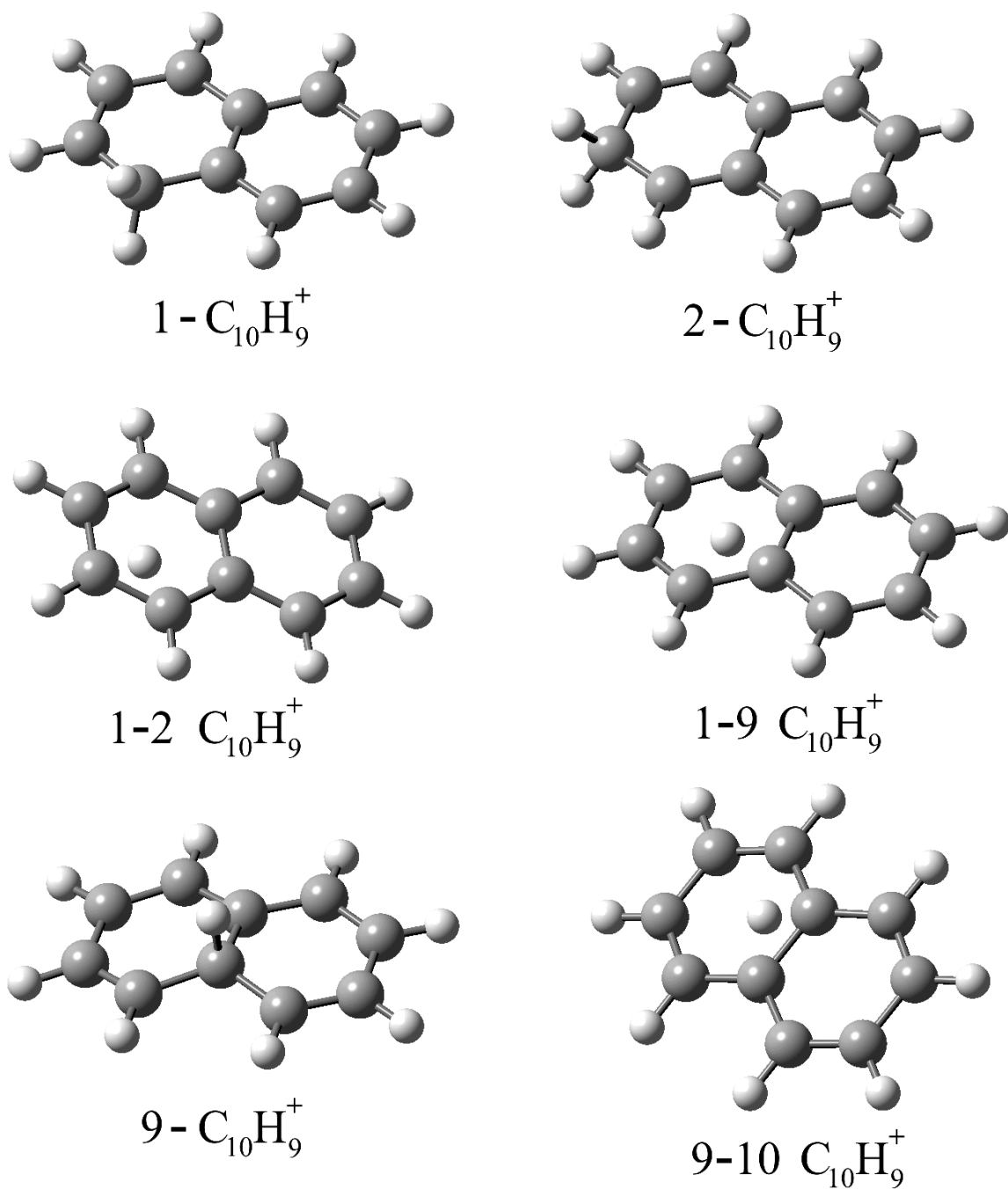


Figure 2.4: Structures of the protonated naphthalene $C_{10}H_9^+$ isomers 1,2 and 9, along with three of the isomerization transition states that connect them.

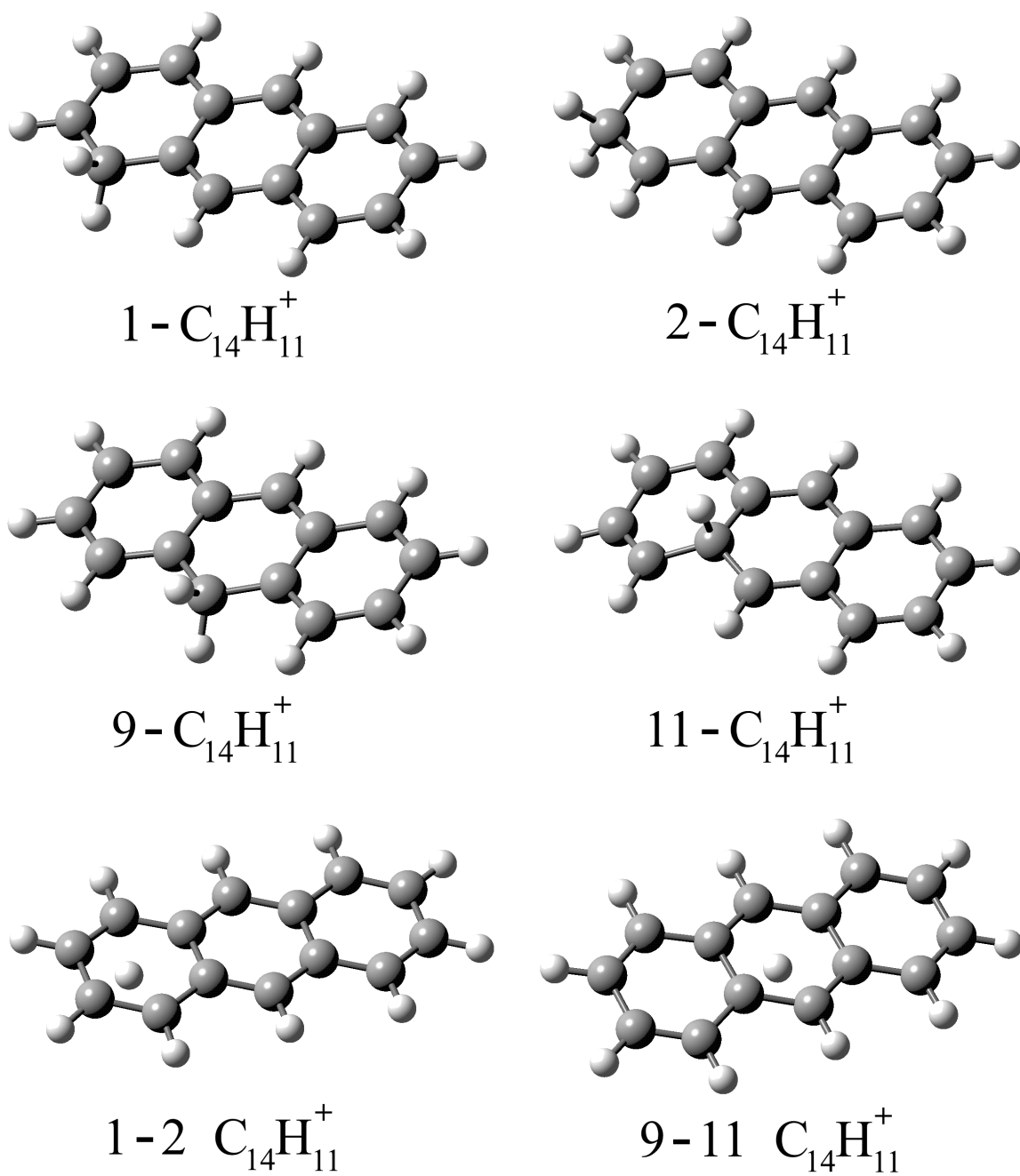


Figure 2.5: Structures of the protonated anthracene $\text{C}_{14}\text{H}_{11}^+$ isomers 1, 2, 9 and 11, along with two of the lowest barrier isomerization transition states.

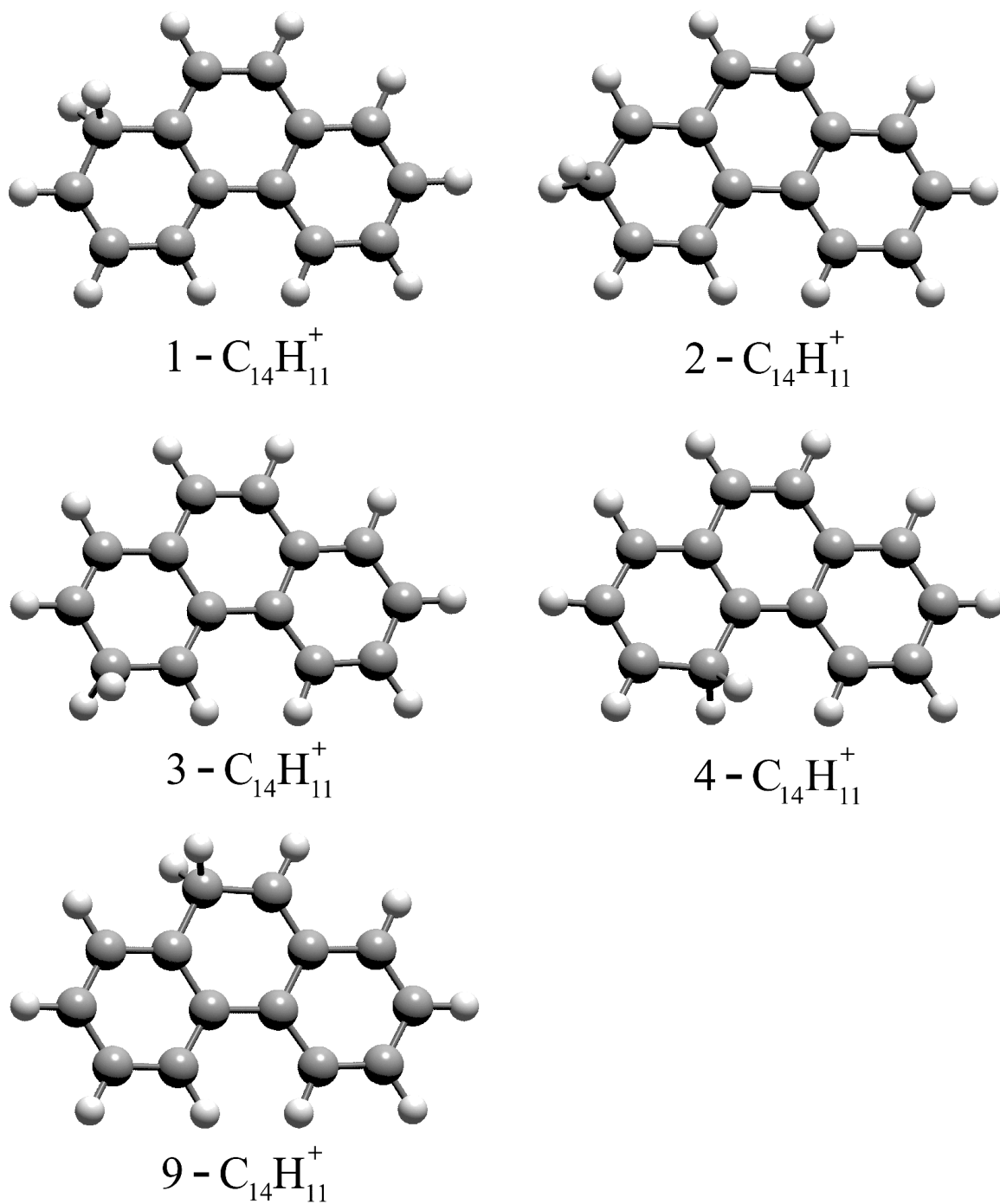


Figure 2.6: Structures of the protonated phenanthrene $C_{14}H_{11}^+$ isomers 1, 2, 3, 4 and 9.

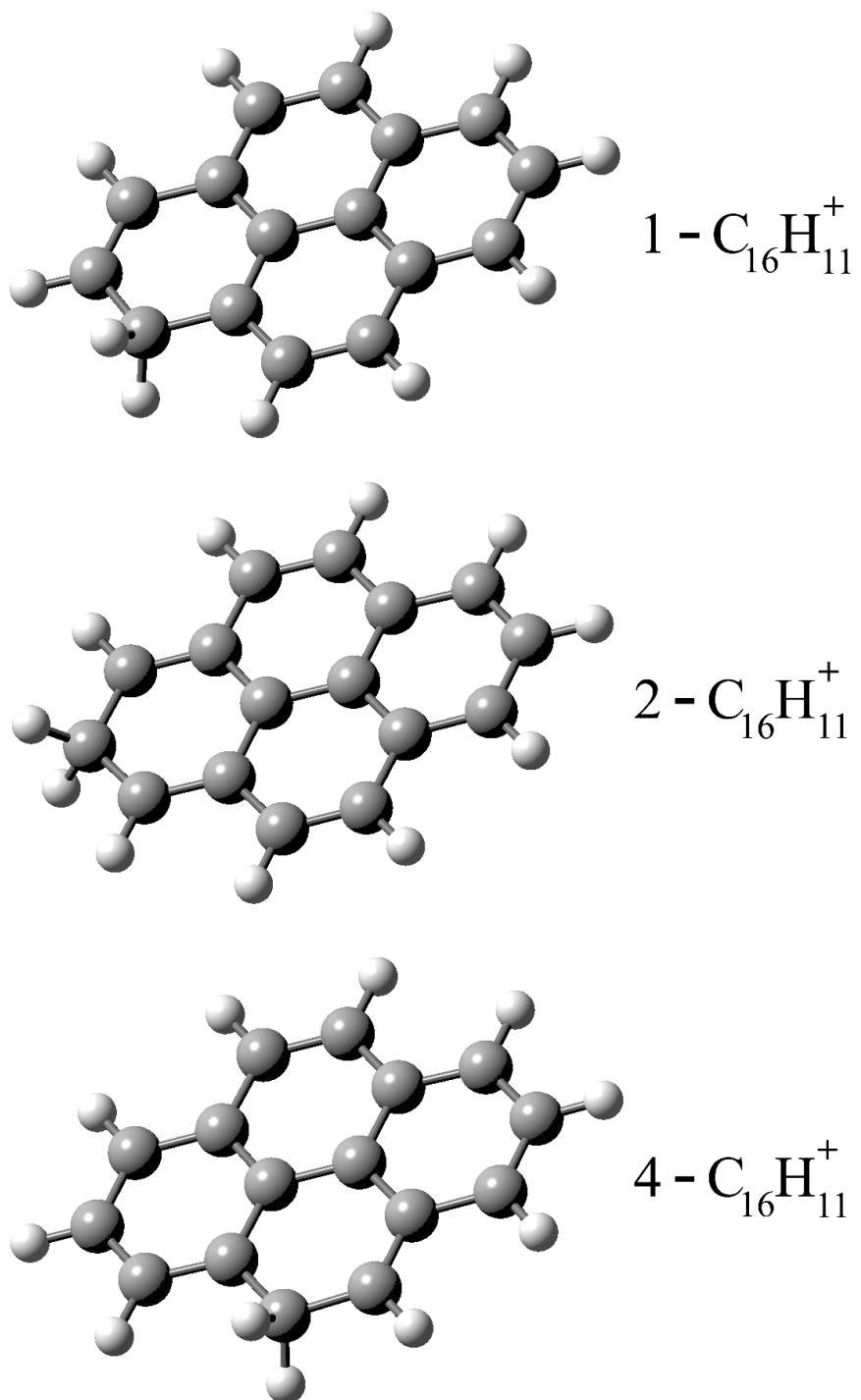


Figure 2.7: Structures of the protonated pyrene $\text{C}_{16}\text{H}_{11}^+$ isomers 1, 2 and 4.

2.3.2 Typical Geometry Changes Upon Protonation

Small but noticeable geometrical changes occur upon the protonation of aromatic hydrocarbons. In stable isomers, the proton binds to the carbon atom, forming a σ complex and changing the hybridization from sp^2 to sp^3 . C–C bonds for the sp^3 carbon elongate due to electron density redistribution by $0.07 - 0.12$ Å, while C–C bonds for an adjacent sp^2 carbon atom shorten by $0.02 - 0.06$ Å (Figure 2.8 – 1). For CH_2 sites, the lengths of the C–H bonds are predicted to be 1.10 Å– somewhat longer than the 1.085 Å predicted for the CH sites. The H–C–H angle values for CH_2 sites are in the range $100 - 104$ degrees.

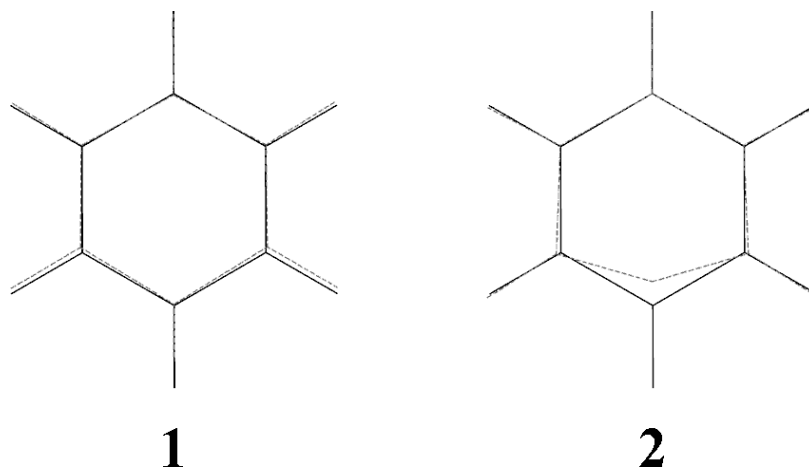


Figure 2.8: Benzene geometry changes (dashed line). 1 – during protonation, 2 – during cation dehydrogenation.

The carbon backbone of the protonated molecule is predicted to remain planar. A few ‘flatness’ tests were performed with protonated naphthalene and anthracene, where the initial geometries of ions were set to resemble cyclohexane. Geometry optimization was then performed with the MP2 and B3LYP methods using different size basis sets. The convergence to a true minimum, not a saddle point on the potential energy surface, was verified by making sure that all vibrational eigenfrequencies were real. In each of these

tests, all carbon atoms settled into a plane. Thus, the protonated PAHs are predicted to have either C_s or C_{2v} symmetry, depending on the isomer (Appendix A, Table A.1).

The less stable isomers, where the proton binds to a ring fusion carbon, are no longer planar thanks to changes in the hybridization at the protonation site. In the transition states, the carbon backbone bends out-of-plane by a small amount. For transition states that do not involve fusion carbons, the change in the dihedral angle is only 1 degree. For transition states with fusion carbon, the bending distortion is closer to 5 degrees.

2.3.3 Geometries of Dehydrogenated PAH Cations

As described below, the properties of various forms of dehydrogenated PAHs may be important in catalytic cycles that can form molecular hydrogen in the diffuse interstellar medium. Here, only the geometries of benzene, naphthalene and anthracene dehydrogenated cations were calculated as a first step in the consideration of such cycles. Theoretically, the dehydrogenated carbon atom is being pulled closer to the middle of the ring. This leads to an increase of the C–C–C angle at the dehydrogenation site from 120° to $143 - 149^\circ$, and a decrease in the adjacent C–C–C angles to $102 - 108^\circ$ (Figure 2.8 – 2). $C_6H_5^+$ and $1-C_{10}H_7^+$ remained flat, while the other dehydrogenated cations considered were found to distort from the planar symmetries of the protonated PAHs.

2.3.4 Geometries of Hydrogenated and Dehydrogenated PAHs

Due to their low ionization energies, atomic carbon and many carbonaceous species are expected to be ionized in diffuse interstellar clouds. The amount of free electrons in these objects is then approximately the same as the amount of carbon, and electron recombination may be one of the major ways of removal for protonated PAHs. Geometries for singly

hydrogenated and dehydrogenated benzene, naphthalene, and anthracene are calculated as a part of the recombination process investigation.

From all of the considered hydrogenated PAHs which essentially are neutralized protonated PAHs, the carbon backbone was not planar only in 9-C₁₄H₁₁. C–C bonds of the hydrogenation site were longer by ~ 0.01 Å and the H–C–H angle was $\sim 1^\circ$ larger than in protonated PAHs. The rest of the geometry was similar to protonated PAHs.

All considered dehydrogenated PAHs had planar geometries. Dehydrogenation would typically result in the radical site carbon atom retraction into the ring, which led to C–C bond shortening by $\sim 0.02 - 0.03$ Å.

2.4 Calculated Values

2.4.1 Vibrational Frequencies

As was mentioned above, the vibrational frequencies and IR intensities of the protonated PAH isomers were calculated here as a part of the geometry optimization. The effect of the level of theory and basis set size on the calculated vibrational frequencies of organic molecules has been studied previously [108–110]. Typically, the calculated vibrational frequencies are larger than the experimental values due to the harmonic nature of the *ab initio* estimate. Thus, the predicted vibrational frequencies must be scaled down by modest amounts to agree with the experiment. The actual scaling factor depends on the level of theory employed, the basis set, and the type of vibration.

To derive the scaling factors for the B3LYP 6-311++G(d,p) calculations presented here, the vibrational frequencies were calculated for neutral benzene and anthracene and compared to the experimental gas phase frequencies [111,112]. A detailed comparison of

the results are presented in Appendix A (Tables A.21, A.22), which shows that the scaling factors are ~ 0.962 for C–H stretching vibrations (frequencies above 2000 cm^{-1}) and ~ 0.982 for the rest. These scaling factors were then used to determine vibrational frequencies of protonated PAHs, neutral PAHs and their cations and to thereby calculate the zero point vibrational energy (ZPE) content of all molecules and ions. The ZPE values were then used to correct the relative energies of isomers and reaction channels (2.5). The full list of the scaled vibrational frequencies for neutral and protonated PAHs is listed in Appendix A (Tables A.23 – A.27) along with the IR vibrational spectra in stick form (Figures A.1 – A.19). In the latter figures, the height of the vertical lines in each spectrum depicts the IR intensities. As a comparison, similar spectra for protonated naphthalene and pyrene convoluted with 20 cm^{-1} linewidth to simulate interstellar spectra were reported in [23].

2.4.2 Proton Affinities

As a part of the ground state energy calculations, the proton affinities for the neutral PAHs were estimated. The resulting values were a good measure of the precision of the calculations. Here, the proton affinities were calculated as an energy difference between the neutral PAH (equivalently, a geometry for PAH-H^+ where the proton is far from the molecule) and the isomers of the protonated PAHs (where the proton is bound to the molecule). These values were then compared with the available experimental values [113, 114]. It should be noted that for molecules with more than one protonation site, it is theoretically possible to calculate the properties for individual isomers, while the experimental data necessarily average over the isomers present in the laboratory. For anthracene and pyrene, the predicted variation in proton affinity is large, with the experimental value nicely bracketed by theory. As one can see from Table 2.2, the match is $\sim 2 - 3\text{ kcal/mol}$, or approximately a

1.5% difference. Hence, the relative values of the energy levels may be trusted to roughly this level.

Table 2.2: Experimental and calculated proton affinities of neutral aromatics.

| Molecule | Experimental (kcal/mol) | Calculated (kcal/mol) | H ⁺ site |
|--------------|----------------------------|--------------------------|---------------------|
| Benzene | 179.3 | 182.19 | 1 |
| Naphthalene | 191.9 | 196.20 | 1 |
| | | 193.30 | 2 |
| Anthracene | 209.7 | 203.84 | 1 |
| | | 200.80 | 2 |
| | | 212.50 | 9 |
| Phenanthrene | 197.3 | 199.80 | 1 |
| | | 197.80 | 2 |
| | | 199.25 | 3 |
| | | 198.73 | 4 |
| | | 199.60 | 9 |
| Pyrene | 207.7 | 211.24 | 1 |
| | | 197.02 | 2 |
| | | 200.98 | 4 |

2.4.3 Ionization Energies

Ionization energies are calculated as the energy difference between the cation and neutral molecule, and were corrected by the ZPE values. The results are compared with the experimental ionization energies [113] for benzene [65,66], naphthalene [68,70], anthracene [69], phenanthrene and pyrene [115] in Table 2.3. The calculated values are consistently lower than experiment by ~ 0.3 eV (6.9 kcal/mol), but the differences predicted here are not as

Table 2.3: Experimental and calculated ionization energies of neutral aromatics.

| Molecule | Experimental (eV) | Calculated (eV) |
|--------------|-------------------|-----------------|
| Benzene | 9.24378 | 9.0562 |
| Naphthalene | 8.1442 | 7.8655 |
| Anthracene | 7.4233 | 7.1002 |
| Phenanthrene | 7.891 | 7.5845 |
| Pyrene | 7.426 | 7.1427 |

large as for those calculated previously with the B3LYP 4–31G method [116].

Ionization energies were also calculated for hydrogenated and dehydrogenated benzene, naphthalene, and anthracene (Appendix A, Table A.36). The typical values for hydrogenated PAHs were in the range of 6.2 – 6.4 eV, which is lower than for neutral PAHs. For deprotonated PAHs, the values were higher (in the 7.7 – 8.0 eV range). If any of these species are present in diffuse interstellar clouds, they should be promptly ionized, yielding protonated PAHs and dehydrogenated PAH cations respectively.

For isomer 2 of protonated naphthalene, the ionization energy needed to yield a doubly charged ion was calculated in order to get an idea of the likely range of values for protonated PAHs. The calculated value is 12.9147 eV, 297.81 kcal/mol. Photons below the ionization threshold of 13.6 eV for hydrogen atoms are widely present in the diffuse interstellar medium. This calculation suggests that doubly charged PAH species will need to be considered in models of the charge states of PAHs in the galaxy.

2.5 Energy Landscapes

The energy landscape diagrams for protonated PAHs were investigated thoroughly in order to compare the energetics of different isomers and possible dissociation channels. These calculations serve two main goals. First, it is essential to find the difference in the stability of different isomers in their ground state for the same protonated PAH molecule, including the heights of the isomerization barriers. This information, together with the excited states calculations presented in Chapter 3, are essential to the interpretation of the experimental data on the photophysical and electronic state properties of protonated PAHs (Chapters 5 and 6). Second, since photodissociation was chosen as a method for recording the spectra of protonated PAHs, it is important to know which dissociation channels are

feasible, their energetics, and their Franck-Condon overlap with the ground state(s).

In all energy landscape diagrams below, the energy of the lowest dissociation channel was set as the energy zero. Hence, in this energy scale, the stable isomers have negative energies.

2.5.1 Protonated Benzene

Isomerization and dissociation calculations on protonated benzene have been performed numerous times [92–95]. At the level of theory employed here, the only isomer of protonated

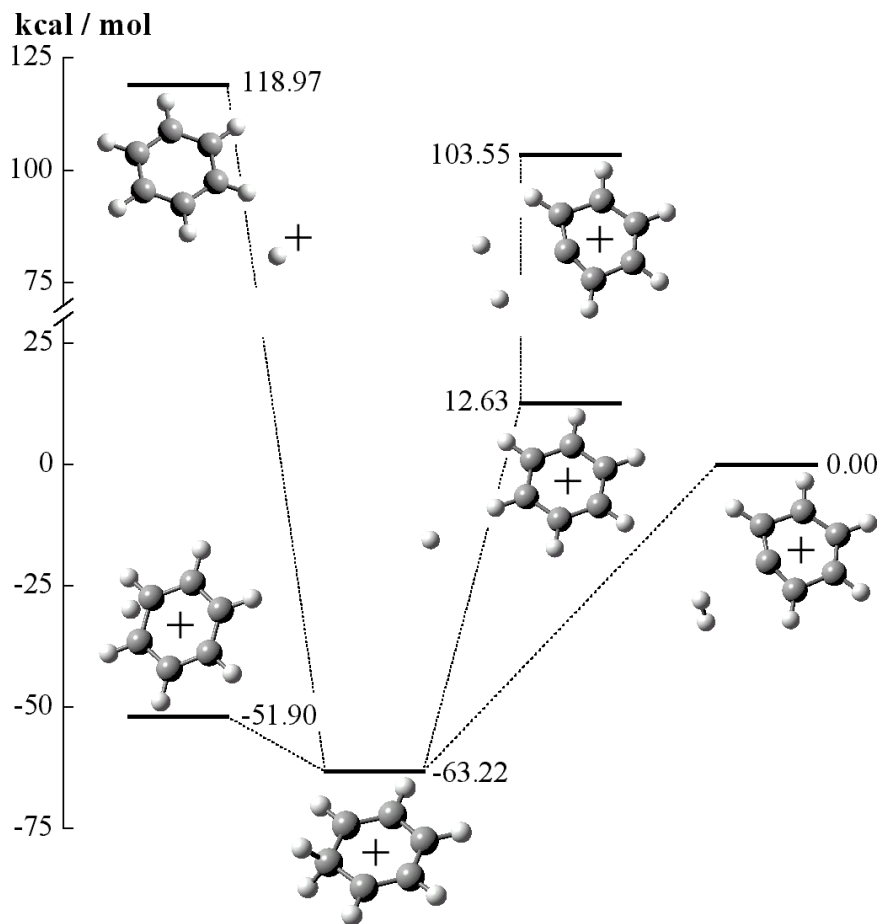


Figure 2.9: The energy landscape for protonated benzene.

benzene is stable with respect to dissociation by 63.22 kcal/mol (Figure 2.9, Table A.28 in Appendix A). The only possible 1–2 isomerization results in the identical isomer and has a barrier height of 11.32 kcal/mol.

The lowest dissociation channels are predicted to occur through the loss of an H_2 molecule (0.00 kcal/mol) or a hydrogen atom (12.63 kcal/mol) from the protonation site. The loss of H_2 most likely has a barrier, but the barrier height was not calculated here due to the difficulty of locating the transition state geometry. The H atom loss channel does not appear to have a barrier. A sequential loss of two hydrogen atoms is much higher in energy than the loss of H_2 molecule. Finally, the loss of an H atom from CH sites and the cleavage of C–C bonds are not considered here as they lie much higher in energy. In addition, the loss of the proton from the CH_2 site lies 118.97 kcal/mol above the lowest dissociation channel – a very large number! Thus, the protonation of neutral benzene in the gas phase cannot occur by simply attaching a proton to it. Thus, the more favorable protonation mechanism in the interstellar medium occurs via proton transfer from H_3^+ in dense clouds or through the radiative association reaction of PAH radical cations with atomic hydrogen in the diffuse clouds. A sequential loss of two H atoms, with the first H atom arising from the CH_2 site, followed by C–H bond cleavage, is 103.55 kcal/mol above the lowest dissociation channel. Such a dissociation pathway would only be possible for very highly vibrationally excited species.

2.5.2 Protonated Naphthalene

The energetics of the reaction between the naphthalene cation ($\text{C}_{10}\text{H}_8^+$) and an H atom, and the energies for isomers 1 and 2 of protonated naphthalene and the isomerization barrier between them, have been calculated previously at the B3LYP 4–31G level [23, 117]. The

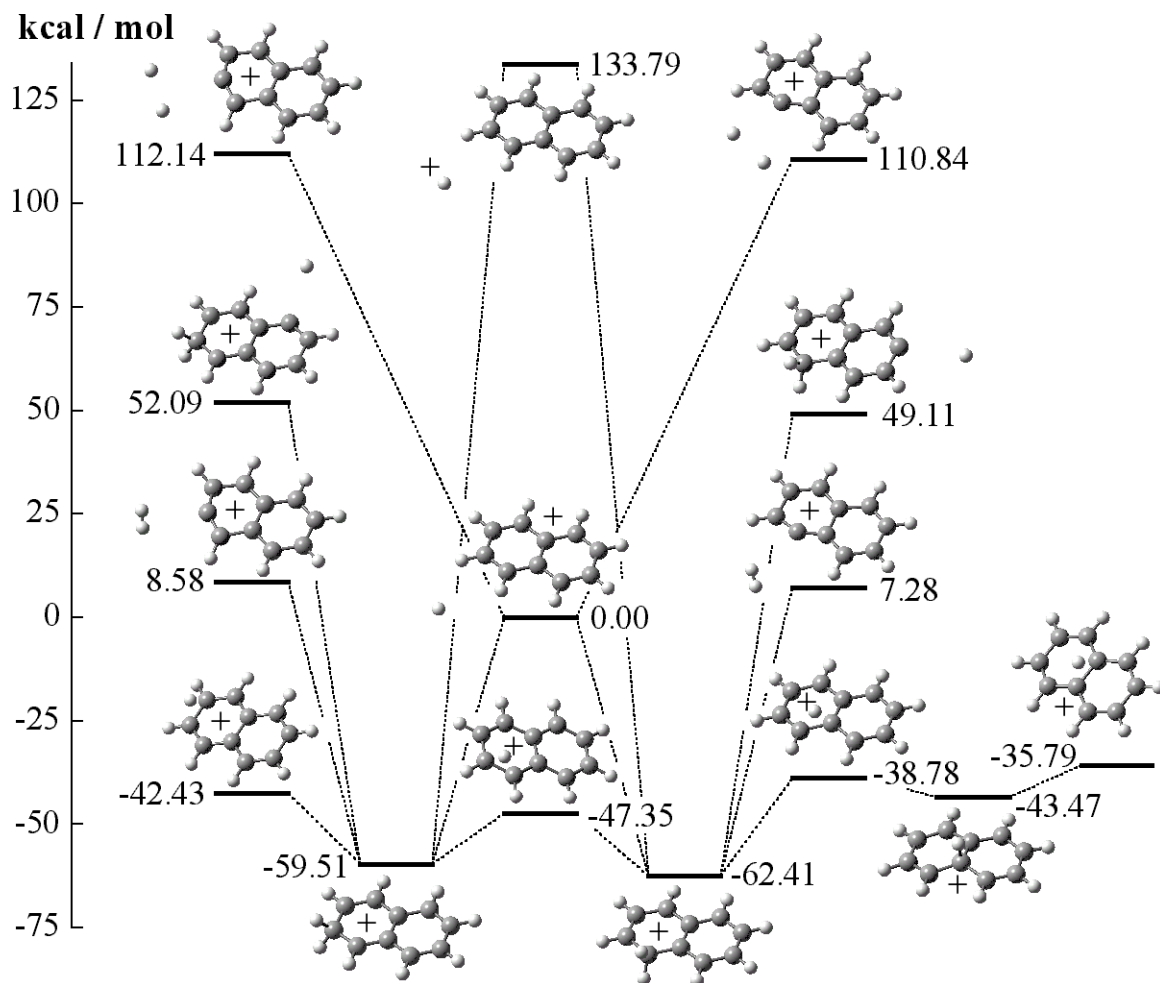


Figure 2.10: The energy landscape of protonated naphthalene.

two isomers of protonated naphthalene are stable with respect to dissociation by 62.41 kcal/mol ($1\text{-C}_{10}\text{H}_9^+$) and 59.51 kcal/mol ($2\text{-C}_{10}\text{H}_9^+$), respectively (Figure 2.10, Table A.29 in Appendix A). Isomer 2 can undergo 2–3 isomerization into an identical isomer (through a barrier of 17.08 kcal/mol) and 2–1 isomerization into the more stable $1\text{-C}_{10}\text{H}_9^+$ isomer (barrier height 12.06 kcal/mol). Given sufficient energy, proton hopping can convert isomer 1 into isomer 2 (barrier height 15.06 kcal/mol) and isomer 9 (barrier height 23.63 kcal/mol) in which the proton is bound to a ring fusion carbon. Energetically, isomer 9 is less stable than isomer 1 by 18.94 kcal/mol and has a low barrier for 9–1 or 9–8 isomerization (barrier

height 4.69 kcal/mol). It can also undergo 9–10 isomerization across the ring fusion into an identical isomer (barrier height 7.68 kcal/mol). Thus, it is unlikely that isomer 9 would be important under interstellar conditions.

The lowest dissociation channel for protonated naphthalene is the loss of an H atom from the protonation site (0.00 kcal/mol). The next – not so distant in energy – occurs via the loss of H₂ from the protonation site (7.28 kcal/mol for isomer 1 and 8.58 kcal/mol for isomer 2). The energies for the loss of H atom from C–H sites (not the protonation sites) were calculated as well. As for protonated benzene, they are substantially higher in energy: 49.11 ± 1.36 kcal/mol for isomer 1 (for a full listing see Table A.29 in Appendix A) and 52.09 ± 1.39 kcal/mol for isomer 2 (c.f. the bottom part of Table A.29 in Appendix A). The CH site dissociation channels of protonated naphthalene are therefore unlikely to be important in the interstellar medium. The loss of a proton from the CH₂ site is 133.79 kcal/mol above the lowest dissociation channel. Finally, the sequential loss of two H atoms, first from the CH₂ site and then another H atom, has energies of 110.84 kcal/mol (for isomer 1) and 112.14 kcal/mol (for isomer 2) above the lowest dissociation channel.

2.5.3 Protonated Anthracene

Protonated anthracene has three isomers that are stable with respect to dissociation by 52.41 kcal/mol (1–C₁₄H₁₁⁺), 49.36 kcal/mol (2–C₁₄H₁₁⁺) and 61.06 kcal/mol (9–C₁₄H₁₁⁺) (Figure 2.11, Table A.30 in Appendix A), respectively. Isomer 2 can undergo 2–3 isomerization into an identical isomer (barrier height 21.20 kcal/mol) and 2–1 isomerization (barrier height 14.49 kcal/mol). The reverse 2–1 isomerization has a barrier height of 17.54 kcal/mol, while the 1–11 isomerization must surmount a barrier height of 27.84 kcal/mol in order to place the proton at a ring fusion carbon. Energetically, isomer 11 is less stable

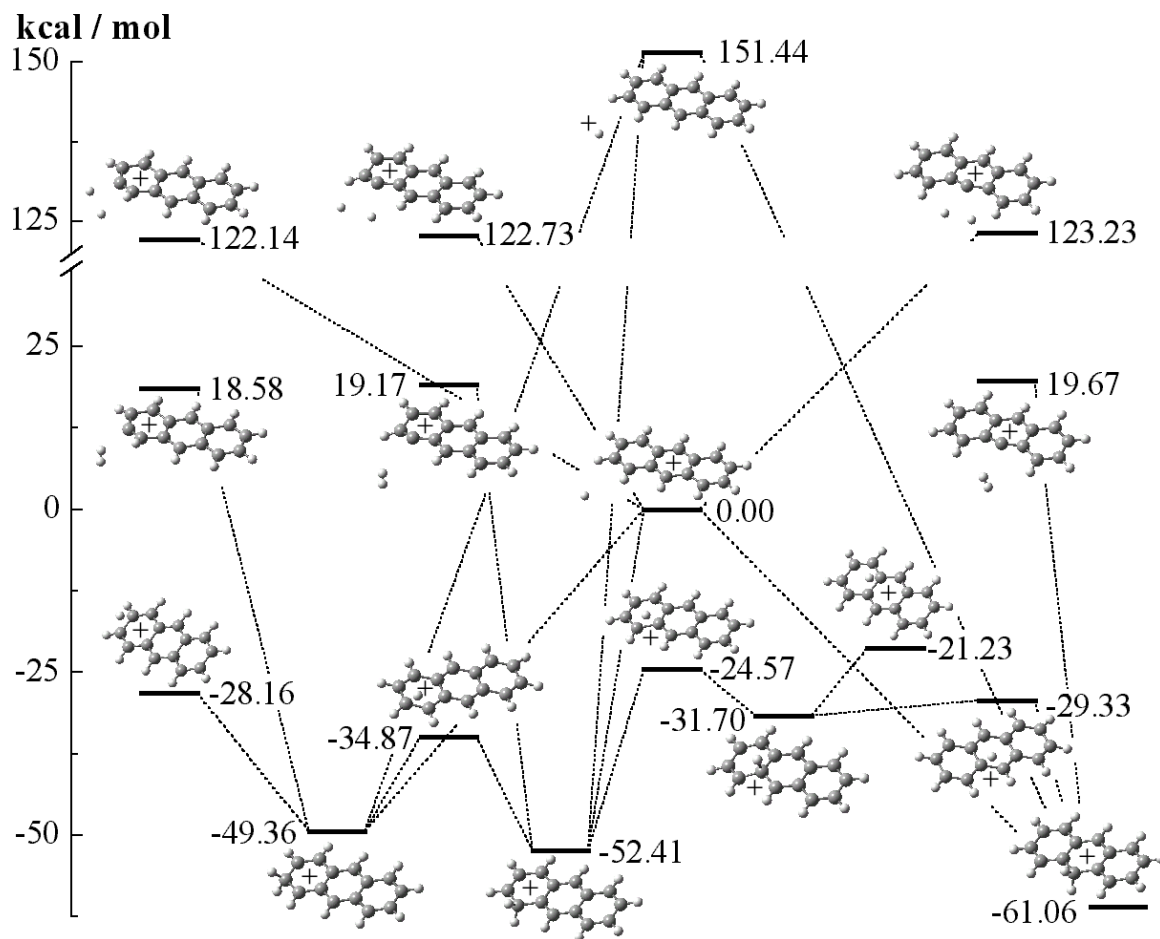


Figure 2.11: Protonated anthracene energy landscape.

than isomer 1 by 20.70 kcal/mol and has a very low barrier for 11–9 isomerization into the most stable isomer 9 (barrier height 2.37 kcal/mol). As with protonated naphthalene, it is therefore unlikely that the ring fusion isomer would be an important DIB carrier. Isomer 11 can also undergo 11–12 isomerization across the ring fusion into an identical isomer (barrier height 10.47 kcal/mol). Isomer 9 can undergo only 9–11 isomerization (barrier height 31.73 kcal/mol).

The lowest dissociation channel for protonated anthracene is the loss of an H atom from the protonation site (0.00 kcal/mol). The loss of an H₂ molecule from the protonation site is nearly isoenergetic for all three isomers (19.17 kcal/mol for isomer 1, 18.58 kcal/mol

for isomer 2 and 19.67 kcal/mol for isomer 9). The loss of a proton from the CH₂ site is again quite unfavorable at an energy of 151.44 kcal/mol above the lowest dissociation channel. A sequential loss of two H atoms, first from the CH₂ site and then another H atom, have energies 122.73 kcal/mol (for the isomer 1), 122.14 kcal/mol (for isomer 2) and 123.23 kcal/mol (for isomer 9) above the lowest dissociation channel.

2.5.4 Protonated Phenanthrene

Protonated phenanthrene provides an interesting and more complex counterpart to protonated anthracene in that it has five stable isomers, each of which can potentially contribute DIB features. Because of its complex potential energy surface, no tunneling and fewer dissociation pathways are calculated here (Figure 2.12, Table A.31 in Appendix A). Unlike the other protonated aromatic molecules discussed in this chapter, the protonated phenanthrene isomers are almost isoenergetic and are stable with respect to dissociation by 59.53 kcal/mol (1-C₁₄H₁₁⁺), 57.53 kcal/mol (2-C₁₄H₁₁⁺), 58.98 kcal/mol (3-C₁₄H₁₁⁺), 58.46 kcal/mol (4-C₁₄H₁₁⁺) and 59.33 kcal/mol (9-C₁₄H₁₁⁺), respectively.

By analogy with protonated naphthalene and anthracene, the lowest dissociation channel for protonated phenanthrene is the loss of an H atom from the protonation site (0.00 kcal/mol). The loss of a proton from the CH₂ site lies 140.27 kcal/mol above the lowest dissociation channel and will not be considered further.

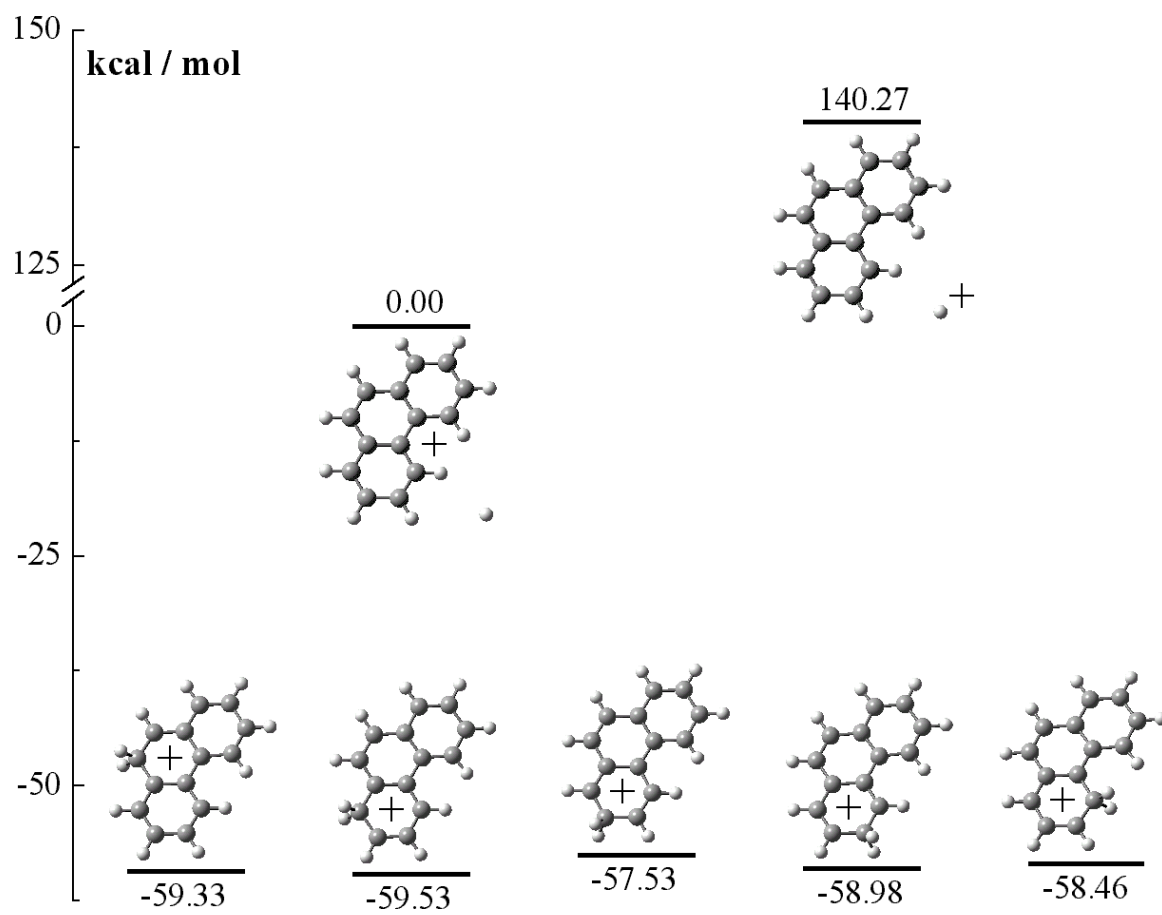


Figure 2.12: A simplified version of the protonated phenanthrene energy landscape.

2.5.5 Protonated Pyrene

Protonated pyrene has three isomers that are stable with respect to dissociation by 60.28 kcal/mol ($1\text{-C}_{16}\text{H}_{11}^+$), 46.57 kcal/mol ($2\text{-C}_{16}\text{H}_{11}^+$) and 50.52 kcal/mol ($4\text{-C}_{16}\text{H}_{11}^+$) (Figure 2.13, Table A.32 in Appendix A). As with the smaller protonated PAHs, the lowest dissociation channel for protonated pyrene is calculated to occur via the loss of an H atom from the protonation site (0.00 kcal/mol). The loss of a proton from the CH_2 site is 150.46 kcal/mol above the H atom loss channel.

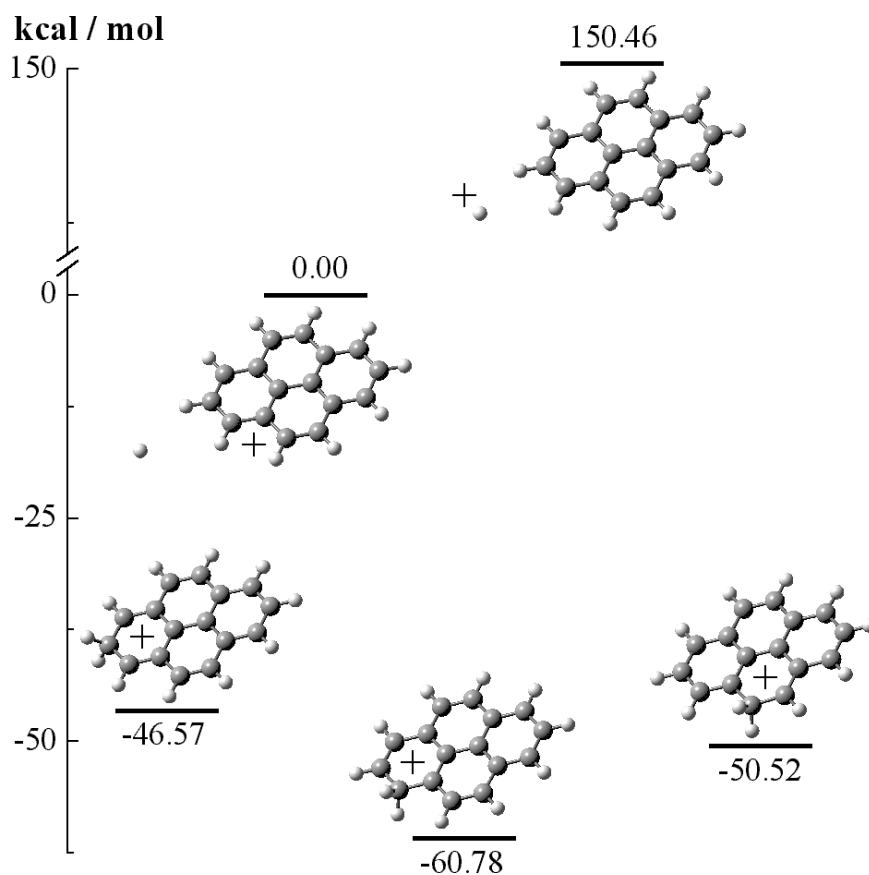


Figure 2.13: The energy landscape of protonated pyrene (not complete).

2.5.6 Hydrogenated PAHs

The main goal of this suite of calculations was to investigate the fate of protonated PAHs during electron recombination. Only the energies of hydrogenated PAH stable isomers and hydrogen loss channels were calculated, and only hydrogenated benzene, naphthalene, and anthracene were considered. The results are presented in Figures 2.14 – 2.16 and Tables A.33 – A.35 (Appendix A).

The lowest energy dissociation channel is the loss of a hydrogen atom from the CH_2 site, and as in the case for protonated PAHs, its energy was set to 0.00 kcal/mol. The next channel is the loss of an H_2 molecule from the hydrogenation site, and lies only 5.5 – 6.0

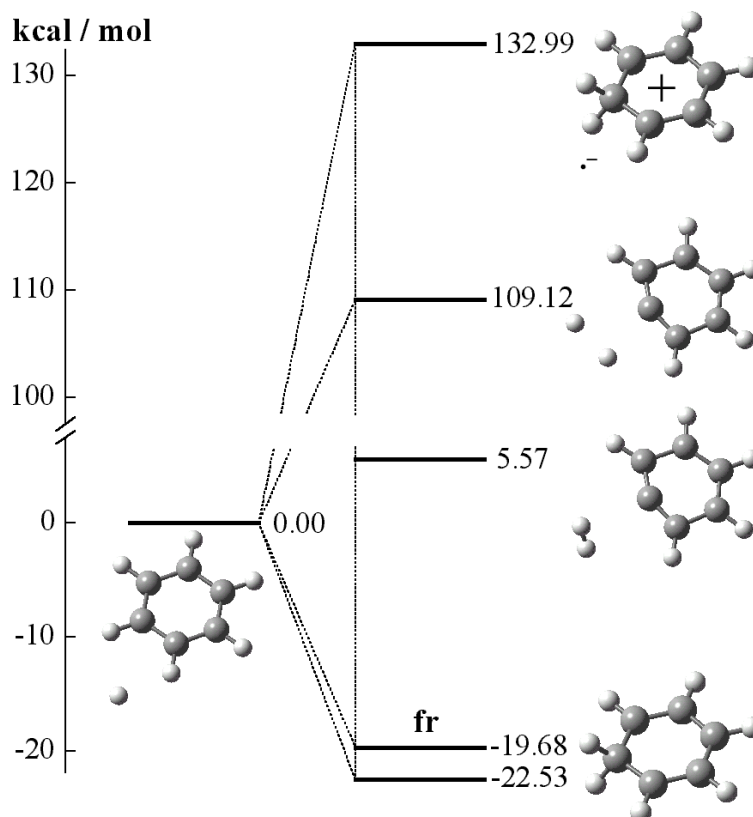


Figure 2.14: Hydrogenated benzene energy landscape.

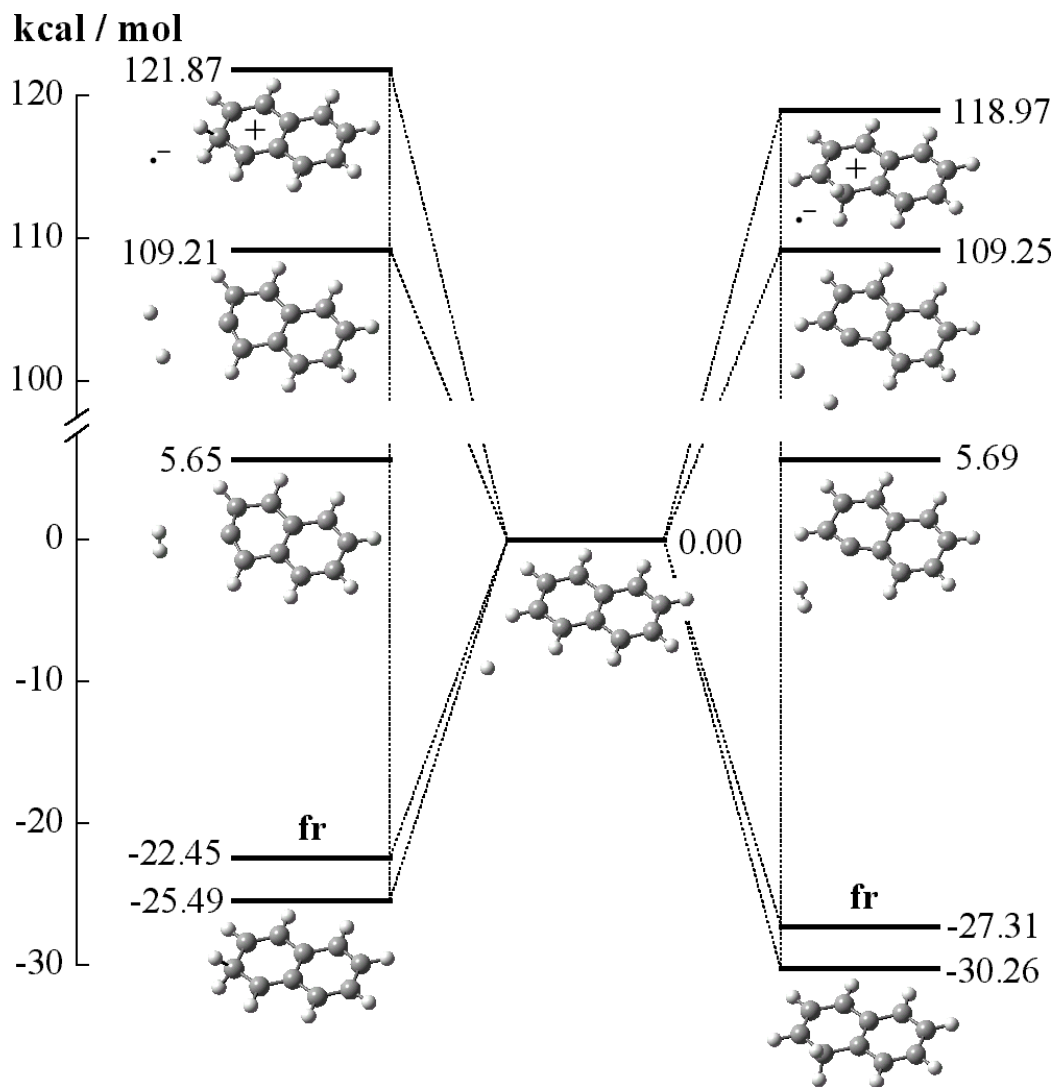


Figure 2.15: Hydrogenated naphthalene energy landscape.

kcal/mol higher in energy. A sequential loss of two hydrogen atoms, one of which is from the hydrogenation site – is almost 110 kcal/mol above the lowest energy channel.

Species labeled as **fr** (frozen) designate hydrogenated PAHs with geometries fixed to that of the protonated PAHs and energies that were corrected by ZPEs of protonated PAHs. Such geometries are not those appropriate for equilibrium, but rather, represent initial structures that are formed immediately after recombination. The energies of these structures are ~ 3 kcal/mol above those of the equilibrium structures.

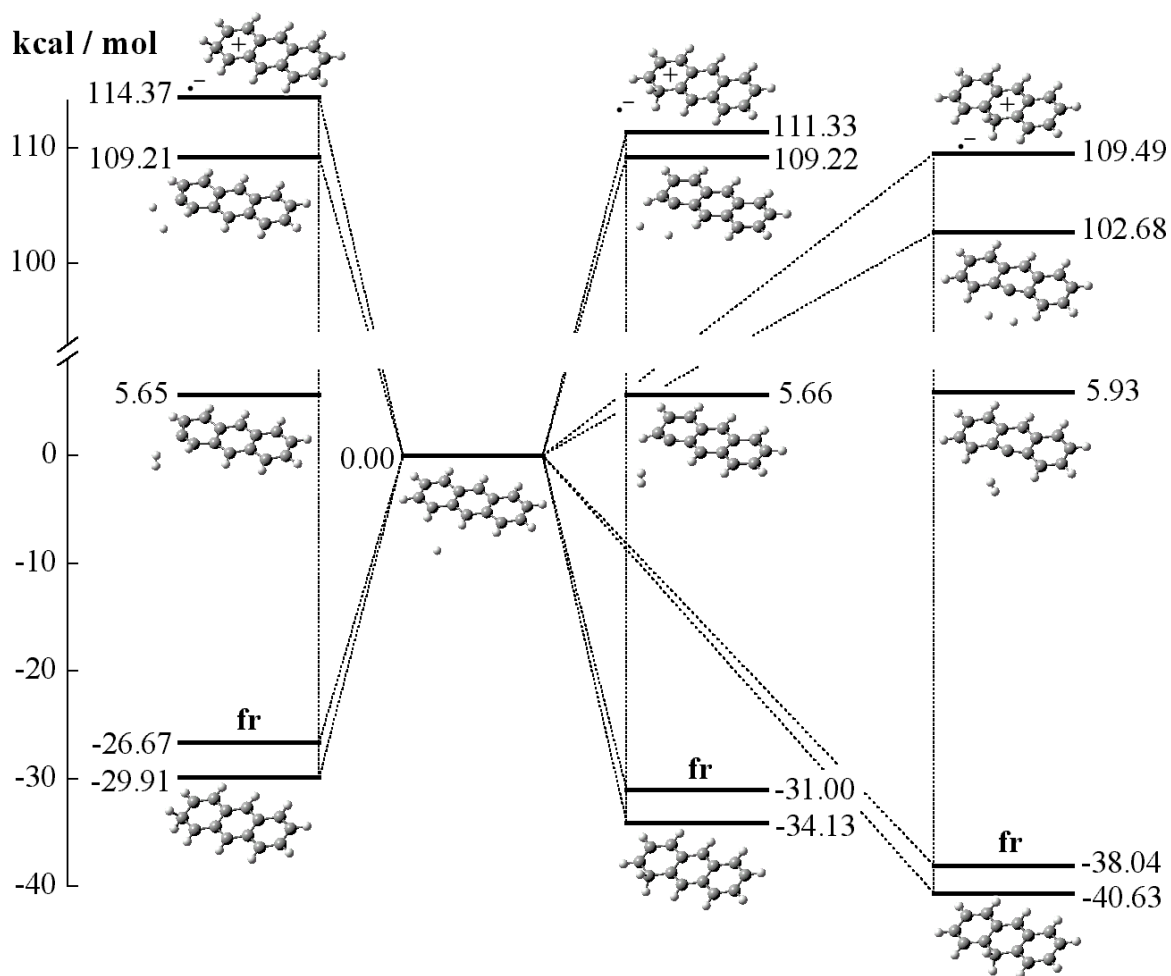


Figure 2.16: Hydrogenated anthracene energy landscape.

As a general trend, hydrogenated species become more stable with respect to dissociation as the size of the molecule grows. While hydrogenated benzene is stable by only 22.53 kcal/mol, isomers 1, 2 and 9 of hydrogenated anthracene are stable by 34.13, 29.91 and 40.63 kcal/mol, respectively. Since protonated PAHs have similar ionization energies, the amount of excess energy decreases with PAH size. For larger PAHs, the dissociation yield should drop substantially because the extra energy can be vibrationally distributed over the full molecule via IVR processes. In all cases, hydrogenated PAHs are less stable than protonated PAHs since they are not closed shell species.

2.6 Discussion

In regions of the interstellar medium exposed to ultraviolet photons (translucent clouds, H II regions, the diffuse medium), PAHs will exist in a variety of charge states. Anions typically have rapid photodetachment rates, and so cationic species are the most likely ionized form of interstellar PAHs. Neutral PAH precursors, for example, can acquire a positive charge either via ionization (UV or cosmic rays) or through the reactions with charged particles. In dense regions of the ISM such as molecular clouds, neutral PAH molecules can be protonated in collisions with H_3^+ or HCO^+ , thanks to their high proton affinities. Being closed-shell species, protonated PAHs are not as reactive as PAH cations – often referred as cation radicals – and would therefore be expected to be rather stable in the interstellar medium. This is reflected in the energetics of the cationic PAH species, with the above calculations demonstrating that protonated PAHs are more stable than their radical cation cousins. In addition, the observed laboratory reaction rates between H atoms and protonated benzene, naphthalene, pyrene, their cations, and dehydrogenated cations [75] all suggest that protonated PAHs can be created efficiently from radical cation precursors. Hence, if PAHs exist in the interstellar medium and can survive UV radiation, an extremely important component of the charge balance is likely to be carried by PAHs in their protonated form.

During protonation of aromatic molecules, the molecular symmetry decreases. This has important spectroscopic implications for the protonated PAHs as DIB and UIR carriers. For example, the IR spectrum of protonated PAHs should be more dense since more vibrational modes would be IR active. While there are no microwave spectra of neutral aromatic hydrocarbons and their cations (unless they heterocyclic forms are examined) due to their

lack of a permanent dipole moment (Appendix A, Table A.1), their protonated analogs do have significant dipole moments (at the protonation site) and should in principle be observable in the microwave with sufficient sensitivity. For example, 1–0 transition in protonated benzene should lie near ~ 8209 MHz and could thus be searched for with standard FTMW techniques in the laboratory, as was successfully carried out for the phenyl radical C_6H_5 [118].

2.6.1 Changes in the Vibrational Spectrum

IR vibrational spectra of PAHs change significantly upon protonation (Appendix A, Figures A.1 – A.19), most likely due to the reduction in the molecular symmetry [23] (Appendix A, Table A.1) and the concomitant increase in the number of allowed IR vibrational transitions. The biggest change is in the $1100 - 1600 \text{ cm}^{-1}$ range, where the neutral PAHs have only few, typically weak vibrations. The protonated PAHs, on the other hand, have their strongest lines in this region and the density of bands is high. Furthermore, the protonated PAH vibrational bands are located very close to $6.2 - 6.3 \text{ }\mu\text{m}$ and $8.6 \text{ }\mu\text{m}$ features in the interstellar UIR spectrum [23].

Another change is the dramatic decrease in the intensities of C–H stretch vibrations in $3000 - 3100 \text{ cm}^{-1}$ range and the appearance of new CH_2 stretching vibrations that are not present at all in the neutral and cation spectra. The CH_2 vibrations (symmetric and asymmetric stretches) are separated by $1 - 20 \text{ cm}^{-1}$ and located from $2830 - 2910 \text{ cm}^{-1}$. Experimentally, it is these vibrations that were recorded in the cluster dissociation spectrum of protonated benzene–Ar [3, 96]. The CH_2 vibrations are red-shifted from the aromatic C–H stretching modes and are located at wavelengths that can contribute to the red wing of $3.29 \text{ }\mu\text{m}$ (3040 cm^{-1}) UIR feature. Since the exact frequencies depend on the

PAH molecule and the isomer, the CH_2 vibrational doublet from protonated PAHs will be difficult to observe astronomically, but these vibrations may well explain a part of, but not all, of the $3.29\ \mu\text{m}$ red wing [23,96].

2.6.2 Proton Mobility

When a protonated PAH molecule is excited vibrationally but without sufficient energy to dissociate, it can isomerize by intramolecular proton transfer from one carbon atom to another. This behavior is uniquely inherent to protonated PAHs. Neutral PAHs and their radical cations do not possess this dynamical possibility, which may have important ramifications under interstellar conditions. Depending on the level of excitation, the proton migration may occur only between two adjacent isomers, within one carbon ring, or over the entire carbon framework. The proton can even migrate from one ring to another via a ring fusion carbon, though this can only occur at rather higher levels of internal excitation since the isomer protonated at the ring fusion is rather unstable. Proton tunneling across the ring fusion is possible only in protonated catacondensed PAHs (naphthalene, anthracene, phenanthrene, tetracene, etc.) In protonated pericondensed PAHs (pyrene, coronene, ovalene, etc.), the migration can only occur on the outside of the molecule via 2-ring fusion carbon isomers since the protonation at the inner, 3-ring fusion sites is energetically prohibitive.

The ratio of the protonated PAH isomers in the ISM during formation is most likely to be statistical. For naphthalene it would be 1 : 1 (isomer 1 : isomer 2); for anthracene – 2 : 2 : 1 (isomer 1 : isomer 2 : isomer 9); for phenanthrene – 2 : 2 : 2 : 2 : 1 (isomer 1 : isomer 2 : isomer 3 : isomer 4 : isomer 9); and for pyrene – 2 : 1 : 2 (isomer 1 : isomer 2 : isomer 4). If the protonated PAH ion is later excited vibrationally (collisionally or by radiation), it may

isomerize. In a large ensemble, this will scramble the initial isomer distribution and is most likely to change it closer to a thermodynamic equilibrium of isomers. On the other hand, the true thermodynamic equilibrium may be not attainable if the UV excitation rate is too high. The actual rate for reaching the equilibrium may be calculated only as a part of a model where isomerization rate dependence on the excitation energy is calculated for each isomer and then compared to the IR fluorescence lifetime. In general, the isomerization probability is the highest shortly after initial excitation, and then is reduced with every emitted IR photon.

Even in cold environments, the isomer distribution will not settle to the most stable isomer only. For example, in the case of interstellar methyl isocyanide, the amount of the metastable isomer CH_3NCH^+ is predicted to be $\sim 10 - 25\%$ of the amount for the stable isomer CH_3CNH^+ , in spite of the isomer energy difference of 10 kcal/mol and the barrier of 65 kcal/mol [119].

Proton mobility also dramatically increases the density of the vibrational states once the internal energy rises above the isomerization barriers. Since these barriers correspond to \sim visible wavelength photons, the proton mobility in protonated PAHs may well lead to significant broadening of their electronic spectra, a topic discussed at greater length in Chapter 6. The photostability should also be greatly enhanced, which would lead to improved survivability of protonated PAHs under interstellar conditions.

2.6.3 Dissociation Channels

For protonated benzene, the lowest energy dissociation channel is the loss of the hydrogen molecule H_2 from the protonation site, with an H atom loss not much higher in energy. The loss of 2 a.m.u. (either H_2 or 2H) was observed in protonated benzene UV photodissociation

experiments [90].

According to the B3LYP calculations for polycyclic molecules, the lowest energy dissociation channel is the loss of a single hydrogen atom (H) from the protonation site, with the loss of a hydrogen molecule (H_2) higher in energy by only 10 – 20 kcal/mol. Interestingly, only the loss of H_2 molecules (or two H atoms) has been observed in the UV multiphoton dissociation of protonated anthracene and pyrene (Chapter 5). The sequential loss of two hydrogens was also observed in the CW visible photodissociation of coronene cations [120]. Both of these experiments illustrate the higher stability of the closed-shell protonated species compared to the open-shell cations. This stability also seems to be strongly influenced by the composition of the photodissociation products.

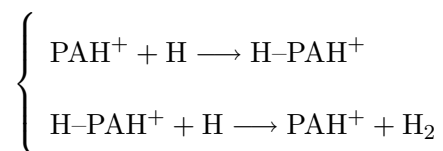
Other dissociation channels (H loss from non-protonation site, C–C bond cleavage or H^+ loss) are much higher in energy and are therefore very unlikely to be important processes in interstellar photodissociation.

Typical dissociation energies for the two lowest channels are on the order of 50 – 80 kcal/mol (2.2 – 3.5 eV or $\lambda \sim 600 - 360$ nm for a single photon). Thus, from energetic considerations alone, protonated PAHs should be able to dissociate even from the absorption of visible or near-UV photons. In Chapter 3, the energies for the excited states will be calculated, with Chapters 5 and 6 turning to experimental analyses of the photostability and spectra of protonated PAHs.

2.6.4 Interstellar H_2 Formation

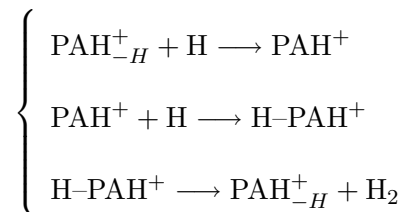
Molecular hydrogen is abundant in the interstellar medium. The mechanisms of H_2 formation are still debated in the literature, especially in warm regions such as diffuse or translucent clouds where dust grain synthesis models have a very difficult time generating

sufficient rates of molecular hydrogen production. One possible ‘out’ is through reactions of PAHs with atomic hydrogen since the effective ‘surface area’ is increased dramatically. From the bond dissociation energies and barrier heights calculated for benzene and naphthalene [117], it is thought that hydrogen atom association reactions with PAH cations and dehydrogenated cations do not have a barrier. From these calculations, it was also suggested that H_2 abstraction by H atoms from protonated PAHs might occur efficiently. This mechanism was later extended to anthracene and pyrene molecules [121], and the general cycle would be:



The first step in this mechanism proceeds almost at collision rate, but the rate for the second step is not known. It should only be a fraction of the collision rate, even if it is almost barrierless since the reaction will proceed only if the hydrogen atom approaches the ‘right’ carbon at a proper angle.

Another way to form molecular H_2 is via protonated PAH dissociation to generate the dehydrogenated PAH cation, as has been suggested in discussions of PAH cation reactivity with H atoms (for benzene and naphthalene [76]). The cycle for this mechanism would be:

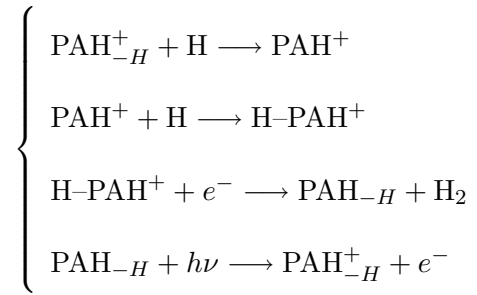


The first two steps in this reaction are exothermic and fast (they occur at nearly the collision rate), but the last step is endothermic. Thus, it is the rate-determining step in this cycle and depends largely on the external sources of protonated PAH excitation in the ISM. The absorption of UV photons may provide a viable option in diffuse clouds or near luminous

young stars [90]. Chapter 5 discusses this in greater detail.

Whichever of the two mechanisms that predominates will depend on the rate for the second step in the first mechanism and the UV flux in the second cycle. Most likely, the first mechanism would be preferred since protonated PAHs were found to be photostable (Chapter 5).

One additional way to make molecular hydrogen would be through the H_2 loss channel by hydrogenated PAHs, formed in protonated PAH electron recombination. This channel is only $5.5 - 6.0$ kcal/mol above the H atom loss channel. It should be energetically accessible since such dissociative recombination reaction for protonated PAHs should be exothermic by ~ 100 kcal/mol. Dehydrogenated PAHs formed in this reaction would be ionized and would acquire hydrogen atoms to reform the protonated PAHs:



Such a cycle would be especially effective for smaller PAHs and would be facilitated by relatively high electron densities such as those found in diffuse clouds where the fractional electron abundance of $f(e^-) = n(e^-)/n(\text{H}) \sim 10^{-4}$ is maintained by atomic carbon photoionization.

2.7 Summary

The above calculations show that protonated PAHs are stable species. They are formed by proton binding to a carbon atom and not the C–C bond or the whole aromatic ring. In the ISM, PAHs are likely to be in protonated form.

Protonated PAHs have a stronger and more complicated IR spectrum than neutral PAHs. Some of the strong IR frequencies are located near UIR bands in the mid-IR range. CH₂ stretch vibrations are located in the red wing region of 3.3 μ m UIR feature and may account for part of it.

The two lowest dissociation channels are loss of an H atom and an H₂ molecule from the protonation site. The dissociation energies are in the range 50 – 80 kcal/mol and in principle may be accessed by near UV or visible photons. The H₂ loss channel may be responsible for molecular hydrogen production in the ISM.

Vibrationally excited protonated PAHs can isomerize without dissociation. The proton can migrate almost everywhere on the outside rim of the PAH molecule. This would lead to broader electronic spectra and possibly to the thermodynamic distribution of the isomers in the ISM.

Chapter 3

Excited States Calculations for Protonated PAHs

3.1 Introduction

Protonated PAHs are closed shell ions. Their electronic structure should therefore be similar to that of neutral PAHs, but as is shown in this chapter, the electronic transitions of protonated PAHs are shifted to the red. The red shift occurs because the HOMO – LUMO gap is reduced due to rehybridization of the protonated carbon atom. Thus, one may expect that even small protonated PAHs would absorb in the visible wavelength range, that is, where the diffuse interstellar bands are located. Based on the assumption that protonated PAHs may be a class of DIB carriers, the experimental measurement of their electronic spectra is an important goal. Before undertaking such experiments, a survey of the expected protonated PAHs excited states could be used to guide the choice of molecules for study, based on the predicted proximity to observed DIBs. *Ab initio* calculations may be very helpful in making such predictions, as well as providing better knowledge of the electronic structure of protonated PAHs. However, it must be realized that such calculations are far from being precise and are best viewed as a guide for further research. Here, the S_1 states are the objects of interest as they participate in the longest wavelength absorption

from the ground electronic state.

3.2 Methodology

To calculate the energies of the excited states for neutral and protonated PAHs, the same hardware and software (GAUSSIAN 98, Revision A.9 [98]) were used as in the ground state calculations (Chapter 2). All excited state calculations were performed on geometries that were first optimized at the B3LYP 6-311++G** level.

3.2.1 Theory Level and Basis Set

A number of methods have been used to calculate excited states of neutral PAHs and their cations [122–127]. The methods for calculating excited states are not as precise as for the ground state, indeed, they are currently an active area of research. Some are rather complicated and require a careful choice of the orbitals to be considered. The goal of the calculations carried out here is not to predict the positions of each excited state precisely, but rather to estimate where they are located. In addition, information about the *relative* energetics of the same state but in different isomers of protonated PAHs would be very useful as a guide to experiments.

The Configuration Interaction – Singles (CIS) method [122] was used here to perform calculations. This is the least precise excited state method, since it is an analog for the ground state Hartree-Fock method, but it does not require a prior knowledge about the electronic structure of the molecule and is reasonably stable for most molecules. Since protonated PAHs are closed shell species, the CIS method may be applied to them as well.

The choice of calculation parameters was based on the benzene calculation discussed in exercise 9.4 of [128]. The full call for the excited states calculation was:

rCIS=(Direct,Singlets,NStates=12)/6-311++G(2d,2p) Density=Current
IOP(9/40=2) Pop=Full

The 6-311++G(2d,2p) basis set was chosen based on the convergence analysis described in 3.2.2. Only singlet states were considered (*Singlets* keyword) as relevant to one-photon electronic absorption spectroscopy. The first twelve singlet excited states were calculated (*NStates=12*). Such a large number was not required, but used to avoid missing any degenerate or forbidden transitions. *Density=Current* was used for better estimates of the oscillator strengths for each transition. *Pop=Full* ensured that all orbitals were considered in the orbital population analysis, and *IOP(9/40=2)* specified which wavefunction coefficients were to be included in the output. The *Direct* keyword was used to avoid problems with disk space for larger molecules.

3.2.2 Convergence Tests

The accuracy of the excited states calculation depends on the basis set and the geometry optimization. To investigate the effect of both factors on the first singlet excited state, a number of tests were performed on neutral and protonated naphthalene. A summary of the results is presented in Table 3.1. A general trend is the increase in the wavelength with the increase in the CIS basis set. However, even with the biggest basis set used, the photon energy was overestimated because the experimental value for neutral naphthalene is known to be at a much longer wavelength (312 nm).

For the geometry optimization, tests were carried out with and without diffuse functions, but the difference was found to be negligible (0.06%). The effect of the basis set on CIS energies is seen to be more noticeable. In particular, the addition of both polarized (d,p) and diffuse (+) functions in the basis set improves the performance. The calculated wavelengths

Table 3.1: Convergence dependence on the basis set for the $S_1 \leftarrow S_0$ transition wavelength (nm) calculations in neutral and protonated naphthalene.

| CIS basis set | B3LYP 6-311G(d,p) geom | | B3LYP 6-311++G(d,p) geom | | |
|-----------------|------------------------|-----------------|--------------------------|-----------------|-----------------|
| | $C_{10}H_8$ | $2-C_{10}H_9^+$ | $C_{10}H_8$ | $1-C_{10}H_9^+$ | $2-C_{10}H_9^+$ |
| 3-21G | 225.75 | 329.02 | | | |
| 4-31G | 227.82 | 331.00 | 228.07 | 287.02 | 331.20 |
| 6-31G | 229.37 | 332.66 | 229.62 | 288.29 | 332.87 |
| 6-31G(d,p) | | | 236.21 | 294.69 | 338.55 |
| 6-31+G(d,p) | | | 242.13 | 297.68 | 341.35 |
| 6-31++G(d,p) | | | 242.14 | 297.80 | 341.64 |
| 6-311G | 231.94 | 334.60 | 232.20 | 290.15 | 334.81 |
| 6-311G(d) | 239.94 | 341.31 | | | |
| 6-311G(d,p) | 240.24 | 341.04 | 240.50 | 297.08 | 341.25 |
| 6-311+G(d) | | | 243.56 | 298.48 | 342.96 |
| 6-311+G(d,p) | 243.71 | 342.54 | 243.97 | 298.79 | 342.76 |
| 6-311++G(d,p) | 243.72 | 342.66 | 243.98 | 298.84 | 342.88 |
| 6-311++G(2d,2p) | | | 245.86 | 300.55 | 345.45 |

appear to group together for minor basis set changes and experience a ‘nudge’ towards smaller energies upon more significant changes. The basis set changes explored were 4-31G \longrightarrow 6-31G, 6-31G \longrightarrow 6-311G, the addition of polarized functions [105] (either d or d,p), a change in the level of polarized functions (from d,p to 2d,2p), and the addition of at least one diffuse function [106]. With each change, the calculated values move toward the experimental values. From these tests, the 6-31+G(d) basis set appears to be the minimum required for CIS calculations on neutral and protonated PAHs. Here, the 6-311++G(2d,2p) was selected for excited states calculations. This basis set is relatively large, but at the same time, CIS calculations are still significantly faster than geometry optimizations. Typically, 4 hours were needed to calculate the singlet energies and about another 20 hours to perform the population analysis on the P4-2.7 system.

3.2.3 Scaling Factors

Clearly, the CIS calculations tend to overestimate the excited states energies. The easiest way to compensate for this in a homologous suite of compounds is an empirical approach, that is, scaling the calculated results to better match experimental values. Fortunately, the gas phase $S_1 \leftarrow S_0$ transition wavelengths have been measured for many small neutral aromatics (benzene [129], naphthalene [70], anthracene [69], phenanthrene [130,131], pyrene [131,132]). The ratios of the calculated and experimental values are presented in Table 3.2. They lie mainly in the range 0.77 ± 0.01 for all molecules considered, except anthracene (0.846). Based on this result, the scaling factor for protonated PAHs should be somewhere in the 0.75 – 0.85 range. Here, the scaling factors obtained from the respective neutral molecule calculations are used.

Table 3.2: Scaling factors for the $S_1 \leftarrow S_0$ transitions in neutral aromatic hydrocarbons.

| Molecule | $S_1 \leftarrow S_0$ wavelength (nm) | | Scaling factor |
|---|--------------------------------------|--------------|----------------|
| | Calculated | Experimental | |
| Benzene (C ₆ H ₆) | 206.22 | 262.56 | 0.78542 |
| Naphthalene (C ₁₀ H ₈) | 243.98 | 312.30 | 0.78123 |
| Anthracene (C ₁₄ H ₁₀) | 305.39 | 361.17 | 0.84556 |
| Phenanthrene (C ₁₄ H ₁₀) | 258.26 | 340.99 | 0.75738 |
| Pyrene (C ₁₆ H ₁₀) | 282.19 | 367.43 | 0.76801 |

The validity of scaling down the calculated values may be questioned, especially whether the factor for the neutral molecule can be applied to its protonated versions. To date, experimental data are available only for protonated benzene [89,90]. Calculated but scaled wavelengths for the C₆H₇⁺ $S_1 \leftarrow S_0$ transition (349.77 nm in Table 3.3) is slightly red-shifter from the experimentally measured band maximum at ~ 335 nm. The scaled predicted and experimental values also turn out to be very close for isomer 1 of protonated anthracene, and somewhat red-shifted for isomer 2 (Chapter 6).

3.3 Valence Molecular Orbitals

In neutral aromatic molecules, the transitions from the ground to the first few excited electronic states are $\pi - \pi^*$ transitions. The electronic structure of protonated PAHs should therefore not differ drastically from neutral PAHs. In particular, their $S_1 \leftarrow S_0$ transitions should be $\pi - \pi^*$ as well. To illustrate the changes in the molecular π orbitals upon protonation, the benzene molecule is first considered as an example system.

3.3.1 Protonated Benzene

The benzene molecule is one of the most popular benchmark systems in chemistry. Its molecular orbital system is well-studied and is described in nearly every general chemistry textbook. The molecular π orbitals of neutral benzene based on Hückel theory are shown in Figure 3.1. These are the *NaturalOrbitals* from an energy calculation (HF STO-3G) on previously optimized geometries (B3LYP 6-311++G**) and visualized in Chem3D [133].

Upon protonation, the hybridization of one of the carbon atoms changes from sp^2 to sp^3 (Figure 3.2). As a result, its p_z orbital is not a part of the aromatic system and the ring is no longer aromatic. The p_z orbitals of the other five carbon atoms remain unchanged and still form a conjugated system, as can best be seen in the $2b_2$ orbital that is lying just below the HOMO.

Because of this reduction in symmetry, the orbitals of protonated benzene are no longer degenerate. Two out of the six benzene orbitals (one e_{1g} and one e_{2u}) do not overlap with the protonation site, and therefore have the same appearance in protonated benzene (two a_2 orbitals), with energies that are barely perturbed by protonation. The other four orbitals, however, are altered substantially by the protonation process and become a hybrid of carbon p_z orbitals and hydrogen s orbitals (four b_2 orbitals), since the C-H bonds at

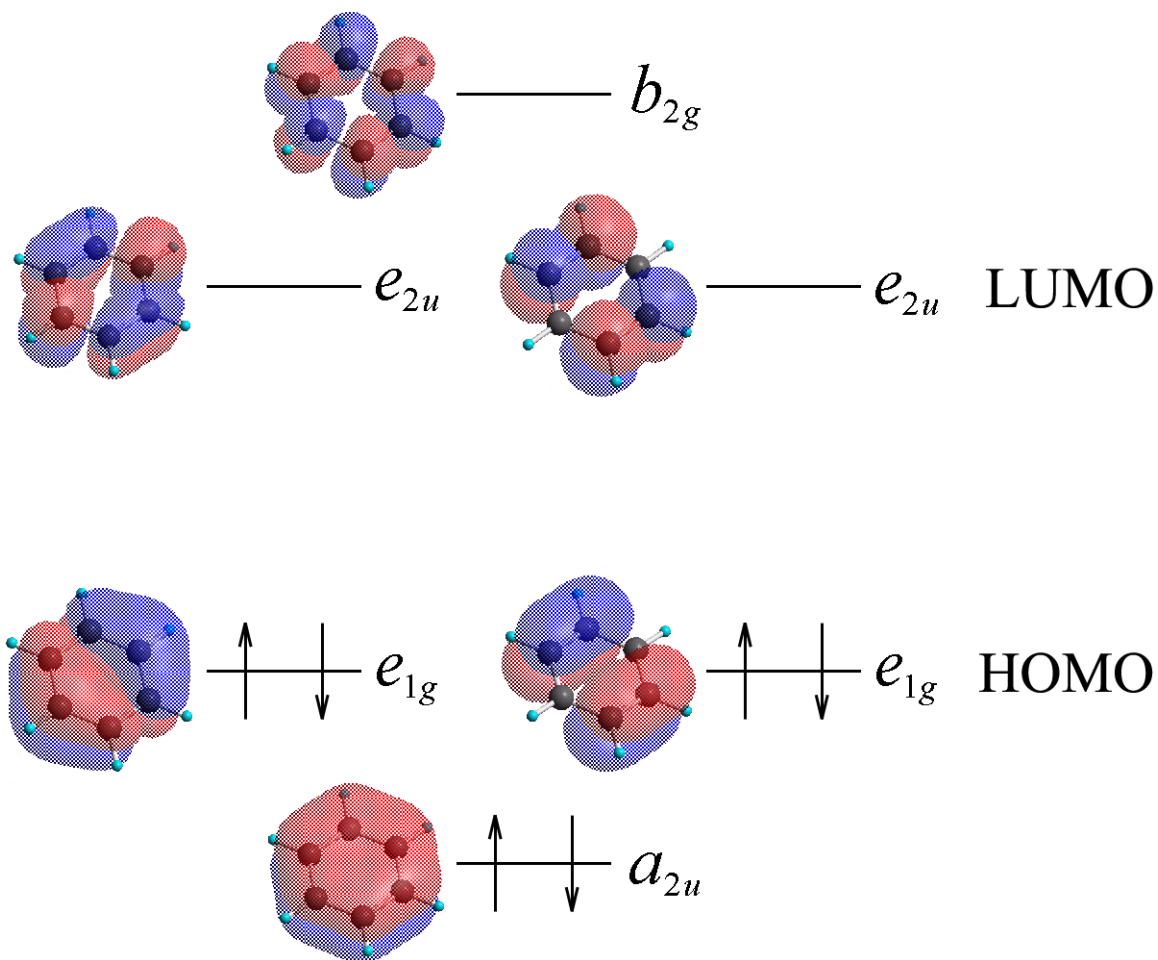


Figure 3.1: The π molecular orbitals of benzene.

the CH_2 site are σ bonds. As a result, their energies are lowered with respect to neutral benzene orbitals (solid *vs.* dashed lines in Figure 3.2). Since the HOMO is unaffected, this reduces the HOMO – LUMO gap, which leads to a red shift in the absorption spectrum.

3.3.2 Other Protonated Aromatics

When a molecule with more than one ring is protonated, the changes in orbitals are similar to benzene, that is, the aromaticity is lost only in the ring with the protonation site while other rings remain aromatic. Unlike the benzene molecule, the HOMOs and

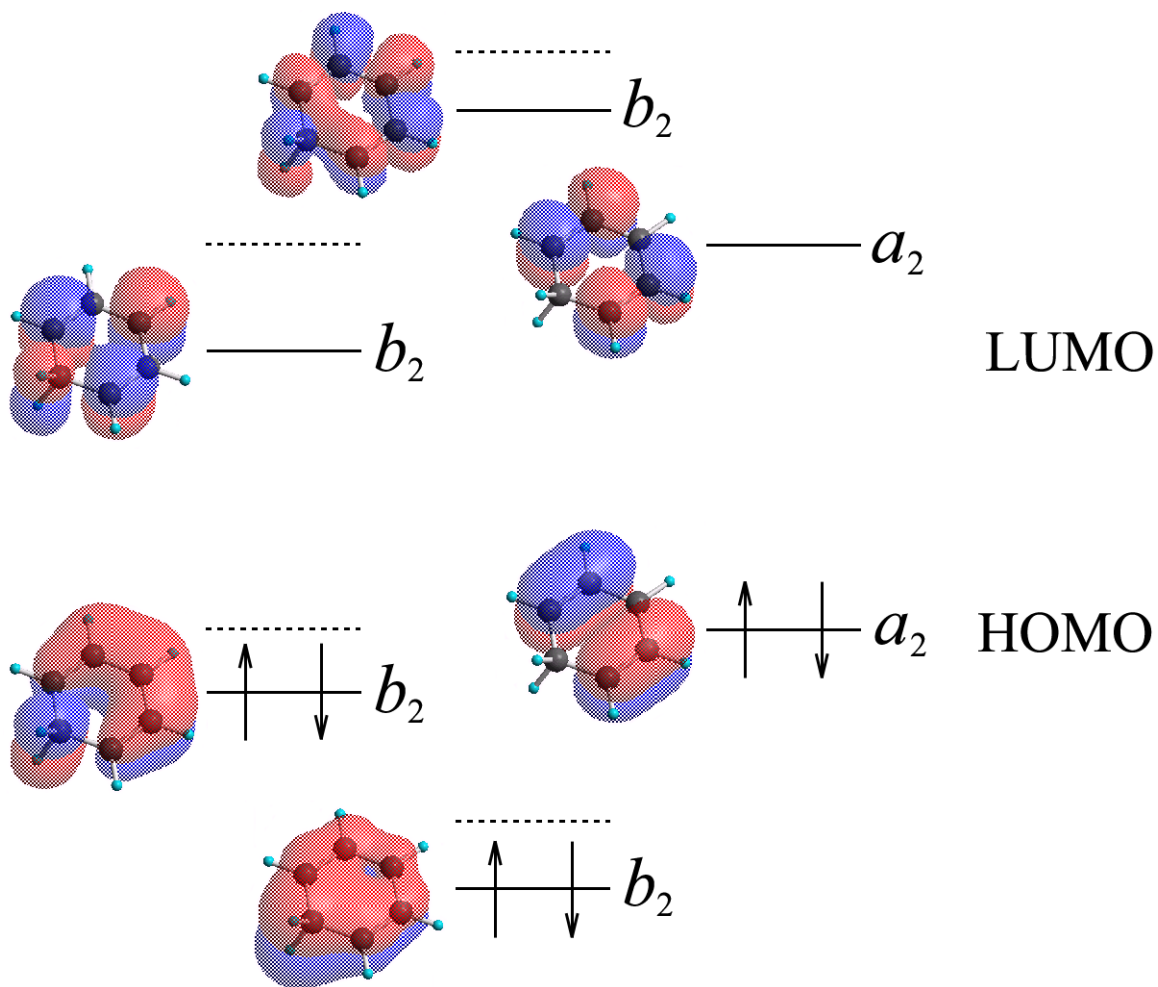


Figure 3.2: The π molecular orbitals of protonated benzene.

LUMOs of neutral polycyclic aromatic molecules are non-degenerate and remain that way after protonation. Orbital images of the HOMOs and LUMOs of neutral and protonated PAHs are shown in Appendix A, Table A.39.

3.3.3 Electronic States Assignment

The assignment of electronic states is based on the molecular orbital symmetry [134]. Among neutral PAHs, benzene belongs to the D_{6h} symmetry group, naphthalene, anthracene and pyrene to the D_{2h} group, and phenanthrene to the C_{2v} group. The symmetry

is reduced in protonated PAHs. Protonated benzene, isomer 9 of protonated anthracene and isomer 2 of protonated pyrene are members of the C_{2v} symmetry group, while the rest have C_s symmetry.

The exact assignment of the orbital symmetry depends on the choice of the orthogonal coordinate system. Here, for all non- C_{2v} symmetric molecules, the Z axis is set to be normal to the molecular plane by analogy with neutral benzene (Figure 3.3 1). In molecules with C_{2v} symmetry, the Z axis is selected as the rotational C_2 symmetry axis (Figure 3.3 2), with the X axis set orthogonal to the Z axis in the molecular plane and in the prolate direction. The Y axis is orthogonal to the X and Z axes. It is therefore in the molecular plane for non- C_{2v} symmetric molecules. This coincides with the coordinate system used in studies of the valence states of polyacenes [127].

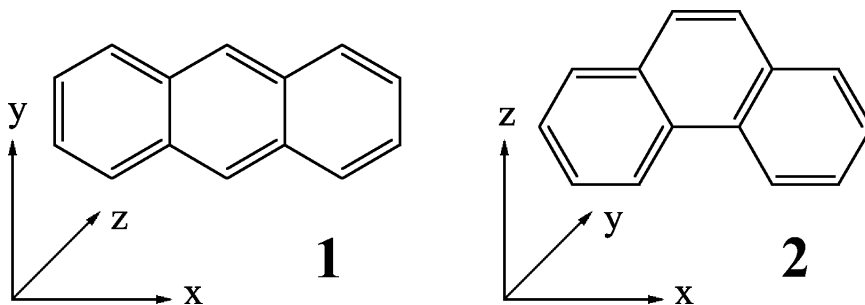


Figure 3.3: Orthogonal axis selection for molecules with different symmetry.

Based on this coordinate system, the ground and the first singlet electronic states, as well as electronic configurations, were assigned (Appendix A, Table A.38). The total number of π orbitals was the same as the number of carbon atoms. The symmetries of orbitals were determined by visual inspection. The electronic states were then labeled using the symmetry of HOMO and LUMO orbitals (the ones that have x and y electrons in Table A.38).

C_s -symmetric molecules (the majority of protonated PAHs) present the simplest case. For them, all orbitals have a'' symmetry. Thus, the ground state (S_0) is \tilde{X}^1A' and the first singlet excited state (S_1) is \tilde{A}^1A' . For C_{2v} -symmetric molecules, the HOMOs and LUMOs have a_2 and b_2 symmetry, leading to \tilde{X}^1A_1 ground states and to \tilde{A}^1B_1 for S_1 states. The orbital symmetries become more diverse for D_{xh} -symmetric molecules. Molecules with D_{2h} symmetry have \tilde{X}^1A_g S_0 states and \tilde{A}^1B_{xu} ($x = 1, 2$ or 3) S_1 states. For the benzene molecule (D_{6h}), it is well known that the S_0 state is \tilde{X}^1A_{1g} and the S_1 state is \tilde{A}^1E_{1u} .

3.4 Excited States Energies

The first singlet excited state energies and $S_1 \leftarrow S_0$ transition wavelengths were calculated for the neutral and stable isomers of protonated benzene, naphthalene, anthracene, phenanthrene, and pyrene. A short overview of the results is presented in Table 3.3, and the full version is presented in Appendix A, Table A.37. The wavelengths in both tables are scaled by the neutral PAHs experimental values. The scaling in Table A.37 ranges for $0.75 - 0.85$.

As one would expect, the $S_1 \leftarrow S_0$ wavelengths for protonated PAHs are shifted to the red, as compared to their neutral PAH precursors. There is a wide range of red shifts, from 15 nm for isomer 9 of protonated anthracene to just over 200 nm for isomer 2 of protonated pyrene. The majority are significant, on the order of 100 nm (Appendix A, Table A.37).

The $S_1 \leftarrow S_0$ transitions for small neutral PAHs lie at UV wavelengths range, and so are not important to the DIBs. With the exception of protonated benzene, however, all of the protonated versions of small PAHs have isomers that should absorb visible wavelength photons. In fact, all isomers of protonated phenanthrene and pyrene absorb in the visible. Roughly, it appears that the closer the protonation site is to the center-of-mass of the

Table 3.3: Scaled calculated $S_1 \leftarrow S_0$ wavelengths for neutral and protonated PAHs.

| Molecule | $S_1 \leftarrow S_0$ Wavelength (nm) |
|---------------------|--------------------------------------|
| Benzene | |
| C_6H_6 | 262.56 |
| $C_6H_7^+$ | 349.77 |
| Naphthalene | |
| $C_{10}H_8$ | 312.30 |
| 1- $C_{10}H_9^+$ | 382.53 |
| 2- $C_{10}H_9^+$ | 438.90 |
| Anthracene | |
| $C_{14}H_{10}$ | 361.17 |
| 1- $C_{14}H_{11}^+$ | 443.09 |
| 2- $C_{14}H_{11}^+$ | 490.41 |
| 9- $C_{14}H_{11}^+$ | 376.47 |
| Phenanthrene | |
| $C_{14}H_{10}$ | 340.99 |
| 1- $C_{14}H_{11}^+$ | 477.20 |
| 2- $C_{14}H_{11}^+$ | 497.78 |
| 3- $C_{14}H_{11}^+$ | 460.81 |
| 4- $C_{14}H_{11}^+$ | 493.13 |
| 9- $C_{14}H_{11}^+$ | 479.36 |
| Pyrene | |
| $C_{16}H_{10}$ | 367.43 |
| 1- $C_{16}H_{11}^+$ | 442.82 |
| 2- $C_{16}H_{11}^+$ | 569.30 |
| 4- $C_{16}H_{11}^+$ | 499.23 |

molecule, the shorter the wavelength of the $S_1 \leftarrow S_0$ transition. For polyacenes (naphthalene, anthracene), this also correlates with isomer ground state stability; more stable isomers absorb at shorter wavelengths.

The photon energies for the $S_1 \leftarrow S_0$ transitions are close to the ground state dissociation thresholds for protonated PAHs calculated in Chapter 2 (Table 3.4). After absorbing a UV/visible photon, the protonated PAH ion ends up in an electronically excited state that may undergo an internal conversion to the ground electronic state. The photon energy in this case would be converted into vibrations via intramolecular vibrational energy redistribution (IVR). This means that protonated benzene, naphthalene and anthracene would, in

principle, have enough energy to dissociate even when excited to the S_1 electronic state. Larger protonated PAHs would have enough energy to dissociate when excited to higher electronic states. Thus, it may be possible to record absorption spectra of protonated PAHs by resonance-enhanced dissociation method. Such an attempt is made in Chapter 5. At the same time, this casts a shadow on the prospective of protonated PAHs survival in the interstellar medium.

Protonated PAHs are expected to be strong absorbers, since the calculated oscillator strengths for the $S_1 \leftarrow S_0$ transitions are in the 0.14 – 0.7 range (Appendix A, Table A.37). Depending on the isomer, some of them may absorb better than their neutral cousins.

Table 3.4: Comparison of the calculated $S_1 \leftarrow S_0$ wavelengths and ground state dissociation energies for protonated PAHs, in kcal/mol.

| Molecule | $S_1 \leftarrow S_0$ Wavelength | Dissociation Energy |
|---------------------|------------------------------------|------------------------|
| Benzene | | |
| $C_6H_7^+$ | 81.74 | 63.22 |
| Naphthalene | | |
| $1-C_{10}H_9^+$ | 74.32 | 62.41 |
| $2-C_{10}H_9^+$ | 64.66 | 59.51 |
| Anthracene | | |
| $1-C_{14}H_{11}^+$ | 64.53 | 52.41 |
| $2-C_{14}H_{11}^+$ | 58.30 | 49.36 |
| $9-C_{14}H_{11}^+$ | 75.95 | 61.06 |
| Phenanthrene | | |
| $1-C_{14}H_{11}^+$ | 59.92 | 59.53 |
| $2-C_{14}H_{11}^+$ | 57.44 | 57.53 |
| $3-C_{14}H_{11}^+$ | 62.05 | 58.98 |
| $4-C_{14}H_{11}^+$ | 57.98 | 58.46 |
| $9-C_{14}H_{11}^+$ | 59.64 | 59.33 |
| Pyrene | | |
| $1-C_{16}H_{11}^+$ | 64.57 | 60.78 |
| $2-C_{16}H_{11}^+$ | 50.22 | 46.57 |
| $4-C_{16}H_{11}^+$ | 57.27 | 50.52 |

3.4.1 Comparison with DIB spectrum

Since protonated PAHs are predicted to be strong absorbers of visible wavelength photons, it is interesting to compare calculated $S_1 \leftarrow S_0$ transition wavelengths with the spectrum of the diffuse interstellar bands. The DIB synthetic absorption spectrum is calculated based on extensive DIB surveys [31–33] that were compiled from many different astronomical sources [1]. In Figure 3.4, the black solid line is the synthetic DIB spectrum; vertical colored dashed lines are the scaled $S_1 \leftarrow S_0$ wavelengths; and the horizontal colored solid lines are the scaled wavelengths ranges for each transition.

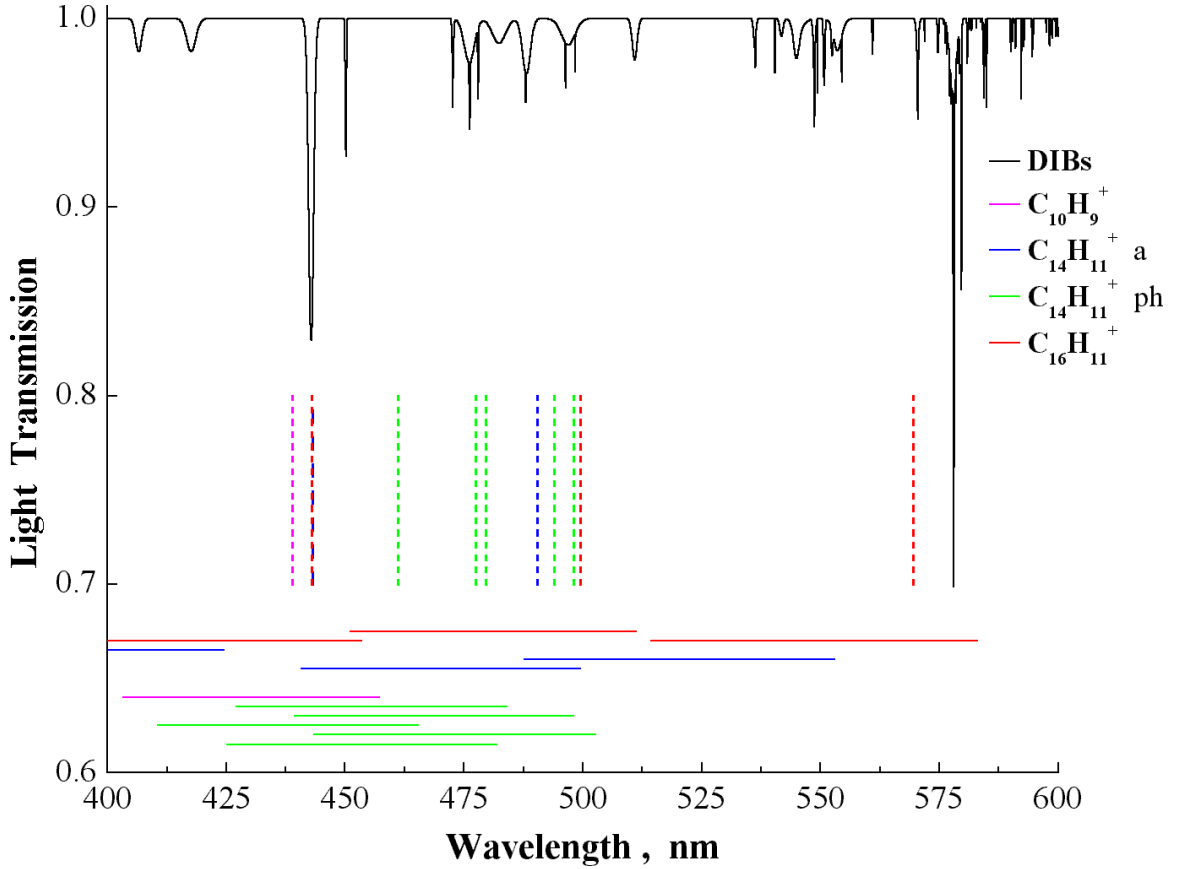


Figure 3.4: Diffuse interstellar bands and calculated $S_1 \leftarrow S_0$ wavelengths for protonated PAHs.

Since protonated PAHs are relatively large molecular ions, their absorption bands should be broader than for small molecules. Hence, if protonated PAHs are the DIB carriers, they should contribute to broad DIB features (1 – 3 nm wide). There are three different protonated PAH isomers (from naphthalene, anthracene and pyrene) that absorb near the strong 443 nm band. Four isomers of protonated phenanthrene and one from protonated anthracene and pyrene should absorb in 470 – 520 nm range, where five broad bands are located. One isomer of protonated pyrene is in the vicinity of the 578 nm band. The proximity of the calculated transitions to the broad DIBs makes a good argument in favor of protonated PAHs as DIB carriers, however, it should be tested experimentally. The UV/visible absorption spectra of protonated PAHs in the gas phase need to be measured. This issue is addressed in Chapters 5 and 6.

3.5 Summary

$S_1 \leftarrow S_0$ transition wavelengths were calculated for neutral and protonated PAHs with CIS method. The symmetries of the ground and the first singlet excited states were assigned together with their electronic configurations. It was determined that most protonated PAHs have \tilde{X}^1A' ground state and \tilde{A}^1A' excited S_1 state.

The $S_1 \leftarrow S_0$ transitions for most protonated PAHs are estimated to be in the visible, where the DIBs are located. They are fairly close to a number of the broad DIB features. This is encouraging news for the theory that protonated PAHs are DIB carriers. For species with a few isomers in the DIB range, the match of a few experimentally measured bands with DIBs would be solid proof for such a theory.

The energy differences between LUMO and HOMO in protonated PAHs are close to their dissociation thresholds. In the absence of IVR, this makes them potentially unstable

in the ISM, but as the size of the molecule gets larger, IVR has a profound effect on the stabilization of PAHs. As was found in Chapter 5, even relatively small protonated PAHs may be photostable in the ISM.

Chapter 4

Experimental Setup

4.1 Introduction

To measure the electronic spectra of protonated PAHs, appropriate protonation and detection methods need to be selected. In general, protonated PAHs can be produced in a hydrogen discharge of some kind, or by a proton transfer from other protonated molecules. The method for recording the spectrum may strongly depend on the way the protonation has been performed, and so should be considered in tandem with the production techniques.

In afterglow discharge experiments [75], for example, the reactions of PAH cations with hydrogen were studied. As a result of these reactions, the cations of aromatic molecules (benzene, naphthalene and pyrene) acquired hydrogen atoms, making protonated PAHs with nearly 100% efficiency. For this fairly high pressure method, the protonated PAH spectra would have to be recorded in direct absorption. Even with multipass configurations for the laser beam, the sensitivity of such methods is usually low. The absorption strength would strongly depend on the concentration of protonated PAHs, but high concentrations are not easily achievable for multi-ring PAHs due to their low vapor pressures. The sample and possibly the flow cell would therefore need to be heated to increase the amount of absorbing ions, and the high temperatures and collision frequency would broaden the

spectrum significantly.

In the IR cluster photodissociation experiments on C_6H_7^+ [3, 96], protonated benzene was created by proton transfer from the H_3^+ produced as a result of H_2 molecule ionization by an electron gun. This method produced protonated benzene that was sufficiently cold to cluster with Ar, N_2 , etc. Such a protonation method requires high pressure at the pulsed valve throat which can be achieved by increasing the carrier gas pressure behind the pulsed valve (i.e. the backing pressure) to ~ 10 atm. This creates a significant load on vacuum pumps and requires multiple differential pumping stages with good ion guides. It is possible to decrease the gas load on the pumps by shortening the gas pulse duration, but the piezo-based pulsed valves must be used in this case. Piezo valves cannot be heated above $80 - 100^\circ\text{C}$ and would be useful only when working with benzene and naphthalene, but not larger PAHs.

Alternatively, PAHs may be protonated in a longitudinal pulsed discharge source (pin-hole or slit). Discharge sources of this kind have been used successfully to create a wide array of species, including neutral, cationic and anionic carbon chains, and miscellaneous radicals [40, 135–137]. These discharge sources do not require high gas backing pressure and are easy to operate. When heated, they may be used with large PAHs as well, although it must be noted that the ions produced are typically vibrationally warmer than the ones from electron gun ionization-based sources.

A suitable way to record the spectra needs to be selected once the production method is set. Absorption or photodissociation would be the most appropriate methods for the gas phase spectroscopy of positive ions. As mentioned earlier, a typical absorption experiment requires a large number of protonated PAH molecules to be produced, even if some kind of multipass scheme for the light is implemented. The most sensitive of such methods –

cavity ringdown spectroscopy – has been used successfully to record absorption spectra of PAH cations (naphthalene, pyrene) produced in a slit pulsed discharge source [62–64]. It was estimated that with our discharge source, the cavity ringdown method would barely be able to detect any absorption due to the low number of protonated PAH ions and was therefore discarded.

An alternative method would be to conduct photodissociation measurements on protonated ions. Resonance Enhanced Multiphoton Dissociation (REMPD) was used previously to record the electronic spectra of the naphthalene [67], anthracene and phenanthrene [138] cations. Photodissociation was also used for protonated benzene [89,90] as well. The central problem with this method lies in its multiphoton character, therefore either high radiation intensity or long interaction time between the ions and photons are needed.

In our experiments, a longitudinal pinhole pulsed discharge source was used for PAH protonation due to its robustness and compatibility with existing equipment. Laser photodissociation was chosen to record spectra, and a reflectron time-of-flight mass spectrometer was used as a detection method.

4.2 Pulsed Discharge Source

4.2.1 Design

The pulsed discharge source was based on the Thaddeus group design used for the Fourier-transform microwave spectroscopy of carbon chains [40]. It was modified for use with the time-of-flight mass spectrometer, but the electronic circuitry was kept the same. The design for our source is shown in Figure 4.1 (see Appendix B, Figures B.1–B.7 for detailed shop drawings). The discharge source consisted of two electrodes mounted on a Parker General

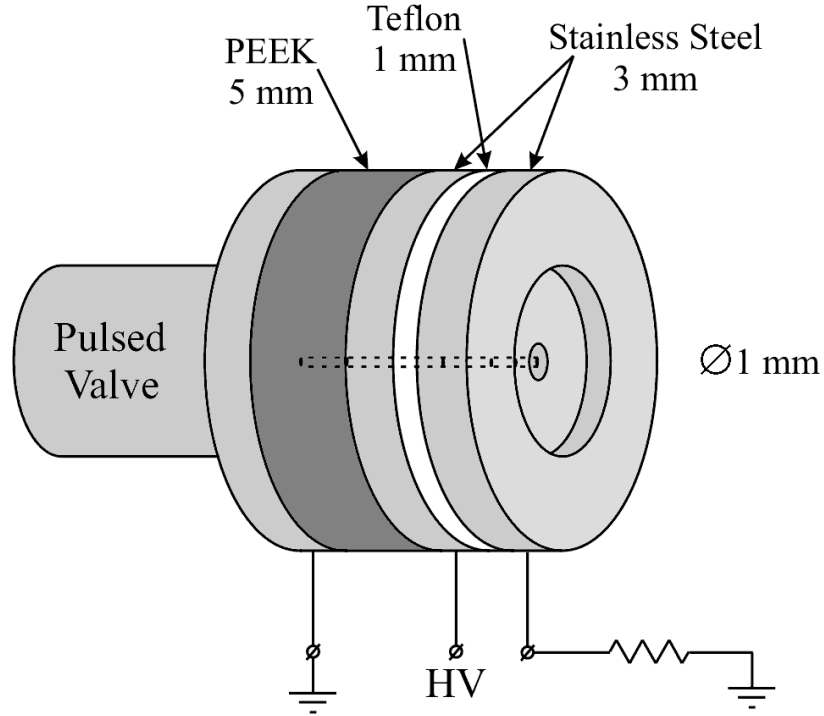


Figure 4.1: The pulsed discharge source design.

Valve series 9 pulsed valve, separated from the valve and each other by insulating spacers. A small channel for the gas flow was drilled in the center of the electrodes and spacers. The diameter of the channel was 1.0 mm. This value was optimized for the best discharge conditions which consisted of balancing the preferably low pressure for the discharge with the preferably high pressure for gas cooling during the expansion into vacuum. The diameter of the pulsed valve orifice was 0.7 mm. To avoid a parasitic volume next to the pulsed valve, the face of the valve body was flat, that is, there was no standard cone around the orifice. The outside diameter of the electrodes and spacers was the same as for the pulsed valve body – 1.33" (33.9 mm). The spacer between the electrodes was made of teflon and was 1.0 mm thick. The spacer between the pulsed valve and the inside electrode was made of PEEK (poly-ether-ether ketone) to insulate the heated pulsed valve thermally from the rest of the

discharge assembly. Either a 5.0 or 7.0 mm thick spacer was used. Electrodes were made of stainless steel to prevent their sputtering by the discharge. High voltage rated (up to 5 kV) electric wires were attached to the side of the electrodes with 0–80 screws. Ideally, the electrodes should be as thin as possible (down to 0.5 mm) to avoid plasma neutralization by the electrodes. In our case, they were 2.54 mm thick due to the size of wire lugs and screw heads. The middle part of the outside electrode was made 1.7 mm thick and had a 90° cone to improve the quality of the gas jet flow. Electrodes and wires were wrapped with teflon tape to prevent arcing between electrodes outside the discharge channel. The entire assembly was held together with four screws, insulated electrically from the electrodes by teflon inserts and washers.

In principle, high voltage could be applied to both electrodes in the discharge. In order to avoid ion deflection by the electrode potential after the plasma left the discharge, the outside electrode was held at almost ground potential. It was connected to ground with a 10 Ω , 10 W current monitoring resistor. The negative DC high voltage pulse (up to –2.0 kV) was applied to the inside electrode, and the pulsed valve body was grounded. The discharge would occur between the electrodes and not between the inside electrode and the valve body due to the large difference in the thickness of the PEEK and teflon spacers.

The pulsed valve was operated at 5 – 7 Hz repetition rate by a driver circuit (Appendix B, B.2.2) that applied a 400 μ s long pulse to open the valve with a setting of 160 – 180 V on the capacitors C_1 . After two to three days of continuous operation, the inside channel of the discharge had to be cleaned of a carbonaceous deposit. The need for cleaning was determined by a decline in the ion signal and an increased surface arcing in the discharge.

4.2.2 Voltage and Current Profiles

The negative high voltage pulse was typically applied to the inside electrode 250 μs after opening the pulsed valve. The duration of the high voltage pulse was 1200 μs to cover the full gas pulse delivered by the valve. Typical voltage and current curves for the discharge are shown in Figure 4.2. In this example, a -560 V pulse was applied. In the absence of gas between discharge electrodes (the front and the tail of the pulse), no discharge occurs. When the gas from the pulsed valve reaches the electrodes, the discharge starts, resulting in the high voltage drop and current flow observed. A dim blue glow was observed at

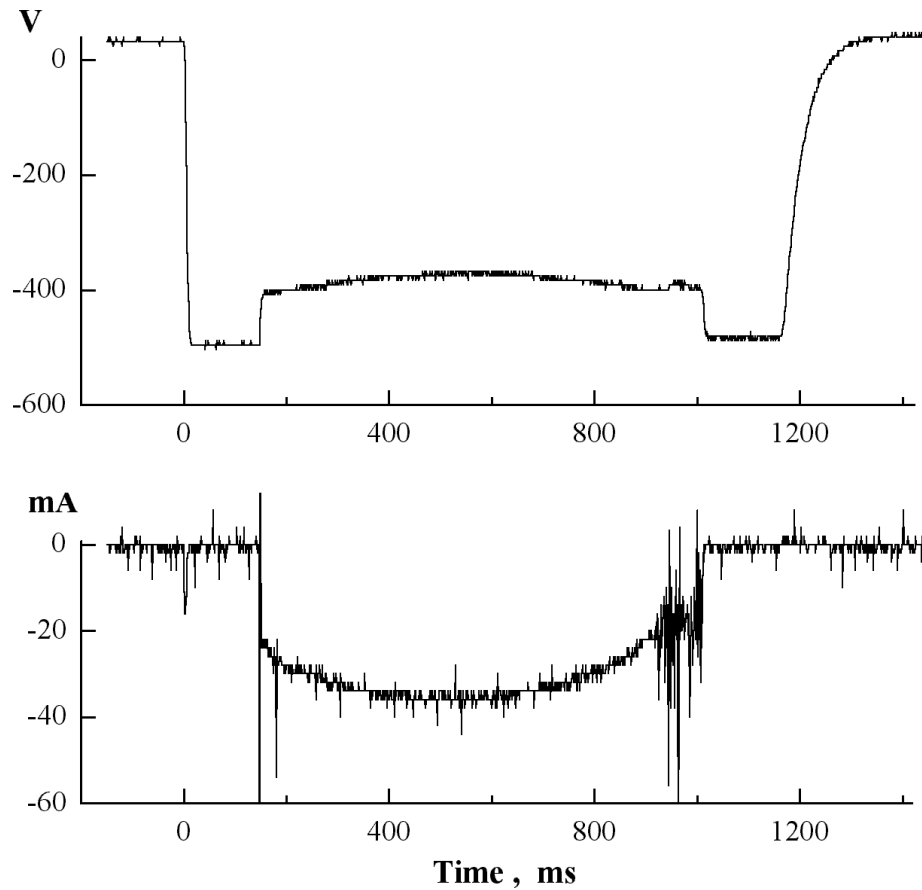


Figure 4.2: Pulsed nozzle discharge voltage and current profiles.

the discharge throat when plasma was expanding into the vacuum chamber of the mass spectrometer. Under these conditions, the discharge is stable and tracks the gas pulse well, as shown in the $V(t)$ and $I(t)$ curves in Figure 4.2.

In the case of an unstable discharge, the discharge start time would fluctuate significantly (by a few hundred microseconds). Sometimes, the discharge would not happen at all when it was ‘poisoned’ by the carbonaceous deposit inside the channel, or if the concentration of PAH molecules was too high. The latter would happen mostly for C_6H_6 . In such cases, the discharge would occur mostly along the surface and not through the gas, resulting in large random spikes in the voltage and current profiles.

4.2.3 Protonation Mechanism and Efficiency

The protonation of PAHs has been performed in discharges with H_2 as the carrier gas ($P_{H_2} = 1 - 2.5$ atm) and a low concentration of PAH molecules (at their nominal vapor pressure for heated samples). Mass spectra for an anthracene discharge with He and H_2 as carrier gases are presented in Figure 4.3. In He, the discharge produced only anthracene cations ($m/z = 178$ a.m.u.), and the cation signal was relatively weak. However, when He was replaced with H_2 , a cation signal with almost the same strength was produced, along with a new peak at ($m/z = 179$ a.m.u.) that is much stronger and corresponds to protonated anthracene. The intensity ratio for the protonated and cation mass peaks ranged from 1 : 1 to 20 : 1, with 8 : 1 being a typical value.

The protonation of PAH molecules in the hydrogen discharge was expected to happen through the mechanism of proton transfer from H_3^+ [3]:

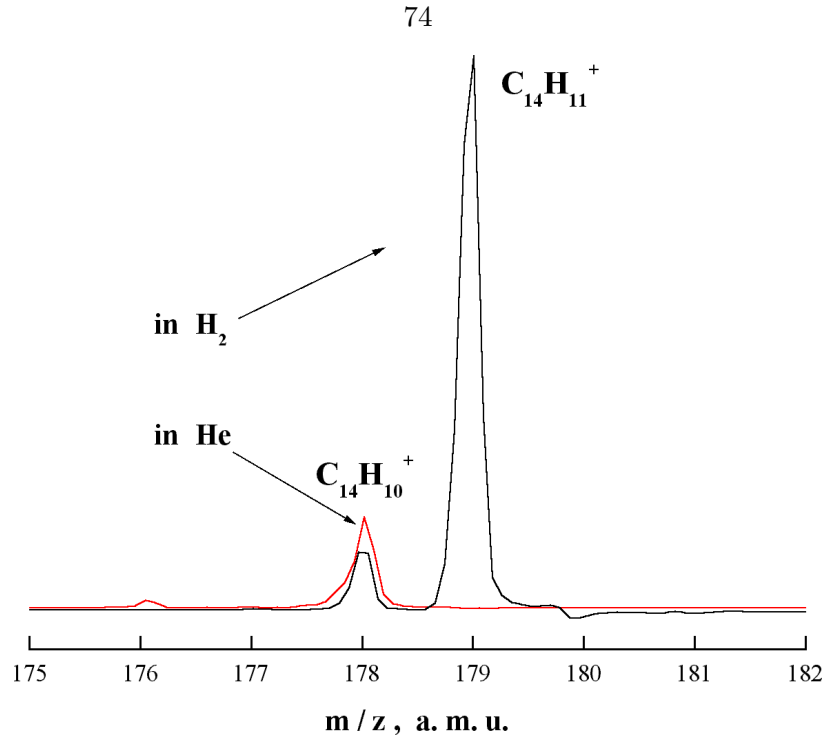
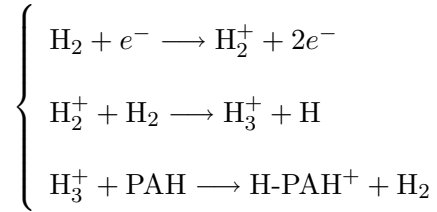


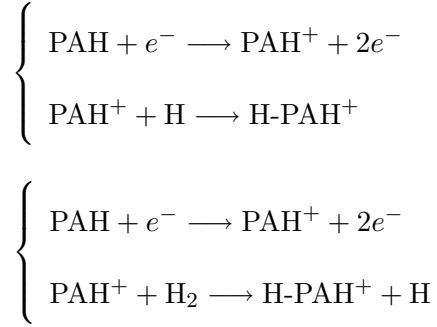
Figure 4.3: Mass spectra of anthracene and protonated anthracene in He *vs.* H₂ discharges.



Indeed, in the mass spectrum of a pure H₂ discharge, the following mass peaks were observed:

H⁺, H₂⁺ and H₃⁺ (m/z = 1, 2 and 3 a.m.u. in Figure 4.4).

The threshold voltage for the discharge to start was −800–900 V in pure H₂. Whenever PAH molecules were added into the discharge, that value dropped to −530–560 V. Simultaneously, the H₃⁺ peak disappeared from the mass spectrum. One explanation for this behavior would be that all the H₃⁺ ions were scavenged by PAH molecules. However, a more realistic mechanism for PAH protonation is likely via PAH ionization by discharge electrons, followed either by association with H atoms or by PAH cation hydrogen abstraction from the H₂ carrier gas:



This would easily explain the threshold voltage drop, and the first process is known to be fast [75]. The second was not observed at room temperature due to a barrier in the hydrogen abstraction reaction, but may be possible at higher temperatures in the discharge, or with internal excitation of the PAH.

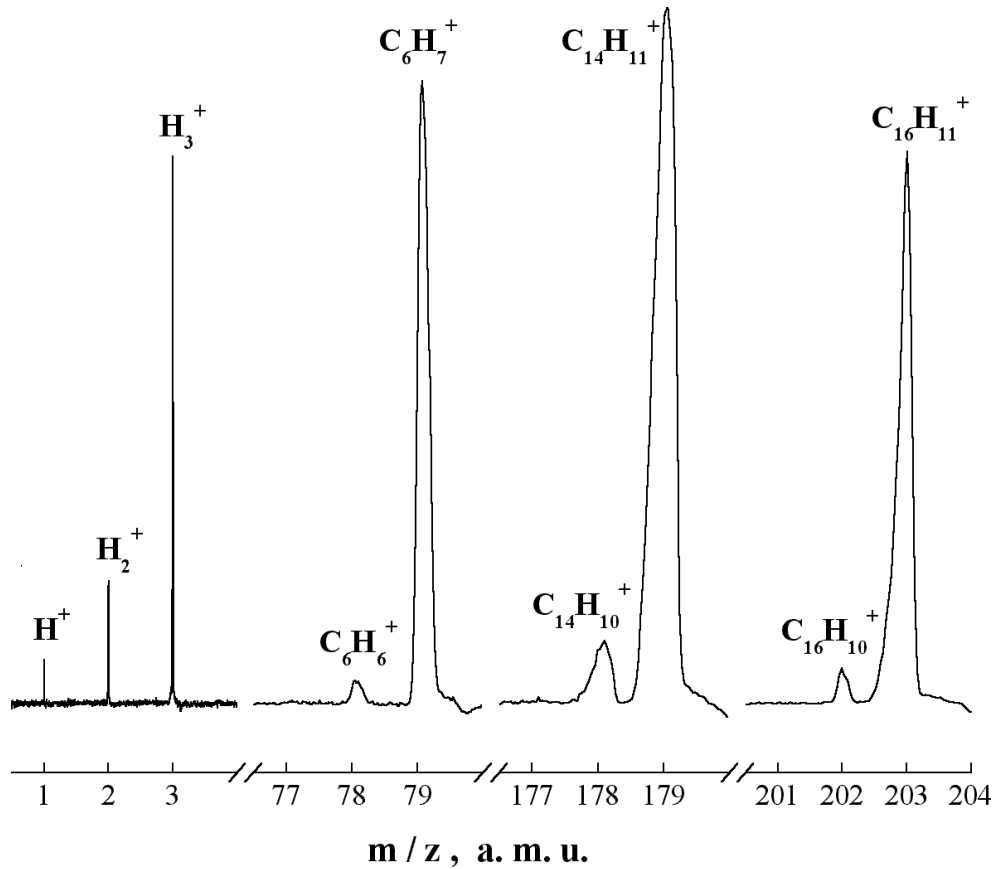


Figure 4.4: H_3^+ formation and the protonation of different aromatic molecules (benzene, anthracene and pyrene) in hydrogen discharges.

The protonation of benzene, anthracene and pyrene has been optimized in a discharge (Figure 4.4). In the case of anthracene and pyrene, $\sim 5 - 10$ g of the crystalline solid (Aldrich, 99% purity) was placed into an aluminium sample holder tube and connected to the pulsed valve with stainless steel tubing, with carrier gas (H_2) supplied to the tubing as well. The pulsed valve and sample holder were placed in thermal contact with, and heated by, electric heating cartridges. The stainless steel tubing was heated by heating tape wrapped around it. Temperatures were measured by K-type thermocouples and controlled by temperature controllers (Omega 7600CN). Typical temperatures used in the experiments were:

$$T_{\text{sample}} = 130\text{ }^{\circ}\text{C},\ T_{\text{tubing}} = 137\text{ }^{\circ}\text{C},\ T_{\text{valve}} = 145\text{ }^{\circ}\text{C}\ \text{for anthracene; and}$$

$$T_{\text{sample}} = 168\text{ }^{\circ}\text{C},\ T_{\text{tubing}} = 174\text{ }^{\circ}\text{C},\ T_{\text{valve}} = 180\text{ }^{\circ}\text{C}\ \text{for pyrene.}$$

The pulsed valve was kept $15\text{ }^{\circ}\text{C}$ warmer than the sample to reduce sample recrystallization on the inside of the valve faceplate due to its cooling from the gas flow into vacuum.

For protonated benzene, $\sim 10 - 20$ mL of benzene were placed into a stainless steel container and hydrogen was bubbled through it. For such an operation, the high concentration of benzene sometimes caused discharge instability. To reduce this instability, the walls of the gas line tubing were passivated with benzene for ~ 10 minutes and then the bubbler was disconnected. The passivated benzene evaporated slowly and sustained a stable signal for $1 - 2$ hours, after which the procedure was repeated.

The signal produced from protonated PAHs was quite strong. For example, 10^5 protonated anthracene ions per shot were estimated to be detected in the mass spectrometer. The high ion density led to noticeable broadening of mass peaks, thereby reducing the mass resolution. However, the deterioration of mass resolution was not an issue for the ions studied.

4.3 Cluster Source

4.3.1 Design

The cluster source used for making clusters of protonated anthracene with water consisted of the discharge source described above and another pulsed valve for delivering cluster partner molecules (Figure 4.5, see Appendix B, Figures B.3–B.10 for the drawings). The

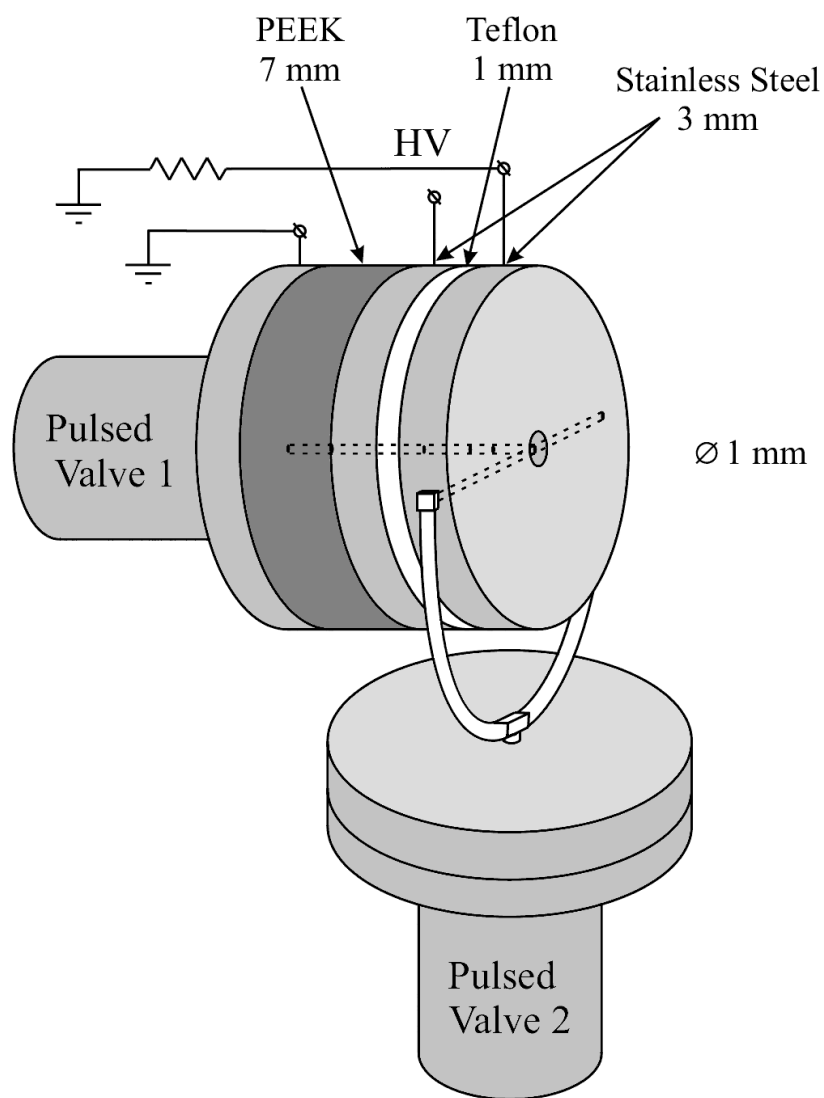


Figure 4.5: Pulsed discharge cluster source with two pulsed valves.

outside electrode of the discharge was modified to be 3 mm thick and had the same thickness in the middle and on the outside. A long 1.0 mm diameter channel was made in the middle of the electrode parallel to the disk plane, crossing the discharge channel at a right angle. The second valve was used for delivering atoms or molecules to create clusters at the discharge exit. Such a design was intended to prevent cluster partner molecules from entering the discharge. On the other hand, clustering occurs most efficiently in high gas pressure regions so clusters must be made at the discharge exit. In our case, PAH molecules are first protonated in the discharge, and as they are about to expand into vacuum, they collide with other molecules.

The second pulsed valve (Parker General Valve series 9) was placed as close as practical to the discharge. It had a faceplate adapter for a gas line. The adapter was equipped with a T-shaped nylon fitting. Similarly, the L-shaped elbow fittings were placed on the side ends of the discharge. Teflon tubing with a 1/16" inner diameter connected the fittings in a 'stethoscope' configuration. When the valve was open, the gas would flow through that tubing and enter the discharge region symmetrically from the opposing sides, thus maintaining the pointing of the gas jet.

It should be pointed out that this source is different from another ion cluster mixing source [139], in which clusters of molecular anions with rare gas atoms are first formed in the high pressure expansion. Cluster ligands are then substituted with another molecule in a low pressure cell, filled by the opening of a second pulsed valve.

4.3.2 Operation

Both pulsed valves of the cluster source were operated at a 0.9 Hz repetition rate, limited by the pumping speed available in the mass spectrometer chamber. At higher repetition

rates, the pressure in the flight tube of the time-of-flight mass spectrometer was above 10^{-6} Torr, which could potentially damage the MCP detectors. When photodissociation spectra of clusters were recorded, the laser had to be operated at 10 Hz. To reduce the operating repetition rate for the pulsed valves, a TTL frequency divider circuit (Appendix B, B.2.4) was used with a dividing ratio of 11 : 1.

The second pulsed valve must be opened before the discharge valve, since time is needed for the gas to reach the mixing region of the discharge. Delay times were optimized for the maximum cluster signal by 2-D scanning of the delays between the two pulsed valves, and between the valves and the ion extraction pulse in the mass spectrometer.

4.4 Mass Spectrometer

A Wiley-McLaren time-of-flight mass spectrometer (TOF MS) [140] with a reflectron [141, 142], manufactured by R.M.Jordan Co., was used to detect and analyze positive ions from the discharge (Figure 4.6). It was previously described in detail [143, 144]. The mass-spectrometer chamber consisted of three independently pumped regions for differential pumping. The first chamber was designed to house the pulsed valve, while the second chamber was designed for ion extraction. The skimmer between the first and second chambers was removed in order to move the discharge as close to the extraction ion optics as feasible. The ion optics were enclosed in an extension of a third chamber and were connected to the second chamber via a skimmer (Beam Dynamics, 1 mm diameter) from the discharge side and an orifice (8 mm diameter) on the opposite side to provide an exit for the molecular beam. The third chamber served as the field free ion flight tube. The reflectron was placed close to the end of the flight tube. Microchannel plate (MCP) detectors were placed at both ends of the flight tube to detect ions in the linear and reflectron operation modes of

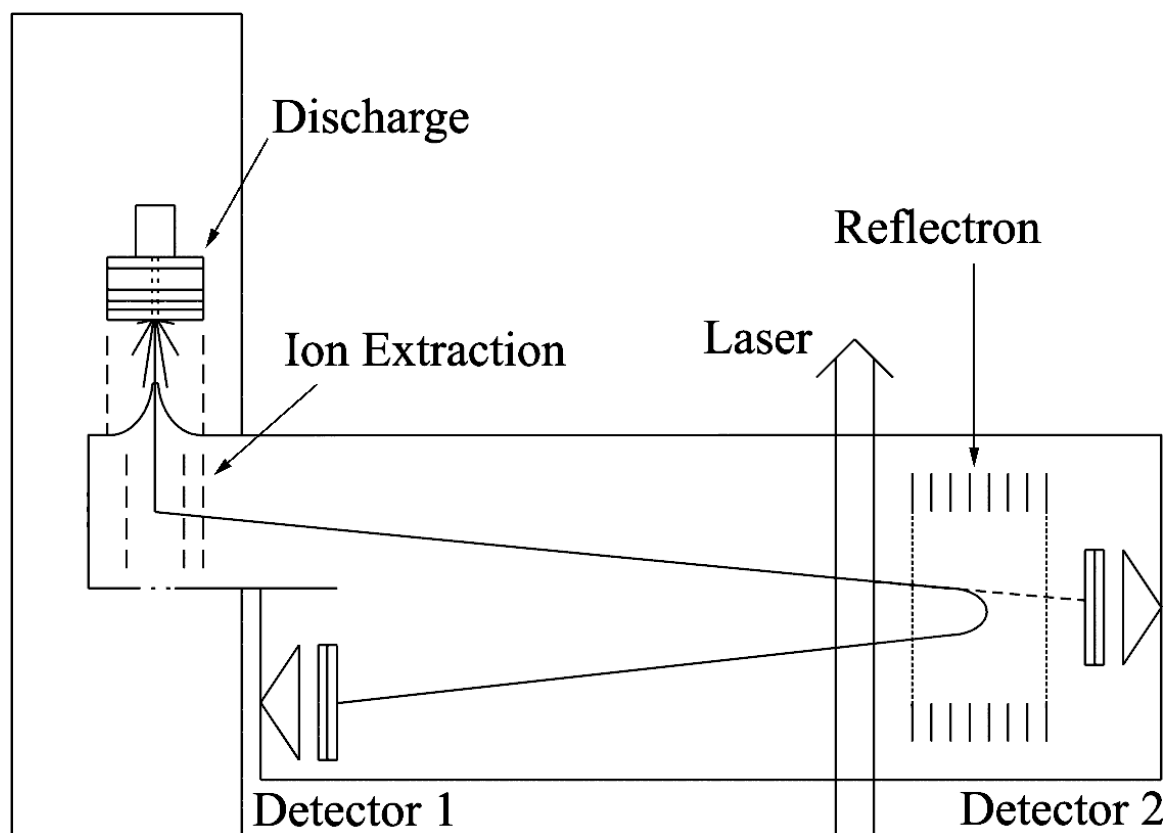


Figure 4.6: The time-of-flight mass spectrometer setup for photodissociation experiments (top view).

the mass-spectrometer.

4.4.1 Ion Shielding

Electrically neutral plasma exited the discharge at almost the thermal supersonic jet velocity, for which the kinetic energy of ions was estimated to be 0.1 eV. Special precautions had to be taken to protect such slow ions from any stray and static voltages inside the chamber.

The discharge source needed to be located as close to the skimmer as possible, and was placed 15 mm from the skimmer. A grounded wire mesh cylinder (1.3'' diameter) was placed around the supersonic jet along its path to the skimmer. Wires that delivered high

voltage to ion optics were ground shielded whenever possible.

All of these measures were not enough, however, since the discharge plasma was creating surface charges on the skimmer and mesh surfaces. To improve the conductivity of the metal surfaces, the face of the discharge source, the skimmer, and the wire mesh were coated with carbon black film (Acheson Aquadag paste dissolved in acetone). This improved the detected ion signal dramatically and enabled ion extraction from any part of the discharge pulse.

4.4.2 Ion Extraction

Positively charged ions were pushed by a repeller grid A_1 (at 3150 V) to an extraction grid A_2 (at 2850 V), and then accelerated to the grounded grid in the direction perpendicular to the molecular beam. An Eisel lens (at 120 V) was used to focus the ion beam, while two XY deflector plates (typically, at 75 – 120 V) were used to accelerate ions in the horizontal direction parallel to the molecular beam to guide the ion beam onto the MCPs.

When the mass spectrometer was operated in the linear mode, the reflectron was kept at ground potential. In the reflectron mode, reflectron voltages were set to 1900 V and 3300 V, respectively. Voltages on the repeller and the extractor could be static when working with a neutral molecular beam and creating ions by photoionization. When working with ions created in the discharge source, these grids must first be grounded to allow unaccelerated plasma to enter the space between the repeller and the extractor. High voltages must then be applied simultaneously to these grids by a two-channel pulser, described in Appendix B, B.2.3.

High voltages for the ion optics and reflectron MCP detector were provided by a R.M.Jordan AREF power supply (5 kV, 1 mA maximum), for the Eisel lens by a Hewlett–

Packard 6525A power supply, and for the linear MCP detector by a Stanford Research Systems PS325 power supply, equipped with a voltage divider.

4.4.3 Reflectron Mode

The mass spectrometer was operated in the reflectron mode when photodissociation experiments were performed for two reasons. First, the reflectron helped to improve the mass resolution. For example, the TOF peaks from anthracene cation (178 a.m.u.) and protonated anthracene (179 a.m.u.) produced in the discharge were only partially resolved in the linear mode. In the reflectron mode, they were separated by at least the peak's full width at half maximum (Figure 4.4). The mass resolution in the mass spectrometer depended on the ion density and was lower for ions created by the discharge as compared to the photoionization. When the cluster discharge source was used for making ions, the ion density was lower and the mass resolution was therefore higher.

Second, the use of the reflectron in the photodissociation experiment gave the ability to monitor both parent ion signal depletion and neutral product formation. In the absence of the laser beam, all ions were turned by the reflectron to the reflectron MCP (detector 1). In the photodissociation experiment, the laser beam intercepted the ions before they entered the reflectron. When the ions absorbed laser radiation and dissociated, at least one ion and one neutral product were formed. The ions would still be turned by the reflectron, but the neutral photodissociation product would strike the linear MCP (detector 2). The depletion of the parent ion peak and possibly, the formation of the ion product would be observed with the reflectron detector. The signal-to-noise ratio on detector 1 was fairly poor, since the low dissociation yields could be buried in the intensity fluctuations of the parent ion peak.

On the other hand, the neutral product channel provided a good alternative to ion channel detection. The velocity of the neutral product would be close to the original velocity of the parent ion which had ~ 3.0 keV kinetic energy. Thus, the neutral product retained sufficient kinetic energy to produce a measurable signal on the linear detector. Unlike the signal on the reflectron detector, the neutral product signal had very little background and thus a much better signal-to-noise ratio.

4.4.4 Detectors

Each TOF MS detector consisted of two stacked Galileo MCPs. The diameter of the MCPs was 25 mm for the linear detector and 50 mm for the reflectron detector. The gain was regulated by applying up to 1000 V voltage to each MCP. The signal was collected by a conical electrode and sent to a preamplifier. The amplified signal was read by a digital oscilloscope. An EG&G ORTEC 9301 fast preamplifier (gain 10, ± 0.7 V output range) was used with the linear detector, while an EG&G ORTEC VT120C fast-timing preamplifier (gain 20, 0 to -5 V output range) was used with the reflectron detector.

4.4.5 Vacuum System

The first chamber was pumped by a 10" Varian VHS-10 diffusion pump (Dow Corning 705 oil); the second chamber was pumped by a 6" Varian VHS-6 diffusion pump (Santovac-5 oil); and the flight tube was equipped with a 4" Edwards Diffstack 100 diffusion pump (Santovac-5 oil). The 10" and 6" pumps were baffled by water-cooled baffles, and the 4" pump had a built-in baffle. Each pump had gate valves on both the intake and exhaust ports. The diffusion pumps were backed by an Edwards EM2-275 mechanical pump.

The pressure in the TOF MS chambers was measured by three MKS cold cathode

pressure gauges, and the backing pressure was measured by a MKS Pirani pressure gauge. With the pulsed valves off, the residual pressure in the chambers was $5 \cdot 10^{-6}$ Torr, $3 \cdot 10^{-7}$ and $2 \cdot 10^{-8}$ Torr, respectively. The backing pressure was $2 \cdot 10^{-3}$ Torr. With the pulsed valve on, the pressure in the second chamber was $6 \cdot 10^{-5}$ Torr and in the flight tube $1 \cdot 10^{-6}$ Torr. Under operating conditions the backing pressure rose to $6 \cdot 10^{-3} - 1 \cdot 10^{-2}$ Torr.

The diffusion pump cooling water was supplied by a closed loop Neslab Coolflow System II Liquid/Liquid recirculator. The mechanical pump was cooled by a Neslab Coolflow CFT-75 refrigerated recirculator.

The system was equipped with an interlock circuit (Appendix B in [143]) that was used to monitor the water flow through diffusion pumps and the backing pressure (set to be below 0.1 Torr). When tripped, it would turn off diffusion pump heaters, close pneumatic gate valves between mass spectrometer chambers and diffusion pumps, and turn off the high voltage power supplies connected to the ion optics and MCP detectors.

4.5 Laser Systems

4.5.1 Excimer Laser

A Lambda Physik LPX-120i excimer laser with NovaTube technology was used to generate UV radiation at 193 and 248 nm. The maximum pulse energy was 200 mJ for a 25×9 mm beam. The beam was passed through a 9 mm pinhole, retaining 25% of the original pulse energy, then guided with a system of 193 nm dielectric-coated mirrors into the TOF MS chamber. The size of the clipped, unfocused beam inside the flight tube was set to 10×15 mm for better spatial overlap with the ion cloud. The pulse energy was adjusted by the discharge voltage in the laser. The laser was triggered externally and synchronized with

the pulsed valve.

A mixture of 0.22% F₂, 8.33% Ar, 4.12% He and 87.33% Ne at a total pressure of 3000 mbar was used to produce $\lambda = 193$ nm, while the $\lambda = 248$ nm pulses were produced in a mixture of 0.19% F₂, 4.84% Kr, 3.68% He and 91.29% Ne at the total pressure of 3300 mbar.

4.5.2 Nd:YAG Lasers

Two nanosecond Nd:YAG lasers were used to pump the OPOs. Both lasers were triggered by an external delay generator to provide synchronization with the experiment. The first, a Coherent Infinity 40–100, had a 4.5 ns long pulse and a single mode beam profile ~ 5 mm in diameter. Its frequency was tripled to 355 nm and operated at the maximum energy of 225 mJ/pulse at the fundamental wavelength (1064 nm) to yield 100 mJ/pulse in the third harmonic. The repetition rate of the laser could be adjusted from 0.1 to 100 Hz at 0.1 Hz increments without significant change in the beam profile or pulse energy.

The second Nd:YAG laser, a Spectra-Physics Quanta-Ray GCR–16S, had a 12 ns long pulse and a beam ~ 7 mm in diameter. The maximum used pulse energy in the third harmonic (355 nm) was 135 mJ. Although the laser repetition rate could be adjusted from 0 – 15 Hz, the optimal frequency was 10 Hz. The pulse energy would drop noticeably when the repetition rate was changed more than ± 1 Hz from that value due to variations in thermal lensing.

4.5.3 BBO Type II OPO

A simple type II β -BaB₂O₄ (BBO) optical parametric oscillator (OPO) described in detail previously [144–146] was used to perform some initial experiments. Two identical

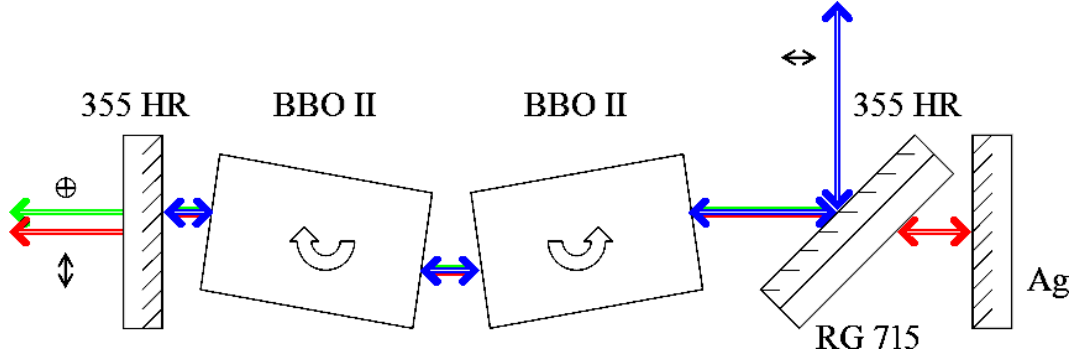


Figure 4.7: A top view of the BBO type II OPO.

type II BBO crystals ($6.3 \times 12.2 \times 12.1$ mm, $\Theta = 36^\circ$, $\phi = 45^\circ$) were used in the counter-rotating configuration (Figure 4.7). The OPO cavity, formed by a silver-coated mirror and an output coupler coated with a 355 nm high reflective (HR) coating, was pumped at 30° by the third harmonic of the Coherent Infinity Nd:YAG laser. A long wavelength pass filter (Schott Glass Technologies, RG715) behind a 45° 355 nm HR mirror was used to absorb the visible (signal) wave, but allowed the IR (idler) wave to resonate.

The working wavelength range for the signal wave was 418 – 630 nm. When it was necessary to employ tunable UV radiation, the signal beam was frequency-doubled in a type I BBO crystal ($10.0 \times 7.0 \times 6.1$ mm, $\Theta = 56^\circ$, $\phi = 0^\circ$). A Pellin–Broca fused silica prism was used to separate the second harmonic beam from the rest (signal, idler and residual pump). The usable wavelength range for the second harmonic (at least 0.2 mJ/pulse) was 212 – 280 nm.

Both OPO crystals, the second harmonic crystal, and the prism were placed on rotation stages driven by Newport 850F series linear actuators, controlled by the BGSpecT software (Appendix C) via Precision MicroControl DCX-PC100 or DC2-PC100 motion control boards.

4.6 Hybrid BBO OPO with a Rotated Prism Cavity

The OPO described above is robust and simple in operation, but it has a few drawbacks. Most significantly, the OPO conversion efficiency is low when approaching the degeneracy point (2λ or 710 nm for 355 nm pumped OPOs). Indeed, very little or no energy is produced by the type II OPO in the 640 – 800 nm wavelength range. This problem is due to the optical properties of the type II BBO crystals and could, in principle, be solved by replacing the type II BBO with some other crystals – for example, a type I BBO – but doing so would generate new problems.

Another issue is the beam shape. In the blue part of the signal spectrum (420 – 460 nm), the beam is nicely round. At longer wavelengths, however, the beam divergence increases in the non-dispersive direction and the beam profile elongates up to a 7 : 1 aspect ratio. This problem is inherent to such a simple cavity design. To circumvent this behavior, image-rotating OPO cavities have recently been implemented [147,148] that incorporate prisms to rotate the image and waveplates to compensate for the phase mismatch introduced. These image-rotating cavities produce beams of nearly round shape, even at wavelengths where the non-rotating cavities have highly elongated beam profiles. The cavity design in [147] is similar to the simple type II BBO OPO (4.5.3) in that it is also a 355 nm pumped type II BBO OPO with only one crystal. It utilizes the same double pass pump scheme, but instead of the metal-coated mirror, it uses a right angle prism rotated at $\alpha = 45^\circ$ in a back reflector geometry. A $\lambda/2$ waveplate was placed into the cavity to maintain the polarization of the signal wave. Such a design solves the beam profile issue, but not the efficiency around the degeneracy point. In addition, the waveplate has to be rotated as the wavelength is tuned.

To further improve the performance of the OPO, the cavity of the simple type II BBO

OPO was modified as described below.

4.6.1 New Cavity Design

The new cavity design is shown in Figure 4.8. In a similar fashion to the image-rotating cavity [147], the metal-coated mirror in the old cavity was replaced with a fused silica right angle prism. The difference was that the back sides of the prism were coated with aluminium to change the phase rotating properties of the prism. Two BBO crystals were used in the new OPO: one type II and one type I. No waveplates were used and the long wavelengths pass filter was retained to resonate the idler.

The new design may at first seem to be not very logical, but in fact, it has some advantages. Let us take a closer look at its operating principles.

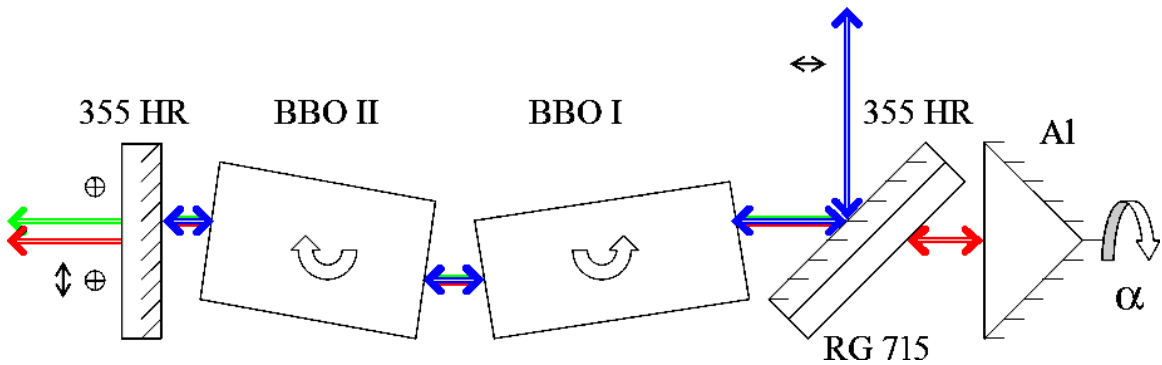


Figure 4.8: A top view of the BBO type I and II hybrid OPO with rotated prism cavity.

4.6.2 Phase Matching

The prism in the cavity introduces a new phase delay to the idler wave. When only the geometric image rotation is considered (Figure 4.9), the general expression for the wave polarization of the original S and P polarized light during prism rotation by α degrees is:

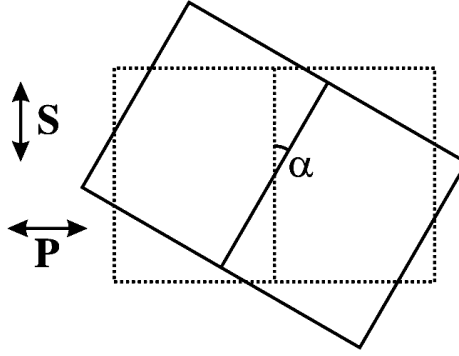


Figure 4.9: A rotated right angle prism.

$$\text{Polarization Rotation} = \begin{cases} 90^\circ(1 + \cos(2\alpha)) & , \quad \text{for P polarization} \\ 90^\circ(1 - \cos(2\alpha)) & , \quad \text{for S polarization} \end{cases}$$

If the prism is not rotated (its 90° angle edge is parallel to the crystal rotation axis), the image is mirrored in the vertical plane. When the prism is rotated 90° , the image is mirrored in the horizontal plane. At $\alpha = 45^\circ$, both the S and P polarizations are rotated by 90° .

Another factor is the phase delay due to reflections on the prism surfaces. This delay is zero for the non-coated prism and 180° per each internal reflection for the metal coated prism. Delays from the prism refractive index wavelength dependence must also be considered. The overall phase change due to these factors combined is shown in Figure 4.10 for the example of an Al-coated BK-7 glass right angle prism. In the operational range of the OPO, the delay for P polarization is $335 - 350$ degrees, which is close to the needed 360° phase shift. For S polarization, it is close to 180 degrees (mirror imaging).

When the prism is rotated by $\alpha = 45^\circ$, the net effect is a 90° polarization rotation with almost complete phase matching. It is possible to achieve better phase matching by slightly rotating the prism. Thus, there is no need for the waveplate. The analysis would change if

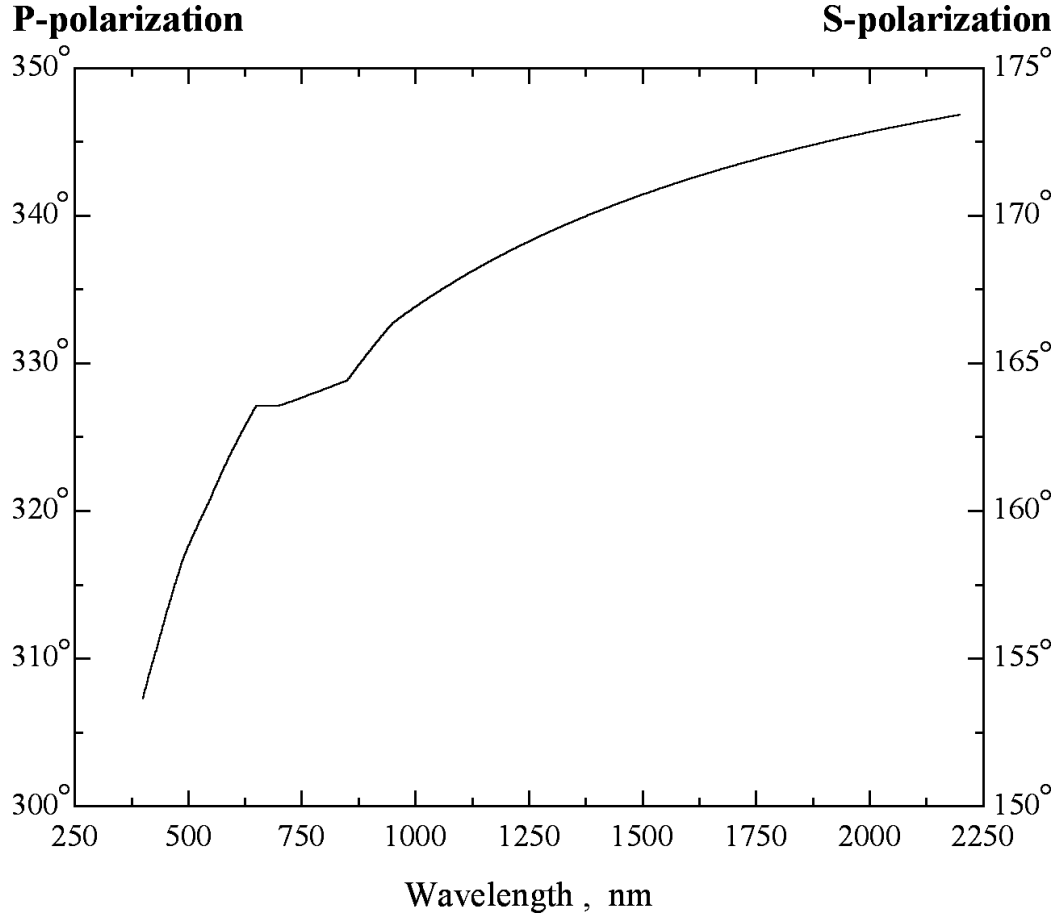


Figure 4.10: The additional phase delay caused by an Al-coated BK-7 right angle prism. Calculated by Foreal Spectrum Co.

the prism were not coated or if the signal wave was resonated.

A polarization rotation of 90° makes the wave unusable for the next pass through the *same* crystal. This may be circumvented by the careful selection of OPO crystals, as described next.

4.6.3 The Choice of Crystals

Crystals used in OPOs must be able to match the group velocities for the pump and signal/idler waves. This is easily achieved in birefringent crystals. For the radiation propagating in such crystals, the polarization has two components (Figure 4.11). The ordinary

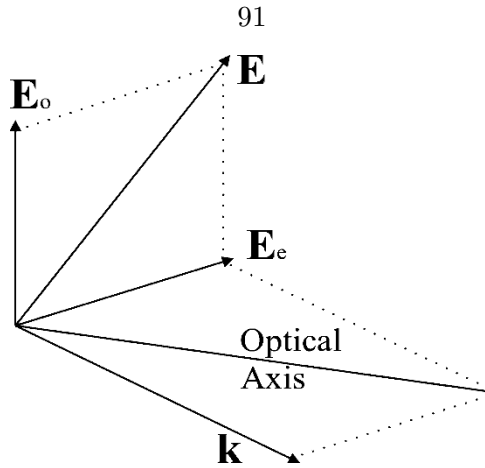


Figure 4.11: Light polarizations in a birefringent nonlinear crystal.

polarization is normal to the plane, formed by the light k -vector and the crystal optical axis, and the extraordinary polarization is in that plane. The refractive index of the ordinary wave does not depend on the angle between the k -vector and the optical axis, but the refractive index of the extraordinary wave does depend on it.

The proper OPO polarizations for BBO crystals are shown in Table 4.1. For both type I and type II BBO, the signal wave polarization is perpendicular to the pump wave polarization, but the idler polarization varies with the crystal type – a fact we exploit in our image/polarization rotating cavity. For the old, non-rotating cavity, the best performance could be achieved only when crystals of the same type are used. For the rotated prism OPO, however, when there are crystals of both types in the cavity, the idler polarization is rotated after each pass and is sequentially amplified by one of the crystals.

Table 4.1: OPO wave polarizations for BBO type I and II crystals.

| Wave | BBO I | BBO II |
|--------|-------|--------|
| Pump | e | e |
| Signal | o | o |
| Idler | o | e |

This new OPO, with both BBO type I and type II crystals housed in the cavity, inherits

many of the advantages of each crystal. BBO type I, for example, has better performance around the degeneracy point and a better overall conversion efficiency compared to type II crystals. Hence, in our cavity it serves as the main amplifying crystal. Alternatively, BBO type II has higher $d\lambda/d\Theta$, which means a smaller acceptance angle and narrower bandwidth. In our cavity it therefore serves as a bandpass filter for the type I crystal.

Thus, the new cavity is expected to have a much better beam profile (due to the image rotation by the prism) with as good a linewidth as the old BBO type II only OPO (BBO type II filtering), much better performance around the degeneracy point, and perhaps, higher pulse energy (BBO type I gain).

4.6.4 Hybrid Cavity Performance

The performance of the new OPO has been characterized for $\alpha \simeq 45^\circ$ rotation of the prism. The beam shape in the blue part of the signal wave spectrum is unchanged and circular. In the red part of the signal spectrum, the beam has a shape of the cross with nearly all of the energy concentrated in a small spot at the center of the beam (Figure 4.12). This is similar to the beam shapes from other image-rotating cavities. The measured beam divergence is ≤ 3 mrad at 2 m.

The signal wave was linearly polarized in the direction perpendicular to the pump polarization, which is the same as in the old cavity. The idler wave, however, was elliptically polarized. Thus, the efficiency of the OPO depended on the prism rotation angle α . When it was set to exactly 45° , the pulse energy dependence *vs.* wavelength was similar to the old BBO type II cavity. The pulse energy maximized at 435 nm and steadily dropped as the wavelength was tuned to the red. This behavior most likely resulted from incomplete phase matching. To alleviate this problem, the prism was rotated to $\alpha \simeq 30 - 35^\circ$, which

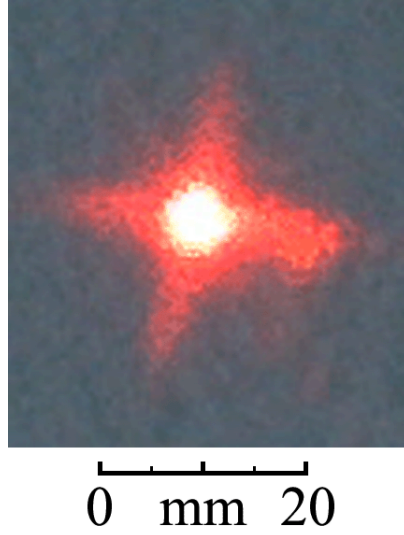


Figure 4.12: Beam shape for the mixed BBO type I and II prism cavity OPO.

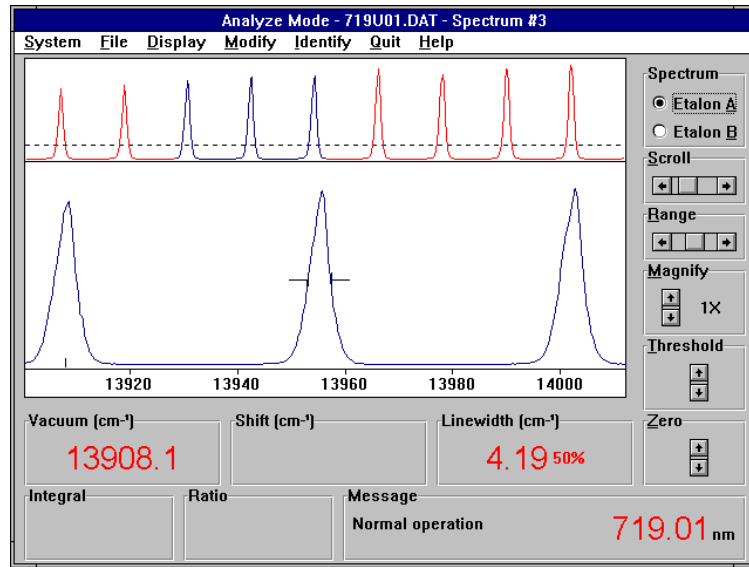


Figure 4.13: Hybrid cavity OPO wavemeter reading at $\lambda_{\text{idler}} = 719$ nm.

drastically improved the efficiency near the degeneracy point. Indeed, tuning to signal wavelengths as long as 710 nm was straightforward, with good efficiency in both the signal and idler beams. Furthermore, the linewidth did not deteriorate significantly around the

degeneracy point as is seen in type I OPOs. The idler wave linewidth at 719 nm was $\sim 4 \text{ cm}^{-1}$ (Figure 4.13), for example, which is close to the $2 - 3 \text{ cm}^{-1}$ measured for the signal wave linewidth far from the degeneracy point.

4.7 Other Hardware

The wavelength of the OPO signal wave was measured by a Burleigh WA-4500 pulsed wavemeter in order to calibrate the OPOs. The OPO linewidth was measured by a Burleigh PLSA-3500 pulsed laser spectrum analyzer.

The OPO pulse energy was measured by a Newport model 818J-25 pyroelectric energy meter detector. Pulse energies of the excimer laser and Nd:YAG lasers were measured by a Newport model 818T-150 high power thermopile detector. The outputs of both detectors were read with a Newport model 1825-C power/energy meter.

Two Stanford Research Systems DG535 pulse/delay generators were used to trigger all devices used in the experiments and to set the appropriate delay times. All delay generator parameters could be controlled from a PC via a GPIB interface.

A GaGe CompuScope 85G digital oscilloscope PC plug-in card was used to read the signal from both mass spectrometer detectors. A GaGe CompuScope 1450 digital oscilloscope card was used to read the signal from the pyroelectric detector that measured the OPO pulse energy. Both cards were plugged into PCI slots of a personal computer and were controlled by software described at length in Appendix C. A Tektronix TDS 210 digital oscilloscope was used to monitor the discharge voltage and current profiles, and was accessible from a PC via a GPIB interface.

4.8 Data Acquisition

The data acquisition for all experiments was conducted by the PC that also controlled all necessary devices. The following was installed in the PC: both GaGe oscilloscope cards, a National Instruments PCI-GPIB card for remote control of GPIB devices, and a Precision MicroControl DCX-PC100 card for OPO wavelength tuning.

Software written for these experiments remotely controlled both delay generators and laser delays, read out the TOF mass spectra and OPO pulse energy traces from oscilloscopes, and analyzed the data, saving the spectrum to a file on the PC hard drive.

4.8.1 Blake Group Spectroscopy Tools Software

The Blake Group Spectroscopy Tools (BGSpect) is designed to be a multipurpose spectrometer software package. For flexibility, it has a modular structure. On the device module level it performs the remote control (GPIB, RS232, PC plug-in cards) of numerous devices that are used in the experiment. For example, when scanning a spectrum, BGSpectTunes the laser wavelength and reads the signal from a digital oscilloscope. A separate spectrometer module uses the device modules to perform the actual scan. The advantage of such a system is that the spectrometer module does not need to know any device-specific commands (differences between the models of the same device type, etc.) since it works at a higher software level. Thus, the spectrometer module can be used for different experiments simply by changing the software configuration, but not the code behind it.

The device modules may be used to control devices independently, almost as if the user was turning knobs on the device itself. In addition, they allow communication with multiple devices of the same kind. For example, reading the waveforms from multiple 2-channel oscilloscopes simultaneously is essentially the same as reading them from one 4- or

8-channel oscilloscope. In some cases, this helps to conduct affordable experiments with the existing equipment.

BGSpect is written and compiled in Microsoft Visual Basic. When the modules were first coded, the available computers were slow and there was a noticeable speed difference between software designed in LabView and Basic or C++. Nowadays, the bottleneck is usually in the speed of the experiment itself or the data transfer from the device to the computer. Historically, Visual Basic was used to ensure interoperability with other software developed by the group.

4.8.2 Choice of Delay Times

It was important to carefully select delay times for experimental synchronization. First, since protonation was performed in a hydrogen discharge (4.2), it was necessary to adjust the delay time between the valve opening (discharge start) and ion extraction to maximize the intensity of the protonated ion peak. The long term stability of this signal was ensured by first ‘seasoning’ the discharge for 0.5 – 1 hour. Usually, ions produced in the beginning of the discharge were used. The ion beam was then intercepted with an intense pulse from the excimer laser ($\lambda = 193$ nm, $E = 25 - 35$ mJ/pulse, 10×15 mm spot size) to dissociate the molecular ions. The delay time for the excimer laser was adjusted to maximize the photodissociation of ions of a selected mass, usually protonated PAHs. This delay then was fixed.

When an OPO was used to scan the spectrum, the delay time for the OPO pump Nd:YAG laser was adjusted for optimum temporal overlap with the excimer pulse as measured by a fast photodiode.

During the spectral scan, the ion signal without the laser was collected as well, nearly in real time. For each OPO wavelength, the MCP signals with the laser was acquired. The laser delay time was then increased by more than $50 \mu s$ (longer than the mass spectrum time range) and the ‘background’ signal was acquired. Finally, the laser delay was returned to its original position.

Typical delay generator parameters were:

Delay generator #1. Internal triggering mode at 5 Hz rate.

$$\left\{ \begin{array}{ll} T_0 = 0 \mu s & , \text{ open pulsed valve } (400 \mu s) \\ A = T_0 + 320.00 \mu s & , \text{ turn discharge On; trigger delay generator \#2;} \\ & \text{trigger Tektronix TDS 210 oscilloscope (discharge monitor)} \\ B = A + 460.00 \mu s & , \text{ turn discharge Off} \\ C = D - 260.00 \mu s & , \text{ turn Coherent Infinity Nd:YAG lamp On} \\ D = A + 198.61 \mu s & , \text{ turn Coherent Infinity Nd:YAG Q-switch On (OPO);} \\ & \text{trigger GaGe CS 1450 oscilloscope (OPO pulse energy)} \end{array} \right.$$

Delay generator #2. External triggering mode, triggered by delay generator #1.

$$\left\{ \begin{array}{ll} T_0 = 0 \mu s & - \text{ from DG \#1, line A} \\ A = B - 1.09 \mu s & , \text{ trigger Lambda Physik excimer laser} \\ B = C + 18.54 \mu s & , \text{ actual excimer pulse produced, for protonated anthracene} \\ & 20.13 \mu s \quad , \quad \text{for protonated pyrene} \\ & 12.56 \mu s \quad , \quad \text{for protonated benzene} \\ C = T_0 + 180.00 \mu s & , \text{ TOF MS ion extraction pulse On } (7 \mu s) \\ D = C + 0.35 \mu s & , \text{ trigger GaGe CS 85G oscilloscope (TOF MS spectra)} \end{array} \right.$$

When the cluster discharge source was used (4.3), there was an additional pulsed valve to trigger. In that case, typical delay times were:

Delay generator #1. Internal triggering mode at 10 Hz rate.

$$\left\{ \begin{array}{ll} T_0 = 0 \mu s & , \text{ send to TTL frequency divider, to trigger delay generator \#2} \\ A = B - 0.95 \mu s & , \text{ trigger Lambda Physik excimer laser} \\ B = D + 0.47 \mu s & , \text{ actual excimer pulse produced} \\ C = D - 120.00 \mu s & , \text{ turn Spectra-Physics GCR Nd:YAG lamp On} \\ D = T_0 + 789.44 \mu s & , \text{ turn Spectra-Physics GCR Nd:YAG Q-switch On (OPO)} \end{array} \right.$$

Delay generator #2. External triggering mode, triggered by TTL frequency divider at 0.91 (10/11) Hz.

$$\left\{ \begin{array}{ll} T_0 = 0 \mu s & , \text{ open H}_2\text{O pulsed valve (400 } \mu s) \\ A = T_0 + 280.00 \mu s & , \text{ open discharge pulsed valve (400 } \mu s) \\ B = C + 240.00 \mu s & , \text{ TOF MS ion extraction pulse On (7 } \mu s); \\ & \text{ trigger GaGe CS 1450 oscilloscope (OPO pulse energy)} \\ C = A + 250.00 \mu s & , \text{ turn discharge On (1200 } \mu s); \\ & \text{ trigger Tektronix TDS 210 oscilloscope (discharge monitor)} \\ D = B + 0.35 \mu s & , \text{ trigger GaGe CS 85G oscilloscope (TOF MS spectra)} \end{array} \right.$$

4.8.3 Data Analysis

Raw data were processed by the software as soon as it was acquired. After each discharge pulse, the oscilloscope traces were read by the software and then analyzed. For the mass spectra, there was always a mass peak produced by the discharge whose intensity could be monitored. For example, while recording the cluster photodissociation spectrum, the intensity of the protonated PAH peak was monitored. The dynamic range option from the Oscilloscope panel of BGSpecT was used to make sure that the intensity of the desired peak from each shot was within a user selected range. If the signal at that mass was too weak (too few ions) or too strong (saturated), all data from that shot were discarded. ‘Good’ traces were then averaged, typically up to 60 or 100 traces per wavelength. Averaged mass spectra were then baselined by subtracting a linear fit and saved onto the hard drive for the future analysis, if needed.

The signal for mass spectra was the area under a peak of selected mass. A few masses could be monitored simultaneously. For the OPO pulse energy, the signal was the difference between the maximum and the minimum of the pyroelectric detector signal.

The results were saved into an ASCII file with several columns: laser wavelength, laser pulse energy, and one column per each monitored mass peak. Two files were created: one for the data with the laser, and one without.

After the scan was completed, the data underwent further manual processing. For the neutral dissociation product peak, the value without the laser was subtracted from the value with the laser to improve the baselining. The parent ion and neutral product peaks were then normalized by the parent signal in the absence of the laser to adjust for long term discharge source intensity fluctuations, and then normalized by the OPO pulse energy to yield a final spectrum.

Chapter 5

Laser Dissociation of Protonated PAHs

5.1 Experiments

The photodissociation experiments were performed with protonated PAHs using different laser sources. The calculations from Chapter 3 indicated that it might be energetically feasible to dissociate protonated PAHs with visible/near UV photons from the OPO in one- or two-photon process. The original goal was therefore to measure visible electronic spectra of protonated PAHs by one-photon photodissociation. Thanks to the photostability of protonated PAHs described below, a combined excimer laser and OPO experiment has been performed to yield better results.

Most experiments were performed with protonated anthracene, and some with protonated pyrene and protonated benzene. Protonated anthracene was selected as the smallest protonated PAH molecule since it had a predicted absorption in the visible wavelength region, where 355 nm -pumped OPOs have several mJ of pulse energy. Protonated pyrene is heavier and has lower vapor pressure; therefore, it was the second molecule of choice. The S_2 state of protonated benzene lies within reach of frequency-doubled BBO OPOs and its spectrum, although broad, was measured previously [90]. The S_1 state of protonated ben-

zene and protonated naphthalene, as well as neutral naphthalene, anthracene and pyrene, are all located between 300 – 400 nm and therefore, could not be accessed either by the fundamental or second harmonic of our OPO. It would be possible to generate such photons by sum frequency mixing of the OPO signal with the fundamental from the Nd:YAG laser (1064 nm) or by doubling a 532 nm pumped OPO, but neither of these methods has yet been implemented to extend the OPO wavelength range.

The single-valve hydrogen discharge source was used to protonate neutral aromatic molecules (Chapter 4, 4.2), and the delay times for the discharge and ion extraction were optimized to produce the maximum protonated ion signal. The laser delay time was then adjusted to selectively dissociate the protonated ions. The signals from both the reflectron (parent ion depletion) and linear (neutral product formation) detectors were recorded.

5.1.1 The Type II BBO OPO as a Laser Photodissociation Source

Our first attempt to the photodissociation spectrum of protonated anthracene used the signal (visible) beam from the BBO type II OPO (Chapter 4, 4.5.3). The wavelength range covered was 418 – 600 nm, with a resolution 0.1 nm and a pulse energy from 0.3 to 5 mJ/pulse at the intersection with the ion beam. The laser beam was unfocused and had a round spot with diameter of 5 mm at $\lambda = 425$ nm and a 7×18 mm (vertical \times horizontal) spot at $\lambda = 600$ nm.

No dissociation was observed for protonated anthracene. That is, the parent ion signal on the reflectron detector was within the fluctuation limits and the neutral products signal on the linear detector remained within the noise level. After this first attempt, the OPO signal beam was focused into the TOF MS chamber either into a dot with a spherical lens (fused silica, $f = 250$ mm), or into a horizontal line with a cylindrical lens (fused silica,

$f = 250$ mm) . Again, no dissociation was observed.

Finally, the OPO signal frequency was doubled (209 – 280 nm, with a resolution of 0.05 nm) to search for more highly excited states. Still, no dissociation was recorded for protonated anthracene, and a similar attempt to record the spectrum of the S_2 state of protonated benzene around 250 nm (as was found previously [90]) resulted in no observed dissociation.

5.1.2 Two-color Dissociation – OPO and Excimer Laser

The OPO scan demonstrated that more intense pulses may be needed to dissociate protonated PAHs on nanosecond timescales; therefore, the dissociation experiment was performed with pulses from two lasers. The idea was to perform $1 + 1'$ resonance-enhanced multiphoton dissociation. The first photon (1) from the OPO (visible wavelengths) would excite the protonated PAH ion electronically. Then, the second photon ($1'$) from the excimer laser ($\lambda = 193$ nm) would provide the additional energy needed to dissociate the excited ion. The excimer pulse energy was kept below ~ 10 mJ/pulse to ensure that the dissociation was produced by both lasers and not the excimer laser alone. The pulse duration for the OPO was $\sim 2.5 - 3.5$ ns while that for the excimer laser was 20 ns. The time delay between the two lasers was synchronized with a fast photodiode, and set either to have the OPO pulse arrive 1 ns ahead of the excimer pulse or during its maximum intensity. As in the case of the OPO only scans, the neutral fragment signal did not depend on the OPO wavelength and thus, no $1 + 1'$ protonated anthracene dissociation was observed.

5.1.3 Dissociation Yield with Excimer Laser

In order to better understand the lack of dissociation in the OPO and OPO with excimer experiments, additional high energy excimer studies at $\lambda = 193$ and 248 nm were performed on protonated anthracene, pyrene and benzene. Good depletion signals were observed once the delay time of the laser was set in order to dissociate ions of the appropriate mass. Typical mass spectra for protonated pyrene (Figure 5.2), protonated anthracene (Figure 5.1) and the neutral product from protonated anthracene (Figure 5.3) are shown below. Figure 5.4 demonstrates that the neutral product signal arises from protonated anthracene dissociation because it has the same flight time as the parent ion in the linear TOF MS mode. A strong and narrow peak was produced on the linear detector (neutral channel) by the excimer laser and was not RF induced (Figure 5.3). This peak was present even when there were no ions (that is, with the discharge turned off) and it moved in time when the laser delay was changed, but disappeared when the beam was blocked. No signal was produced by UV photons striking the reflectron detector or by visible photons on either detector.

The dependence of the dissociation yield on the UV pulse energy was measured for protonated anthracene and protonated pyrene by recording the signal at every laser intensity with the laser ON and OFF (blocked beam) for normalization purposes. The laser delay was chosen to maximize the depletion of the parent ion peak in the mass spectrum, and the signals from both reflectron and linear detectors were recorded. When the data were plotted, the curves for parent ion depletion and neutral products showed similar behavior, but the neutral products data were less noisy and therefore used in the subsequent analysis.

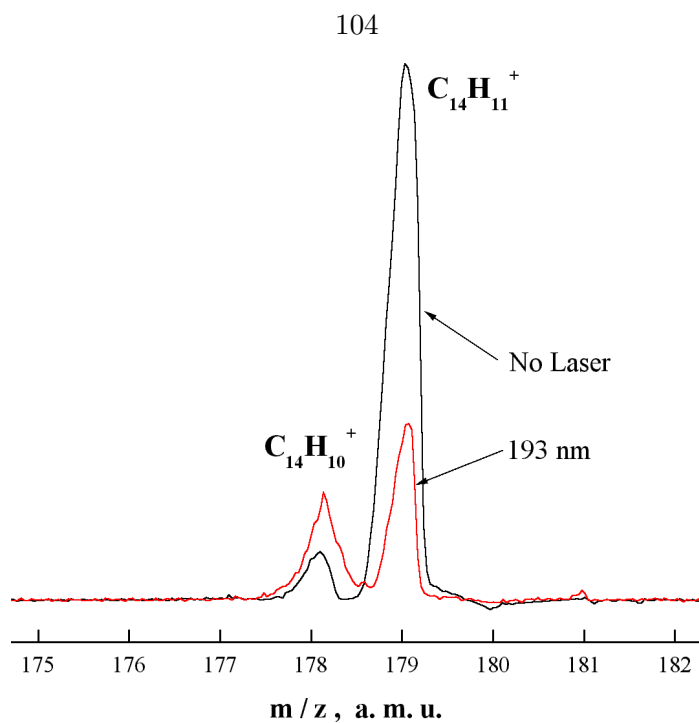


Figure 5.1: An ion channel mass spectrum of protonated anthracene photodissociation with $\lambda = 193$ nm excimer laser pulses.

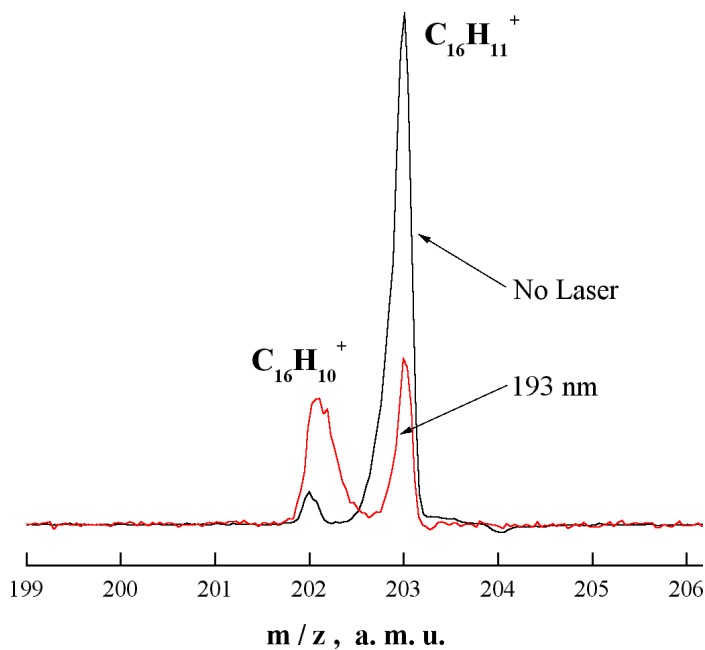


Figure 5.2: An ion channel mass spectrum of protonated pyrene photodissociation with $\lambda = 193$ nm excimer laser pulses.

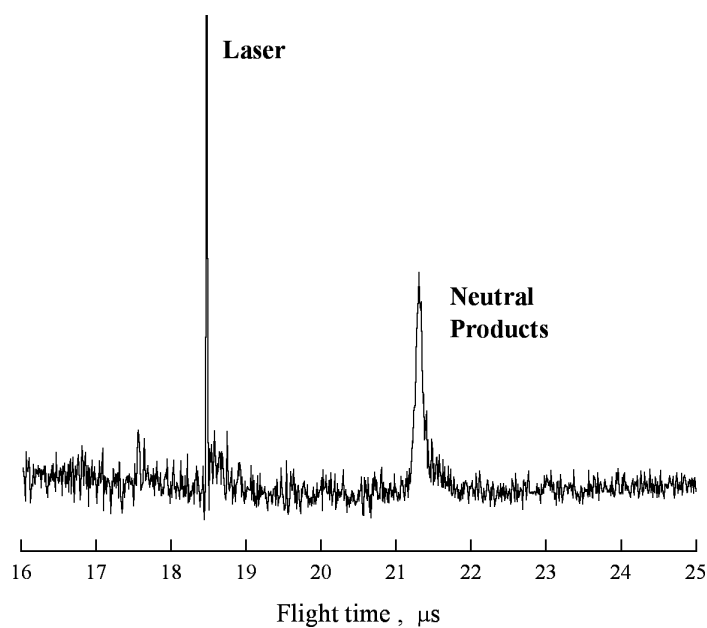


Figure 5.3: Mass spectrum of the neutral products from protonated anthracene photodissociation.

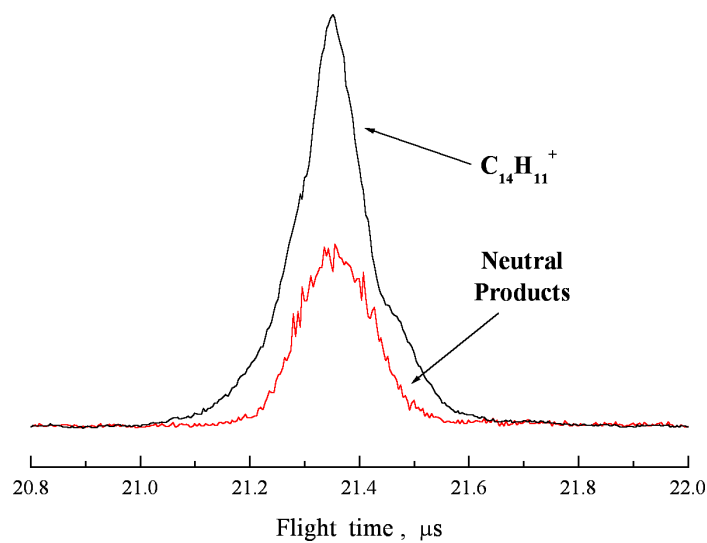


Figure 5.4: Comparison of the linear mode mass spectra for protonated anthracene and its neutral photodissociation products.

5.2 Observed Results

Under our experimental conditions, protonated anthracene and protonated benzene did not dissociate from low energy (<10 mJ/pulse) pulses produced by nanosecond visible and UV lasers. However, all studied ions (protonated anthracene, protonated pyrene and protonated benzene) dissociated after interaction with $10 \leq E \leq 35$ mJ pulses. This implies the dissociation is multiphoton in nature.

5.2.1 Photodissociation Products

No experiments were conducted to determine the exact nature of the neutral photodissociation products, although some information may be derived from the ion mass spectra in the reflectron channel. Ground state DFT calculations (Chapter 2) have shown that the two lowest dissociation channels should be the loss of a hydrogen atom or the hydrogen molecule, and so these are expected to be the primary neutral dissociation products. Primary ion dissociation products (the cation and dehydrogenated cation) may undergo further dissociation in intense laser fields. Since the laser intercepts the ion beam before it enters the reflectron, only neutral products can pass through the reflectron to produce the signal on the linear detector. The ion dissociation products (ions with positive charge), however, cannot penetrate the reflectron and are deflected toward the reflectron detector. Ions from fast dissociation with small recoil velocities will be collected efficiently by the reflectron and produce reasonably narrow enough mass peaks at the reflectron detector.

The only observed changes in the ion mass spectrum under high intensity laser pulses were the decrease in the intensity of the parent ion peak for protonated PAHs ($m/z = M + 1$) and a concomitant increase in the intensity of the cation peak ($m/z = M$) (see Figures 5.1, 5.2). No other new peaks appeared in the mass spectrum when the laser was used.

The decrease in the parent ion peak intensity is due to protonated PAH dissociation, and can be as high as 90%. The complete depletion of this peak depends on the spatial overlap of the laser beam with the mass $M + 1$ ion packet and may be less than 100%. The intensity increase in the cation peak is significantly smaller than the observed protonated ion loss. This suggests that either the dissociation is not sufficiently prompt or that secondary, tertiary, etc. dissociations are possible. One way to test this idea would be to intercept the ions as soon as they are extracted into the mass spectrometer field-free flight region. Unfortunately, this has to be done very close to the reflectron detector which is saturated by the scattered UV light from the laser for an extended time period (more than 100 μs), making it impossible to draw a conclusion. On the other hand, the neutral products signal changes with laser intensity. This may mean that the dissociation is sufficiently fast for the neutral products to be concentrated into a small solid angle.

The intensity increase in the cation peak does not mean that the dissociation happens through the H atom loss channel. In fact, it indicates that the primary dissociation channel is the loss of an H_2 molecule (or two H atoms). This is due to the fact that the dissociation occurs approximately in the middle of the ion flight. In this case, the ions that produce the additional cation signal have mass $M + 1$ before dissociation (about half of the flight time) and mass $M - 1$ after (second half of the flight), averaging to mass M . For the H atom loss channel, the ion peak shift would be only 0.5 a.m.u., not the observed 1 a.m.u. The shift would be 2 a.m.u. if the dissociation was performed immediately after the ions were extracted into the mass spectrometer from the discharge.

The loss of two H atoms or the H_2 molecule is in good agreement with the previously observed products in the photodissociation of protonated benzene [90] and the coronene cation [120].

5.2.2 Yield Dependence on the Pulse Energy

In general, photodissociation product yields with respect to the light intensity (pulse energy) can be expected as a power law relationship with exponent γ :

$$S \propto I^\gamma$$

The slope of the S *vs.* I curve on a log-log plot gives γ , which corresponds approximately to the number of photons in the process. Data for the photodissociation of protonated anthracene with 193 and 248 nm photons are plotted in Figures 5.5 and 5.6, those for

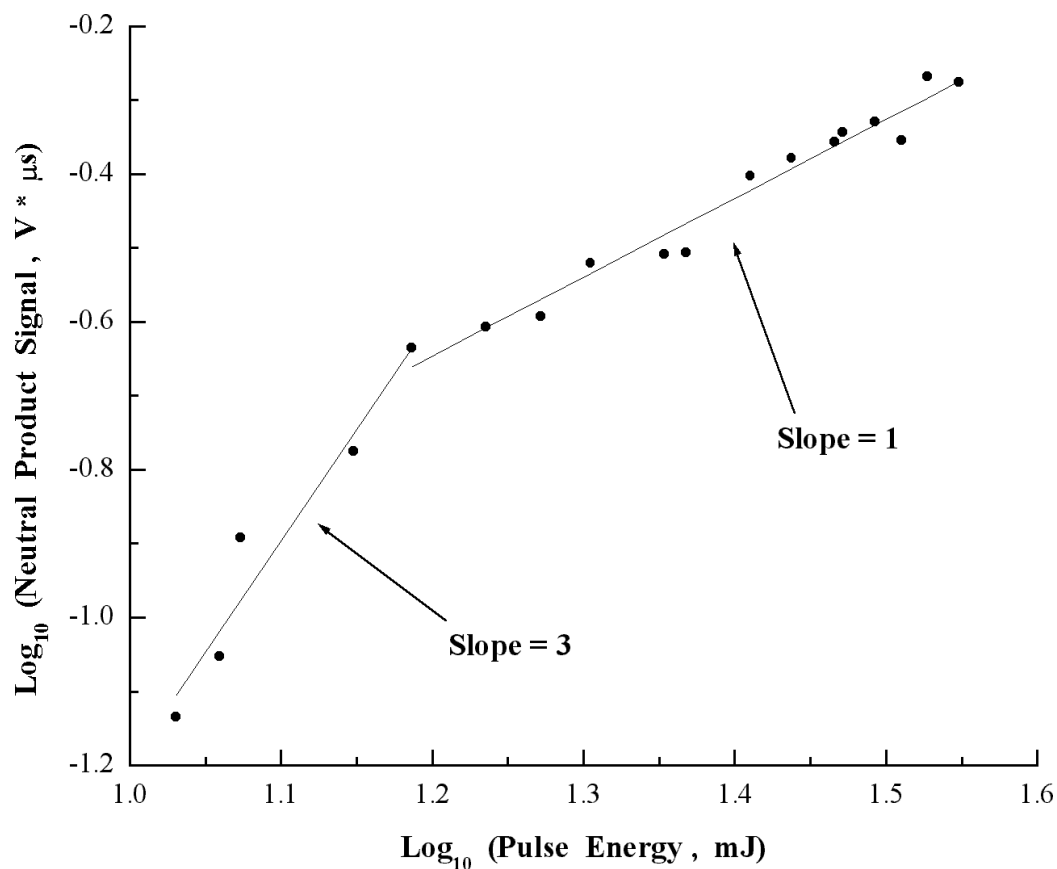


Figure 5.5: Protonated anthracene photodissociation with $\lambda = 193$ nm excimer laser pulses. The dependence of neutral products yield on the pulse energy is indicated by the linear fits in this and subsequent log-log plots.

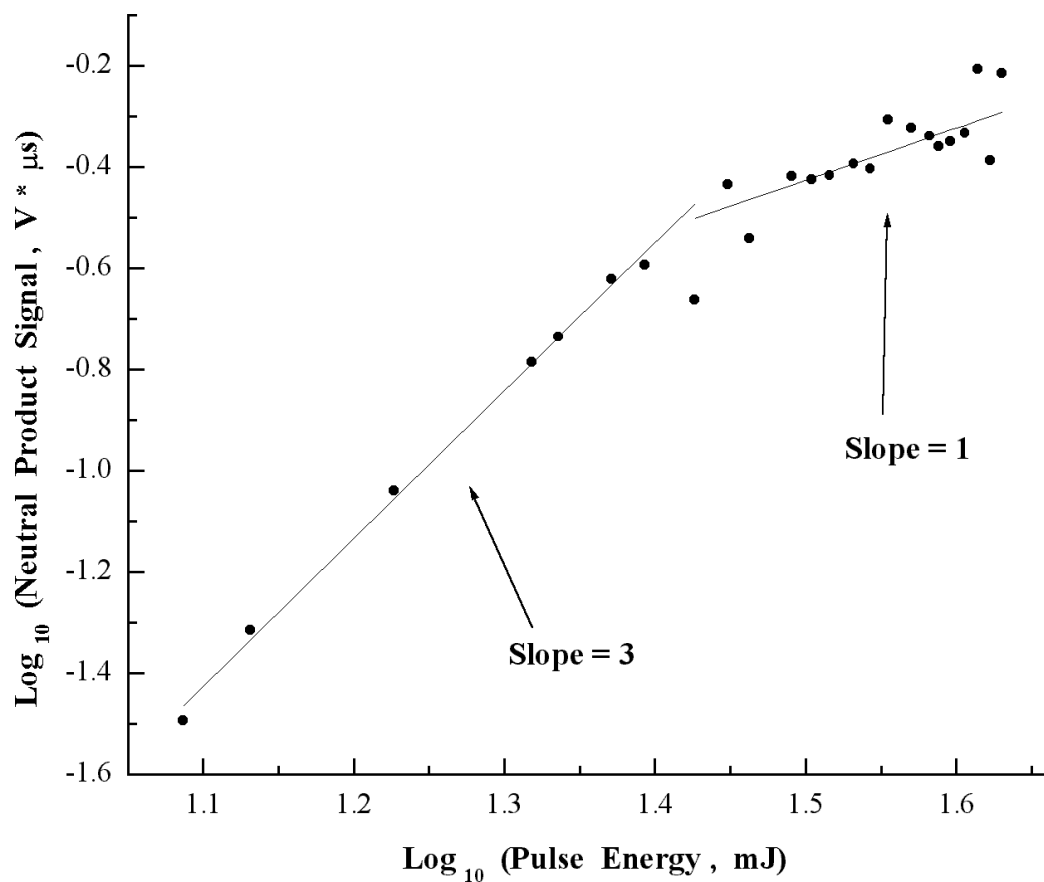


Figure 5.6: Protonated anthracene photodissociation with $\lambda = 248$ nm excimer laser pulses.

protonated pyrene with 193 nm photons in Figure 5.7.

At low pulse energies, the curves for protonated anthracene have a slope of 3. This means that nonresonant dissociation at both 193 and 248 nm is a three-photon process. Both curves have a slope of 1 at higher pulse energies due to the saturation of some of the dissociation steps.

For protonated pyrene, the slope at low intensities was 11. There were two reasons for this unphysical result. First, the pulse energy fluctuations were quite high in this experiment, increasing the uncertainty. Second, protonated pyrene clearly dissociates noticeably easier than does protonated anthracene. This indicates that the transition to one of its

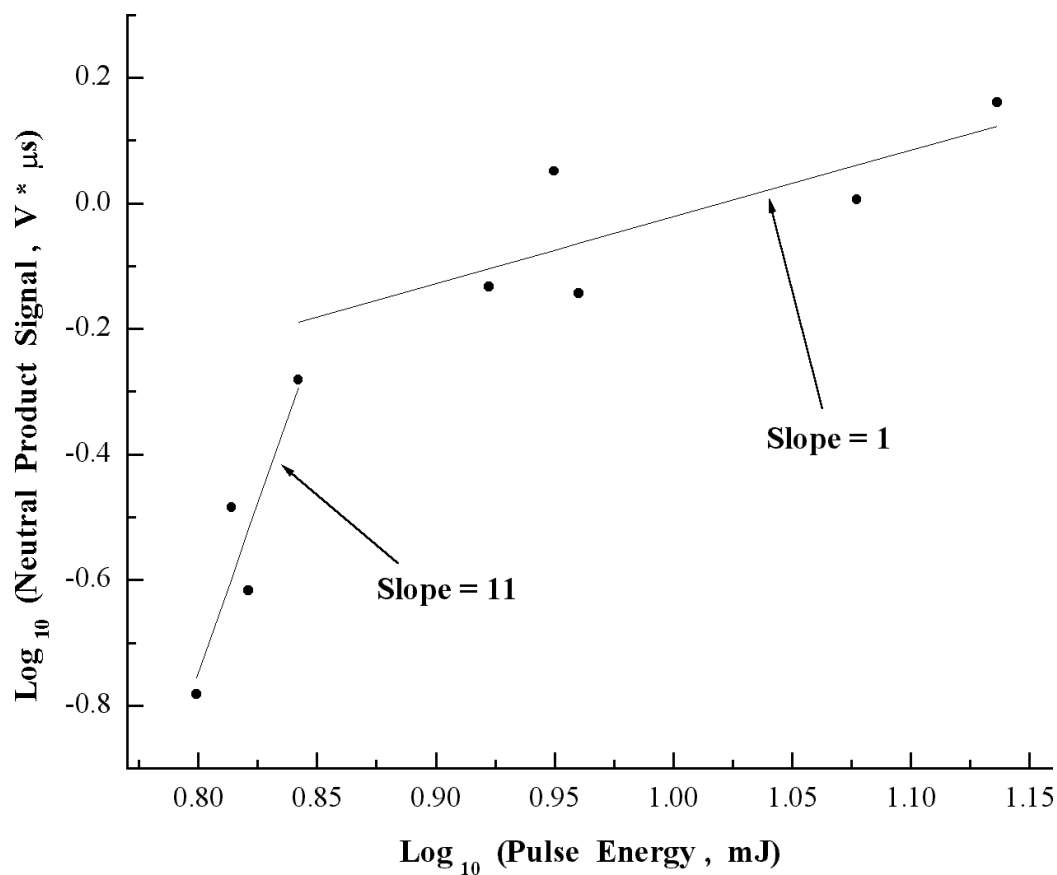


Figure 5.7: Protonated pyrene photodissociation with $\lambda = 193$ nm excimer laser pulses.

excited states lies close to 193 nm, and that the dissociation efficiency was influenced by the proximity to a resonance. The overall nature of dissociation was still multiphoton, but the direct relationship of the slope to the number of photons needed no longer applies.

The observed behavior for protonated benzene was similar to protonated anthracene, although the detailed dissociation yield versus energy was not measured accurately.

5.3 Discussion

5.3.1 Multiphoton Nature of the Photodissociation

The excimer experiments show that the UV photodissociation of protonated PAHs is clearly multiphoton. For protonated anthracene, it is possible to estimate the internal energy required for dissociation (Figure 5.8). Since both 193 and 248 nm dissociation is a three photon process, protonated anthracene dissociates rapidly after absorbing three photons, but not from two photons. Three 248 nm photons therefore establish the upper limit for the dissociation energy while two 193 nm photons determine the lower limit.

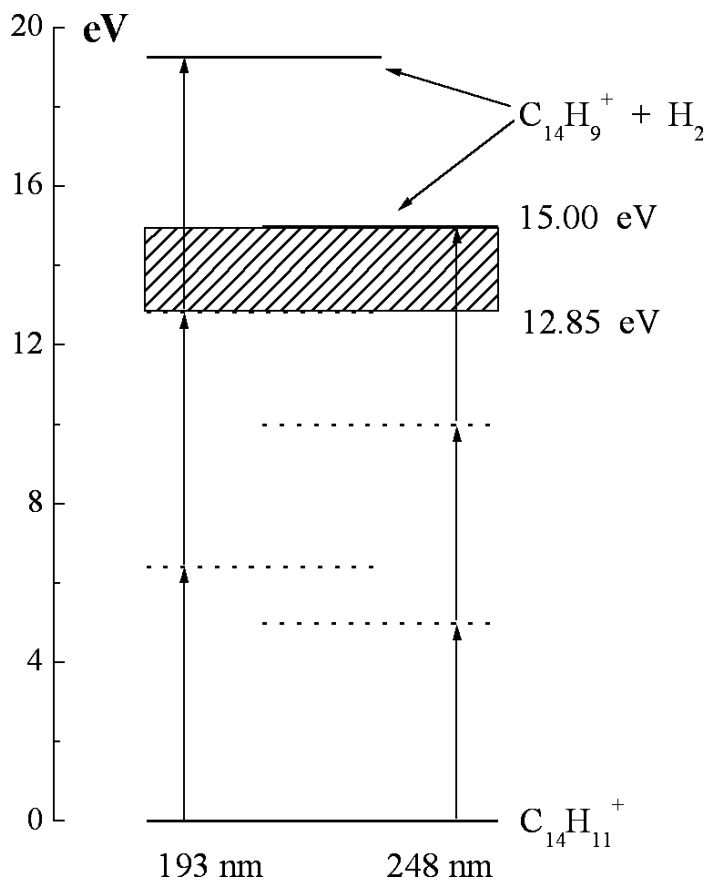


Figure 5.8: Estimates of dissociation energy for protonated anthracene by multiphoton nanosecond laser excitation.

Thus, when using a nanosecond laser, one needs to place $12.85 - 15.00$ eV ($296.3 - 345.9$ kcal/mol) of internal energy into the protonated anthracene ion for it to dissociate in these nanosecond experiments. This is the total amount of energy required and not that needed thermodynamically to break the bonds. Indeed, it is much higher than the dissociation energies ($60 - 70$ kcal/mol) calculated in Chapter 2. The excess energy goes mostly into the vibrational degrees of freedom of the products, especially in the heavy ion produced. Intramolecular vibrational energy redistribution (IVR) plays a crucial role here.

Two-photon dissociation has been observed in the dissociation of the benzene [149] and naphthalene [67] cations. Here, IVR was also seen to lead to the broadening of the absorption bands in the spectrum. The spectral broadening grew very fast with the number of vibrational modes in the molecule and similar effects may make it impossible to record the photodissociation spectra of large PAHs or PAH cations.

A picture of the dissociation that explains the experimental results is as follows: photons are absorbed quickly during the laser pulse (a few nanoseconds) simultaneously, sequentially, or a combination of both. Then, an electronically excited molecule returns to the ground electronic state potential energy surface via internal conversion and IVR, in the process becoming vibrationally excited. The vibrational energy is distributed over the many different vibrations in the molecule. When the vibrational excitation is sufficiently high, the molecule dissociates. For protonated anthracene, this requires on the order of 4.6 kcal/mol (1620 cm^{-1}) per vibrational mode, which is calculated by dividing the estimated dissociation threshold by the total number of vibrational modes.

This explains why one-photon and $1 + 1'$ two-photon dissociation was not observed with lower energy laser pulses. For example, the dissociation of protonated anthracene with visible nanosecond pulses would be a five-photon process. To observe any noticeable

dissociation signal with the visible wavelength photons, the light intensity needs to be much higher than was available here. Such intensities are achievable using much shorter pulses (picosecond or femtosecond duration), but it is not possible to produce enough energy with widely tunable nanosecond lasers (OPOs, dye, etc.) such as those used in the current setup.

To circumvent such pulse energy limitations with high spectral resolution lasers, the experiment needs to be modified. One possibility is to increase the interaction time of the ions with laser radiation by placing the ions into a trap. Photodissociation experiments of this type used a FT ICR trap for protonated benzene [90] and the coronene cation [120], and an RF trap for the anthracene and phenanthrene cations [138]. Alternatively, clusters of protonated PAHs with rare gas atoms or volatile molecules can be made. In this case, the approach would be to measure the one-photon dissociation spectrum of the cluster. This approach is described in Chapter 6 for the specific case of clusters of protonated anthracene with water.

5.3.2 Photostability and Implications for ISM

The observed photostability of protonated PAHs makes it very difficult to record their electronic absorption spectra in TOF systems. On the other hand, this is a very good argument towards the existence of protonated PAHs in the interstellar medium. The ground state calculations described in Chapter 2 have shown that if PAHs exist in the ISM, at least a sizable fraction would exist in the protonated form. The calculations for the excited states from Chapter 3 predict that most protonated PAHs will absorb in the visible and near-UV regions. Our attempts to record photodissociation spectra of protonated PAHs demonstrate that they are extremely resilient against single visible and UV photon dissociation

The estimated single photon dissociation energy of protonated anthracene is close to 13.6

eV. Thanks to the high abundance of hydrogen in a gas of solar composition, most radiation with photon energies above 13.6 eV is absorbed by the ISM and hence is unavailable to dissociate or ionize atoms and molecules. If species do not dissociate through photons with wavelength longer than 912 Å, they are photostable in the ISM. The radiation fluxes in interstellar clouds are not nearly sufficient for multiphoton absorption to occur.

Thus, should protonated PAHs exist in the diffuse ISM, their life cycle would be as follows. An ion in the ground state absorbs a visible or UV photon; it does not dissociate but rather, becomes vibrationally excited. The excess vibrational energy is then emitted at IR wavelengths over a period of milliseconds to seconds, the radiative lifetime for vibrational states. Cold ions can cycle through this loop for long time, and since the UV photon absorption interval is much larger than the IR emission lifetime, most protonated PAHs will exist in their ground states. Such a picture is in perfect agreement with the theory that PAHs (or protonated PAHs) are the species that emit the 3.3 – 11.3 μm UIRs. The question of whether protonated PAHs are DIB carriers still remains to be answered.

Removal mechanisms for protonated PAHs in the ISM include the absorption of more than one photon (highly unlikely), undergoing a chemical reaction, neutralization by dissociative electron recombination, or destruction by high energy particles (e.g. cosmic rays).

5.4 Summary

Several attempts were made to record single- and two-color visible and UV photodissociation spectra of protonated PAHs, but were not successful. Protonated PAHs were found, however, to dissociate under sufficiently intense UV laser pulse excitation. The photodissociation yield measurements demonstrate that nanosecond dissociation is multiphoton in nature. For protonated anthracene, dissociation is a three-photon process at 193 and 248

nm.

The photodissociation energy of protonated anthracene was estimated to be 12.85 – 15.00 eV, a value much higher than the thermodynamic threshold predicted in calculations reported in Chapter 2. Thus, even small protonated PAHs are very photostable, likely due to rapid IVR in the excited states.

This pronounced photostability of protonated PAHs argues in favor of their existence in interstellar clouds.

Chapter 6

Cluster Predissociation Spectroscopy of Protonated Anthracene

6.1 Introduction

As determined in Chapter 5, protonated PAHs are very photostable – a fact that makes recording their direct dissociation spectra with nanosecond lasers quite difficult. To enable single photon experiments to be conducted, the spectra of van der Waals clusters of protonated PAHs with volatile atoms or molecules may be recorded. Since van der Waals interactions are much weaker than chemical bonds, even the vibrational excitation of intramolecular bonds in the components can lead to dissociation. Recording the photodissociation of the cluster gives the predissociation spectrum of the chromophore molecule or ion in the cluster. The spectral lines of the cluster are shifted from the gas phase values of the chromophore due to its interaction with the cluster partner. For clusters with rare gases, the shift is usually within 100 cm^{-1} .

The cluster photodissociation method has been successfully used in the past to record the vibrational [3, 96, 150–154] and electronic [71–74] spectra of clusters of protonated benzene and PAH cations with rare gases. Here it is used to record the visible spectrum of protonated

anthracene.

6.2 Experiment

Ideally, for optimum cluster production, the partner gas should be mixed with protonated PAHs in the discharge under high pressure and then expanded into vacuum. In most experiments, the number of molecules for this gas significantly exceeds the number of PAH molecules. The single-valve discharge source (Chapter 4, 4.2) that has been used to protonate PAHs has an inconvenient property in this regard. Whenever a third gas is added to the hydrogen:PAH mixture, it changes the discharge charge transfer characteristics because the cluster partner competes with PAH molecules for protonation. As a result, the PAH protonation efficiency is decreased. For example, no protonation was observed for anthracene when the discharge was run with 1% of argon added to mixture.

To avoid this problem, the third gas can be mixed into the discharge flow after the protonation has already happened. This may be done either in a crossed molecular beam setup, or as the ions expand into vacuum. The latter method also helps to cool the clusters and therefore, was selected here. In particular, the clusters of protonated anthracene with water were made in the two-valve discharge source described in Chapter 4 (4.3) with the second pulsed valve used to deliver the cluster partner into the discharge through two symmetric channels in the last electrode. When the pressure and delay times were adjusted properly, the third gas was picked up by the discharge stream and carried into vacuum without entering the discharge.

Argon, krypton and xenon were first tested as the cluster partner, but they did not produce any clusters with protonated anthracene. Apparently, the discharge was too hot and the pressure at the mixing point was not high enough to provide the cooling needed

for cluster formation. A molecule that would create a stronger bound cluster is needed.

Water and ammonia are well known for their ability to cluster with other molecules and were therefore tested as well. One important consideration here is the effect of the cluster partner on the protonated PAHs. The proton affinities of PAHs are in 190 – 210 kcal/mol range and that for H_2O and NH_3 is 165 kcal/mol and 204 kcal/mol, respectively [113]. Since the proton affinity of water is lower than that for PAHs, it will not significantly affect the protonation level of ground state PAH molecules. Ammonia, on the other hand, may attract the proton, thus making a cluster of a neutral PAH and protonated ammonia instead of protonated PAH and ammonia. For this reason, ammonia was discarded.

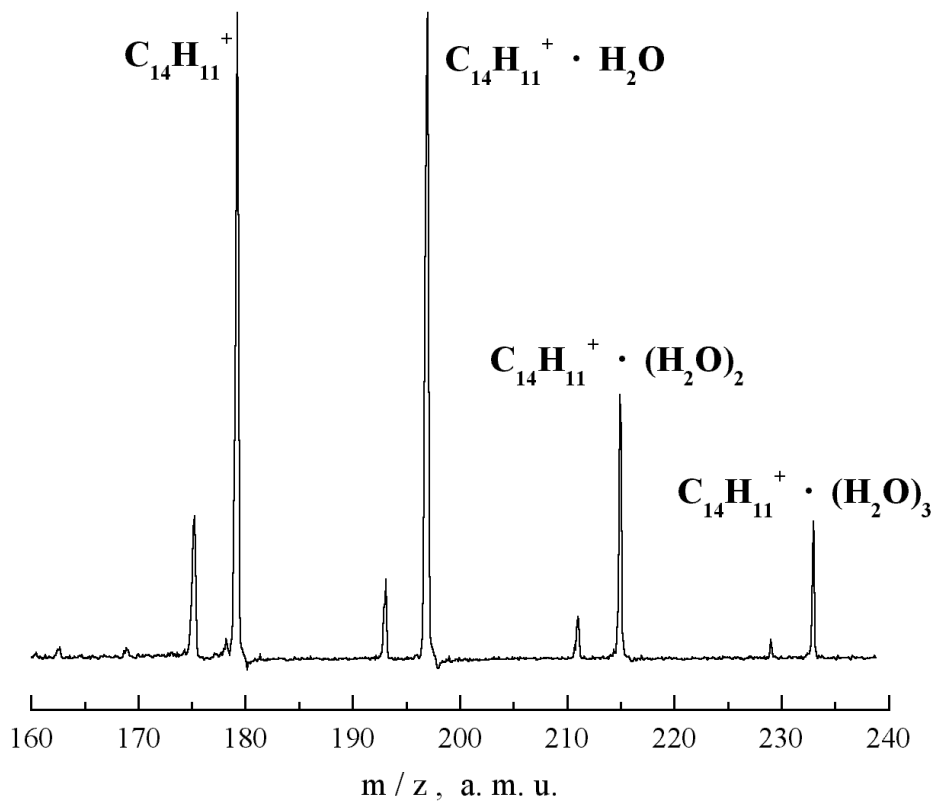


Figure 6.1: A mass spectrum of the two-nozzle source of protonated anthracene–water clusters.

Hydrogen was flowed over the surface of distilled water and used as a carrier gas to deliver H_2O molecules to the discharge. This method was preferred over hydrogen bubbling through water since it assured more stable pressure for the $\text{H}_2\text{O}/\text{H}_2$ mixture. With this setup, the water mixing ratio and the total pressure in the mixing region was high enough to allow clustering. Indeed, water was found to cluster with protonated anthracene very efficiently. Clusters with up to three water molecules were observed (Figure 6.1). Spectroscopy could be performed with any of these clusters, but $\text{C}_{14}\text{H}_{11}^+ \cdot \text{H}_2\text{O}$ was selected as it possessed the strongest and most stable signal.

The experiments were performed in the same way as that outlined for the photodissociation of protonated PAHs in Chapter 5, with the OPO with mixed BBO Type I and II rotated prism cavity (Chapter 4, 4.6) used as the laser source.

6.3 Results and Discussion

6.3.1 Cluster Geometry

The geometry of $\text{PAH} \cdot \text{H}_2\text{O}$ clusters is determined by the balance of the electrostatic interaction and repulsive forces between the cluster partners. For example, in $\text{C}_6\text{H}_6 \cdot \text{H}_2\text{O}$

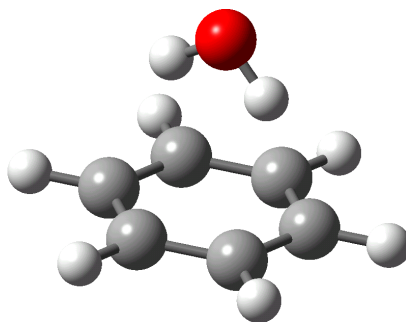


Figure 6.2: The benzene–water ($\text{C}_6\text{H}_6 \cdot \text{H}_2\text{O}$) dimer geometry.

(Figure 6.2), the water molecule binds with its hydrogens pointed toward the π aromatic system of benzene [155], thanks to the electrostatic interaction of the water molecule dipole moment with the quadrupole moment of the benzene molecule.

The picture is different in the case of protonated PAHs since they are a positively charged species. To zeroth order, the electrostatic interaction is dominated by charge-dipole forces. As a result, water prefers to bind via the oxygen side and can no longer bind to the aromatic system of protonated PAH due to the repulsion between the aromatic π system electrons and the oxygen lone pairs. Hence, water binds in the PAH plane. To be more precise, it will bind to the site with the largest positive charge: the CH_2 site hydrogens. The cluster geometry for isomer 1 of protonated anthracene was optimized at a low level of theory and is shown in Figure 6.3. The geometry is similar to that of the protonated benzene–water cluster [156], although for $\text{C}_6\text{H}_7^+ \cdot \text{H}_2\text{O}$, the isomer of the cluster with the bridged structure was estimated to be more stable.

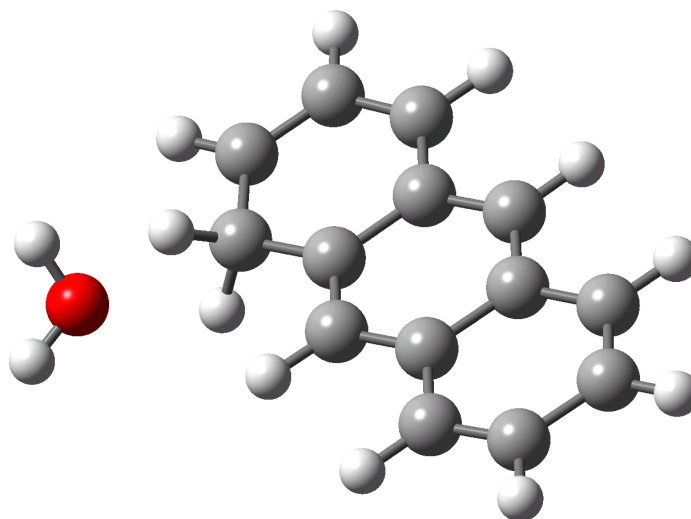


Figure 6.3: Protonated anthracene–water ($1\text{-C}_{14}\text{H}_{11}^+ \cdot \text{H}_2\text{O}$) cluster geometry.

It is not known whether successive water molecules bind to the PAH protonation site or to other H_2O molecules in the cluster. This question, however, is not considered further as no results were acquired for $\text{C}_{14}\text{H}_{11}^+ \cdot (\text{H}_2\text{O})_n$, $n \geq 2$.

6.3.2 Measured Spectrum

The photodissociation spectrum of the $\text{C}_{14}\text{H}_{11}^+ \cdot \text{H}_2\text{O}$ cluster was recorded in the 422 – 540 nm range with a resolution of 0.1 nm. Longer wavelengths were not scanned because no excited states for protonated anthracene were predicted to lie at such low energies. The predicted dissociation products are protonated anthracene and water, but this could not be verified experimentally. The neutral product (presumably H_2O) signal was normalized by the value of the cluster signal without the laser, and by the laser pulse energy. The resulting absorption spectrum is shown as the upper trace in Figure 6.4.

At longer wavelengths, there is no measurable absorption. As the wavelength is decreased, the cluster begins to absorb with a threshold wavelength of ~ 490 nm. The absorption continually increases toward the blue and is never saturated. The maximum cluster dissociation occurred at 435 nm, where the dissociation efficiency reached 50% due to higher OPO pulse energies.

At first glance, the spectrum appears nearly exponential. A more careful inspection reveals two noticeable bumps that we assign to the excited electronic states of protonated anthracene isomers. The spectrum can be fit nicely by an exponential (grey curve) and two Gaussian or Lorentzian (blue and green curves) functions, resulting in the red curve. The lower trace in Figure 6.4 is the spectrum at the top with the exponential dependence removed for better contrast in the remaining features. Here, the red curve displays the fit of the two Lorentzians alone (fits with Gaussians are quite similar).

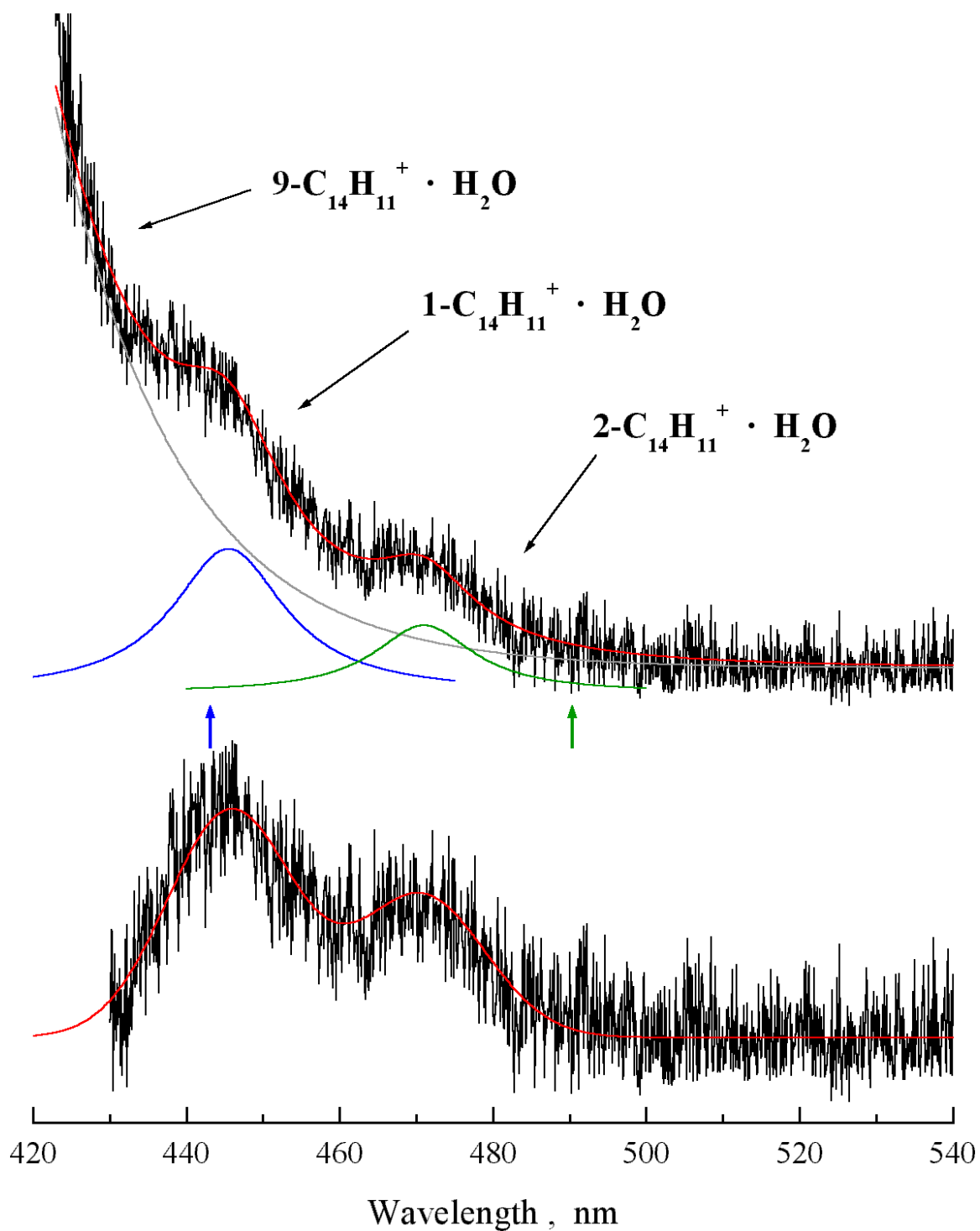


Figure 6.4: Protonated anthracene–water ($\text{C}_{14}\text{H}_{11}^{+} \cdot \text{H}_2\text{O}$) cluster photodissociation spectrum. Top: The recorded spectrum and exponential+Lorentzian fit. Bottom: Data with the exponential rise to short wavelengths removed.

We base our assignment of the observed bands to the $S_1 \leftarrow S_0$ transition for protonated anthracene based on the excited state calculations presented in Chapter 3. The longer wavelength band corresponds to isomer 2 of protonated anthracene, while the shorter wavelength band corresponds to isomer 1. The overall exponential increase at short wavelengths is most likely due to the most stable isomer, isomer 9, but a final assignment of this blue increase may only be accomplished when the spectrum down to ~ 350 nm is recorded.

Isomer 9 is more stable than the other two isomers by ~ 10 kcal/mol and isomer 1 is more stable than isomer 2 by 3 kcal/mol. If the clusters are in thermodynamic equilibrium, the majority of them will be in the form of isomer 9. Similarly, the oscillator strength for isomer 9 is twice as large as for isomer 1, which in turn, has a larger oscillator strength than isomer 2 (Table A.37 in Appendix A). The combined effects of the isomer population distribution and the inherent strengths of the bands may explain the steep rise in absorption at short wavelengths.

6.3.3 Band Positions and Widths

In the fit to the measured spectrum, the two gaussian curves have their maxima at 445.8 nm and 470.7 nm, with full width at half maxima (FWHM) of 19.6 nm. For Lorentzian fits to the data, band positions of 445.5 and 471.0 nm are derived with FWHM of 17.2 and 16.0 nm, respectively. In either case, the band origins (that is, the wavelength of the feature maximum) are about 445.6 nm for isomer 1 and 471 nm for isomer 2. The predicted transition wavelengths (443.1 nm and 490.4 nm) are shown in Figure 6.4 as vertical arrows. The predicted transition wavelength for isomer 1 is remarkably close to the band origin in the measured spectrum (443.1 nm *vs.* 445.6 nm), while for isomer 2 the experimental value is shifted to the blue by ~ 19 nm from that predicted.

At the available signal-to-noise ratio, no internal structure is seen in the bands. The spectra are either vibrationally or lifetime broadened. The vibrational broadening of the excited state leads to band blue shift, while the vibrational broadening of the ground state and the lifetime broadening are expected to work in both directions from the band origin.

6.3.4 Comparison with Spectra of Other Clusters

The measured $\text{C}_{14}\text{H}_{11}^+ \cdot \text{H}_2\text{O}$ cluster spectrum should be compared to the spectra of similar clusters in order to draw any conclusions about the cluster properties and especially about the spectrum of bare protonated anthracene. The dissociation spectrum for the naphthalene cation–argon cluster [71, 73] is red-shifted from the gas phase spectrum of the naphthalene cation [62] by 2 nm (50 cm^{-1}), but has similar widths ($25 - 30 \text{ cm}^{-1}$ FWHM) of the vibronic features therein. For the phenanthrene–argon cluster [72, 73], the red shift is 13 cm^{-1} . REMPI spectral lines for the anthracene–argon cluster [69] are also very narrow (10 cm^{-1} FWHM) and the red shift is 47 cm^{-1} . However, these shifts are for clusters with argon, whose spectra do not have as large a red shift as those with polar molecules. For clusters of anthracene with water [157] and methanol [158], the band widths increase slightly compared to those with Ar but are no more than $30 - 40 \text{ cm}^{-1}$, and the red shifts remain tolerably small at $100 - 150 \text{ cm}^{-1}$.

Based on these data, one would expect the absorption bands for the protonated anthracene–water cluster to be no more than 50 cm^{-1} wide, versus the measured value of 1100 cm^{-1} . The red shift in the protonated anthracene gas phase spectrum would be about $100 - 200 \text{ cm}^{-1}$ (4 nm) if it behaved similarly to PAHs and PAH cations. The comparison of the calculated $S_1 \leftarrow S_0$ transition wavelength (as in Chapter 3) for isomer 1 of protonated anthracene and its cluster with water gives a similar shift value. Using these shifts and the measured

band origins, the photodissociation spectrum for the $\text{C}_{14}\text{H}_{11}^+ \cdot \text{H}_2\text{O}$ cluster should look similar to that shown in Figure 6.5. Clearly, this is not the case. Thus, absorption bands as measured experimentally must be broadened by either a property intrinsic to protonated anthracene or created by the cluster environment.

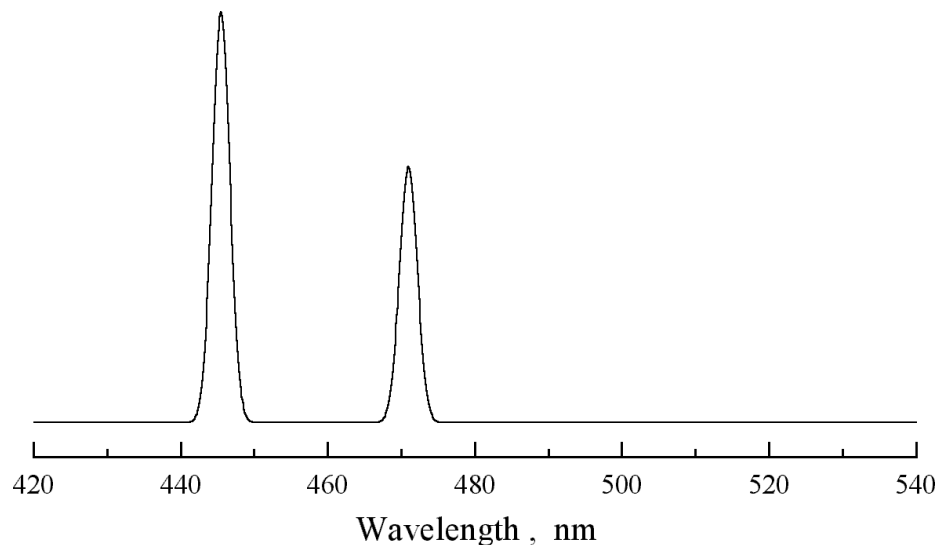


Figure 6.5: The expected protonated anthracene–water cluster photodissociation spectrum from comparisons with PAH and PAH^+ clusters.

6.3.5 Effect of Proton Mobility on the Spectral Width

To answer the important question, “What causes the widths of measured bands to be as high as 1100 cm^{-1} (FWHM)?”, several scenarios must be considered. Is it due to some experimental procedure, or is it due to a property of the cluster or of protonated anthracene itself?

As was found in Chapter 2, protonated aromatics have one thing in common that neutral PAHs and their cations do not: an ability to isomerize by proton hopping from one carbon atom to another. This dramatically increases the density of vibrational states for the highly

excited protonated PAHs, increase that is largely due to the contribution of all isomers since they are coupled to each other. No such coupling exists for neutral PAHs and their cations, and although they have nearly the same number of atoms (and hence the number of vibrational modes) as protonated PAHs, only one isomer is possible.

When a protonated PAH absorbs a visible or UV photon and becomes excited electronically, it can non-radiatively transfer to the ground electronic potential energy surface via internal conversion. The density of vibrational states on the ground state at an excitation of $10,000 - 25,000 \text{ cm}^{-1}$ is the crucial consideration. Higher densities of vibrational states lead to faster internal conversion, shorter excited state lifetimes and broader spectral features. This lifetime broadening mechanism will not depend on whether the protonated PAH exists freely or as a member of a cluster, and explain why the protonated benzene photodissociation spectrum [90] is as broad as the protonated anthracene–water bands observed here.

6.3.6 Other Factors

If protonated anthracene in a cluster retains vibrational excitation, additional spectral broadening of the predissociation spectrum can result. Since protonated anthracene was made in a discharge, it is expected to be vibrationally warm, thanks to the high electron temperature of such environments. This is the likely explanation for why the attempts to generate protonated PAH clusters with rare gases were unsuccessful. On the other hand, the clusters cannot be too hot because clusters with up to three water molecules were produced. Based on this observation, one would expect the vibrational temperature of the clusters be somewhere in the range of $50 - 150 \text{ K}$. At these temperatures, intermolecular and the very lowest intramolecular modes could be populated, but it is unlikely they could cause the

level of broadening observed or create a spectral profile that is as smooth as that measured experimentally.

Another thing that may lead to spectral broadening is C–H bond softening at the protonation site through interactions with the water molecule. For the protonated benzene–water dimer, for example, the energy difference between the two protonation sites (one on benzene, the other on water) was calculated to be only 2.6 kcal/mol [156] with a barrier to proton transfer of only 2.5 kcal/mol, despite the fact that the proton affinity of benzene is 14.3 kcal/mol larger than in water. The effect should be not as noticeable in the protonated anthracene–water cluster since the proton affinity of anthracene is higher than for benzene by another 20 – 30 kcal/mol, depending on the protonated isomer (1, 2, or 9).

6.3.7 Comparison with the DIBs

There is a strong diffuse interstellar band at 4430 Å (FWHM = 1.15 nm) which is very close to the expected band origin of the transition for isomer 2 of protonated anthracene (Chapter 3, Figure 3.4). There are also four broad diffuse interstellar bands in the 470 – 500 nm region, one of which ($\lambda_{max} = 476.2$ nm, FWHM = 2.36 nm) red-shifted by $\sim 6 - 10$ nm from the expected band origin of the isomer 2 transition. This is a rather large discrepancy for a good match, but given the uncertainties in the cluster spectrum, the coincidence is worth considering further if additional experimental data are generated. Little can be said at present about isomer 9. Further, even the broadest currently known DIB features are one order of magnitude narrower than the measured bands. Thus, it is most likely that protonated anthracene is not a DIB carrier. Such broad electronic transitions do make protonated PAHs excellent ‘harvesters’ of interstellar visible and UV photons, however, and this combined with the high photostability makes them excellent candidates for UIR

emitters.

If other protonated PAHs have electronic absorption spectra with bands that are similarly broadened, they are equally unlikely to be DIB carriers. This depends largely on the spectral broadening nature. If the proton mobility is a major factor to that, then the isomerization within one PAH ring is a larger contributor than the isomerization across the ring fusion, because such process has a higher barrier. This may lead to narrower absorption band widths in species like coronene. If the vibrational temperatures of protonated PAHs in the ISM are lower than those in laboratory experiments, interstellar absorption bands may be even narrower. The cumulative effect of these factors may bring the expected interstellar band widths close to those for wide DIBs.

6.4 Summary

The visible photodissociation spectrum of the protonated anthracene–water ($\text{C}_{14}\text{H}_{11}^+ \cdot \text{H}_2\text{O}$) cluster was recorded using our modified BBO OPO type I and type II cavity. The two absorption bands observed were assigned to isomers 1 and 2 of protonated anthracene. The origin of one of these bands was very close to the predicted value, but the observed absorption bands were very broad: FWHM were close to $\simeq 20$ nm or 1100 cm^{-1} . The smooth nature of the bands suggests that a substantial component of the broadening is most likely due to the increase in the density of vibrational states resulting from the proton mobility in protonated anthracene. Internal vibrational excitation of the anthracene or of the cluster intermolecular modes may contribute as well, as may proton transfer interactions with the water molecule.

The measured absorption bands are 10 times wider than even the broadest diffuse interstellar bands. While there is a DIB next to the band origin for isomer 1 of protonated

anthracene, no such close coincidence exists for isomer 2. Protonated anthracene is therefore unlikely to be a DIB carrier. If all protonated PAHs share the dynamical properties of $\text{C}_{14}\text{H}_{11}^+$ inferred from the predissociation spectrum, their role as DIB carriers is suspect as well. The excellent photostability of these species, along with their vibrational band positions, however, means that they would be very efficient sources of UIR emission.

Chapter 7

Summary

Several of the properties of protonated PAHs that are important to their abundance and photophysics in the interstellar medium have been explored in this thesis. The key findings are outlined below.

7.1 Structures and Reaction Pathways

In Chapter 2, the results of extensive density functional calculations on protonated benzene, naphthalene, anthracene, phenanthrene and pyrene in their ground electronic state were presented. The original goal of these calculations was to determine the relative energies for protonated PAH isomers and to find their most likely dissociation channels. Loss of a hydrogen atom or a hydrogen molecule from the protonation site were identified as the two lowest energy dissociation channels. The former channel was found to be lower in energy for molecules with a few aromatic rings, although the energy difference between these two channels is not very large. In photodissociation experiments in both [90] and Chapter 5, the mass spectra of the ion product showed the loss of 2 a.m.u., which can be explained either by the loss of H_2 or the sequential loss of two H atoms. The former channel is significantly lower in energy, and is therefore more likely. This photodissociation channel of protonated PAHs would provide a way to generate interstellar molecular hydrogen if the single photon

vacuum-UV yield is comparable to that measured in the near-UV multiphoton experiments.

Along with the dissociation channels, barrier heights for unimolecular isomerization of protonated PAHs have been calculated. It was determined that with sufficient vibrational excitation, protonated PAHs may isomerize freely. This process can occur well below the dissociation energy, and is not limited by only one aromatic ring. Indeed, the proton may migrate on the outside rim of PAH molecule, ‘hopping’ from one carbon atom to another. On cosmic time scales, such proton hopping events would lead to a complete statistical scrambling of the different isomers, and the system would therefore lose all memory about the manner in which it was created.

One significant spectroscopic outcome of the proton mobility in protonated PAHs is a dramatically increased density of vibrational states as is described below.

7.2 Molecular Orbitals and Electronic Transitions

Chapter 3 was devoted to understanding the changes of PAH molecular orbitals upon protonation, and estimating the $S_1 \leftarrow S_0$ transition wavelengths for all isomers of a given protonated PAH. In case of the benzene molecule, all π and π^* orbitals have been considered. The protonation of one of its carbon atoms leads to a change from sp^2 to sp^3 hybridization at this site. Those molecular orbitals of protonated benzene that do not overlap with the protonation site have the same energies as in the benzene molecule; energies of the rest of the orbitals shift to lower values (that is, they are more stable) due to the stabilizing effect induced by the hybridization of the proton σ orbital with the carbon p_z orbital. The immediate result of such changes is to reduce the HOMO – LUMO gap, which leads to a red shifting of electronic absorption bands.

For larger PAHs, the changes in HOMO and LUMO orbitals were more pronounced,

although it was still possible to trace their origins to changes in the orbitals of their neutral PAH precursors. Based on the orbital symmetry, the ground and the first singlet excited electronic states of protonated PAHs were assigned. Most protonated PAHs have C_s symmetry, resulting in \tilde{X}^1A' and \tilde{A}^1A' ground and first excited states.

Wavelengths for the $S_1 \leftarrow S_0$ transitions have been calculated for both neutral and protonated PAHs using the CIS method. The calculated values had a $\sim 25\%$ discrepancy with the experimental data for neutral PAHs, a data set that was used to establish scaling factors for the excited electronic states of protonated PAHs, much as the fairly low level *ab initio* calculations of vibrational spectra must be scaled to agree with experiment. While this manipulation of the predicted energies has no rigorous physical basis, the scaled *ab initio* wavelengths were somewhat red-shifted from experimentally measured values for protonated benzene and isomer 2 of protonated anthracene while being very close to the experimental band position for isomer 1 of protonated anthracene. Such proximity of predicted and experimental wavelengths lend credence to the approach for other aromatic systems.

The predicted red shifts from the analogous transitions in neutral PAHs were some 15 – 200 nm, with a median shift of more than 100 nm. All protonated aromatic hydrocarbons except protonated benzene were found to have strong transitions at visible wavelengths. Many of the calculated values were close to broad bands in the DIB spectrum, a result that encourages the further investigation of protonated PAHs as possible DIB carriers. Although the predicted wavelengths are not sufficiently precise to make conclusions about any exact matches with known DIBs, they do serve as a relatively good guide for laboratory searches for these electronic transitions.

The calculated $S_1 \leftarrow S_0$ transition energies of protonated PAHs turned out to be very close to the predicted thermodynamic threshold for dissociation at the protonated site.

Thus, one might expect them to be photophysically unstable. The opposite behavior has been determined experimentally, as is described next.

7.3 Photostability of Protonated PAHs

Chapter 5 focuses on attempts to record the photodissociation spectra of bare protonated benzene, anthracene and pyrene. The protonation of neutral PAH molecules was performed in a hydrogen discharge source, and mass selected ions were allowed to interact with the pulses from tunable visible/UV nanosecond OPO and excimer lasers. Both the depletion of the parent ion signal and photodissociation products were detected in a reflectron time-of-flight mass spectrometer. No photodissociation by low energy laser pulses was observed, but high energy nanosecond pulses from the excimer laser were found to significantly deplete the protonated PAH ion signal.

The measurements of the photodissociation yield versus radiation intensity revealed the dissociation process to be multiphoton in nature. In the case of protonated anthracene, nanosecond photodissociation required three photons at both 193 and 248 nm. This fact allowed the nanosecond dissociation energy of protonated anthracene to be constrained to 13 – 15 eV. This is significantly higher than the predicted thermodynamic threshold of ~ 60 kcal/mol, and shows that the lowest excited electronic states of protonated PAHs have poor Franck-Condon overlap with states that lead to C–H bond cleavage.

Rapid internal conversion and intramolecular vibrational energy redistribution processes are likely responsible for the high photostability observed for protonated PAHs. Thus, even small systems of this type have an excellent probability of surviving the UV radiation field in diffuse and translucent interstellar clouds. This is another factor in support of the presence of protonated PAHs in the ISM.

7.4 Visible Spectrum of Protonated Anthracene

The photodissociation spectrum of clusters of protonated anthracene with water was recorded in the visible wavelength region in Chapter 6. Protonated anthracene served as the chromophore, with the cluster method serving to circumvent the high photostability of bare protonated PAHs and enable single photon experiments. Although the cluster spectrum is not identical to that of bare protonated anthracene, the expected shifts are small and the overall nature of the spectrum is expected to be preserved.

The measured spectrum had two very broad ($\sim 1100\text{ cm}^{-1}$ FWHM) absorption bands that were assigned to isomers 1 and 2 of protonated anthracene based on the *ab initio* predictions from Chapter 3. The widths of these bands were quite similar to that measured for protonated benzene in a continuous wave ion trap dissociation experiment [90]. For both species, the broadening may well arise from the extremely high density of vibrational states induced by the proton mobility in such systems, although the degree of internal vibrational excitation in the clusters has not been determined and must be considered as well.

While there is a strong DIB feature near the band origin for the isomer 1 of protonated anthracene, no such close features have been seen in the vicinity of the expected band origin for the isomer 2. Furthermore, the widths of the observed bands were an order of magnitude larger than widest DIB features currently known. Thus, it is unlikely that protonated anthracene is a DIB carrier unless the conditions of our experiment are vastly different than those in the ISM. For larger PAHs, the vibrational density of states and hence, the vibrational energy redistribution rates would be even larger, so the general case for protonated PAHs as DIB carriers would seem to be weakened by our results.

7.5 Conclusions

Perhaps the most important result of this thesis is the high measured photostability of protonated PAHs under nanosecond laser pulse illumination. Thus, if they are created efficiently in the ISM as is suggested by laboratory kinetics experiments [75,82], the chances of their removal by UV radiation are very small. This provides another strong argument in favor of the presence of protonated PAHs in the ISM.

The measured photodissociation spectrum of protonated anthracene – water cluster had very broad absorption bands, however, with only one being in even reasonable proximity to a known DIB. This indicates that protonated anthracene, and by extension the entire class of small protonated PAHs, are not the carriers of the diffuse interstellar bands. The observed spectral widths can naturally be explained by the proton mobility in protonated PAHs.

7.6 Future Research Directions

To further investigate protonated PAHs and to clarify unresolved questions raised by this thesis, a number of experiments or observations come to mind. In the laboratory, more spectra of protonated PAHs should be recorded in the same fashion as that outlined in Chapter 6. This involves measuring the spectrum of protonated anthracene at shorter wavelengths to determine whether isomer 9 contributes to the blue absorption seen, as well as recording the spectra of other protonated PAHs (e.g. protonated naphthalene, phenanthrene, pyrene, and coronene). Protonated coronene would be an especially interesting species to study because it has a larger size, but like benzene, has only one stable isomer. The relative proportion of ring fusion hopping steps needed to scan the PAH periphery is also rather

larger than in the small protonated PAHs studied here, and the effect of this on the excited state dynamics could play an important role in the spectral broadening of large protonated PAHs in the ISM.

To minimize the potential broadening due to internal vibrational excitation of protonated PAHs in the discharge source, additional experiments should be performed at cryogenic temperatures. The best way to do this would be to perform visible/UV spectroscopy of protonated PAHs in liquid helium nanodroplets. In such an environment, protonated PAHs would have a temperature 0.38 K, along with a minimal amount of perturbation by the surrounding helium atoms which would permit a better measurement of the band origin positions of the electronic absorption bands. This would be a challenging experiment to perform, and as an easier first step, protonated PAHs could be deposited into rare gas matrices (argon or neon). In this case, the proton may well be confined to only one carbon atom. As a result, the absorption band profiles may be quite different from those in the gas phase or in nanodroplets.

If protonated PAHs do exist in diffuse interstellar clouds, they may produce DIBs that are wider than those measured with current astronomical surveys that are limited to a maximum spectral width of 50 Å for robust feature extraction from complex stellar spectra. Targeted DIB surveys can be conducted that are sensitive to even wider DIB features. Another interesting trend to follow would be to measure the dependence of the DIB width versus environment. For example, DIB profiles from different parts of the same diffuse cloud that are at different temperatures or exposed to different levels of UV radiation could be compared in order to draw conclusions about the rigidity/stability of the absorbing species.

Protonated PAHs have relatively large permanent dipole moments and therefore should be detectable via pure rotational techniques. Indeed, laboratory microwave spectra should

in principle be measurable for a wide range of protonated PAHs, including those that are deuterated or that contain heteroatoms. The data obtained may be used in the search for protonated PAHs in the ISM by radio astronomy tools, and the measured frequencies may be compared to those predicted theoretically for improved structure determinations. At the highest resolution achievable, it may even be possible to observe spectral line shifts or splittings that would provide insight into the importance of proton mobility in the electronic ground state of protonated PAHs.

Theoretically, the distribution of the different isomers of protonated PAHs in actual interstellar environments can be calculated based on their relative energies, proton mobilities, UV excitation and IR emission rates. This would permit more accurate estimates of intensity ratios for different protonated PAH isomers that could be compared to astronomical observations. Other effects such as deuteration, dissociative electron recombination, and chemical reactions may be considered as well.

Appendix A

GAUSSIAN 98 Results

A.1 Geometries

Table A.1: Symmetry Groups, Dipole Moments, Rotational Constants.

| Molecule | Symmetry Group | Dipole Moment (Debye) | Rotational Constants (GHz) | | |
|---------------------|----------------|-----------------------|----------------------------|---------|---------|
| | | | A | B | C |
| Benzene | | | | | |
| C_6H_6 | D_{6h} | 0.0000 | 5.70390 | 5.70358 | 2.85187 |
| $C_6H_7^+$ | C_{2v} | 0.8729 | 5.44292 | 5.31711 | 2.73189 |
| Naphthalene | | | | | |
| $C_{10}H_8$ | D_{2h} | 0.0000 | 3.12608 | 1.23304 | 0.88426 |
| 1- $C_{10}H_9^+$ | C_s | 2.0089 | 3.02746 | 1.19994 | 0.86371 |
| 2- $C_{10}H_9^+$ | C_s | 1.9098 | 3.00985 | 1.20301 | 0.86381 |
| Anthracene | | | | | |
| $C_{14}H_{10}$ | D_{2h} | 0.0004 | 2.15007 | 0.45211 | 0.37356 |
| 1- $C_{14}H_{11}^+$ | C_s | 3.6691 | 2.09822 | 0.44507 | 0.36799 |
| 2- $C_{14}H_{11}^+$ | C_s | 2.9302 | 2.09404 | 0.44523 | 0.36795 |
| 9- $C_{14}H_{11}^+$ | C_{2v} | 18.0182 | 2.09785 | 0.44552 | 0.36829 |
| Phenanthrene | | | | | |
| $C_{14}H_{10}$ | C_{2v} | 0.0148 | 1.61849 | 0.55146 | 0.41132 |
| 1- $C_{14}H_{11}^+$ | C_s | 3.6954 | 1.60553 | 0.53656 | 0.40312 |
| 2- $C_{14}H_{11}^+$ | C_s | 3.5894 | 1.56116 | 0.54831 | 0.40675 |
| 3- $C_{14}H_{11}^+$ | C_s | 2.9631 | 1.60847 | 0.53527 | 0.40256 |
| 4- $C_{14}H_{11}^+$ | C_s | 3.5209 | 1.56388 | 0.54928 | 0.40749 |
| 9- $C_{14}H_{11}^+$ | C_s | 2.6637 | 1.56907 | 0.54629 | 0.40618 |
| Pyrene | | | | | |
| $C_{16}H_{10}$ | D_{2h} | 0.0006 | 1.01227 | 0.55629 | 0.35900 |
| 1- $C_{16}H_{11}^+$ | C_s | 0.9957 | 1.01056 | 0.54208 | 0.35356 |
| 2- $C_{16}H_{11}^+$ | C_{2v} | 3.5447 | 0.98544 | 0.55087 | 0.35408 |
| 4- $C_{16}H_{11}^+$ | C_s | 3.3564 | 0.98697 | 0.55073 | 0.35422 |

A.1.1 Z-Matrices

Table A.2: Benzene (C_6H_6) Z-Matrix.

| Atom 1 | Atom 2 | Bond, Å | Atom 3 | Angle, ° | Atom 4 | Dihedral Angle, ° |
|--------|--------|----------|--------|------------|--------|-------------------|
| C | | | | | | |
| C | 1 | 1.394654 | | | | |
| C | 2 | 1.394666 | 1 | 120.001991 | | |
| C | 3 | 1.394666 | 2 | 119.996074 | 1 | 0.000000 |
| C | 4 | 1.394654 | 3 | 120.001976 | 2 | 0.000000 |
| C | 1 | 1.394667 | 2 | 120.001971 | 3 | 0.000000 |
| H | 1 | 1.084426 | 2 | 119.998426 | 3 | 180.000000 |
| H | 2 | 1.084425 | 1 | 119.999042 | 6 | 180.000000 |
| H | 3 | 1.084418 | 2 | 120.001991 | 1 | 180.000000 |
| H | 4 | 1.084426 | 3 | 119.998977 | 2 | 180.000000 |
| H | 5 | 1.084426 | 4 | 119.998467 | 3 | 180.000000 |
| H | 6 | 1.084418 | 1 | 120.002023 | 2 | 180.000000 |

Table A.3: Protonated benzene (C_6H_7^+) Z-Matrix.

| Atom 1 | Atom 2 | Bond, Å | Atom 3 | Angle, ° | Atom 4 | Dihedral Angle, ° |
|--------|--------|----------|--------|------------|--------|-------------------|
| C | | | | | | |
| C | 1 | 1.368727 | | | | |
| C | 2 | 1.410091 | 1 | 119.091029 | | |
| C | 3 | 1.410091 | 2 | 122.978924 | 1 | 0.000000 |
| C | 4 | 1.368727 | 3 | 119.091029 | 2 | 0.000000 |
| C | 1 | 1.468723 | 2 | 120.870021 | 3 | 0.000000 |
| H | 1 | 1.085006 | 2 | 120.934222 | 3 | 180.000000 |
| H | 2 | 1.082815 | 1 | 121.103374 | 6 | 180.000000 |
| H | 3 | 1.086011 | 2 | 118.510538 | 1 | 180.000000 |
| H | 4 | 1.082815 | 3 | 119.805596 | 2 | 180.000000 |
| H | 5 | 1.085006 | 4 | 120.934222 | 3 | 180.000000 |
| H | 6 | 1.107768 | 1 | 109.582298 | 2 | -125.565642 |
| H | 6 | 1.107768 | 1 | 109.582298 | 2 | 125.565642 |

Table A.4: Naphthalene ($C_{10}H_8$) Z-Matrix.

| Atom 1 | Atom 2 | Bond, Å | Atom 3 | Angle, ° | Atom 4 | Dihedral Angle, ° |
|--------|--------|----------|--------|------------|--------|-------------------|
| C | | | | | | |
| C | 1 | 1.374287 | | | | |
| C | 2 | 1.419949 | 1 | 120.859505 | | |
| C | 3 | 1.431358 | 2 | 118.849618 | 1 | 0.000000 |
| C | 4 | 1.419949 | 3 | 118.849618 | 2 | 0.000000 |
| C | 5 | 1.374287 | 4 | 120.859505 | 3 | 0.000000 |
| H | 3 | 2.162862 | 2 | 96.213583 | 1 | 180.000000 |
| H | 1 | 1.084246 | 2 | 120.105825 | 3 | 180.000000 |
| H | 2 | 1.085201 | 1 | 120.354128 | 6 | 180.000000 |
| C | 3 | 1.419949 | 2 | 122.300764 | 1 | 180.000000 |
| C | 4 | 1.419949 | 3 | 118.849618 | 2 | 180.000000 |
| H | 5 | 1.085201 | 4 | 118.786367 | 3 | 180.000000 |
| H | 6 | 1.084246 | 5 | 120.105825 | 4 | 180.000000 |
| C | 11 | 1.374287 | 4 | 120.859505 | 3 | 0.000000 |
| C | 10 | 1.374287 | 3 | 120.859505 | 2 | 180.000000 |
| H | 11 | 1.085201 | 4 | 118.786367 | 3 | 180.000000 |
| H | 14 | 1.084246 | 11 | 120.105825 | 4 | 180.000000 |
| H | 15 | 1.084246 | 10 | 120.105825 | 3 | 180.000000 |

Table A.5: Protonated naphthalene ($1-C_{10}H_9^+$) Z-Matrix.

| Atom 1 | Atom 2 | Bond, Å | Atom 3 | Angle, ° | Atom 4 | Dihedral Angle, ° |
|--------|--------|----------|--------|------------|--------|-------------------|
| C | | | | | | |
| C | 1 | 1.474279 | | | | |
| C | 2 | 1.494690 | 1 | 116.787133 | | |
| C | 3 | 1.431159 | 2 | 119.092662 | 1 | 0.000000 |
| C | 4 | 1.404226 | 3 | 119.070231 | 2 | 0.000000 |
| C | 1 | 1.364716 | 2 | 122.183322 | 3 | 0.000000 |
| H | 3 | 2.150313 | 2 | 96.202424 | 1 | 180.000000 |
| H | 1 | 1.085343 | 2 | 117.497804 | 3 | 180.000000 |
| H | 2 | 1.103342 | 1 | 108.112234 | 6 | -124.958072 |
| C | 3 | 1.389728 | 2 | 122.030912 | 1 | 180.000000 |
| C | 4 | 1.422179 | 3 | 120.071957 | 2 | 180.000000 |
| H | 5 | 1.086579 | 4 | 118.059944 | 3 | 180.000000 |
| H | 6 | 1.082676 | 1 | 121.003188 | 2 | 180.000000 |
| C | 11 | 1.375768 | 4 | 119.879439 | 3 | 0.000000 |
| C | 10 | 1.393535 | 3 | 120.053953 | 2 | 180.000000 |
| H | 11 | 1.083991 | 4 | 119.251121 | 3 | 180.000000 |
| H | 14 | 1.082707 | 11 | 120.532382 | 4 | 180.000000 |
| H | 15 | 1.084106 | 10 | 119.200021 | 3 | 180.000000 |
| H | 2 | 1.103342 | 1 | 108.112269 | 6 | 124.958072 |

Table A.6: Protonated naphthalene ($2\text{-C}_{10}\text{H}_9^+$) Z-Matrix.

| Atom 1 | Atom 2 | Bond, Å | Atom 3 | Angle, ° | Atom 4 | Dihedral Angle, ° |
|--------|--------|----------|--------|------------|--------|-------------------|
| C | | | | | | |
| C | 1 | 1.467137 | | | | |
| C | 2 | 1.375120 | 1 | 122.320057 | | |
| C | 3 | 1.453306 | 2 | 118.929699 | 1 | 0.000000 |
| C | 4 | 1.437357 | 3 | 119.984361 | 2 | 0.000000 |
| C | 5 | 1.351281 | 4 | 121.171920 | 3 | 0.000000 |
| H | 3 | 2.176465 | 2 | 95.396030 | 1 | 180.000000 |
| H | 1 | 1.105786 | 2 | 108.533743 | 3 | 125.434348 |
| H | 2 | 1.086393 | 1 | 117.910108 | 6 | 180.000000 |
| C | 3 | 1.435418 | 2 | 121.261956 | 1 | 180.000000 |
| C | 4 | 1.400581 | 3 | 118.151009 | 2 | 180.000000 |
| H | 5 | 1.083869 | 4 | 118.198098 | 3 | 180.000000 |
| H | 6 | 1.083716 | 5 | 120.954631 | 4 | 180.000000 |
| C | 11 | 1.386258 | 4 | 120.326676 | 3 | 0.000000 |
| C | 10 | 1.367430 | 3 | 120.103584 | 2 | 180.000000 |
| H | 11 | 1.083408 | 4 | 119.625693 | 3 | 180.000000 |
| H | 14 | 1.084505 | 11 | 119.119868 | 4 | 180.000000 |
| H | 15 | 1.082661 | 10 | 120.737318 | 3 | 180.000000 |
| H | 1 | 1.105787 | 2 | 108.533724 | 3 | -125.434348 |

Table A.7: Anthracene (C₁₄H₁₀) Z-Matrix.

| Atom 1 | Atom 2 | Bond, Å | Atom 3 | Angle, ° | Atom 4 | Dihedral Angle, ° |
|--------|--------|----------|--------|------------|--------|-------------------|
| C | | | | | | |
| C | 1 | 1.367410 | | | | |
| C | 2 | 1.429250 | 1 | 120.967249 | | |
| C | 3 | 1.443006 | 2 | 118.582161 | 1 | 0.000000 |
| C | 4 | 1.429172 | 3 | 118.590960 | 2 | 0.000000 |
| C | 5 | 1.367437 | 4 | 120.968419 | 3 | 0.000000 |
| C | 3 | 1.398763 | 2 | 122.305297 | 1 | 180.000000 |
| C | 4 | 1.398832 | 3 | 119.107531 | 2 | 180.000000 |
| C | 8 | 1.398760 | 4 | 121.779438 | 3 | 0.000000 |
| C | 7 | 1.398812 | 3 | 121.778585 | 2 | 180.000000 |
| C | 10 | 1.429139 | 7 | 122.297882 | 3 | 180.000000 |
| H | 11 | 1.085123 | 10 | 118.562270 | 7 | 0.000000 |
| C | 11 | 1.367419 | 10 | 120.972114 | 7 | 180.000000 |
| C | 13 | 1.424931 | 11 | 120.437315 | 10 | 0.000000 |
| C | 14 | 1.367412 | 13 | 120.450640 | 11 | 0.000000 |
| H | 7 | 1.085938 | 3 | 119.114219 | 2 | 0.000000 |
| H | 1 | 1.084221 | 2 | 120.150061 | 3 | 180.000000 |
| H | 2 | 1.085119 | 1 | 120.470108 | 6 | 180.000000 |
| H | 5 | 1.085112 | 4 | 118.566980 | 3 | 180.000000 |
| H | 6 | 1.084213 | 5 | 120.156221 | 4 | 180.000000 |
| H | 8 | 1.085940 | 4 | 119.106858 | 3 | 180.000000 |
| H | 13 | 1.084214 | 11 | 120.159346 | 10 | 180.000000 |
| H | 14 | 1.084218 | 13 | 119.397937 | 11 | 180.000000 |
| H | 15 | 1.085113 | 14 | 120.470891 | 13 | 180.000000 |

Table A.8: Protonated anthracene ($1\text{-C}_{14}\text{H}_{11}^+$) Z-Matrix.

| Atom 1 | Atom 2 | Bond, Å | Atom 3 | Angle, ° | Atom 4 | Dihedral Angle, ° |
|--------|--------|----------|--------|------------|--------|-------------------|
| C | | | | | | |
| C | 1 | 1.479937 | | | | |
| C | 2 | 1.504130 | 1 | 116.134837 | | |
| C | 3 | 1.446275 | 2 | 118.713966 | 1 | 0.000000 |
| C | 4 | 1.397695 | 3 | 119.648300 | 2 | 0.000000 |
| C | 1 | 1.361794 | 2 | 122.814749 | 3 | 0.000000 |
| C | 3 | 1.367795 | 2 | 122.450139 | 1 | 180.000000 |
| C | 4 | 1.411540 | 3 | 120.113776 | 2 | 180.000000 |
| C | 8 | 1.392425 | 4 | 121.097815 | 3 | 0.000000 |
| C | 7 | 1.423370 | 3 | 121.704778 | 2 | 180.000000 |
| C | 10 | 1.410808 | 7 | 121.877995 | 3 | 180.000000 |
| H | 11 | 1.083777 | 10 | 119.373319 | 7 | 0.000000 |
| C | 11 | 1.378894 | 10 | 120.411623 | 7 | 180.000000 |
| C | 13 | 1.418182 | 11 | 121.286124 | 10 | 0.000000 |
| C | 14 | 1.368859 | 13 | 120.060713 | 11 | 0.000000 |
| H | 7 | 1.085400 | 3 | 120.148250 | 2 | 0.000000 |
| H | 1 | 1.085497 | 2 | 117.205039 | 3 | 180.000000 |
| H | 2 | 1.101786 | 1 | 107.799292 | 6 | -124.661354 |
| H | 5 | 1.086207 | 4 | 118.348002 | 3 | 180.000000 |
| H | 6 | 1.082671 | 1 | 120.880352 | 2 | 180.000000 |
| H | 8 | 1.085112 | 4 | 119.110324 | 3 | 180.000000 |
| H | 13 | 1.083867 | 11 | 119.567690 | 10 | 180.000000 |
| H | 14 | 1.082946 | 13 | 119.532146 | 11 | 180.000000 |
| H | 15 | 1.084048 | 14 | 120.796350 | 13 | 180.000000 |
| H | 2 | 1.101786 | 1 | 107.799292 | 6 | 124.661354 |

Table A.9: Protonated anthracene ($2\text{-C}_{14}\text{H}_{11}^+$) Z-Matrix.

| Atom 1 | Atom 2 | Bond, Å | Atom 3 | Angle, ° | Atom 4 | Dihedral Angle, ° |
|--------|--------|----------|--------|------------|--------|-------------------|
| C | | | | | | |
| C | 1 | 1.470852 | | | | |
| C | 2 | 1.373405 | 1 | 122.499303 | | |
| C | 3 | 1.461045 | 2 | 119.639274 | 1 | 0.000000 |
| C | 4 | 1.446288 | 3 | 118.819264 | 2 | 0.000000 |
| C | 5 | 1.345776 | 4 | 121.680143 | 3 | 0.000000 |
| C | 3 | 1.425471 | 2 | 120.538285 | 1 | 180.000000 |
| C | 4 | 1.376667 | 3 | 118.384766 | 2 | 180.000000 |
| C | 8 | 1.417533 | 4 | 121.864294 | 3 | 0.000000 |
| C | 7 | 1.383412 | 3 | 121.227119 | 2 | 180.000000 |
| C | 10 | 1.432854 | 7 | 121.737433 | 3 | 180.000000 |
| H | 11 | 1.084028 | 10 | 118.843158 | 7 | 0.000000 |
| C | 11 | 1.366052 | 10 | 120.256134 | 7 | 180.000000 |
| C | 13 | 1.421761 | 11 | 119.983428 | 10 | 0.000000 |
| C | 14 | 1.377650 | 13 | 121.548968 | 11 | 0.000000 |
| H | 7 | 1.085283 | 3 | 118.800838 | 2 | 0.000000 |
| H | 1 | 1.104819 | 2 | 108.298282 | 3 | 125.207578 |
| H | 2 | 1.086639 | 1 | 117.878499 | 6 | 180.000000 |
| H | 5 | 1.084132 | 4 | 117.885071 | 3 | 180.000000 |
| H | 6 | 1.083467 | 5 | 120.850716 | 4 | 180.000000 |
| H | 8 | 1.084449 | 4 | 119.633165 | 3 | 180.000000 |
| H | 13 | 1.082870 | 11 | 120.529047 | 10 | 180.000000 |
| H | 14 | 1.084041 | 13 | 118.987048 | 11 | 180.000000 |
| H | 15 | 1.083601 | 14 | 120.244026 | 13 | 180.000000 |
| H | 1 | 1.104819 | 2 | 108.298282 | 3 | -125.207578 |

Table A.10: Protonated anthracene ($9\text{-C}_{14}\text{H}_{11}^+$) Z-Matrix.

| Atom 1 | Atom 2 | Bond, Å | Atom 3 | Angle, ° | Atom 4 | Dihedral Angle, ° |
|--------|--------|----------|--------|------------|--------|-------------------|
| C | | | | | | |
| C | 1 | 1.394050 | | | | |
| C | 2 | 1.390144 | 1 | 120.384604 | | |
| C | 3 | 1.426659 | 2 | 118.563098 | 1 | 0.000000 |
| C | 4 | 1.421758 | 3 | 120.213063 | 2 | 0.000000 |
| C | 5 | 1.376545 | 4 | 120.061211 | 3 | 0.000000 |
| C | 3 | 1.500143 | 2 | 121.279835 | 1 | 180.000000 |
| C | 4 | 1.405851 | 3 | 119.297043 | 2 | 180.000000 |
| C | 8 | 1.405754 | 4 | 124.242978 | 3 | 0.000000 |
| C | 9 | 1.426652 | 8 | 119.299897 | 4 | 0.000000 |
| C | 10 | 1.390096 | 9 | 118.567217 | 8 | 180.000000 |
| H | 11 | 1.084358 | 10 | 120.019811 | 9 | 180.000000 |
| C | 11 | 1.394074 | 10 | 120.385302 | 9 | 0.000000 |
| C | 13 | 1.405176 | 11 | 121.406514 | 10 | 0.000000 |
| C | 14 | 1.376488 | 13 | 119.373490 | 11 | 0.000000 |
| H | 7 | 1.098956 | 3 | 108.760842 | 2 | 56.468647 |
| H | 1 | 1.084108 | 2 | 119.220050 | 3 | 180.000000 |
| H | 2 | 1.084337 | 1 | 119.602837 | 6 | 180.000000 |
| H | 5 | 1.084148 | 4 | 119.192679 | 3 | 180.000000 |
| H | 6 | 1.082638 | 5 | 120.608464 | 4 | 180.000000 |
| H | 8 | 1.087236 | 4 | 117.880126 | 3 | 180.000000 |
| H | 13 | 1.084112 | 11 | 119.225093 | 10 | 180.000000 |
| H | 14 | 1.082633 | 13 | 120.022690 | 11 | 180.000000 |
| H | 15 | 1.084158 | 14 | 120.752494 | 13 | 180.000000 |
| H | 7 | 1.098957 | 3 | 108.760828 | 2 | -56.468647 |

Table A.11: Phenanthrene (C₁₄H₁₀) Z-Matrix.

| Atom 1 | Atom 2 | Bond, Å | Atom 3 | Angle, ° | Atom 4 | Dihedral Angle, ° |
|--------|--------|----------|--------|------------|--------|-------------------|
| C | | | | | | |
| C | 1 | 1.378471 | | | | |
| C | 2 | 1.413354 | 1 | 121.099608 | | |
| C | 3 | 1.424475 | 2 | 119.606717 | 1 | 0.000000 |
| C | 4 | 1.413263 | 3 | 117.893357 | 2 | 0.000000 |
| C | 5 | 1.380988 | 4 | 121.472309 | 3 | 0.000000 |
| C | 3 | 1.434162 | 2 | 120.693861 | 1 | 180.000000 |
| C | 4 | 1.456723 | 3 | 119.103793 | 2 | 180.000000 |
| C | 8 | 1.424418 | 4 | 119.119975 | 3 | 0.000000 |
| C | 7 | 1.357291 | 3 | 121.194763 | 2 | 180.000000 |
| C | 9 | 1.413327 | 8 | 119.617736 | 4 | 180.000000 |
| H | 11 | 1.085131 | 9 | 118.616545 | 8 | 180.000000 |
| C | 11 | 1.378483 | 9 | 121.099180 | 8 | 0.000000 |
| C | 13 | 1.405687 | 11 | 119.543123 | 9 | 0.000000 |
| C | 14 | 1.380987 | 13 | 120.384090 | 11 | 0.000000 |
| H | 7 | 1.085024 | 3 | 118.339687 | 2 | 0.000000 |
| H | 1 | 1.084076 | 2 | 120.342319 | 3 | 180.000000 |
| H | 2 | 1.085155 | 1 | 120.282458 | 6 | 180.000000 |
| H | 5 | 1.082285 | 4 | 119.966771 | 3 | 180.000000 |
| H | 6 | 1.084211 | 5 | 119.725356 | 4 | 180.000000 |
| H | 10 | 1.085012 | 7 | 120.474034 | 3 | 180.000000 |
| H | 13 | 1.084075 | 11 | 120.345031 | 9 | 180.000000 |
| H | 14 | 1.084214 | 13 | 119.895385 | 11 | 180.000000 |
| H | 15 | 1.082261 | 14 | 118.565856 | 13 | 180.000000 |

Table A.12: Protonated phenanthrene ($1\text{-C}_{14}\text{H}_{11}^+$) Z-Matrix.

| Atom 1 | Atom 2 | Bond, Å | Atom 3 | Angle, ° | Atom 4 | Dihedral Angle, ° |
|--------|--------|----------|--------|------------|--------|-------------------|
| C | | | | | | |
| C | 1 | 1.475058 | | | | |
| C | 2 | 1.495222 | 1 | 117.156059 | | |
| C | 3 | 1.429831 | 2 | 119.928125 | 1 | 0.000000 |
| C | 4 | 1.397021 | 3 | 117.632924 | 2 | 0.000000 |
| C | 1 | 1.357960 | 2 | 121.068904 | 3 | 0.000000 |
| C | 3 | 1.396177 | 2 | 119.977555 | 1 | 180.000000 |
| C | 4 | 1.458290 | 3 | 119.954821 | 2 | 180.000000 |
| C | 8 | 1.429284 | 4 | 117.985263 | 3 | 0.000000 |
| C | 7 | 1.381595 | 3 | 120.200220 | 2 | 180.000000 |
| C | 9 | 1.416074 | 8 | 120.091030 | 4 | 180.000000 |
| H | 11 | 1.083990 | 9 | 118.970714 | 8 | 180.000000 |
| C | 11 | 1.376454 | 9 | 120.402602 | 8 | 0.000000 |
| C | 13 | 1.405888 | 11 | 119.610147 | 9 | 0.000000 |
| C | 14 | 1.384319 | 13 | 121.074294 | 11 | 0.000000 |
| H | 7 | 1.083982 | 3 | 119.908381 | 2 | 0.000000 |
| H | 1 | 1.084605 | 2 | 117.932331 | 3 | 180.000000 |
| H | 2 | 1.102707 | 1 | 108.543914 | 6 | -124.640168 |
| H | 5 | 1.083506 | 4 | 118.850365 | 3 | 180.000000 |
| H | 6 | 1.082766 | 1 | 121.086017 | 2 | 180.000000 |
| H | 10 | 1.085082 | 7 | 119.266283 | 3 | 180.000000 |
| H | 13 | 1.082956 | 11 | 120.436629 | 9 | 180.000000 |
| H | 14 | 1.083552 | 13 | 119.585358 | 11 | 180.000000 |
| H | 15 | 1.082101 | 14 | 118.206244 | 13 | 180.000000 |
| H | 2 | 1.102707 | 1 | 108.543914 | 6 | 124.640168 |

Table A.13: Protonated phenanthrene ($2\text{-C}_{14}\text{H}_{11}^+$) Z-Matrix.

| Atom 1 | Atom 2 | Bond, Å | Atom 3 | Angle, ° | Atom 4 | Dihedral Angle, ° |
|--------|--------|----------|--------|------------|--------|-------------------|
| C | | | | | | |
| C | 1 | 1.468189 | | | | |
| C | 2 | 1.371631 | 1 | 123.007747 | | |
| C | 3 | 1.453814 | 2 | 119.369366 | 1 | 0.000000 |
| C | 4 | 1.438253 | 3 | 118.739306 | 2 | 0.000000 |
| C | 5 | 1.352055 | 4 | 121.934392 | 3 | 0.000000 |
| C | 3 | 1.443040 | 2 | 120.413984 | 1 | 180.000000 |
| C | 4 | 1.425593 | 3 | 118.728614 | 2 | 180.000000 |
| C | 8 | 1.438723 | 4 | 119.093138 | 3 | 0.000000 |
| C | 7 | 1.351442 | 3 | 120.404293 | 2 | 180.000000 |
| C | 9 | 1.404716 | 8 | 119.290368 | 4 | 180.000000 |
| H | 11 | 1.083654 | 9 | 119.084496 | 8 | 180.000000 |
| C | 11 | 1.382611 | 9 | 120.739391 | 8 | 0.000000 |
| C | 13 | 1.408608 | 11 | 120.515032 | 9 | 0.000000 |
| C | 14 | 1.374795 | 13 | 120.140008 | 11 | 0.000000 |
| H | 7 | 1.083471 | 3 | 118.420100 | 2 | 0.000000 |
| H | 1 | 1.104947 | 2 | 109.117261 | 3 | -124.872435 |
| H | 2 | 1.085882 | 1 | 117.712241 | 6 | 180.000000 |
| H | 5 | 1.080344 | 4 | 119.305093 | 3 | 180.000000 |
| H | 6 | 1.083960 | 5 | 120.448393 | 4 | 180.000000 |
| H | 10 | 1.083716 | 7 | 120.591244 | 3 | 180.000000 |
| H | 13 | 1.083774 | 11 | 119.841247 | 9 | 180.000000 |
| H | 14 | 1.082905 | 13 | 119.841770 | 11 | 180.000000 |
| H | 15 | 1.080833 | 14 | 118.558351 | 13 | 180.000000 |
| H | 1 | 1.104947 | 2 | 109.117261 | 3 | 124.872435 |

Table A.14: Protonated phenanthrene (3-C₁₄H₁₁⁺) Z-Matrix.

| Atom 1 | Atom 2 | Bond, Å | Atom 3 | Angle, ° | Atom 4 | Dihedral Angle, ° |
|--------|--------|----------|--------|------------|--------|-------------------|
| C | | | | | | |
| C | 1 | 1.349837 | | | | |
| C | 2 | 1.437289 | 1 | 121.504799 | | |
| C | 3 | 1.455246 | 2 | 120.547628 | 1 | 0.000000 |
| C | 4 | 1.368844 | 3 | 117.608897 | 2 | 0.000000 |
| C | 5 | 1.472927 | 4 | 123.494302 | 3 | 0.000000 |
| C | 3 | 1.402309 | 2 | 119.988905 | 1 | 180.000000 |
| C | 4 | 1.469299 | 3 | 119.529611 | 2 | 180.000000 |
| C | 8 | 1.426660 | 4 | 118.228638 | 3 | 0.000000 |
| C | 7 | 1.378836 | 3 | 120.535509 | 2 | 180.000000 |
| C | 9 | 1.413852 | 8 | 120.233021 | 4 | 180.000000 |
| H | 11 | 1.083994 | 9 | 119.042150 | 8 | 180.000000 |
| C | 11 | 1.378811 | 9 | 120.359355 | 8 | 0.000000 |
| C | 13 | 1.403063 | 11 | 119.474904 | 9 | 0.000000 |
| C | 14 | 1.388080 | 13 | 121.075577 | 11 | 0.000000 |
| H | 7 | 1.083173 | 3 | 119.380933 | 2 | 0.000000 |
| H | 1 | 1.083877 | 2 | 121.020169 | 3 | 180.000000 |
| H | 2 | 1.083861 | 1 | 120.641768 | 6 | 180.000000 |
| H | 5 | 1.083615 | 4 | 120.416548 | 3 | 180.000000 |
| H | 6 | 1.104827 | 5 | 108.822075 | 4 | 124.978246 |
| H | 10 | 1.085435 | 7 | 119.108259 | 3 | 180.000000 |
| H | 13 | 1.082886 | 11 | 120.465931 | 9 | 180.000000 |
| H | 14 | 1.083608 | 13 | 119.631552 | 11 | 180.000000 |
| H | 15 | 1.082239 | 14 | 118.231429 | 13 | 180.000000 |
| H | 6 | 1.104827 | 5 | 108.822075 | 4 | -124.978246 |

Table A.15: Protonated phenanthrene ($4\text{-C}_{14}\text{H}_{11}^+$) Z-Matrix.

| Atom 1 | Atom 2 | Bond, Å | Atom 3 | Angle, ° | Atom 4 | Dihedral Angle, ° |
|--------|--------|----------|--------|------------|--------|-------------------|
| C | | | | | | |
| C | 1 | 1.414522 | | | | |
| C | 2 | 1.400366 | 1 | 124.034567 | | |
| C | 3 | 1.425577 | 2 | 119.275536 | 1 | 0.000000 |
| C | 4 | 1.496064 | 3 | 118.412385 | 2 | 0.000000 |
| C | 1 | 1.359082 | 2 | 118.975596 | 3 | 0.000000 |
| C | 3 | 1.434704 | 2 | 120.212430 | 1 | 180.000000 |
| C | 4 | 1.415902 | 3 | 119.543093 | 2 | 180.000000 |
| C | 8 | 1.438788 | 4 | 118.792358 | 3 | 0.000000 |
| C | 7 | 1.357530 | 3 | 120.045392 | 2 | 180.000000 |
| C | 9 | 1.409865 | 8 | 119.139024 | 4 | 180.000000 |
| H | 11 | 1.083749 | 9 | 119.007502 | 8 | 180.000000 |
| C | 11 | 1.378720 | 9 | 120.716313 | 8 | 0.000000 |
| C | 13 | 1.413083 | 11 | 120.540746 | 9 | 0.000000 |
| C | 14 | 1.372471 | 13 | 120.247478 | 11 | 0.000000 |
| H | 7 | 1.083473 | 3 | 118.883919 | 2 | 0.000000 |
| H | 1 | 1.082629 | 2 | 119.722248 | 3 | 180.000000 |
| H | 2 | 1.086326 | 1 | 118.232708 | 6 | 180.000000 |
| H | 5 | 1.101896 | 4 | 110.145502 | 3 | 123.648080 |
| H | 6 | 1.084860 | 1 | 120.841278 | 2 | 180.000000 |
| H | 10 | 1.083752 | 7 | 120.510711 | 3 | 180.000000 |
| H | 13 | 1.083638 | 11 | 119.922542 | 9 | 180.000000 |
| H | 14 | 1.083081 | 13 | 119.677417 | 11 | 180.000000 |
| H | 15 | 1.082535 | 14 | 118.943540 | 13 | 180.000000 |
| H | 5 | 1.101896 | 4 | 110.145502 | 3 | -123.648080 |

Table A.16: Protonated phenanthrene (9-C₁₄H₁₁⁺) Z-Matrix.

| Atom 1 | Atom 2 | Bond, Å | Atom 3 | Angle, ° | Atom 4 | Dihedral Angle, ° |
|--------|--------|----------|--------|------------|--------|-------------------|
| C | | | | | | |
| C | 1 | 1.387024 | | | | |
| C | 2 | 1.395878 | 1 | 120.545143 | | |
| C | 3 | 1.418994 | 2 | 120.003489 | 1 | 0.000000 |
| C | 4 | 1.414289 | 3 | 118.352881 | 2 | 0.000000 |
| C | 5 | 1.380516 | 4 | 120.916427 | 3 | 0.000000 |
| C | 3 | 1.495940 | 2 | 119.564894 | 1 | 180.000000 |
| C | 4 | 1.453414 | 3 | 119.668931 | 2 | 180.000000 |
| C | 8 | 1.454793 | 4 | 120.291054 | 3 | 0.000000 |
| C | 9 | 1.372561 | 8 | 119.859447 | 4 | 0.000000 |
| C | 9 | 1.438144 | 8 | 120.542370 | 4 | 180.000000 |
| H | 11 | 1.084022 | 9 | 118.423935 | 8 | 180.000000 |
| C | 11 | 1.364187 | 9 | 120.472239 | 8 | 0.000000 |
| C | 13 | 1.416186 | 11 | 118.825375 | 9 | 0.000000 |
| C | 14 | 1.384560 | 13 | 122.337737 | 11 | 0.000000 |
| H | 7 | 1.103694 | 3 | 110.793487 | 2 | 56.406843 |
| H | 1 | 1.083425 | 2 | 119.929275 | 3 | 180.000000 |
| H | 2 | 1.084633 | 1 | 119.854537 | 6 | 180.000000 |
| H | 5 | 1.081033 | 4 | 120.497171 | 3 | 180.000000 |
| H | 6 | 1.083025 | 5 | 119.875098 | 4 | 180.000000 |
| H | 10 | 1.086570 | 9 | 119.285883 | 8 | 180.000000 |
| H | 13 | 1.082451 | 11 | 121.136248 | 9 | 180.000000 |
| H | 14 | 1.084548 | 13 | 118.908638 | 11 | 180.000000 |
| H | 15 | 1.080279 | 14 | 118.314757 | 13 | 180.000000 |
| H | 7 | 1.103694 | 3 | 110.793487 | 2 | -56.406843 |

Table A.17: Pyrene (C₁₆H₁₀) Z-Matrix.

| Atom 1 | Atom 2 | Bond, Å | Atom 3 | Angle, ° | Atom 4 | Dihedral Angle, ° |
|--------|--------|----------|--------|------------|--------|-------------------|
| C | | | | | | |
| C | 1 | 1.391972 | | | | |
| C | 2 | 1.402633 | 1 | 120.739411 | | |
| C | 3 | 1.426444 | 2 | 119.022027 | 1 | 0.000000 |
| C | 4 | 1.426438 | 3 | 119.872623 | 2 | 0.000000 |
| C | 1 | 1.391990 | 2 | 120.604218 | 3 | 0.000000 |
| C | 3 | 1.436672 | 2 | 122.403096 | 1 | 180.000000 |
| C | 4 | 1.425474 | 3 | 120.063823 | 2 | 180.000000 |
| C | 8 | 1.426442 | 4 | 120.061143 | 3 | 0.000000 |
| C | 7 | 1.359189 | 3 | 121.363114 | 2 | 180.000000 |
| C | 9 | 1.402616 | 8 | 119.026347 | 4 | 180.000000 |
| H | 11 | 1.084904 | 9 | 119.192936 | 8 | 180.000000 |
| C | 11 | 1.391981 | 9 | 120.732880 | 8 | 0.000000 |
| C | 13 | 1.391970 | 11 | 120.604589 | 9 | 0.000000 |
| C | 14 | 1.402620 | 13 | 120.740171 | 11 | 0.000000 |
| C | 15 | 1.436675 | 14 | 122.405817 | 13 | 180.000000 |
| C | 16 | 1.359181 | 15 | 121.363180 | 14 | 180.000000 |
| H | 17 | 1.085067 | 16 | 120.309077 | 15 | 180.000000 |
| H | 16 | 1.085075 | 15 | 118.340550 | 14 | 0.000000 |
| H | 7 | 1.085085 | 3 | 118.339160 | 2 | 0.000000 |
| H | 1 | 1.084285 | 2 | 119.695651 | 3 | 180.000000 |
| H | 2 | 1.084924 | 1 | 120.065041 | 6 | 180.000000 |
| H | 6 | 1.084910 | 1 | 120.073577 | 2 | 180.000000 |
| H | 10 | 1.085068 | 7 | 120.310576 | 3 | 180.000000 |
| H | 13 | 1.084278 | 11 | 119.697237 | 9 | 180.000000 |
| H | 14 | 1.084911 | 13 | 120.063643 | 11 | 180.000000 |

Table A.18: Protonated pyrene (1-C₁₆H₁₁⁺) Z-Matrix.

| Atom 1 | Atom 2 | Bond, Å | Atom 3 | Angle, ° | Atom 4 | Dihedral Angle, ° |
|--------|--------|----------|--------|------------|--------|-------------------|
| C | | | | | | |
| C | 1 | 1.484870 | | | | |
| C | 2 | 1.495981 | 1 | 116.069518 | | |
| C | 3 | 1.414417 | 2 | 119.884321 | 1 | 0.000000 |
| C | 4 | 1.433524 | 3 | 120.512709 | 2 | 0.000000 |
| C | 1 | 1.348258 | 2 | 122.403726 | 3 | 0.000000 |
| C | 3 | 1.405577 | 2 | 120.558883 | 1 | 180.000000 |
| C | 4 | 1.419838 | 3 | 119.807855 | 2 | 180.000000 |
| C | 8 | 1.419956 | 4 | 120.025833 | 3 | 0.000000 |
| C | 7 | 1.379499 | 3 | 120.814162 | 2 | 180.000000 |
| C | 9 | 1.412935 | 8 | 119.069663 | 4 | 180.000000 |
| H | 11 | 1.084554 | 9 | 119.124196 | 8 | 180.000000 |
| C | 11 | 1.389014 | 9 | 120.955320 | 8 | 0.000000 |
| C | 13 | 1.393620 | 11 | 120.082406 | 9 | 0.000000 |
| C | 14 | 1.407498 | 13 | 120.899101 | 11 | 0.000000 |
| C | 15 | 1.421901 | 14 | 122.171238 | 13 | 180.000000 |
| C | 16 | 1.377167 | 15 | 121.470626 | 14 | 180.000000 |
| H | 17 | 1.083416 | 16 | 120.008081 | 15 | 180.000000 |
| H | 16 | 1.084811 | 15 | 118.824382 | 14 | 0.000000 |
| H | 7 | 1.084157 | 3 | 119.425269 | 2 | 0.000000 |
| H | 1 | 1.084400 | 2 | 117.236511 | 3 | 180.000000 |
| H | 2 | 1.101319 | 1 | 109.050961 | 6 | -123.962510 |
| H | 6 | 1.083807 | 1 | 120.603305 | 2 | 180.000000 |
| H | 10 | 1.084577 | 7 | 119.796588 | 3 | 180.000000 |
| H | 13 | 1.082770 | 11 | 119.992475 | 9 | 180.000000 |
| H | 14 | 1.084523 | 13 | 119.870945 | 11 | 180.000000 |
| H | 2 | 1.101319 | 1 | 109.050961 | 6 | 123.962510 |

Table A.19: Protonated pyrene ($2\text{-C}_{16}\text{H}_{11}^+$) Z-Matrix.

| Atom 1 | Atom 2 | Bond, Å | Atom 3 | Angle, ° | Atom 4 | Dihedral Angle, ° |
|--------|--------|----------|--------|------------|--------|-------------------|
| C | | | | | | |
| C | 1 | 1.470333 | | | | |
| C | 2 | 1.370219 | 1 | 122.014273 | | |
| C | 3 | 1.449838 | 2 | 119.169522 | 1 | 0.000000 |
| C | 4 | 1.449797 | 3 | 120.877687 | 2 | 0.000000 |
| C | 5 | 1.370208 | 4 | 119.187924 | 3 | 0.000000 |
| C | 3 | 1.444090 | 2 | 121.766917 | 1 | 180.000000 |
| C | 4 | 1.404630 | 3 | 119.557230 | 2 | 180.000000 |
| C | 8 | 1.436828 | 4 | 120.047808 | 3 | 0.000000 |
| C | 7 | 1.353812 | 3 | 120.807526 | 2 | 180.000000 |
| C | 9 | 1.396269 | 8 | 118.875480 | 4 | 180.000000 |
| H | 11 | 1.083632 | 9 | 119.501513 | 8 | 180.000000 |
| C | 11 | 1.394449 | 9 | 120.551358 | 8 | 0.000000 |
| C | 13 | 1.394442 | 11 | 121.238994 | 9 | 0.000000 |
| C | 14 | 1.396281 | 13 | 120.563951 | 11 | 0.000000 |
| C | 15 | 1.437984 | 14 | 121.863348 | 13 | 180.000000 |
| C | 16 | 1.353803 | 15 | 121.250554 | 14 | 180.000000 |
| H | 17 | 1.083581 | 16 | 120.875361 | 15 | 180.000000 |
| H | 16 | 1.083857 | 15 | 118.337050 | 14 | 0.000000 |
| H | 7 | 1.083598 | 3 | 118.324929 | 2 | 0.000000 |
| H | 1 | 1.105615 | 2 | 109.416144 | 3 | 124.925482 |
| H | 2 | 1.084883 | 1 | 117.889640 | 6 | 180.000000 |
| H | 6 | 1.084883 | 5 | 120.094581 | 4 | 180.000000 |
| H | 10 | 1.083847 | 7 | 120.424528 | 3 | 180.000000 |
| H | 13 | 1.083778 | 11 | 119.379209 | 9 | 180.000000 |
| H | 14 | 1.083611 | 13 | 119.928590 | 11 | 180.000000 |
| H | 1 | 1.105614 | 2 | 109.416162 | 3 | -124.925482 |

Table A.20: Protonated pyrene (4-C₁₆H₁₁⁺) Z-Matrix.

| Atom 1 | Atom 2 | Bond, Å | Atom 3 | Angle, ° | Atom 4 | Dihedral Angle, ° |
|--------|--------|----------|--------|------------|--------|-------------------|
| C | | | | | | |
| C | 1 | 1.403163 | | | | |
| C | 2 | 1.383145 | 1 | 120.462718 | | |
| C | 3 | 1.424514 | 2 | 119.424834 | 1 | 0.000000 |
| C | 4 | 1.430585 | 3 | 119.996056 | 2 | 0.000000 |
| C | 1 | 1.385091 | 2 | 120.932708 | 3 | 0.000000 |
| C | 3 | 1.500997 | 2 | 121.360907 | 1 | 180.000000 |
| C | 4 | 1.418265 | 3 | 120.735705 | 2 | 180.000000 |
| C | 8 | 1.452571 | 4 | 121.170269 | 3 | 0.000000 |
| C | 9 | 1.372498 | 8 | 119.175629 | 4 | 0.000000 |
| C | 9 | 1.430775 | 8 | 119.986412 | 4 | 180.000000 |
| H | 11 | 1.084010 | 9 | 118.930752 | 8 | 180.000000 |
| C | 11 | 1.373249 | 9 | 120.150324 | 8 | 0.000000 |
| C | 13 | 1.406652 | 11 | 119.749260 | 9 | 0.000000 |
| C | 14 | 1.402902 | 13 | 122.902081 | 11 | 0.000000 |
| C | 15 | 1.435077 | 14 | 121.963798 | 13 | 180.000000 |
| C | 16 | 1.358524 | 15 | 120.464711 | 14 | 180.000000 |
| H | 17 | 1.083899 | 16 | 120.295556 | 15 | 180.000000 |
| H | 16 | 1.083575 | 15 | 118.776176 | 14 | 0.000000 |
| H | 7 | 1.103321 | 3 | 110.887915 | 2 | 56.559860 |
| H | 1 | 1.083491 | 2 | 119.316120 | 3 | 180.000000 |
| H | 2 | 1.084600 | 1 | 119.468008 | 6 | 180.000000 |
| H | 6 | 1.083747 | 1 | 120.135217 | 2 | 180.000000 |
| H | 10 | 1.086607 | 9 | 119.435423 | 8 | 180.000000 |
| H | 13 | 1.082628 | 11 | 120.614238 | 9 | 180.000000 |
| H | 14 | 1.085420 | 13 | 118.748334 | 11 | 180.000000 |
| H | 7 | 1.103321 | 3 | 110.887948 | 2 | -56.559860 |

A.2 Vibrational Frequencies

The scaling factors are determined to be 0.9619 for C–H stretching vibrations (frequencies above 2000 cm^{-1}) and 0.9815 for lower frequency vibrations by comparing gas phase experimental and B3LYP 6–311++G(d,p) calculated frequencies for neutral benzene and anthracene (Tables A.21, A.22).

Table A.21: Scaling of the benzene molecule vibrational frequencies.

| Mode | Symmetry | Experimental, cm^{-1} | Calculated, cm^{-1} |
|------------|----------|--------------------------------|------------------------------|
| ν_{16} | e_{2u} | 398.131 | 409.2508 |
| ν_6 | e_{2g} | 608.13 | 622.2075 |
| ν_{11} | a_{2u} | 673.9747 | 686.4609 |
| ν_4 | b_{2g} | 702.24 | 719.2481 |
| ν_{10} | e_{1g} | 847.1062 | 863.6909 |
| ν_{17} | e_{2u} | 967.98 | 980.5364 |
| ν_5 | b_{2g} | 992.93 | 1010.6745 |
| ν_1 | a_{1g} | 993.071 | 1011.0642 |
| ν_{12} | b_{1u} | 1013.74 | 1022.4331 |
| ν_{18} | e_{1u} | 1038.267 | 1058.9918 |
| ν_{15} | b_{2u} | 1147.6751 | 1174.6646 |
| ν_9 | e_{2g} | 1177.776 | 1197.1716 |
| ν_{14} | b_{2u} | 1309.4 | 1335.6178 |
| ν_3 | a_{2g} | 1350 | 1380.8794 |
| ν_{19} | e_{1u} | 1483.9854 | 1510.0520 |
| ν_8 | e_{2g} | 1609.518 | 1633.1875 |
| ν_{20} | e_{1u} | 3047.908 | 3154.9144 |
| ν_{13} | b_{1u} | 3057 | 3181.3283 |
| ν_7 | e_{2g} | 3057.04 | 3181.6125 |
| ν_2 | a_{1g} | 3073.942 | 3191.8678 |

Experimental data taken from [111].

Table A.22: Scaling of the anthracene molecule vibrational frequencies.

| Mode | Symmetry | Experimental, cm^{-1} | Calculated, cm^{-1} |
|------------|----------|--------------------------------|------------------------------|
| ν_{64} | b_{3u} | 465.2 | 476.961 |
| ν_{49} | b_{2u} | 601.4 | 617.0831 |
| ν_{63} | b_{3u} | 725.3 | 739.3821 |
| ν_{48} | b_{2u} | 794.8 | 820.8065 |
| ν_{62} | b_{3u} | 876.7 | 864.1561 |
| ν_{30} | b_{1u} | 907.8 | 911.1968 |
| ν_{61} | b_{3u} | 954.2 | 972.5292 |
| ν_{47} | b_{2u} | 996 | 1026.1756 |
| ν_{46} | b_{2u} | 1128 | 1159.9346 |
| ν_{29} | b_{1u} | 1150.4 | 1172.6212 |
| ν_{45} | b_{2u} | 1165.5 | 1189.8674 |
| ν_{28} | b_{1u} | 1271.3 | 1290.8509 |
| ν_{27} | b_{1u} | 1316.5 | 1338.2374 |
| ν_{44} | b_{2u} | 1341.7 | 1377.5670 |
| ν_{43} | b_{2u} | 1396.8 | 1416.7486 |
| ν_{26} | b_{1u} | 1450 | 1480.8151 |
| ν_{42} | b_{2u} | 1476 | 1486.1868 |
| ν_{41} | b_{2u} | 1539.6 | 1578.3891 |
| ν_{25} | b_{1u} | 1626 | 1667.6092 |
| ν_{24} | b_{1u} | 3028 | 3157.7870 |
| ν_{23} | b_{1u} | 3052 | 3165.7045 |
| ν_{22} | b_{1u} | 3061 | 3189.7013 |
| ν_{39} | b_{2u} | 3067 | 3190.0427 |

Experimental data taken from [112].

Table A.23: Benzene and protonated benzene: scaled vibrational frequencies and IR intensities.

| C ₆ H ₆ | | C ₆ H ₇ ⁺ | |
|-------------------------------|----------|--|----------|
| ν , cm ⁻¹ | IR int | ν , cm ⁻¹ | IR int |
| 401.6797 | 0.0000 | 207.0374 | 12.1219 |
| 402.4736 | 0.0013 | 323.8184 | 0.0000 |
| 610.6967 | 0.0000 | 406.2831 | 1.5535 |
| 610.7172 | 0.0000 | 579.2896 | 5.4868 |
| 673.7614 | 122.0287 | 584.4683 | 0.0265 |
| 705.9420 | 0.0000 | 647.6300 | 57.2190 |
| 845.1487 | 0.0000 | 791.8260 | 0.0000 |
| 847.7126 | 0.0000 | 832.6574 | 16.0955 |
| 961.0158 | 0.0000 | 882.0701 | 13.8096 |
| 962.3965 | 0.0041 | 971.7421 | 16.5344 |
| 991.9770 | 0.0004 | 982.5926 | 0.4828 |
| 992.3595 | 0.0000 | 992.5469 | 0.0000 |
| 1003.5181 | 0.0000 | 995.5653 | 0.2352 |
| 1039.0731 | 6.3651 | 1027.9043 | 0.0152 |
| 1039.4005 | 6.3744 | 1048.1727 | 2.5553 |
| 1152.9333 | 0.0000 | 1129.6961 | 0.3245 |
| 1175.0239 | 0.0001 | 1131.1016 | 0.0000 |
| 1175.2203 | 0.0001 | 1183.2846 | 19.5856 |
| 1310.9089 | 0.0002 | 1190.0769 | 23.3059 |
| 1355.3331 | 0.0000 | 1257.4158 | 113.9668 |
| 1482.1160 | 7.1996 | 1336.8588 | 14.3341 |
| 1482.3507 | 7.1487 | 1393.8416 | 6.8657 |
| 1602.9325 | 0.0002 | 1448.8265 | 175.8423 |
| 1602.9735 | 0.0005 | 1457.2509 | 26.4624 |
| 3034.7122 | 0.0463 | 1541.7174 | 2.1079 |
| 3044.9359 | 0.0051 | 1608.1701 | 74.4622 |
| 3045.1460 | 0.0073 | 2833.8540 | 24.0384 |
| 3060.1197 | 36.9916 | 2839.2640 | 62.5214 |
| 3060.3931 | 37.1709 | 3059.5157 | 0.1546 |
| 3070.2576 | 0.0343 | 3067.5970 | 2.5411 |
| | | 3068.8847 | 5.5714 |
| | | 3086.0872 | 6.7612 |
| | | 3088.2879 | 1.7803 |

Table A.24: Naphthalene and protonated naphthalene: scaled vibrational frequencies and IR intensities.

| C_{10}H_8 | | $1\text{-C}_{10}\text{H}_9^+$ | | $2\text{-C}_{10}\text{H}_9^+$ | |
|---------------------------|----------|-------------------------------|----------|-------------------------------|----------|
| ν, cm^{-1} | IR int | ν, cm^{-1} | IR int | ν, cm^{-1} | IR int |
| 169.4145 | 2.8104 | 115.0238 | 0.4088 | 134.2035 | 5.7151 |
| 181.4778 | 0.0000 | 169.8269 | 1.5821 | 166.2855 | 0.7202 |
| 358.3695 | 1.8304 | 242.3699 | 11.6633 | 260.9555 | 1.8114 |
| 388.2838 | 0.0003 | 350.0190 | 0.9599 | 355.7677 | 2.4700 |
| 469.5430 | 0.0001 | 399.2639 | 0.0106 | 371.0291 | 1.1248 |
| 479.2424 | 24.1588 | 427.0042 | 13.0135 | 439.1710 | 3.9478 |
| 509.1167 | 0.0051 | 486.2705 | 0.1248 | 481.1385 | 21.2405 |
| 510.1492 | 0.0007 | 492.1717 | 0.4450 | 493.5473 | 4.0892 |
| 619.6614 | 0.0000 | 495.1976 | 16.5382 | 500.4934 | 0.6442 |
| 623.4749 | 3.2877 | 599.8496 | 2.0755 | 607.4839 | 1.3968 |
| 715.1633 | 0.0022 | 662.0221 | 0.0075 | 660.0737 | 2.2940 |
| 758.1406 | 0.0001 | 730.8713 | 28.0030 | 733.5593 | 4.2081 |
| 767.6320 | 0.0001 | 735.0980 | 4.4553 | 767.5992 | 34.0881 |
| 782.9871 | 122.5348 | 776.5801 | 61.6570 | 770.8273 | 4.1169 |
| 793.5282 | 0.3215 | 783.9355 | 0.2020 | 789.7835 | 12.6599 |
| 832.9490 | 0.0000 | 849.4712 | 7.4023 | 799.7599 | 20.4370 |
| 878.2911 | 0.0049 | 909.1840 | 0.9372 | 894.4784 | 9.5482 |
| 932.8070 | 0.0038 | 912.8521 | 1.3963 | 911.6343 | 25.0571 |
| 943.7688 | 0.0013 | 953.7979 | 12.8250 | 920.3033 | 0.1440 |
| 962.1320 | 3.5108 | 979.7361 | 0.0494 | 941.7730 | 20.2299 |
| 971.4251 | 0.0004 | 1002.8414 | 5.0216 | 992.8974 | 2.6962 |
| 979.6829 | 0.0053 | 1016.2134 | 0.3066 | 1005.8365 | 1.0672 |
| 1015.1555 | 11.0855 | 1023.1885 | 0.0330 | 1018.1834 | 2.4280 |
| 1025.6051 | 0.0006 | 1028.7145 | 2.5254 | 1018.9470 | 0.9761 |
| 1129.0893 | 6.7544 | 1091.1212 | 8.4447 | 1032.6991 | 14.6466 |
| 1147.6323 | 0.7540 | 1133.5737 | 6.1211 | 1140.4693 | 5.1158 |
| 1149.4143 | 0.0008 | 1159.2722 | 0.8416 | 1142.4153 | 0.0952 |
| 1163.2484 | 0.0001 | 1169.3644 | 32.8669 | 1161.8284 | 20.6217 |
| 1208.3148 | 0.7037 | 1177.0096 | 9.5891 | 1180.2637 | 18.5647 |
| 1245.7875 | 0.0106 | 1194.0854 | 9.3836 | 1212.1639 | 5.6154 |
| 1262.7006 | 7.3088 | 1244.4128 | 23.9391 | 1246.2730 | 6.5326 |
| 1364.6736 | 0.9743 | 1272.7489 | 23.7537 | 1282.3671 | 68.8119 |
| 1371.7347 | 0.0051 | 1320.2167 | 111.1756 | 1300.1806 | 109.8671 |
| 1390.5500 | 4.2261 | 1348.3846 | 43.0687 | 1353.4166 | 34.2552 |
| 1461.1824 | 0.0000 | 1367.6470 | 57.7761 | 1392.1690 | 98.5422 |
| 1461.4239 | 0.0081 | 1419.0089 | 37.1812 | 1403.9551 | 8.0366 |
| 1517.4368 | 7.9027 | 1442.8935 | 1.8160 | 1438.3395 | 1.1747 |
| 1581.8685 | 0.0049 | 1458.4152 | 130.5548 | 1472.0554 | 126.0498 |

— continued on the next page —

| C_{10}H_8 | | $1\text{-C}_{10}\text{H}_9^+$ | | $2\text{-C}_{10}\text{H}_9^+$ | |
|---------------------------|---------|-------------------------------|----------|-------------------------------|----------|
| ν, cm^{-1} | IR int | ν, cm^{-1} | IR int | ν, cm^{-1} | IR int |
| 1606.6887 | 2.6276 | 1512.8755 | 237.3922 | 1504.3483 | 30.6534 |
| 1636.8155 | 0.0100 | 1553.5685 | 14.5643 | 1544.3416 | 4.1690 |
| 3036.0010 | 0.0268 | 1577.4620 | 64.4722 | 1606.5400 | 29.5076 |
| 3037.8480 | 7.0148 | 1622.2347 | 89.2320 | 1629.3655 | 241.6182 |
| 3040.1955 | 0.3076 | 2863.1685 | 26.2422 | 2846.5401 | 10.2962 |
| 3042.1915 | 0.0292 | 2868.2406 | 6.8228 | 2848.6604 | 53.4301 |
| 3053.1975 | 0.0257 | 3051.0111 | 0.3846 | 3052.8251 | 0.7085 |
| 3054.3243 | 58.9447 | 3059.7462 | 0.1149 | 3063.5692 | 0.1470 |
| 3065.3029 | 42.4607 | 3062.4287 | 1.4124 | 3066.1493 | 1.1471 |
| 3066.5056 | 0.0044 | 3066.9603 | 0.0700 | 3068.5941 | 0.1373 |
| | | 3072.3632 | 0.1745 | 3077.0909 | 0.2662 |
| | | 3086.2220 | 2.8842 | 3081.3179 | 0.5111 |
| | | 3086.8465 | 0.1351 | 3088.0533 | 0.4251 |

Table A.25: Anthracene and protonated anthracene: scaled vibrational frequencies and IR intensities.

| $\text{C}_{14}\text{H}_{10}$ | | $1\text{-C}_{14}\text{H}_{11}^+$ | | $2\text{-C}_{14}\text{H}_{11}^+$ | | $9\text{-C}_{14}\text{H}_{11}^+$ | |
|------------------------------|---------|----------------------------------|---------|----------------------------------|---------|----------------------------------|---------|
| ν, cm^{-1} | IR int | ν, cm^{-1} | IR int | ν, cm^{-1} | IR int | ν, cm^{-1} | IR int |
| 90.6821 | 1.3556 | 70.4991 | 0.2308 | 81.0081 | 3.5138 | 52.4500 | 0.0381 |
| 118.9177 | 0.0007 | 102.3111 | 2.5679 | 107.3786 | 0.1345 | 103.8544 | 0.0005 |
| 231.6094 | 1.4742 | 165.4247 | 3.6131 | 187.9503 | 0.2570 | 176.0060 | 6.0420 |
| 233.5255 | 0.0002 | 228.8075 | 1.2144 | 230.6508 | 2.8025 | 221.8039 | 0.0036 |
| 261.1006 | 0.0000 | 251.6879 | 0.0927 | 242.4070 | 0.3530 | 230.7709 | 0.2675 |
| 382.1054 | 0.0382 | 275.5286 | 2.6684 | 296.2451 | 1.6753 | 314.6469 | 9.1203 |
| 388.3877 | 0.0003 | 380.2106 | 0.2830 | 382.0541 | 0.2912 | 374.6915 | 0.2133 |
| 390.2435 | 0.0001 | 388.4608 | 7.3321 | 383.8827 | 1.7159 | 377.8337 | 2.9451 |
| 468.1372 | 25.9027 | 403.2874 | 5.4686 | 388.9133 | 1.4807 | 407.4422 | 8.9731 |
| 476.2223 | 0.5999 | 425.4458 | 7.6603 | 436.2109 | 13.3598 | 439.2496 | 0.1560 |
| 501.7094 | 0.0089 | 474.1534 | 11.6914 | 461.6315 | 14.5126 | 484.6544 | 0.0271 |
| 525.3630 | 0.0002 | 503.7022 | 0.0121 | 504.2975 | 0.1064 | 512.6018 | 0.8791 |
| 580.9104 | 0.0002 | 513.3926 | 28.7446 | 516.0975 | 4.5531 | 524.3009 | 32.7964 |
| 605.6671 | 8.4296 | 576.6563 | 1.0079 | 592.2181 | 4.6479 | 595.7877 | 2.9941 |
| 629.9297 | 0.0001 | 618.1799 | 2.5412 | 618.1121 | 0.3902 | 607.6497 | 17.4426 |
| 649.0252 | 0.5412 | 642.7178 | 0.2692 | 639.5392 | 7.7584 | 658.2665 | 19.3567 |
| 725.7035 | 90.3199 | 644.6349 | 5.7943 | 640.5587 | 18.3765 | 661.9430 | 0.1347 |
| 745.6664 | 0.0142 | 717.5431 | 25.3305 | 730.8010 | 3.4168 | 723.8486 | 0.3923 |
| 749.4274 | 0.0005 | 735.3701 | 7.6471 | 748.2718 | 6.5237 | 731.5772 | 0.0516 |
| 755.8735 | 0.0009 | 750.8957 | 13.2480 | 756.6004 | 44.7187 | 768.4203 | 93.4549 |
| 770.9059 | 0.0006 | 759.2296 | 29.6253 | 769.5847 | 0.0027 | 778.3522 | 0.4468 |
| 805.6216 | 0.1077 | 792.5464 | 3.5126 | 793.7256 | 3.8758 | 800.0035 | 5.4294 |
| 824.4049 | 0.0002 | 846.0901 | 1.4324 | 794.6408 | 3.7219 | 845.0529 | 0.6468 |
| 848.1692 | 0.0018 | 875.3600 | 3.4960 | 860.9030 | 0.1399 | 881.7706 | 0.0239 |
| 881.2327 | 63.5914 | 890.7972 | 1.6421 | 884.0419 | 25.6619 | 884.7373 | 0.1553 |
| 894.3397 | 0.0219 | 902.0789 | 0.8655 | 897.7396 | 9.7448 | 899.2555 | 0.1569 |
| 901.7842 | 1.9277 | 907.9225 | 40.0565 | 898.3674 | 10.7665 | 922.8449 | 12.8563 |
| 912.1253 | 0.0001 | 925.3737 | 0.3822 | 908.2952 | 15.8457 | 967.2480 | 0.7584 |
| 954.5374 | 0.0337 | 947.9224 | 24.6308 | 914.5663 | 22.3771 | 979.1555 | 0.0272 |
| 959.1014 | 5.6996 | 979.9649 | 1.2422 | 953.5934 | 30.7861 | 997.8273 | 10.6462 |
| 974.8280 | 0.0001 | 996.0797 | 4.1938 | 982.9509 | 4.0744 | 1013.2228 | 0.1865 |
| 976.7700 | 0.0070 | 1006.9014 | 0.1624 | 995.2328 | 0.5992 | 1013.5434 | 0.6463 |
| 1007.1914 | 8.6096 | 1013.1386 | 0.8739 | 1008.2669 | 0.3509 | 1032.8158 | 1.7735 |
| 1011.6642 | 0.0010 | 1018.7456 | 1.1545 | 1014.8512 | 4.8722 | 1033.3012 | 2.0425 |
| 1105.1936 | 0.0002 | 1063.8511 | 14.4432 | 1022.7683 | 10.2104 | 1105.2782 | 0.0017 |
| 1138.4758 | 1.8229 | 1133.4439 | 3.0242 | 1127.2229 | 4.0393 | 1138.4095 | 8.9628 |
| 1150.9277 | 7.9588 | 1159.3612 | 4.5993 | 1152.4063 | 0.0641 | 1164.8411 | 84.5565 |
| 1166.8837 | 1.7153 | 1171.8186 | 2.7104 | 1160.1667 | 1.5577 | 1176.2010 | 7.9884 |

— continued on the next page —

| $\text{C}_{14}\text{H}_{10}$ | | $1\text{-C}_{14}\text{H}_{11}^+$ | | $2\text{-C}_{14}\text{H}_{11}^+$ | | $9\text{-C}_{14}\text{H}_{11}^+$ | |
|------------------------------|---------|----------------------------------|----------|----------------------------------|----------|----------------------------------|----------|
| ν, cm^{-1} | IR int | ν, cm^{-1} | IR int | ν, cm^{-1} | IR int | ν, cm^{-1} | IR int |
| 1167.8549 | 0.0002 | 1175.8036 | 0.6944 | 1173.9367 | 39.6052 | 1184.2331 | 18.9987 |
| 1188.4965 | 0.0001 | 1179.1241 | 22.3166 | 1186.1471 | 7.9572 | 1191.4008 | 0.1469 |
| 1265.5488 | 0.0279 | 1194.2698 | 90.3276 | 1198.2107 | 65.5581 | 1193.5940 | 0.8249 |
| 1266.9702 | 5.4406 | 1242.5586 | 56.7125 | 1242.0685 | 19.2167 | 1207.8722 | 58.1882 |
| 1270.4910 | 0.0009 | 1272.3748 | 11.8002 | 1277.4508 | 12.1036 | 1254.2262 | 0.6617 |
| 1313.4800 | 4.8217 | 1295.1931 | 4.4584 | 1292.8219 | 6.1357 | 1287.8226 | 0.6233 |
| 1352.0820 | 3.8821 | 1296.2105 | 3.5787 | 1308.6672 | 69.3597 | 1294.9944 | 25.4321 |
| 1387.4732 | 0.0004 | 1346.1972 | 129.9891 | 1329.1923 | 121.4536 | 1338.0471 | 191.5836 |
| 1390.5388 | 1.7148 | 1356.3985 | 35.2136 | 1353.7433 | 23.5427 | 1368.0035 | 22.5466 |
| 1402.4687 | 0.0010 | 1380.9868 | 139.6458 | 1392.6826 | 192.7469 | 1372.2968 | 36.3942 |
| 1453.4200 | 1.0785 | 1397.3178 | 15.2257 | 1401.5619 | 0.9555 | 1376.1459 | 38.1824 |
| 1458.6923 | 1.4026 | 1423.8461 | 12.4377 | 1409.8216 | 43.3518 | 1429.4762 | 43.0552 |
| 1488.2130 | 0.0002 | 1442.5450 | 11.4800 | 1437.0955 | 19.6411 | 1460.4157 | 27.6703 |
| 1549.1889 | 6.8078 | 1455.4923 | 315.2885 | 1467.9159 | 72.9368 | 1461.4459 | 172.5045 |
| 1564.2774 | 0.0021 | 1492.5786 | 1.2990 | 1487.6098 | 24.0765 | 1498.1171 | 17.7025 |
| 1592.2151 | 0.0011 | 1516.6483 | 432.8844 | 1533.6015 | 25.3365 | 1526.9723 | 333.9746 |
| 1636.7584 | 2.2566 | 1545.5191 | 99.6921 | 1552.3349 | 53.5095 | 1562.7378 | 12.4701 |
| 1638.1398 | 1.9693 | 1579.8629 | 99.3710 | 1596.8177 | 62.0961 | 1567.1575 | 37.8833 |
| 3035.5251 | 6.2658 | 1616.2389 | 13.6839 | 1621.4964 | 468.4955 | 1606.6280 | 465.5735 |
| 3037.4753 | 0.0070 | 1630.0135 | 239.0029 | 1641.9146 | 147.5208 | 1621.2268 | 22.8080 |
| 3039.0372 | 0.0228 | 2869.2120 | 13.6976 | 2851.7368 | 4.2058 | 2889.8988 | 5.3718 |
| 3040.1899 | 14.3112 | 2876.6619 | 2.2066 | 2853.1486 | 45.1824 | 2909.4276 | 2.3259 |
| 3043.4351 | 0.0195 | 3047.7182 | 1.4657 | 3049.2952 | 0.0527 | 3043.5688 | 0.2756 |
| 3045.0912 | 0.0036 | 3052.0445 | 1.4101 | 3057.8757 | 0.0645 | 3059.6297 | 0.4408 |
| 3056.5217 | 0.8022 | 3056.7136 | 0.2753 | 3059.8703 | 0.0859 | 3060.0267 | 0.3601 |
| 3056.8791 | 58.1490 | 3058.7498 | 0.3353 | 3062.2724 | 1.9275 | 3065.2655 | 0.5332 |
| 3068.1737 | 51.2160 | 3059.7848 | 0.2688 | 3063.4827 | 0.7386 | 3066.3259 | 0.4517 |
| 3068.5021 | 0.0259 | 3063.2490 | 0.2375 | 3066.8913 | 0.0191 | 3074.0746 | 0.3602 |
| | | 3073.2910 | 2.0092 | 3076.7803 | 1.1404 | 3075.0717 | 0.2486 |
| | | 3083.8449 | 1.3084 | 3079.1873 | 0.5177 | 3088.7548 | 0.2418 |
| | | 3084.6358 | 0.2419 | 3087.1170 | 0.4328 | 3089.0265 | 0.1823 |

Table A.26: Phenanthrene and protonated phenanthrene: scaled vibrational frequencies and IR intensities.

| $\text{C}_{14}\text{H}_{10}$ | | $1\text{-C}_{14}\text{H}_{11}^+$ | | $2\text{-C}_{14}\text{H}_{11}^+$ | |
|------------------------------|---------|----------------------------------|---------|----------------------------------|---------|
| ν, cm^{-1} | IR int | ν, cm^{-1} | IR int | ν, cm^{-1} | IR int |
| 94.1967 | 0.0033 | 66.8310 | 0.4078 | 77.8542 | 3.0516 |
| 99.2912 | 0.9067 | 98.6964 | 2.0581 | 89.8509 | 0.7524 |
| 223.1468 | 4.1778 | 157.7058 | 0.4744 | 186.4559 | 0.2077 |
| 238.5203 | 0.0003 | 213.0964 | 4.1247 | 218.4536 | 4.4060 |
| 242.9889 | 0.4580 | 235.8947 | 1.5378 | 246.0627 | 1.1656 |
| 394.2872 | 0.0018 | 279.8484 | 10.7683 | 295.4089 | 2.3895 |
| 403.6186 | 0.5392 | 384.2937 | 0.2044 | 366.0720 | 1.1431 |
| 428.9911 | 8.0648 | 394.0992 | 3.8387 | 402.5492 | 4.2092 |
| 437.9531 | 1.9032 | 428.4114 | 3.0333 | 416.8031 | 12.4927 |
| 496.5687 | 1.0243 | 434.9084 | 3.8347 | 433.9158 | 0.6284 |
| 497.6790 | 5.6189 | 486.5031 | 1.0467 | 481.1466 | 1.6061 |
| 533.9579 | 0.0116 | 487.3224 | 1.9428 | 486.4599 | 0.5875 |
| 546.5301 | 0.2733 | 499.0529 | 4.5097 | 535.6937 | 2.7991 |
| 587.0511 | 0.0002 | 542.7338 | 17.2577 | 536.0105 | 0.3361 |
| 631.9821 | 5.3449 | 602.1786 | 0.6744 | 599.7317 | 8.3489 |
| 709.4696 | 0.0716 | 627.1811 | 9.3719 | 633.1490 | 4.1356 |
| 710.2180 | 2.1936 | 685.6043 | 1.7118 | 689.6513 | 8.2423 |
| 713.3346 | 2.0777 | 705.8554 | 0.0620 | 700.6441 | 1.2351 |
| 733.4026 | 89.9634 | 717.6209 | 22.3442 | 724.6895 | 9.5247 |
| 753.8650 | 0.0422 | 738.6946 | 3.0845 | 751.1034 | 52.1083 |
| 784.0600 | 0.0082 | 759.9602 | 47.8919 | 791.2935 | 12.8500 |
| 812.8769 | 60.4701 | 821.7176 | 4.6482 | 795.6133 | 18.9122 |
| 827.3557 | 0.0612 | 829.0989 | 39.3086 | 812.6907 | 7.2791 |
| 860.4947 | 0.1014 | 867.3581 | 2.1852 | 818.3090 | 9.8546 |
| 865.2298 | 10.6824 | 871.1894 | 4.2033 | 852.1372 | 1.9636 |
| 871.2405 | 2.0618 | 888.7542 | 3.2588 | 877.6763 | 10.0076 |
| 942.2343 | 0.0220 | 941.6789 | 15.1545 | 922.0052 | 27.8659 |
| 950.5919 | 3.0042 | 967.1783 | 0.1676 | 933.6127 | 20.6802 |
| 966.1769 | 0.0196 | 984.7964 | 2.1972 | 972.2705 | 1.6940 |
| 976.5710 | 0.0134 | 994.5599 | 5.8541 | 984.7952 | 0.4064 |
| 977.9282 | 0.0138 | 994.6051 | 0.5520 | 988.7993 | 7.9596 |
| 997.7435 | 2.5449 | 1004.5687 | 0.4170 | 999.5386 | 0.9301 |
| 1040.5756 | 7.2705 | 1008.5462 | 0.5162 | 1008.7296 | 0.4787 |
| 1041.1145 | 1.6881 | 1040.8573 | 1.5861 | 1026.0300 | 14.9448 |
| 1093.7494 | 2.2897 | 1063.0781 | 1.8768 | 1041.6504 | 5.7341 |
| 1143.4660 | 2.2286 | 1120.9165 | 4.4267 | 1110.0456 | 11.0717 |
| 1151.6246 | 0.0295 | 1158.1179 | 24.2629 | 1143.4355 | 0.0053 |

— continued on the next page —

| $\text{C}_{14}\text{H}_{10}$ | | $1\text{-C}_{14}\text{H}_{11}^+$ | | $2\text{-C}_{14}\text{H}_{11}^+$ | |
|------------------------------|---------|----------------------------------|----------|----------------------------------|----------|
| ν, cm^{-1} | IR int | ν, cm^{-1} | IR int | ν, cm^{-1} | IR int |
| 1163.9952 | 0.1991 | 1161.9644 | 1.1146 | 1158.8326 | 6.4067 |
| 1167.0895 | 0.4953 | 1169.4978 | 1.1270 | 1167.1523 | 23.8018 |
| 1201.5408 | 1.8410 | 1180.2455 | 4.3025 | 1179.6339 | 12.7273 |
| 1218.6117 | 0.5131 | 1203.2989 | 8.9504 | 1206.5033 | 1.3420 |
| 1242.3857 | 10.2436 | 1233.7048 | 20.7813 | 1220.6362 | 20.7024 |
| 1279.9567 | 0.0045 | 1250.8571 | 79.8095 | 1257.3717 | 26.2570 |
| 1299.8082 | 2.5612 | 1282.9118 | 11.3405 | 1282.2228 | 11.3503 |
| 1342.7728 | 0.1215 | 1302.4900 | 5.8559 | 1308.3848 | 127.4549 |
| 1349.2786 | 0.7828 | 1326.1043 | 217.1552 | 1330.7162 | 90.1603 |
| 1417.3657 | 0.4096 | 1346.5572 | 312.6771 | 1355.1865 | 14.7231 |
| 1423.0397 | 1.2301 | 1359.6256 | 6.8524 | 1369.6733 | 112.5547 |
| 1442.6138 | 3.5413 | 1390.9642 | 200.7722 | 1406.3337 | 41.5622 |
| 1461.7055 | 10.5507 | 1423.9572 | 14.8492 | 1420.4206 | 4.1091 |
| 1505.2961 | 5.9138 | 1449.6666 | 1.1361 | 1440.4158 | 10.4778 |
| 1531.6928 | 1.8858 | 1456.8742 | 31.9259 | 1467.0203 | 108.8570 |
| 1576.6635 | 0.0790 | 1507.4256 | 51.1561 | 1477.4480 | 107.8114 |
| 1610.3195 | 1.8366 | 1530.5348 | 204.1641 | 1532.6130 | 10.1197 |
| 1622.4005 | 0.0971 | 1546.2847 | 27.3673 | 1551.0334 | 23.5177 |
| 1627.2943 | 0.1731 | 1574.5060 | 135.7502 | 1599.7978 | 224.8536 |
| 3036.2905 | 0.1077 | 1609.9637 | 1.0527 | 1618.4424 | 94.9944 |
| 3039.0293 | 3.3461 | 1616.2117 | 49.5613 | 1627.6335 | 108.0935 |
| 3040.0193 | 1.7506 | 2867.0308 | 30.7786 | 2852.5979 | 7.0315 |
| 3048.6770 | 0.0697 | 2874.0203 | 5.3546 | 2853.1429 | 49.0977 |
| 3049.8867 | 13.4446 | 3055.1147 | 0.0577 | 3054.3693 | 0.2865 |
| 3055.5026 | 33.1547 | 3061.9167 | 0.7137 | 3061.8476 | 0.2341 |
| 3061.6454 | 37.5327 | 3064.4682 | 2.2472 | 3063.9347 | 0.2851 |
| 3064.6472 | 0.8129 | 3066.6230 | 0.4275 | 3069.8651 | 0.9510 |
| 3071.4832 | 14.1301 | 3068.6839 | 0.3912 | 3072.5380 | 0.2769 |
| 3083.3012 | 19.3960 | 3073.4131 | 0.9389 | 3077.5952 | 0.5478 |
| | | 3081.1743 | 1.9590 | 3080.6354 | 0.6591 |
| | | 3085.4837 | 0.4133 | 3091.2866 | 0.4981 |
| | | 3088.5864 | 0.6645 | 3108.2634 | 0.5539 |

— continued on the next page —

| 3-C ₁₄ H ₁₁ ⁺ | | 4-C ₁₄ H ₁₁ ⁺ | | 9-C ₁₄ H ₁₁ ⁺ | |
|--|---------|--|---------|--|---------|
| ν , cm ⁻¹ | IR int | ν , cm ⁻¹ | IR int | ν , cm ⁻¹ | IR int |
| 67.9947 | 0.7722 | 82.5920 | 0.0418 | 68.4213 | 0.3489 |
| 98.5772 | 1.0773 | 102.3673 | 0.9208 | 89.4593 | 0.1729 |
| 185.4722 | 8.4139 | 170.6658 | 6.4054 | 174.6351 | 8.9753 |
| 226.1071 | 0.0598 | 215.7809 | 2.0827 | 218.9379 | 3.2365 |
| 237.5229 | 0.3890 | 229.2664 | 1.0655 | 242.6537 | 1.8744 |
| 282.0925 | 0.0002 | 273.5060 | 7.1988 | 265.0713 | 0.8130 |
| 394.5469 | 4.3574 | 396.4172 | 3.8341 | 393.6559 | 6.6158 |
| 396.6824 | 2.8436 | 401.1307 | 10.8642 | 412.8374 | 7.7328 |
| 407.0016 | 3.7319 | 431.5685 | 0.7363 | 428.1788 | 0.0147 |
| 433.7555 | 0.9466 | 434.8214 | 0.1069 | 429.8925 | 0.7838 |
| 490.8570 | 4.4328 | 487.4470 | 1.7129 | 465.2069 | 0.8464 |
| 491.7979 | 6.8949 | 487.8313 | 1.5712 | 488.8239 | 2.4661 |
| 511.4307 | 3.3446 | 518.8698 | 3.2033 | 517.9534 | 3.3654 |
| 538.4446 | 5.7051 | 532.6294 | 5.4806 | 537.3154 | 0.2199 |
| 601.7457 | 4.1965 | 597.4887 | 0.7408 | 612.2059 | 2.6280 |
| 640.5680 | 23.0381 | 628.3979 | 0.7553 | 670.3057 | 1.5372 |
| 695.1468 | 0.3791 | 684.2585 | 17.2016 | 689.4227 | 4.3614 |
| 706.4309 | 3.5485 | 706.1690 | 3.2121 | 694.8828 | 11.7230 |
| 726.6655 | 0.7419 | 712.6530 | 47.0578 | 716.3663 | 23.0627 |
| 759.7846 | 45.3178 | 745.0416 | 21.3160 | 759.9382 | 11.6892 |
| 778.3826 | 0.0059 | 767.9317 | 8.7694 | 772.8323 | 82.6562 |
| 803.6541 | 0.0376 | 809.7642 | 29.2338 | 800.2659 | 6.2465 |
| 815.6690 | 1.4822 | 822.1024 | 0.7905 | 806.1470 | 2.5926 |
| 858.3347 | 25.2080 | 845.0012 | 0.1111 | 851.0204 | 0.3472 |
| 861.5825 | 1.0793 | 874.0899 | 19.6783 | 868.8398 | 5.9128 |
| 880.2520 | 20.1095 | 884.7413 | 12.0839 | 878.5173 | 0.0033 |
| 913.7954 | 31.5725 | 951.8956 | 13.2277 | 951.8135 | 1.9611 |
| 937.7633 | 22.0480 | 971.6525 | 0.1309 | 970.4054 | 0.0149 |
| 969.1507 | 2.3836 | 981.7815 | 1.5604 | 988.5470 | 0.7264 |
| 988.7445 | 3.9067 | 992.2869 | 5.3997 | 993.5013 | 4.1198 |
| 997.5475 | 0.0105 | 993.6547 | 1.4459 | 1005.9900 | 0.3402 |
| 1004.8626 | 0.1122 | 1004.2919 | 0.3685 | 1014.9348 | 0.4616 |
| 1006.0397 | 0.0095 | 1014.7714 | 0.0003 | 1025.2669 | 13.7296 |
| 1033.8640 | 4.3175 | 1032.3690 | 1.3793 | 1035.3078 | 14.4911 |
| 1045.6648 | 0.2482 | 1060.9424 | 6.8796 | 1047.9238 | 4.0291 |
| 1114.7411 | 2.0098 | 1121.6351 | 11.1129 | 1106.5516 | 1.0762 |
| 1149.2280 | 0.0014 | 1159.6033 | 7.4670 | 1149.3712 | 20.2114 |
| 1157.7243 | 20.0859 | 1162.1242 | 0.0922 | 1159.7551 | 1.2183 |
| 1166.3319 | 40.8071 | 1174.0277 | 5.3250 | 1176.8140 | 22.0567 |

— continued on the next page —

| 3-C ₁₄ H ₁₁ ⁺ | | 4-C ₁₄ H ₁₁ ⁺ | | 9-C ₁₄ H ₁₁ ⁺ | |
|--|----------|--|----------|--|----------|
| ν , cm ⁻¹ | IR int | ν , cm ⁻¹ | IR int | ν , cm ⁻¹ | IR int |
| 1178.6581 | 5.0714 | 1178.0795 | 13.8555 | 1181.3182 | 43.9946 |
| 1221.7659 | 96.2017 | 1186.1501 | 9.4292 | 1187.1326 | 0.2769 |
| 1238.0347 | 22.3805 | 1220.7042 | 4.8264 | 1219.4820 | 5.5773 |
| 1259.8949 | 41.4472 | 1241.4692 | 19.3288 | 1256.6658 | 69.6261 |
| 1286.2212 | 8.5068 | 1274.6392 | 5.5811 | 1283.6424 | 1.8351 |
| 1296.0576 | 4.4107 | 1326.9125 | 6.5054 | 1308.1174 | 69.9866 |
| 1319.6674 | 155.1110 | 1356.5073 | 50.8937 | 1325.4735 | 111.5601 |
| 1344.9203 | 94.3402 | 1391.4536 | 44.1385 | 1332.7650 | 89.0793 |
| 1362.0603 | 33.0623 | 1391.4536 | 209.8578 | 1363.6392 | 13.3516 |
| 1404.3831 | 163.6224 | 1399.9653 | 118.6090 | 1389.2988 | 73.3719 |
| 1428.8197 | 0.6698 | 1415.0769 | 23.6905 | 1419.9175 | 16.1036 |
| 1441.5497 | 15.2252 | 1435.9622 | 56.1361 | 1453.8930 | 197.3566 |
| 1465.3018 | 82.1274 | 1455.9324 | 58.6101 | 1464.9969 | 23.4654 |
| 1513.9608 | 232.0720 | 1480.6514 | 227.3070 | 1480.3588 | 90.3283 |
| 1524.3456 | 12.7466 | 1520.5825 | 82.3635 | 1532.0905 | 39.3648 |
| 1552.5484 | 45.0630 | 1546.0982 | 32.9404 | 1551.1872 | 5.2345 |
| 1579.5118 | 224.7362 | 1587.9698 | 17.2206 | 1578.6360 | 24.8403 |
| 1606.8414 | 36.2921 | 1613.3280 | 41.8340 | 1611.4547 | 54.4120 |
| 1638.6240 | 94.8078 | 1626.2855 | 113.2273 | 1622.8728 | 222.2757 |
| 2851.5043 | 5.0708 | 2872.6139 | 12.8384 | 2858.2511 | 30.7022 |
| 2852.3017 | 35.5274 | 2882.1236 | 5.1109 | 2862.3105 | 5.1553 |
| 3056.5632 | 0.1851 | 3051.3575 | 0.8473 | 3049.2919 | 0.4121 |
| 3063.1680 | 0.4819 | 3061.8519 | 0.3702 | 3174.8125 | 1.4671 |
| 3064.1178 | 1.1686 | 3064.4351 | 0.2226 | 3063.9745 | 0.1645 |
| 3066.8565 | 0.0052 | 3065.4902 | 0.9536 | 3068.0785 | 0.0523 |
| 3073.6479 | 0.8403 | 3068.8017 | 0.0042 | 3069.9035 | 0.3538 |
| 3077.4879 | 0.0715 | 3076.7139 | 1.0855 | 3080.2951 | 0.7615 |
| 3079.8730 | 0.2102 | 3078.5850 | 1.2314 | 3088.2247 | 0.1210 |
| 3082.8876 | 1.2366 | 3085.7359 | 0.9976 | 3090.4592 | 0.6643 |
| 3087.9075 | 0.7155 | 3087.6694 | 0.5761 | 3106.8336 | 0.6655 |

Table A.27: Pyrene and protonated pyrene: scaled vibrational frequencies and IR intensities.

| $\text{C}_{16}\text{H}_{10}$ | | $1\text{-C}_{16}\text{H}_{11}^+$ | | $2\text{-C}_{16}\text{H}_{11}^+$ | | $4\text{-C}_{16}\text{H}_{11}^+$ | |
|------------------------------|----------|----------------------------------|---------|----------------------------------|---------|----------------------------------|---------|
| ν, cm^{-1} | IR int | ν, cm^{-1} | IR int | ν, cm^{-1} | IR int | ν, cm^{-1} | IR int |
| 97.1181 | 0.5821 | 95.5462 | 1.5344 | 83.3823 | 3.5085 | 78.6657 | 0.0415 |
| 148.5445 | 0.0009 | 110.9925 | 1.0065 | 138.6492 | 0.0001 | 127.2766 | 1.6657 |
| 208.6291 | 10.4254 | 188.6274 | 2.5206 | 202.0453 | 0.8603 | 183.3704 | 8.2686 |
| 243.5924 | 0.0001 | 195.5718 | 8.9718 | 213.1682 | 15.4343 | 208.5666 | 8.7083 |
| 257.3209 | 0.0005 | 249.6784 | 0.5228 | 228.6481 | 0.0007 | 244.5676 | 0.0549 |
| 351.8438 | 1.8199 | 324.7912 | 2.4638 | 287.7624 | 3.2037 | 271.6604 | 1.1672 |
| 395.9707 | 0.0005 | 343.7002 | 1.8267 | 350.8490 | 4.9552 | 347.2684 | 1.4075 |
| 404.1908 | 0.0001 | 400.9396 | 4.8102 | 371.2372 | 0.0001 | 395.5658 | 5.0511 |
| 453.7523 | 0.0002 | 402.3490 | 1.0714 | 399.3193 | 2.2867 | 419.7240 | 0.4333 |
| 490.5197 | 2.2572 | 449.6438 | 4.3214 | 443.9150 | 1.7838 | 446.2471 | 0.5545 |
| 498.3130 | 0.0058 | 463.9985 | 0.9676 | 483.6031 | 0.8495 | 464.4044 | 0.0058 |
| 498.5643 | 3.2297 | 487.7195 | 0.5154 | 488.2543 | 0.0325 | 488.5639 | 3.1973 |
| 503.7334 | 0.0570 | 494.2288 | 3.7523 | 493.2542 | 0.1501 | 496.6897 | 0.8321 |
| 527.9526 | 0.0030 | 497.7693 | 1.5129 | 495.2806 | 0.1378 | 499.9849 | 2.2666 |
| 544.0087 | 2.5088 | 528.3905 | 1.3358 | 508.4643 | 0.0004 | 518.7121 | 0.9348 |
| 571.7413 | 0.0002 | 538.3323 | 0.5091 | 537.9310 | 0.6465 | 537.6307 | 2.5327 |
| 583.7679 | 0.0003 | 584.1907 | 1.1131 | 571.2952 | 2.1281 | 570.9713 | 2.0852 |
| 674.3892 | 0.0311 | 631.8460 | 15.0741 | 645.8913 | 1.3784 | 599.6938 | 0.1137 |
| 690.5622 | 0.0155 | 661.6750 | 8.0910 | 662.9864 | 0.0320 | 676.8108 | 2.6968 |
| 708.3842 | 43.8722 | 674.3356 | 0.2393 | 673.6081 | 1.1642 | 692.5809 | 28.5727 |
| 735.3980 | 0.0001 | 700.6681 | 12.1358 | 715.8940 | 23.6626 | 715.2946 | 0.8365 |
| 742.5187 | 17.8701 | 720.2445 | 2.0603 | 728.0312 | 3.2390 | 720.0007 | 1.9308 |
| 761.0679 | 0.3744 | 765.5098 | 6.1663 | 757.1292 | 10.8156 | 766.4817 | 14.5960 |
| 799.5707 | 0.0001 | 790.1094 | 0.2612 | 773.9228 | 0.1563 | 785.8267 | 11.1992 |
| 799.8627 | 0.0442 | 790.3971 | 0.0173 | 782.9817 | 0.8948 | 786.3504 | 1.9686 |
| 802.9084 | 0.6643 | 816.9432 | 0.6102 | 793.1654 | 0.0045 | 793.8929 | 0.2380 |
| 818.1137 | 4.1177 | 828.3045 | 16.8187 | 803.7679 | 1.5999 | 804.6890 | 0.1777 |
| 841.0556 | 111.8551 | 863.5597 | 86.5014 | 841.4280 | 83.1074 | 840.2639 | 89.1334 |
| 891.9943 | 0.0027 | 901.3692 | 0.6784 | 854.2992 | 0.0000 | 915.5988 | 0.2863 |
| 904.0837 | 0.0013 | 934.3861 | 15.6847 | 926.0139 | 0.0059 | 933.1823 | 8.0193 |
| 960.5316 | 0.0040 | 948.0922 | 0.0934 | 946.8781 | 12.3960 | 947.0653 | 4.3745 |
| 961.7593 | 0.0023 | 966.5755 | 5.8640 | 947.3105 | 3.5174 | 964.7524 | 0.0256 |
| 967.0518 | 0.1565 | 985.0209 | 0.0753 | 948.6760 | 28.7649 | 981.7520 | 0.0323 |
| 967.3023 | 1.1345 | 992.2696 | 0.0411 | 984.9485 | 0.0484 | 990.4956 | 1.7576 |
| 975.6922 | 0.0000 | 993.1250 | 8.1706 | 985.8101 | 0.1118 | 998.4249 | 0.4085 |
| 995.3900 | 1.9656 | 998.5797 | 1.1418 | 998.5920 | 19.7050 | 1001.1393 | 0.1302 |
| 1069.2168 | 0.0004 | 1003.9566 | 0.0026 | 1004.0496 | 0.3997 | 1040.9955 | 15.9617 |
| 1092.1416 | 8.5560 | 1083.9496 | 0.4941 | 1057.6170 | 27.0444 | 1070.4810 | 11.7216 |

— continued on the next page —

| $\text{C}_{16}\text{H}_{10}$ | | $1\text{-C}_{16}\text{H}_{11}^+$ | | $2\text{-C}_{16}\text{H}_{11}^+$ | | $4\text{-C}_{16}\text{H}_{11}^+$ | |
|------------------------------|---------|----------------------------------|----------|----------------------------------|----------|----------------------------------|----------|
| ν, cm^{-1} | IR int | ν, cm^{-1} | IR int | ν, cm^{-1} | IR int | ν, cm^{-1} | IR int |
| 1105.3650 | 0.0000 | 1127.3516 | 10.2833 | 1083.0996 | 0.2665 | 1092.7238 | 1.9344 |
| 1144.0798 | 0.4214 | 1146.1586 | 30.9353 | 1107.5940 | 2.7481 | 1100.6467 | 9.3081 |
| 1146.6601 | 0.0001 | 1162.9392 | 10.1137 | 1131.1866 | 0.0000 | 1159.1800 | 18.6460 |
| 1175.9907 | 0.0001 | 1174.4712 | 0.9650 | 1151.7842 | 9.8735 | 1162.8441 | 1.2149 |
| 1182.4068 | 14.3182 | 1175.8038 | 3.1648 | 1172.8496 | 8.4850 | 1179.1170 | 11.4306 |
| 1208.2526 | 0.0040 | 1191.7900 | 3.3840 | 1186.2498 | 21.0161 | 1187.6893 | 0.7535 |
| 1238.0825 | 0.0008 | 1204.2396 | 34.0111 | 1213.5664 | 5.3738 | 1203.7399 | 18.9939 |
| 1240.3292 | 0.0001 | 1229.3335 | 81.7602 | 1238.2736 | 3.9808 | 1234.5776 | 20.1997 |
| 1244.2157 | 2.1748 | 1234.6502 | 83.4711 | 1245.7966 | 5.0913 | 1237.7360 | 18.5845 |
| 1317.7591 | 5.2586 | 1252.4066 | 26.7257 | 1251.1884 | 12.2932 | 1252.9277 | 9.3160 |
| 1325.5821 | 0.0007 | 1322.5934 | 11.0836 | 1293.6961 | 158.2851 | 1325.6396 | 112.2704 |
| 1373.1458 | 0.0003 | 1357.3778 | 78.4578 | 1346.0674 | 103.5324 | 1334.6865 | 11.1933 |
| 1399.1937 | 0.0018 | 1362.0484 | 55.3707 | 1346.5580 | 7.5443 | 1335.4976 | 24.6094 |
| 1407.3476 | 0.0008 | 1364.3560 | 70.0057 | 1355.3209 | 23.3295 | 1370.0729 | 9.2170 |
| 1429.4404 | 3.2860 | 1383.6554 | 87.0799 | 1407.3655 | 1.3157 | 1380.6631 | 154.5740 |
| 1431.5310 | 6.9852 | 1410.7907 | 27.1735 | 1407.5246 | 18.1018 | 1407.1274 | 12.5503 |
| 1454.9869 | 1.2825 | 1420.8215 | 4.2517 | 1425.5012 | 80.1772 | 1424.0572 | 65.6510 |
| 1485.0450 | 3.1353 | 1432.8487 | 4.7756 | 1427.3118 | 6.4131 | 1429.4466 | 4.6571 |
| 1504.9519 | 0.0003 | 1450.7626 | 0.2849 | 1442.4997 | 14.6186 | 1440.0267 | 15.5180 |
| 1563.0586 | 0.0005 | 1487.1203 | 54.2065 | 1472.8360 | 58.1742 | 1479.1663 | 48.3764 |
| 1593.7654 | 0.0003 | 1504.2297 | 2.0058 | 1513.0355 | 46.2821 | 1513.1456 | 51.4439 |
| 1602.4305 | 12.1115 | 1538.2747 | 153.1500 | 1562.9437 | 115.5723 | 1549.9078 | 4.2840 |
| 1611.9029 | 1.5195 | 1572.0022 | 84.3038 | 1564.1022 | 3.3750 | 1565.5552 | 23.6833 |
| 1637.0552 | 0.0007 | 1584.9714 | 116.3863 | 1607.1853 | 4.0784 | 1595.0864 | 75.7052 |
| 3036.7044 | 2.6658 | 1610.7141 | 266.9465 | 1607.7609 | 33.5238 | 1604.1307 | 36.8072 |
| 3037.0646 | 0.0445 | 1633.3277 | 33.9505 | 1624.1268 | 87.4592 | 1629.3258 | 159.0258 |
| 3039.5478 | 0.0097 | 2874.3037 | 21.0480 | 2848.5199 | 7.9957 | 2859.6963 | 30.1848 |
| 3040.1169 | 0.0993 | 2883.7229 | 1.4680 | 2849.8495 | 44.5904 | 2864.3705 | 4.3288 |
| 3046.7735 | 16.0856 | 3056.6725 | 0.0690 | 3060.6343 | 0.1379 | 3048.3867 | 0.1898 |
| 3047.5586 | 0.0445 | 3058.2026 | 0.0572 | 3060.8045 | 0.0862 | 3053.8725 | 1.4159 |
| 3055.2178 | 12.3247 | 3059.2597 | 0.4489 | 3062.1924 | 0.0519 | 3056.2523 | 0.5670 |
| 3055.2749 | 52.6730 | 3060.9412 | 0.0809 | 3062.7257 | 0.6191 | 3060.3166 | 0.3360 |
| 3063.0471 | 53.4440 | 3064.5143 | 0.1818 | 3063.6648 | 2.1822 | 3064.0593 | 1.0369 |
| 3063.6080 | 2.7379 | 3069.8436 | 0.6518 | 3069.4393 | 1.0050 | 3067.5172 | 0.4729 |
| | | 3073.0496 | 0.1959 | 3076.0615 | 1.1421 | 3074.8974 | 1.5060 |
| | | 3075.1417 | 1.1855 | 3076.1686 | 1.1011 | 3079.7530 | 1.2761 |
| | | 3084.0800 | 0.3097 | 3079.4115 | 0.7470 | 3086.2294 | 0.0157 |

A.3 Vibrational Spectra

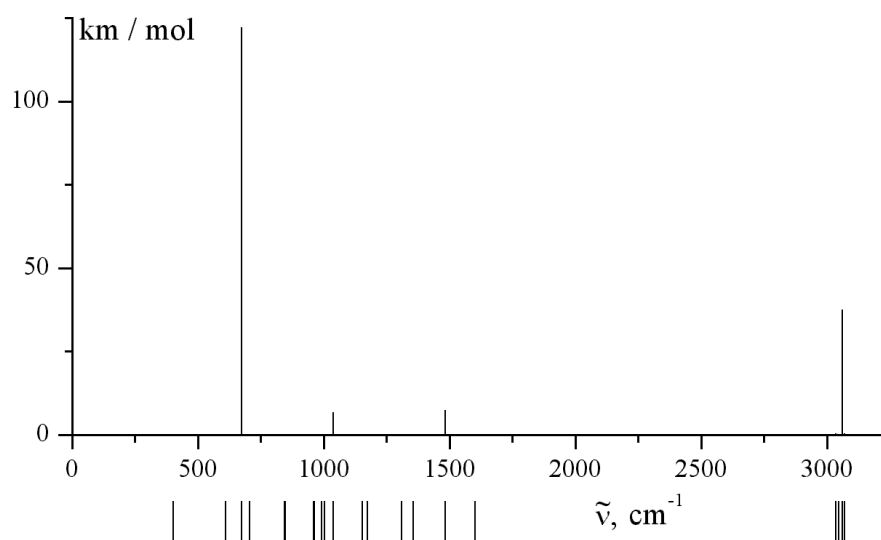


Figure A.1: Calculated benzene C_6H_6 IR vibrational spectrum.

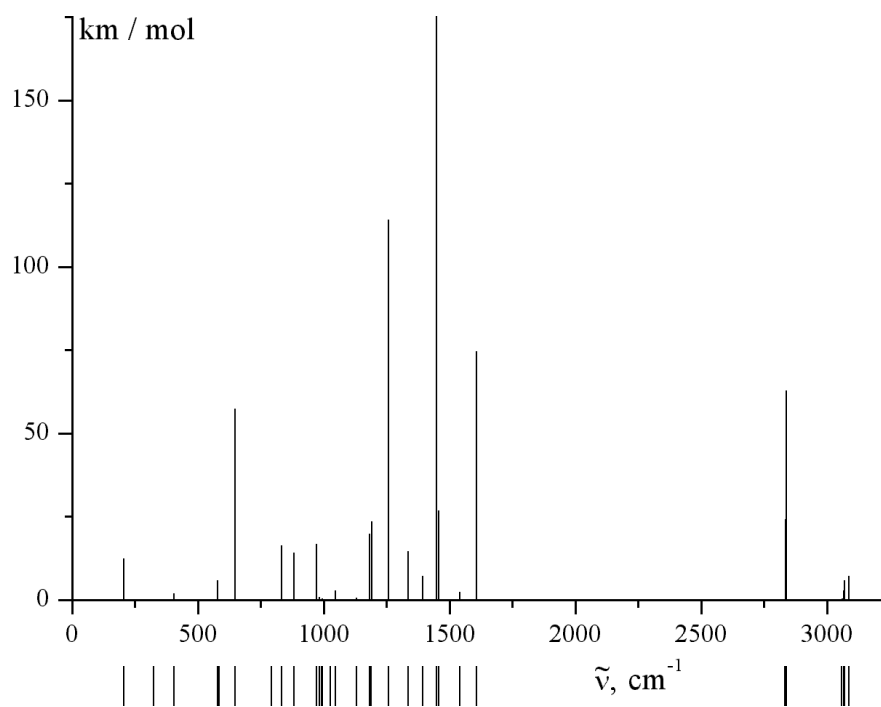


Figure A.2: Calculated protonated benzene C_6H_7^+ IR vibrational spectrum.

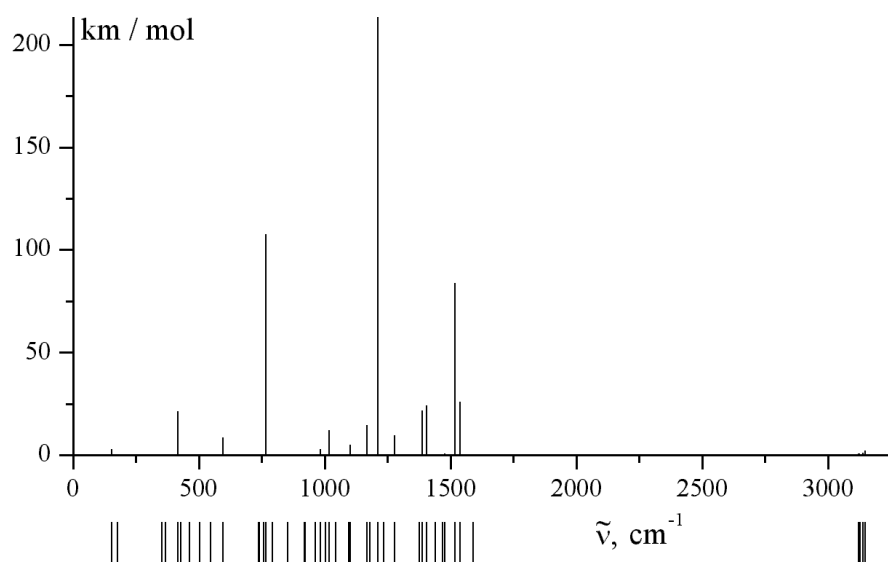


Figure A.3: Calculated naphthalene $C_{10}H_8$ IR vibrational spectrum.

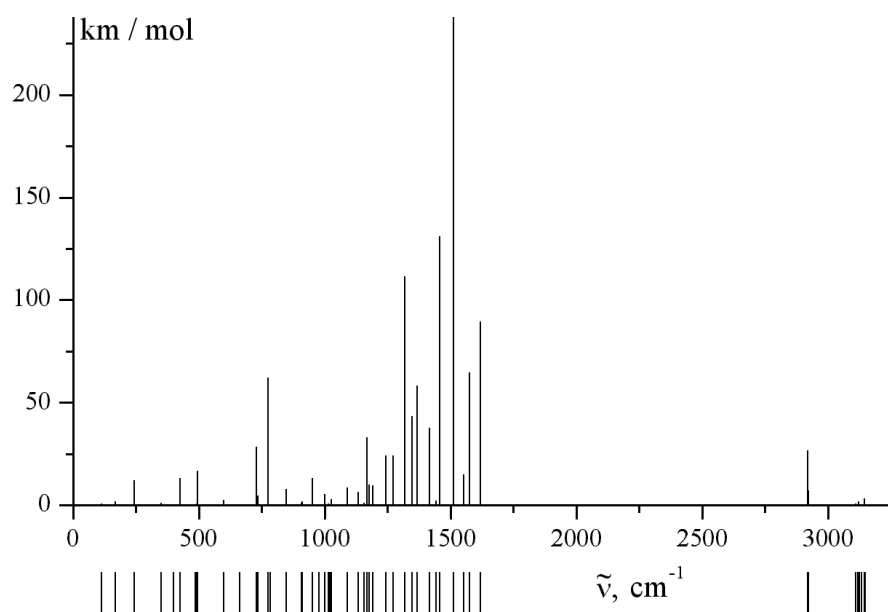


Figure A.4: Calculated protonated naphthalene 1- $C_{10}H_9^+$ IR vibrational spectrum.

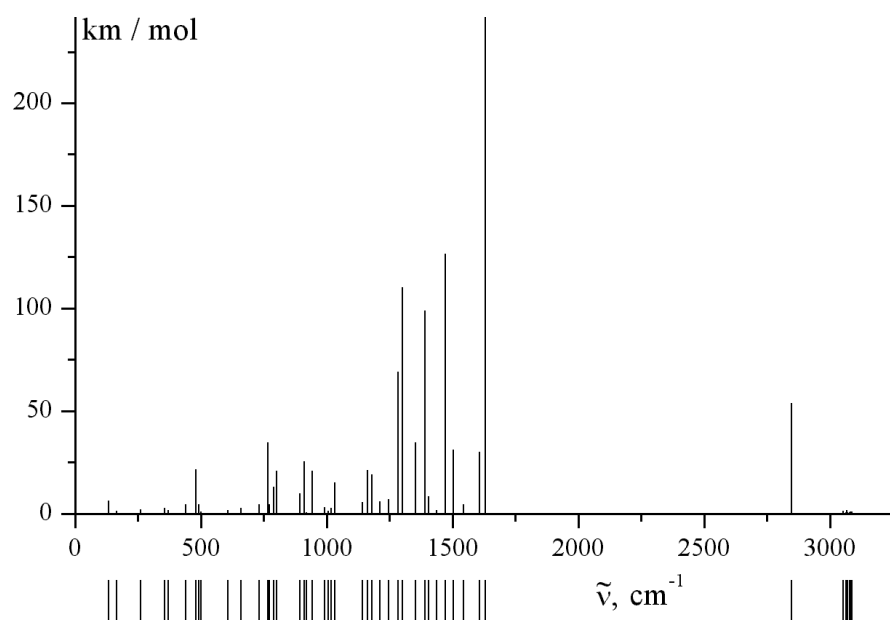


Figure A.5: Calculated protonated naphthalene 2-C₁₀H₉⁺ IR vibrational spectrum.

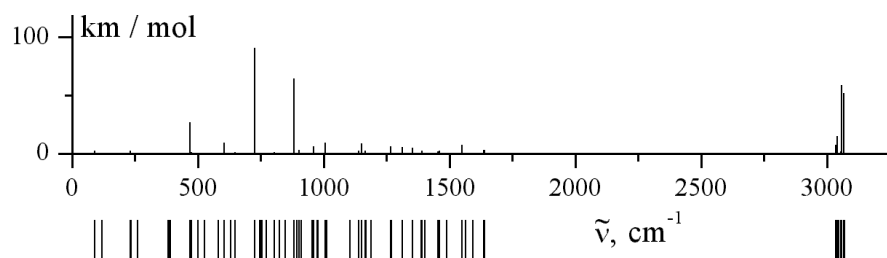


Figure A.6: Calculated anthracene $C_{14}H_{10}$ IR vibrational spectrum.

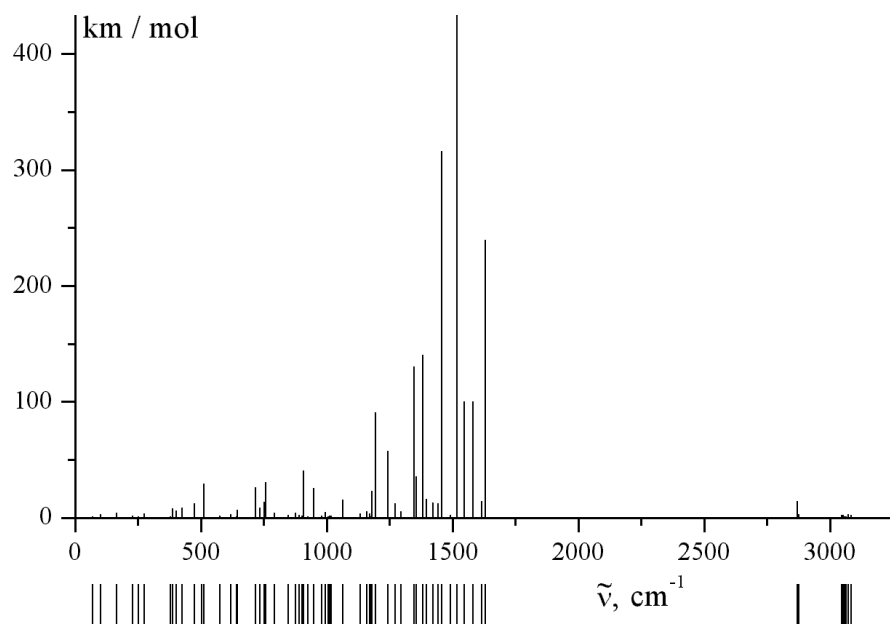


Figure A.7: Calculated protonated anthracene $1-C_{14}H_{11}^+$ IR vibrational spectrum.

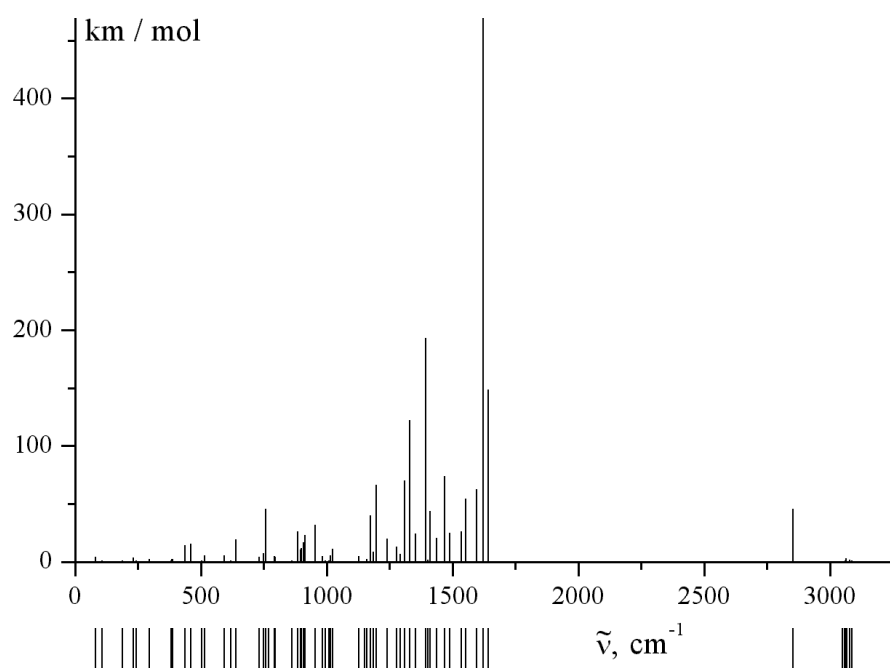


Figure A.8: Calculated protonated anthracene 2- $\text{C}_{14}\text{H}_{11}^+$ IR vibrational spectrum.

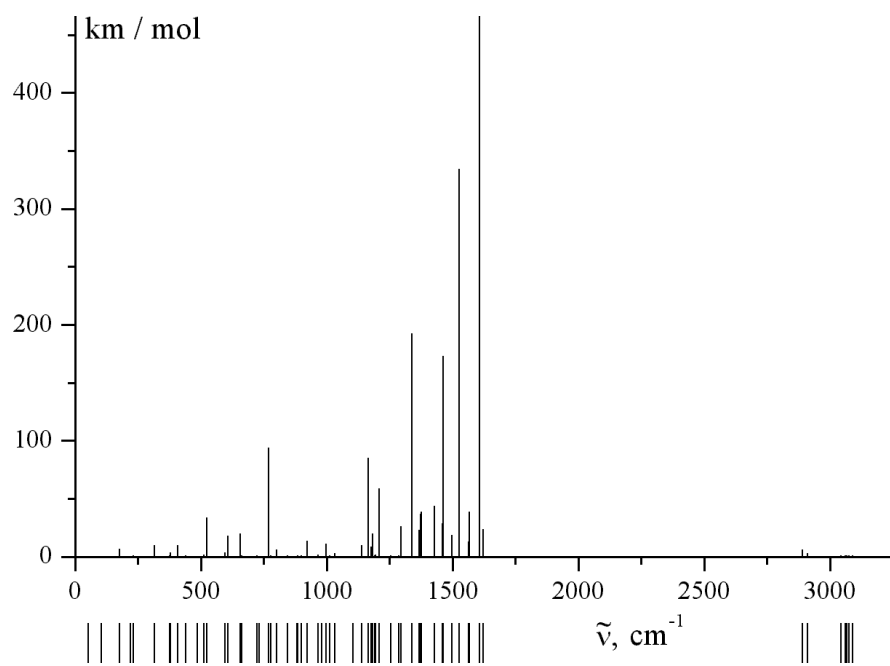


Figure A.9: Calculated protonated anthracene 9- $\text{C}_{14}\text{H}_{11}^+$ IR vibrational spectrum.

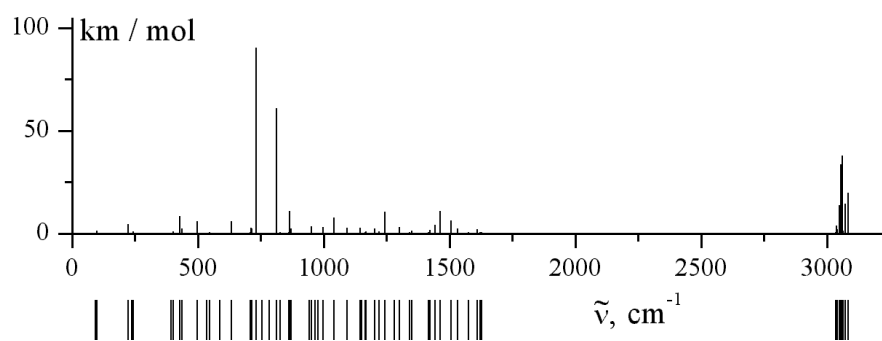


Figure A.10: Calculated phenanthrene $C_{14}H_{10}$ IR vibrational spectrum.

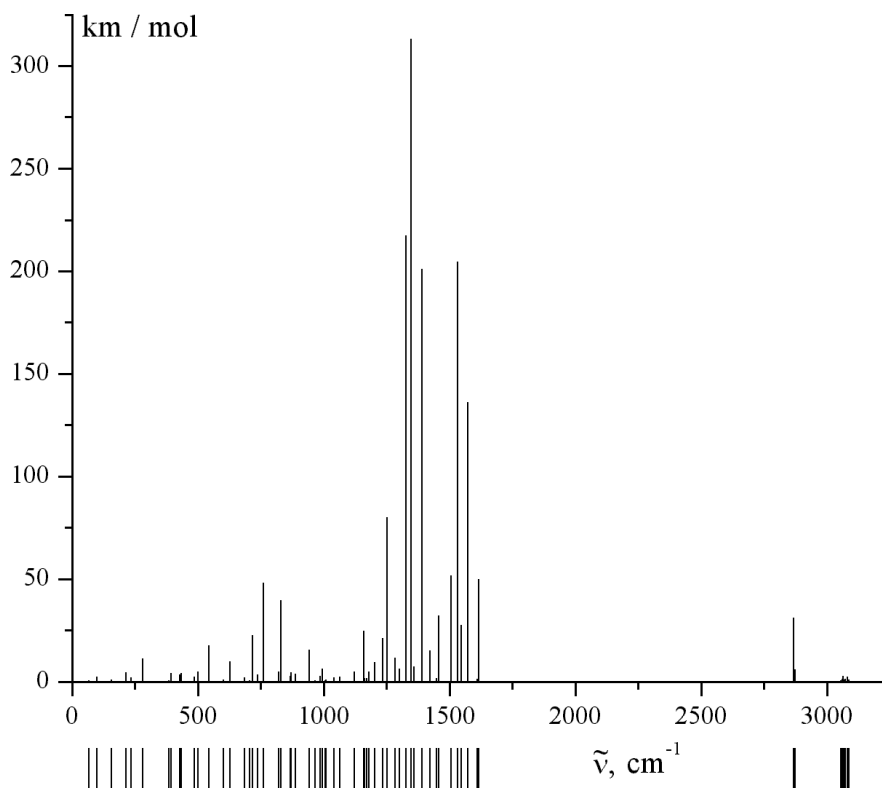


Figure A.11: Calculated protonated phenanthrene 1- $C_{14}H_{11}^+$ IR vibrational spectrum.

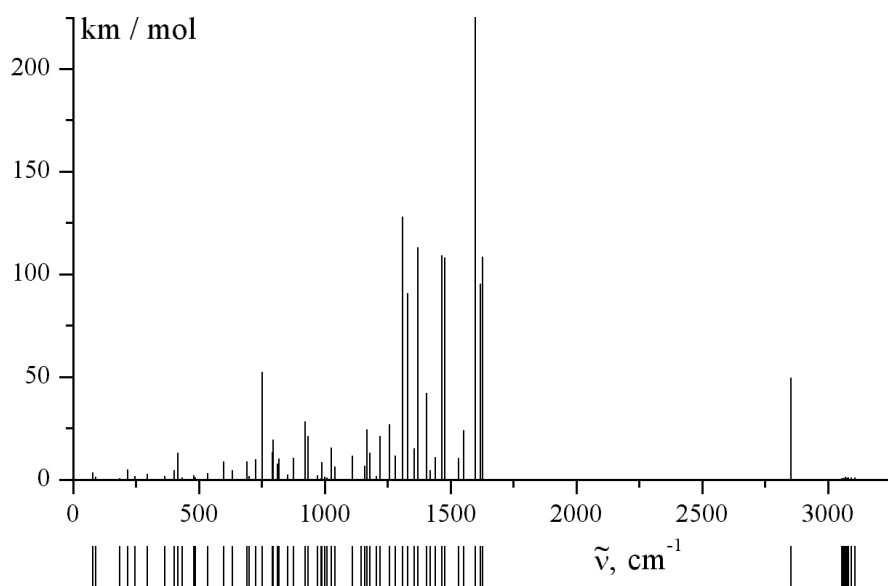


Figure A.12: Calculated protonated phenanthrene 2-C₁₄H₁₁⁺ IR vibrational spectrum.

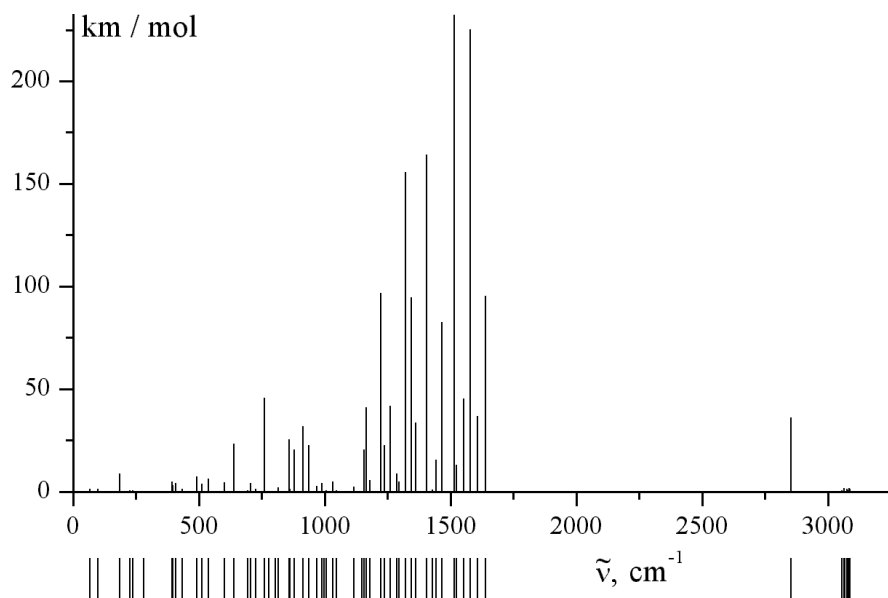


Figure A.13: Calculated protonated phenanthrene 3-C₁₄H₁₁⁺ IR vibrational spectrum.

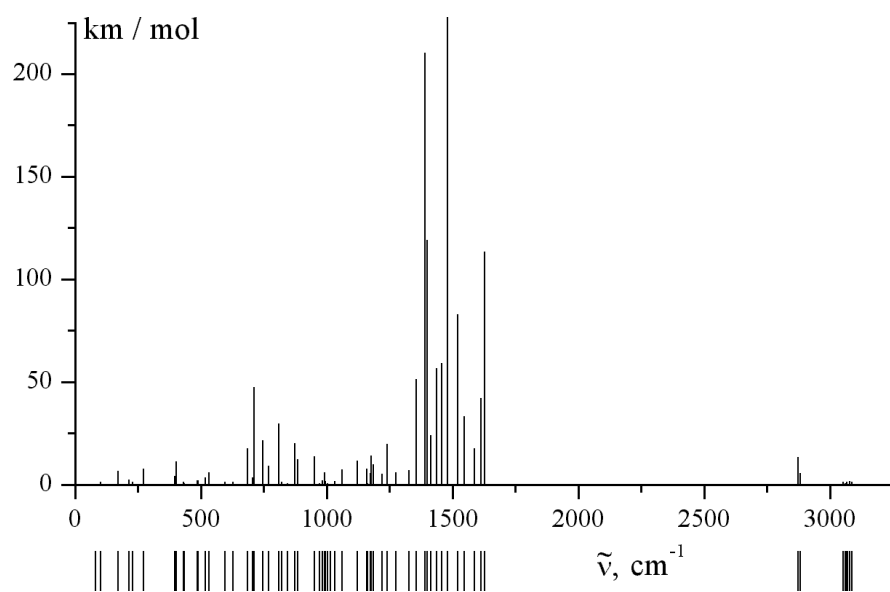


Figure A.14: Calculated protonated phenanthrene 4- $\text{C}_{14}\text{H}_{11}^+$ IR vibrational spectrum.

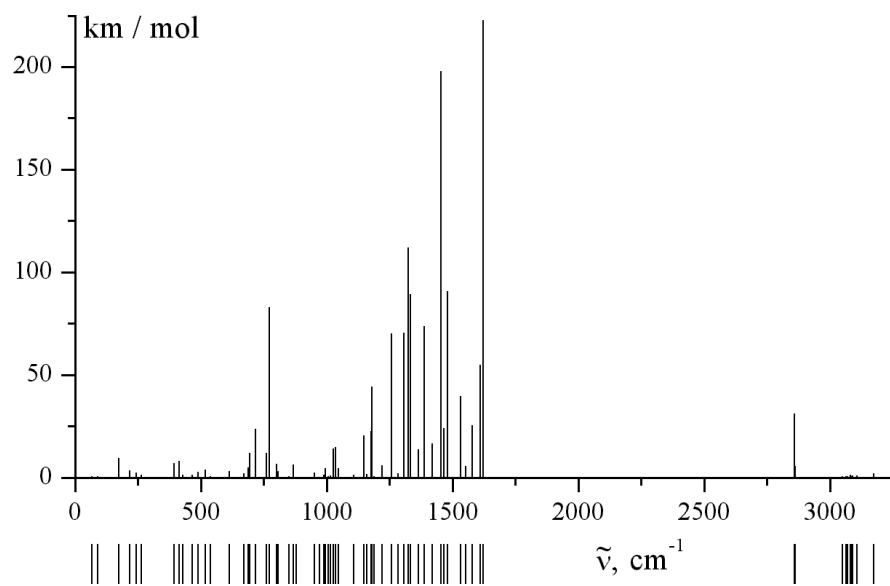


Figure A.15: Calculated protonated phenanthrene 9- $\text{C}_{14}\text{H}_{11}^+$ IR vibrational spectrum.

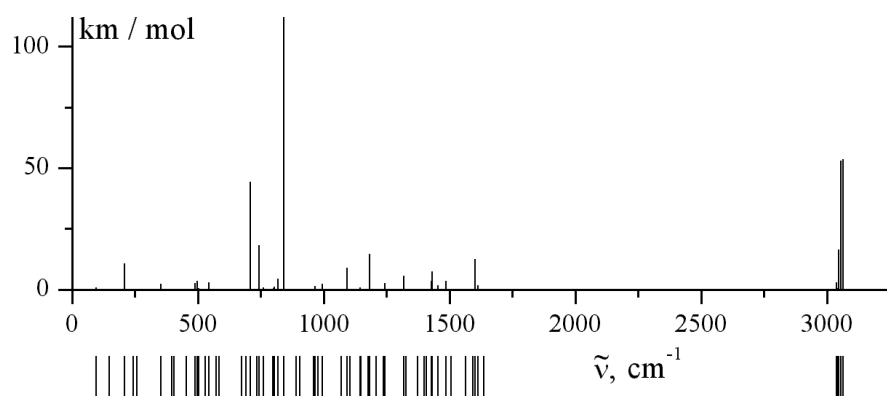


Figure A.16: Calculated pyrene $C_{16}H_{10}$ IR vibrational spectrum.

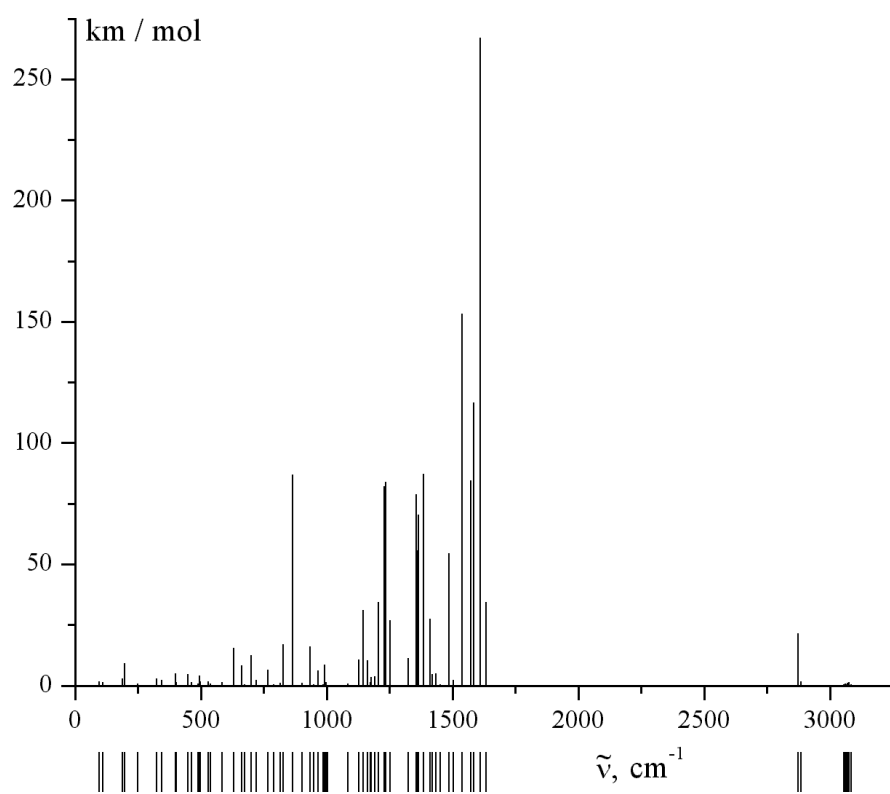


Figure A.17: Calculated protonated pyrene 1- $C_{16}H_{11}^+$ IR vibrational spectrum.

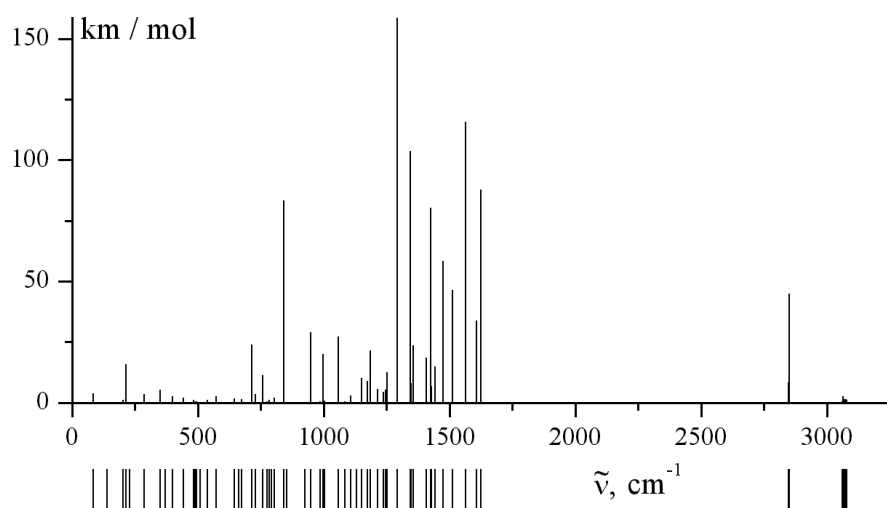


Figure A.18: Calculated protonated pyrene 2- $\text{C}_{16}\text{H}_{11}^+$ IR vibrational spectrum.

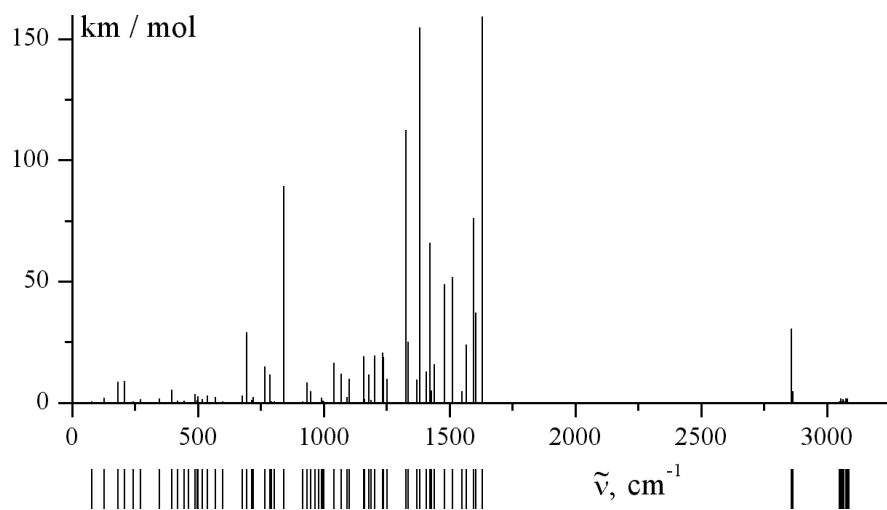


Figure A.19: Calculated protonated pyrene 4- $\text{C}_{16}\text{H}_{11}^+$ IR vibrational spectrum.

A.4 Energy Landscapes for Protonated PAHs

Table A.28: Protonated benzene energy landscape.

| | Energy (kcal/mol) | Description |
|---------------------------------------|----------------------|--|
| C_6H_7^+ | -63.22 | Stable isomer |
| 1-2 C_6H_7^+ | -51.90 | 1-2 isomerization transition state |
| $\text{C}_6\text{H}_5^+ + \text{H}_2$ | 0.00 | Dissociation via H_2 loss from CH_2 site |
| $\text{C}_6\text{H}_6^+ + \text{H}$ | 12.63 | Dissociation via H loss from CH_2 site |
| $\text{C}_6\text{H}_5^+ + 2\text{H}$ | 103.55 | Dissociation via 2 H atoms loss, one from CH_2 site |
| $\text{C}_6\text{H}_6 + \text{H}^+$ | 118.97 | Dissociation via H^+ loss from CH_2 site |

Table A.29: Protonated naphthalene energy landscape.

| | Energy (kcal/mol) | Description |
|---|----------------------|--|
| 1- $\text{C}_{10}\text{H}_9^+$ | -62.41 | Stable isomer (C 1) |
| 2- $\text{C}_{10}\text{H}_9^+$ | -59.51 | Stable isomer (C 2) |
| 9- $\text{C}_{10}\text{H}_9^+$ | -43.47 | Unstable isomer (C 9) |
| 1-2 $\text{C}_{10}\text{H}_9^+$ | -47.35 | 1-2 isomerization transition state |
| 2-3 $\text{C}_{10}\text{H}_9^+$ | -42.43 | 2-3 isomerization transition state |
| 1-9 $\text{C}_{10}\text{H}_9^+$ | -38.78 | 1-9 isomerization transition state |
| 9-10 $\text{C}_{10}\text{H}_9^+$ | -35.79 | 9-10 isomerization transition state |
| $\text{C}_{10}\text{H}_8^+ + \text{H}$ | 0.00 | Dissociation via H loss from CH_2 site |
| 1- $\text{C}_{10}\text{H}_7^+ + \text{H}_2$ | 7.28 | Dissociation via H_2 loss from CH_2 site (C 1) |
| 2- $\text{C}_{10}\text{H}_7^+ + \text{H}_2$ | 8.58 | Dissociation via H_2 loss from CH_2 site (C 2) |
| 1- $\text{C}_{10}\text{H}_7^+ + 2\text{H}$ | 110.84 | Dissociation via 2 H atoms loss, one from CH_2 site (C 1) |
| 2- $\text{C}_{10}\text{H}_7^+ + 2\text{H}$ | 112.14 | Dissociation via 2 H atoms loss, one from CH_2 site (C 2) |
| $\text{C}_{10}\text{H}_8 + \text{H}^+$ | 133.79 | Dissociation via H^+ loss from CH_2 site |
| 2→1 $\text{C}_{10}\text{H}_8^+ + \text{H}$ | 48.34 | Dissociation via H loss from C 2 in isomer 1 |
| 3→1 $\text{C}_{10}\text{H}_8^+ + \text{H}$ | 50.23 | Dissociation via H loss from C 3 in isomer 1 |
| 4→1 $\text{C}_{10}\text{H}_8^+ + \text{H}$ | 47.75 | Dissociation via H loss from C 4 in isomer 1 |
| 5→1 $\text{C}_{10}\text{H}_8^+ + \text{H}$ | 49.53 | Dissociation via H loss from C 5 in isomer 1 |
| 6→1 $\text{C}_{10}\text{H}_8^+ + \text{H}$ | 49.97 | Dissociation via H loss from C 6 in isomer 1 |
| 7→1 $\text{C}_{10}\text{H}_8^+ + \text{H}$ | 48.78 | Dissociation via H loss from C 7 in isomer 1 |
| 8→1 $\text{C}_{10}\text{H}_8^+ + \text{H}$ | 49.17 | Dissociation via H loss from C 8 in isomer 1 |
| 1→2 $\text{C}_{10}\text{H}_8^+ + \text{H}$ | 50.70 | Dissociation via H loss from C 1 in isomer 2 |
| 3→2 $\text{C}_{10}\text{H}_8^+ + \text{H}$ | 52.34 | Dissociation via H loss from C 3 in isomer 2 |
| 4→2 $\text{C}_{10}\text{H}_8^+ + \text{H}$ | 52.05 | Dissociation via H loss from C 4 in isomer 2 |
| 5→2 $\text{C}_{10}\text{H}_8^+ + \text{H}$ | 52.76 | Dissociation via H loss from C 5 in isomer 2 |
| 6→2 $\text{C}_{10}\text{H}_8^+ + \text{H}$ | 51.44 | Dissociation via H loss from C 6 in isomer 2 |
| 7→2 $\text{C}_{10}\text{H}_8^+ + \text{H}$ | 52.98 | Dissociation via H loss from C 7 in isomer 2 |
| 8→2 $\text{C}_{10}\text{H}_8^+ + \text{H}$ | 52.40 | Dissociation via H loss from C 8 in isomer 2 |

Table A.30: Protonated anthracene energy landscape.

| | Energy (kcal/mol) | Description |
|--|----------------------|--|
| 1-C ₁₄ H ₁₁ ⁺ | -52.41 | Stable isomer (C 1) |
| 2-C ₁₄ H ₁₁ ⁺ | -49.36 | Stable isomer (C 2) |
| 9-C ₁₄ H ₁₁ ⁺ | -61.06 | Stable isomer (C 9) |
| 11-C ₁₄ H ₁₁ ⁺ | -31.70 | Unstable isomer (C 11) |
| 1-2 C ₁₄ H ₁₁ ⁺ | -34.87 | 1-2 isomerization transition state |
| 2-3 C ₁₄ H ₁₁ ⁺ | -28.16 | 2-3 isomerization transition state |
| 1-11 C ₁₄ H ₁₁ ⁺ | -24.57 | 1-11 isomerization transition state |
| 9-11 C ₁₄ H ₁₁ ⁺ | -29.33 | 9-11 isomerization transition state |
| 11-12 C ₁₄ H ₁₁ ⁺ | -21.23 | 11-12 isomerization transition state |
| C ₁₄ H ₁₀ ⁺ + H | 0.00 | Dissociation via H loss from CH ₂ site |
| 1-C ₁₄ H ₉ ⁺ + H ₂ | 19.17 | Dissociation via H ₂ loss from CH ₂ site (C 1) |
| 2-C ₁₄ H ₉ ⁺ + H ₂ | 18.58 | Dissociation via H ₂ loss from CH ₂ site (C 2) |
| 9-C ₁₄ H ₉ ⁺ + H ₂ | 19.67 | Dissociation via H ₂ loss from CH ₂ site (C 9) |
| 1-C ₁₄ H ₉ ⁺ + 2H | 122.73 | Dissociation via 2 H atoms loss, one from CH ₂ site (C 1) |
| 2-C ₁₄ H ₉ ⁺ + 2H | 122.14 | Dissociation via 2 H atoms loss, one from CH ₂ site (C 2) |
| 9-C ₁₄ H ₉ ⁺ + 2H | 123.23 | Dissociation via 2 H atoms loss, one from CH ₂ site (C 9) |
| C ₁₄ H ₁₀ + H ⁺ | 151.44 | Dissociation via H ⁺ loss from CH ₂ site |

Table A.31: Protonated phenanthrene energy landscape.

| | Energy (kcal/mol) | Description |
|--|----------------------|--|
| 1-C ₁₄ H ₁₁ ⁺ | -59.53 | Stable isomer (C 1) |
| 2-C ₁₄ H ₁₁ ⁺ | -57.53 | Stable isomer (C 2) |
| 3-C ₁₄ H ₁₁ ⁺ | -58.98 | Stable isomer (C 3) |
| 4-C ₁₄ H ₁₁ ⁺ | -58.46 | Stable isomer (C 4) |
| 9-C ₁₄ H ₁₁ ⁺ | -59.33 | Stable isomer (C 9) |
| C ₁₄ H ₁₀ ⁺ + H | 0.00 | Dissociation via H loss from CH ₂ site |
| C ₁₄ H ₁₀ + H ⁺ | 140.27 | Dissociation via H ⁺ loss from CH ₂ site |

Table A.32: Protonated pyrene energy landscape.

| | Energy (kcal/mol) | Description |
|--|----------------------|--|
| 1-C ₁₆ H ₁₁ ⁺ | -60.78 | Stable isomer (C 1) |
| 2-C ₁₆ H ₁₁ ⁺ | -46.57 | Stable isomer (C 2) |
| 4-C ₁₆ H ₁₁ ⁺ | -50.52 | Stable isomer (C 4) |
| C ₁₆ H ₁₀ ⁺ + H | 0.00 | Dissociation via H loss from CH ₂ site |
| C ₁₆ H ₁₀ + H ⁺ | 150.46 | Dissociation via H ⁺ loss from CH ₂ site |

A.5 Energy Landscapes for Hydrogenated PAHs

Table A.33: Hydrogenated benzene energy landscape.

| | Energy (kcal/mol) | Description |
|---------------------------------------|----------------------|--|
| C_6H_7 | -22.53 | Stable isomer |
| C_6H_7 fr | -19.68 | Stable isomer, frozen C_6H_7^+ geometry |
| $\text{C}_6\text{H}_6 + \text{H}$ | 0.00 | Dissociation via H loss from CH_2 site |
| $\text{C}_6\text{H}_5 + \text{H}_2$ | 5.57 | Dissociation via H_2 loss from CH_2 site |
| $\text{C}_6\text{H}_5 + 2\text{H}$ | 109.12 | Dissociation via 2 H atoms loss, one from CH_2 site |
| $\text{C}_6\text{H}_7^+ + \text{e}^-$ | 132.99 | Ionization |

Table A.34: Hydrogenated naphthalene energy landscape.

| | Energy (kcal/mol) | Description |
|--|----------------------|--|
| $1\text{-C}_{10}\text{H}_9$ | -30.26 | Stable isomer (C 1) |
| $2\text{-C}_{10}\text{H}_9$ | -25.49 | Stable isomer (C 2) |
| $1\text{-C}_{10}\text{H}_9$ fr | -27.31 | Stable isomer (C 1), frozen $1\text{-C}_{10}\text{H}_9^+$ geometry |
| $2\text{-C}_{10}\text{H}_9$ fr | -22.45 | Stable isomer (C 2), frozen $2\text{-C}_{10}\text{H}_9^+$ geometry |
| $\text{C}_{10}\text{H}_8 + \text{H}$ | 0.00 | Dissociation via H loss from CH_2 site |
| $1\text{-C}_{10}\text{H}_7 + \text{H}_2$ | 5.69 | Dissociation via H_2 loss from CH_2 site (C 1) |
| $2\text{-C}_{10}\text{H}_7 + \text{H}_2$ | 5.65 | Dissociation via H_2 loss from CH_2 site (C 2) |
| $1\text{-C}_{10}\text{H}_7 + 2\text{H}$ | 109.25 | Dissociation via 2 H atoms loss, one from CH_2 site (C 1) |
| $2\text{-C}_{10}\text{H}_7 + 2\text{H}$ | 109.21 | Dissociation via 2 H atoms loss, one from CH_2 site (C 2) |
| $1\text{-C}_{10}\text{H}_9^+ + \text{e}^-$ | 118.97 | Ionization (C 1) |
| $2\text{-C}_{10}\text{H}_9^+ + \text{e}^-$ | 121.87 | Ionization (C 2) |

Table A.35: Hydrogenated anthracene energy landscape.

| | Energy (kcal/mol) | Description |
|---|----------------------|---|
| 1-C ₁₄ H ₁₁ | -34.13 | Stable isomer (C 1) |
| 2-C ₁₄ H ₁₁ | -29.91 | Stable isomer (C 2) |
| 9-C ₁₄ H ₁₁ | -40.63 | Stable isomer (C 9) |
| 1-C ₁₄ H ₁₁ fr | -31.00 | Stable isomer (C 1), frozen 1-C ₁₄ H ₁₁ ⁺ geometry |
| 2-C ₁₄ H ₁₁ fr | -26.67 | Stable isomer (C 2), frozen 2-C ₁₄ H ₁₁ ⁺ geometry |
| 9-C ₁₄ H ₁₁ fr | -38.04 | Stable isomer (C 9), frozen 9-C ₁₄ H ₁₁ ⁺ geometry |
| C ₁₄ H ₁₀ + H | 0.00 | Dissociation via H loss from CH ₂ site |
| 1-C ₁₄ H ₉ + H ₂ | 5.66 | Dissociation via H ₂ loss from CH ₂ site (C 1) |
| 2-C ₁₄ H ₉ + H ₂ | 5.65 | Dissociation via H ₂ loss from CH ₂ site (C 2) |
| 9-C ₁₄ H ₉ + H ₂ | 5.93 | Dissociation via H ₂ loss from CH ₂ site (C 9) |
| 1-C ₁₄ H ₉ + 2H | 109.22 | Dissociation via 2 H atoms loss, one from CH ₂ site (C 1) |
| 2-C ₁₄ H ₉ + 2H | 109.21 | Dissociation via 2 H atoms loss, one from CH ₂ site (C 2) |
| 9-C ₁₄ H ₉ + 2H | 109.49 | Dissociation via 2 H atoms loss, one from CH ₂ site (C 9) |
| 1-C ₁₄ H ₁₁ ⁺ + e ⁻ | 111.33 | Ionization (C 1) |
| 2-C ₁₄ H ₁₁ ⁺ + e ⁻ | 114.37 | Ionization (C 2) |
| 9-C ₁₄ H ₁₁ ⁺ + e ⁻ | 102.68 | Ionization (C 9) |

A.6 Ionization Energies

Table A.36: Ionization energies for PAHs, hydrogenated and dehydrogenated PAHs.

| Molecule | Calculated (eV) | Experimental (eV) |
|------------------------------|-----------------|-------------------|
| C_6H_6 | 9.0562 | 9.24378 |
| $C_{10}H_8$ | 7.8655 | 8.1442 |
| $C_{14}H_{10}$ anthracene | 7.1002 | 7.4233 |
| $C_{14}H_{10}$ phenanthrene | 7.5845 | 7.891 |
| $C_{16}H_{10}$ pyrene | 7.1427 | 7.426 |
| Hydrogenated | | |
| C_6H_7 | 6.7439 | |
| 1- $C_{10}H_9$ | 6.4713 | |
| 2- $C_{10}H_9$ | 6.3900 | |
| 1- $C_{14}H_{11}$ anthracene | 6.3078 | |
| 2- $C_{14}H_{11}$ anthracene | 6.2568 | |
| 9- $C_{14}H_{11}$ anthracene | 6.2144 | |
| Dehydrogenated | | |
| C_6H_5 | 8.2670 | |
| 1- $C_{10}H_7$ | 7.9347 | |
| 2- $C_{10}H_7$ | 7.9927 | |
| 1- $C_{14}H_9$ anthracene | 7.6861 | |
| 2- $C_{14}H_9$ anthracene | 7.6607 | |
| 9- $C_{14}H_9$ anthracene | 7.6960 | |

A.7 Excited States

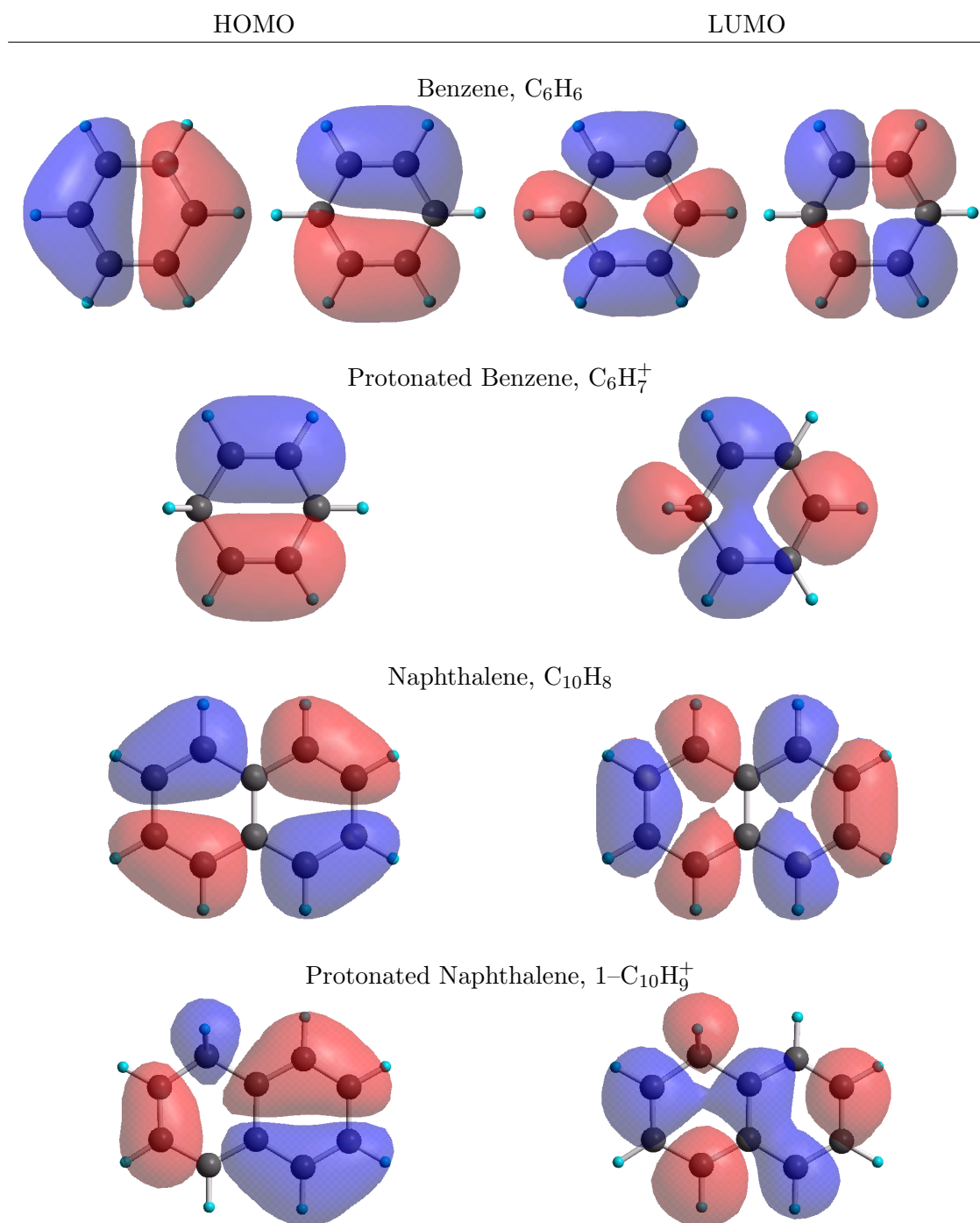
Table A.37: Calculated first singlet excited states of neutral and protonated PAHs. S_1 state energies, $S_1 \leftarrow S_0$ wavelengths, red shifts, oscillator strengths.

| Molecule | S_1 (eV) | $S_1 \leftarrow S_0$ wavelength (nm) | | | Red shift (nm) | Oscillator strength |
|---------------------|------------|--------------------------------------|---------------|-----------------|-------------------|------------------------|
| | Calculated | Scaled | Scaled range | | | |
| Benzene | | | | | | |
| C_6H_6 | 6.0122 | 206.22 | 262.56 | | | 0.0000 |
| $C_6H_7^+$ | 4.5130 | 274.72 | 349.77 | 323.20 – 366.29 | 87.21 | 0.1737 |
| Naphthalene | | | | | | |
| $C_{10}H_8$ | 5.0429 | 243.98 | 312.30 | | | 0.0825 |
| 1- $C_{10}H_9^+$ | 4.1253 | 298.84 | 382.53 | 351.58 – 398.45 | 70.22 | 0.4090 |
| 2- $C_{10}H_9^+$ | 3.5890 | 342.88 | 438.90 | 403.39 – 457.17 | 126.60 | 0.1714 |
| Anthracene | | | | | | |
| $C_{14}H_{10}$ | 4.0598 | 305.39 | 361.17 | | | 0.1399 |
| 1- $C_{14}H_{11}^+$ | 3.3092 | 374.66 | 443.09 | 440.78 – 499.55 | 81.92 | 0.3459 |
| 2- $C_{14}H_{11}^+$ | 2.9899 | 414.67 | 490.41 | 487.85 – 552.89 | 129.24 | 0.1862 |
| 9- $C_{14}H_{11}^+$ | 3.8949 | 318.33 | 376.47 | 374.51 – 424.44 | 15.30 | 0.7120 |
| Phenanthrene | | | | | | |
| $C_{14}H_{10}$ | 4.8007 | 258.26 | 340.99 | | | 0.0318 |
| 1- $C_{14}H_{11}^+$ | 3.4305 | 361.42 | 477.20 | 425.20 – 481.89 | 136.21 | 0.4661 |
| 2- $C_{14}H_{11}^+$ | 3.2886 | 377.01 | 497.78 | 443.54 – 502.68 | 156.79 | 0.1205 |
| 3- $C_{14}H_{11}^+$ | 3.5525 | 349.01 | 460.81 | 410.60 – 465.35 | 119.82 | 0.3068 |
| 4- $C_{14}H_{11}^+$ | 3.3196 | 373.49 | 493.13 | 439.40 – 497.99 | 152.14 | 0.1984 |
| 9- $C_{14}H_{11}^+$ | 3.4149 | 363.06 | 479.36 | 427.13 – 484.08 | 138.37 | 0.2854 |
| Pyrene | | | | | | |
| $C_{16}H_{10}$ | 4.3936 | 282.19 | 367.43 | | | 0.3643 |
| 1- $C_{16}H_{11}^+$ | 3.6456 | 340.09 | 442.82 | 400.11 – 453.45 | 75.39 | 0.3338 |
| 2- $C_{16}H_{11}^+$ | 2.8356 | 437.23 | 569.30 | 514.39 – 582.97 | 201.87 | 0.1419 |
| 4- $C_{16}H_{11}^+$ | 3.2337 | 383.41 | 499.23 | 451.07 – 511.21 | 131.80 | 0.1464 |

Table A.38: Symmetry and S_0 , S_1 electronic states assignment for neutral and protonated PAHs.

| Molecule | Symm group | State Symbol | | Orbital Symmetry and Electronic Configuration. (x,y) = (2,0) for S_0 , (1,1) for S_1 |
|---------------------|------------|---------------------|---------------------|---|
| Benzene | | | | |
| C_6H_6 | D_{6h} | \tilde{X}^1A_{1g} | \tilde{A}^1E_{1u} | $(1a_{2u})^2(1e_{1g})^x(1e_{2u})^y(1b_{2g})^0$, here (x,y) = (4,0) for S_0 , (3,1) for S_1 |
| $C_6H_7^+$ | C_{2v} | \tilde{X}^1A_1 | \tilde{A}^1B_1 | $(1b_2)^2(2b_2)^2(1a_2)^x(3b_2)^y(2a_2)^0(4b_2)^0$ |
| Naphthalene | | | | |
| $C_{10}H_8$ | D_{2h} | \tilde{X}^1A_g | \tilde{A}^1B_{2u} | $(1b_{1u})^2(1b_{3g})^2(1b_{2g})^2(2b_{1u})^2(1a_u)^x(2b_{2g})^y(2b_{3g})^0(3b_{1u})^0(2a_u)^0(3b_{3g})^0$ |
| $1-C_{10}H_9^+$ | C_s | \tilde{X}^1A' | \tilde{A}^1A' | $(1a'')^2(2a'')^2(3a'')^2(4a'')^2(5a'')^x(6a'')^y(7a'')^0(8a'')^0(9a'')^0(10a'')^0$ |
| $2-C_{10}H_9^+$ | C_s | \tilde{X}^1A' | \tilde{A}^1A' | $(1a'')^2(2a'')^2(3a'')^2(4a'')^2(5a'')^x(6a'')^y(7a'')^0(8a'')^0(9a'')^0(10a'')^0$ |
| Anthracene | | | | |
| $C_{14}H_{10}$ | D_{2h} | \tilde{X}^1A_g | \tilde{A}^1B_{2u} | $(1b_{1u})^2(1b_{2g})^2(1b_{3g})^2(2b_{1u})^2(2b_{2g})^2(1a_u)^2(2b_{3g})^x(3b_{1u})^y(2a_u)^0(3b_{2g})^0(3b_{3g})^0(4b_{1u})^0(3a_u)^0 \dots$ |
| $1-C_{14}H_{11}^+$ | C_s | \tilde{X}^1A' | \tilde{A}^1A' | $(1a'')^2(2a'')^2(3a'')^2(4a'')^2(5a'')^2(6a'')^2(7a'')^x(8a'')^y(9a'')^0(10a'')^0(11a'')^0(12a'')^0(13a'')^0(14a'')^0$ |
| $2-C_{14}H_{11}^+$ | C_s | \tilde{X}^1A' | \tilde{A}^1A' | $(1a'')^2(2a'')^2(3a'')^2(4a'')^2(5a'')^2(6a'')^2(7a'')^x(8a'')^y(9a'')^0(10a'')^0(11a'')^0(12a'')^0(13a'')^0(14a'')^0$ |
| $9-C_{14}H_{11}^+$ | C_{2v} | \tilde{X}^1A_1 | \tilde{A}^1B_1 | $(1b_2)^2(2b_2)^2(1a_2)^2(3b_2)^2(2a_2)^2(4b_2)^2(3a_2)^x(5b_2)^y(4a_2)^0(6b_2)^0(5a_2)^0(7b_2)^0(6a_2)^0(8b_2)^0$ |
| Phenanthrene | | | | |
| $C_{14}H_{10}$ | C_{2v} | \tilde{X}^1A_1 | \tilde{A}^1B_1 | $(1b_2)^2(1a_2)^2(2b_2)^2(3b_2)^2(2a_2)^2(3a_2)^2(4b_2)^x(4a_2)^y(5b_2)^0(6b_2)^0(5a_2)^0(6a_2)^0(7b_2)^0(7a_2)^0$ |
| $1-C_{14}H_{11}^+$ | C_s | \tilde{X}^1A' | \tilde{A}^1A' | $(1a'')^2(2a'')^2(3a'')^2(4a'')^2(5a'')^2(6a'')^2(7a'')^x(8a'')^y(9a'')^0(10a'')^0(11a'')^0(12a'')^0(13a'')^0(14a'')^0$ |
| $2-C_{14}H_{11}^+$ | C_s | \tilde{X}^1A' | \tilde{A}^1A' | $(1a'')^2(2a'')^2(3a'')^2(4a'')^2(5a'')^2(6a'')^2(7a'')^x(8a'')^y(9a'')^0(10a'')^0(11a'')^0(12a'')^0(13a'')^0(14a'')^0$ |
| $3-C_{14}H_{11}^+$ | C_s | \tilde{X}^1A' | \tilde{A}^1A' | $(1a'')^2(2a'')^2(3a'')^2(4a'')^2(5a'')^2(6a'')^2(7a'')^x(8a'')^y(9a'')^0(10a'')^0(11a'')^0(12a'')^0(13a'')^0(14a'')^0$ |
| $4-C_{14}H_{11}^+$ | C_s | \tilde{X}^1A' | \tilde{A}^1A' | $(1a'')^2(2a'')^2(3a'')^2(4a'')^2(5a'')^2(6a'')^2(7a'')^x(8a'')^y(9a'')^0(10a'')^0(11a'')^0(12a'')^0(13a'')^0(14a'')^0$ |
| $9-C_{14}H_{11}^+$ | C_s | \tilde{X}^1A' | \tilde{A}^1A' | $(1a'')^2(2a'')^2(3a'')^2(4a'')^2(5a'')^2(6a'')^2(7a'')^x(8a'')^y(9a'')^0(10a'')^0(11a'')^0(12a'')^0(13a'')^0(14a'')^0$ |
| Pyrene | | | | |
| $C_{16}H_{10}$ | D_{2h} | \tilde{X}^1A_g | \tilde{A}^1B_{3u} | $(1b_{1u})^2(2b_{2g})^2(1b_{3g})^2(2b_{1u})^2(1a_u)^2(3b_{1u})^2(2b_{2g})^2(2b_{3g})^x(2a_u)^y(4b_{1u})^0(3b_{2g})^0(3b_{3g})^0(4b_{2g})^0 \dots$ |
| $1-C_{16}H_{11}^+$ | C_s | \tilde{X}^1A' | \tilde{A}^1A' | $(1a'')^2(2a'')^2(3a'')^2(4a'')^2(5a'')^2(6a'')^2(7a'')^2(8a'')^x(9a'')^y(10a'')^0(11a'')^0(12a'')^0(13a'')^0 \dots$ |
| $2-C_{16}H_{11}^+$ | C_{2v} | \tilde{X}^1A_1 | \tilde{A}^1B_1 | $(1b_2)^2(2b_2)^2(1a_2)^2(3b_2)^2(2a_2)^2(4b_2)^2(5b_2)^2(3a_2)^x(6b_2)^y(4a_2)^0(7b_2)^0(8b_2)^0(5a_2)^0(9b_2)^0(6a_2)^0 \dots$ |
| $4-C_{16}H_{11}^+$ | C_s | \tilde{X}^1A' | \tilde{A}^1A' | $(1a'')^2(2a'')^2(3a'')^2(4a'')^2(5a'')^2(6a'')^2(7a'')^2(8a'')^x(9a'')^y(10a'')^0(11a'')^0(12a'')^0(13a'')^0 \dots$ |

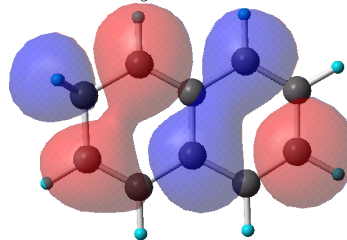
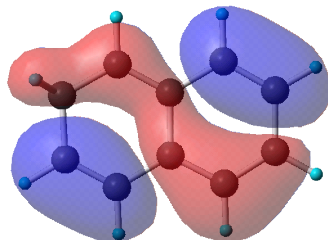
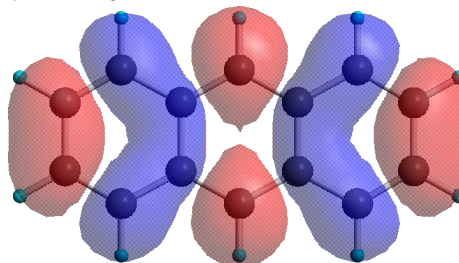
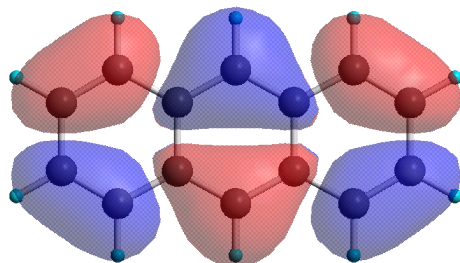
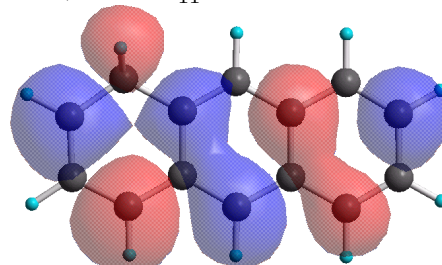
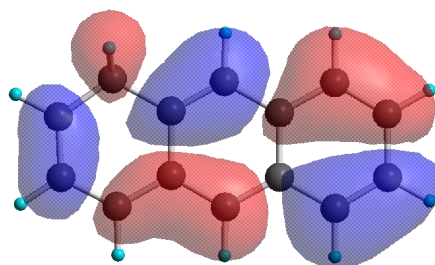
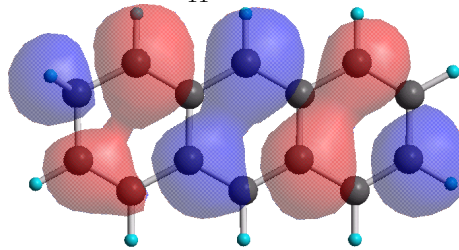
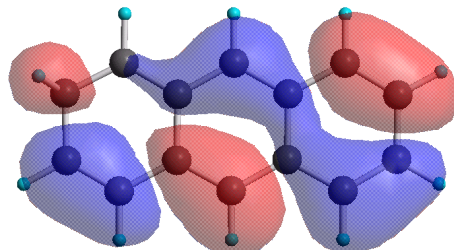
Table A.39: Highest occupied (HOMO) and lowest unoccupied (LUMO) molecular orbitals of neutral and protonated PAHs.



— continued on the next page —

HOMO

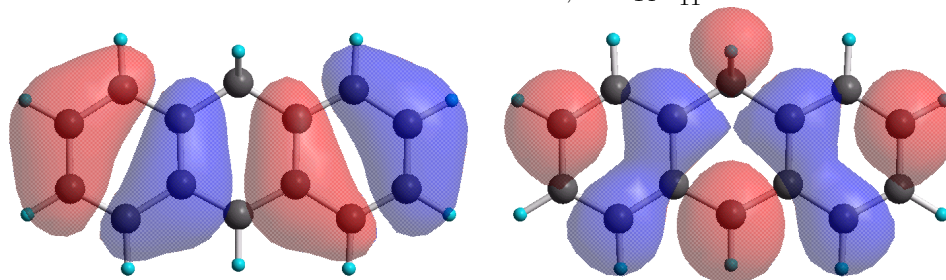
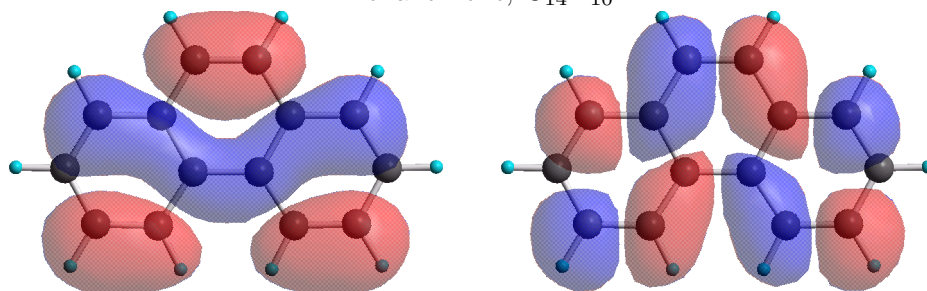
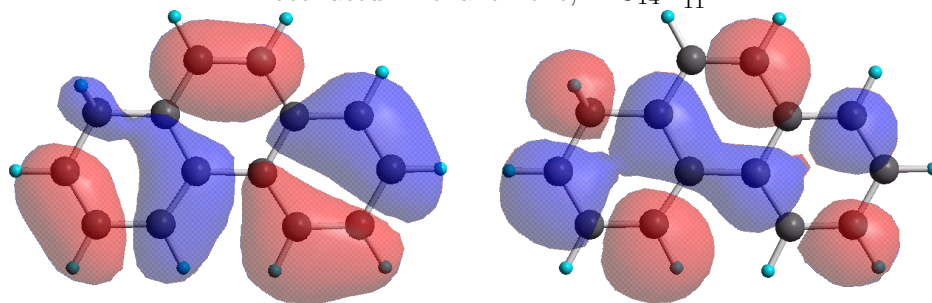
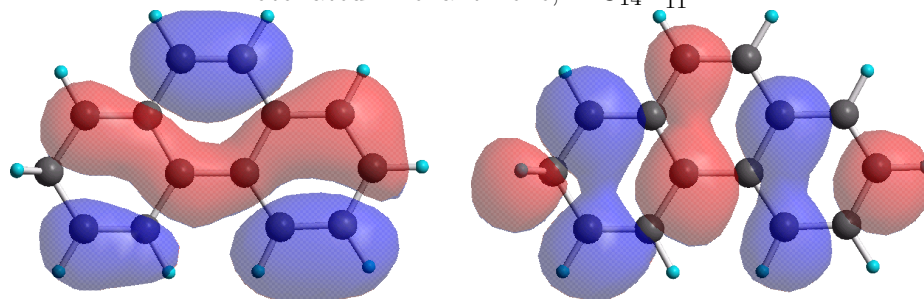
LUMO

Protonated Naphthalene, 2-C₁₀H₉⁺Anthracene, C₁₄H₁₀Protonated Anthracene, 1-C₁₄H₁₁⁺Protonated Anthracene, 2-C₁₄H₁₁⁺

— continued on the next page —

HOMO

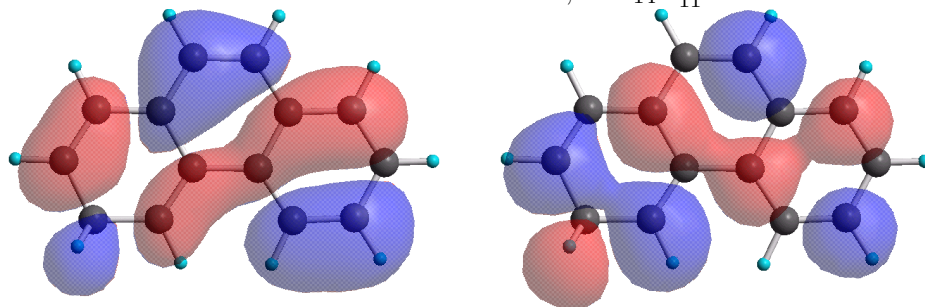
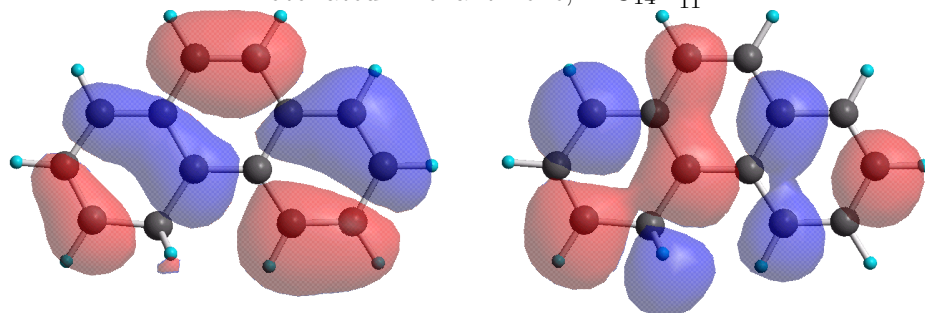
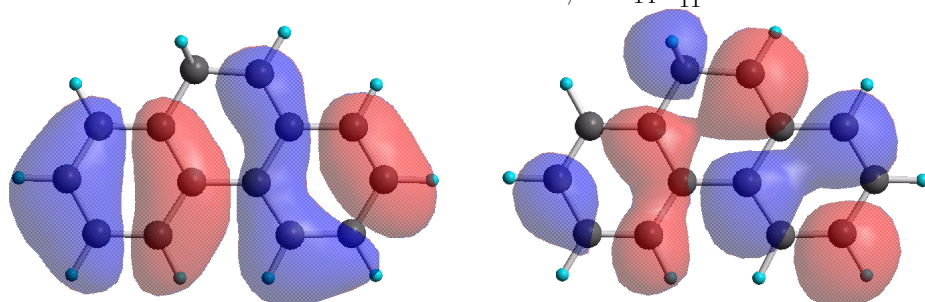
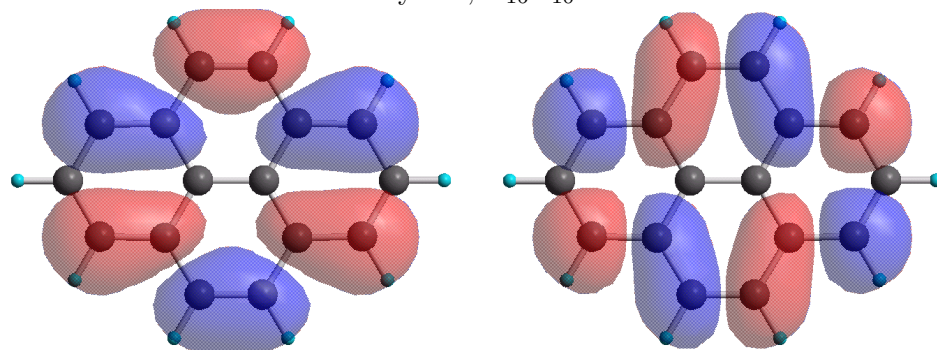
LUMO

Protonated Anthracene, $9\text{-C}_{14}\text{H}_{11}^+$ Phenanthrene, $\text{C}_{14}\text{H}_{10}$ Protonated Phenanthrene, $1\text{-C}_{14}\text{H}_{11}^+$ Protonated Phenanthrene, $2\text{-C}_{14}\text{H}_{11}^+$ 

— continued on the next page —

HOMO

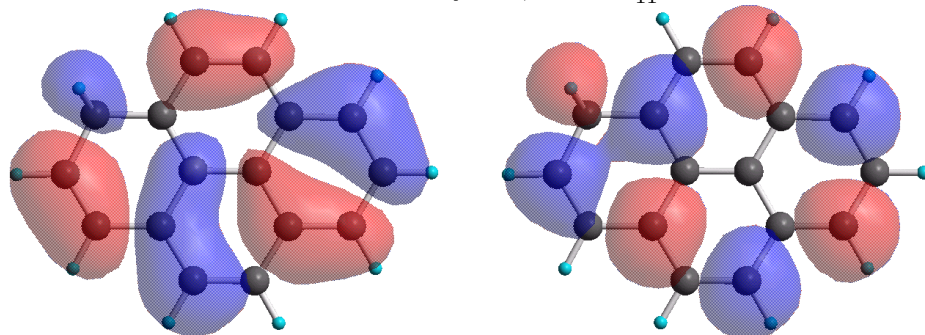
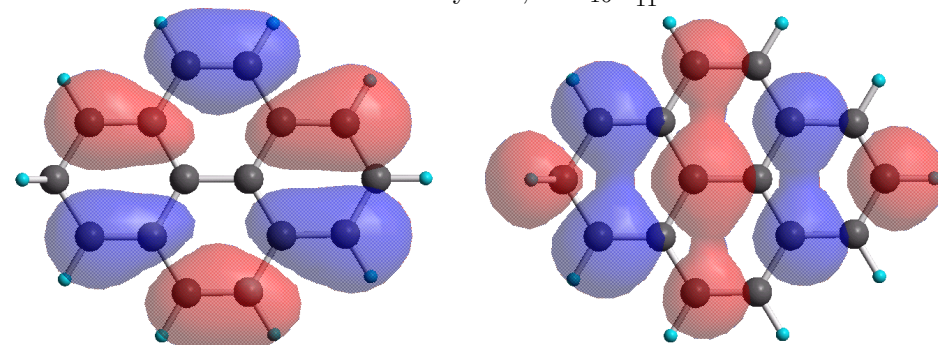
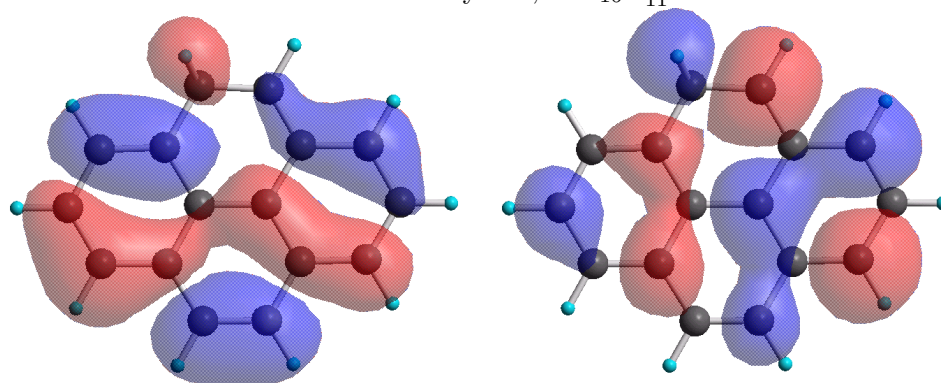
LUMO

Protonated Phenanthrene, 3- $\text{C}_{14}\text{H}_{11}^+$ Protonated Phenanthrene, 4- $\text{C}_{14}\text{H}_{11}^+$ Protonated Phenanthrene, 9- $\text{C}_{14}\text{H}_{11}^+$ Pyrene, $\text{C}_{16}\text{H}_{10}$ 

— continued on the next page —

HOMO

LUMO

Protonated Pyrene, 1-C₁₆H₁₁⁺Protonated Pyrene, 2-C₁₆H₁₁⁺Protonated Pyrene, 4-C₁₆H₁₁⁺

Appendix B

Experimental Setup Descriptions

B.1 Discharge

B.1.1 Pulsed Discharge Source

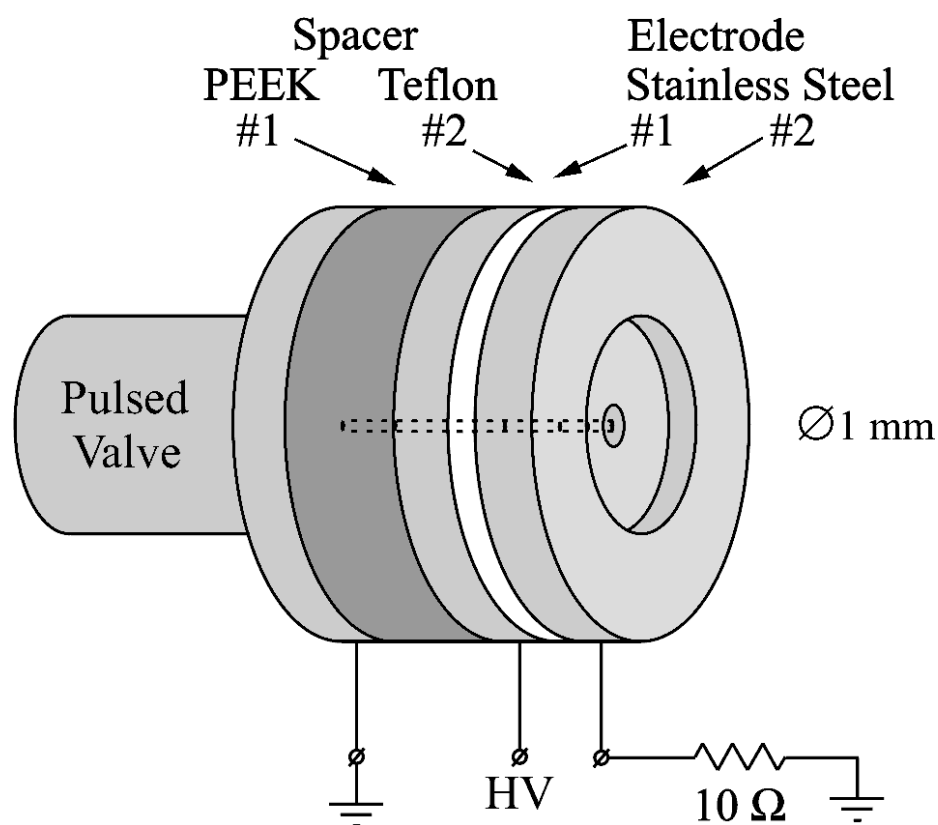


Figure B.1: Pulsed discharge source.

Electrode #2 (GND)

Material: Stainless Steel

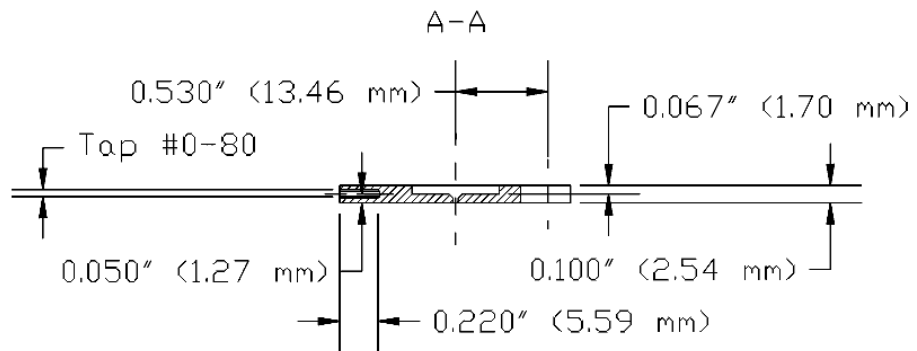
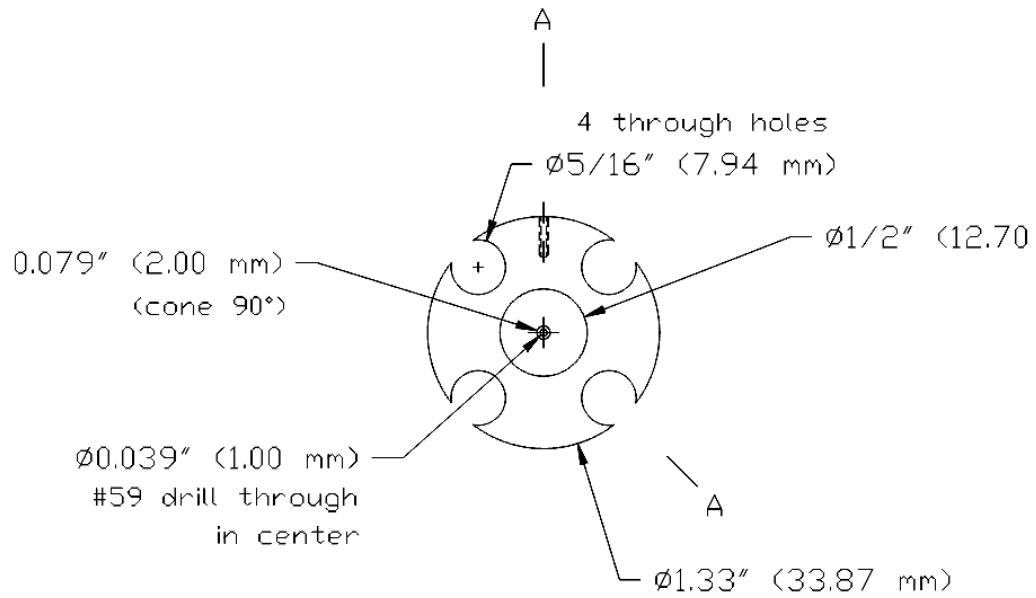


Figure B.2: Ground (outside) pulsed discharge electrode.

Electrode #1 (HV)

Material: Stainless Steel

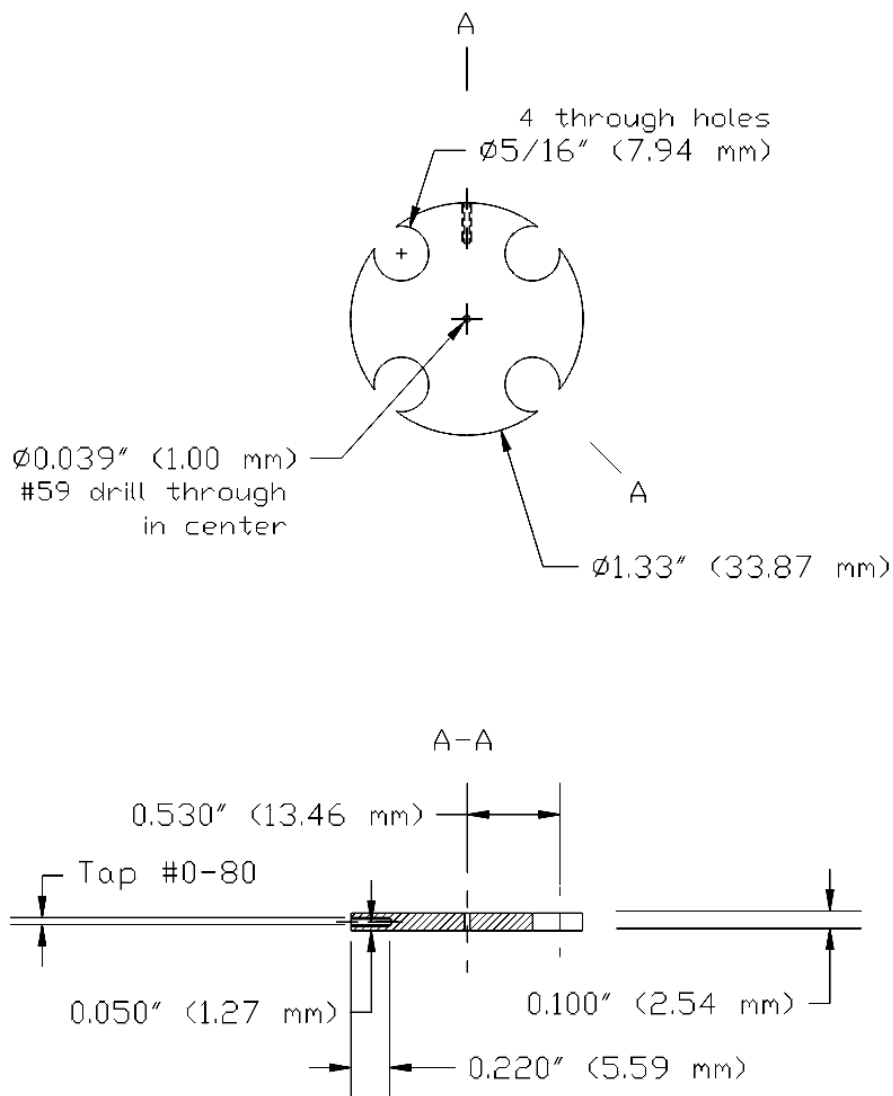


Figure B.3: High voltage (inside) pulsed discharge electrode.

Spacer #2

Material: Teflon

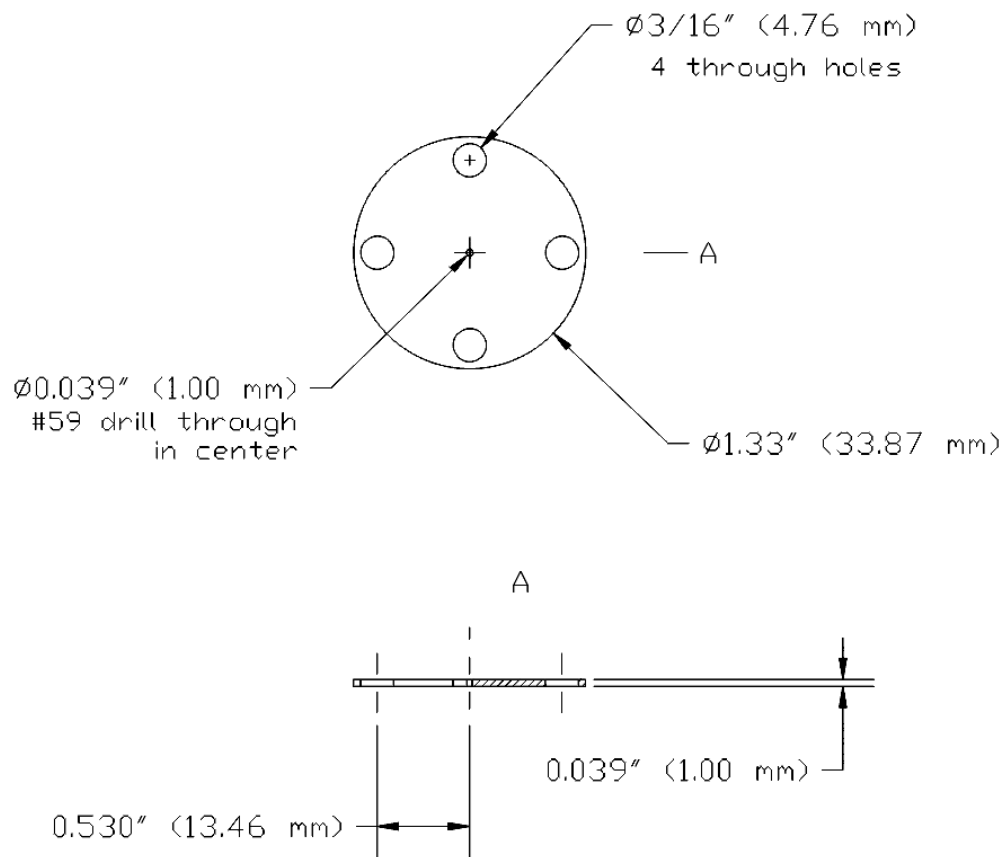


Figure B.4: Teflon insulating spacer between discharge electrodes.

Spacer #1

Material: PEEK

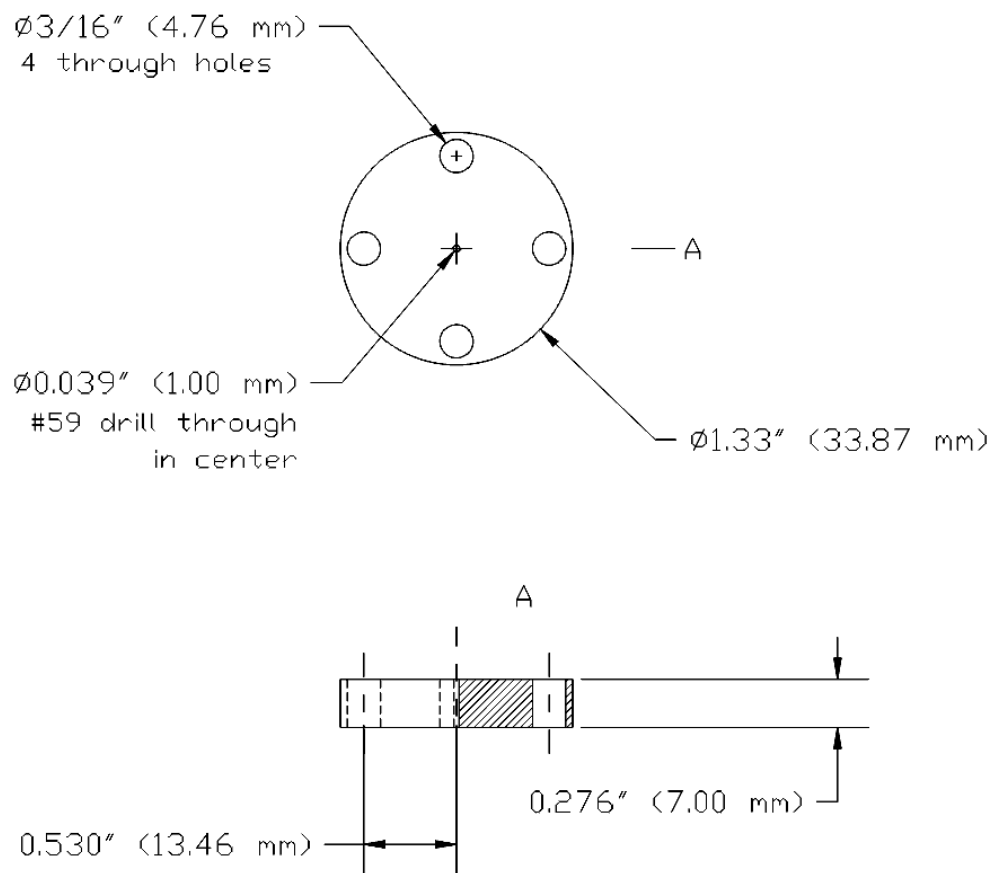


Figure B.5: PEEK insulating spacer between inside electrode and pulsed valve.

Insulating Insert

Material: Teflon

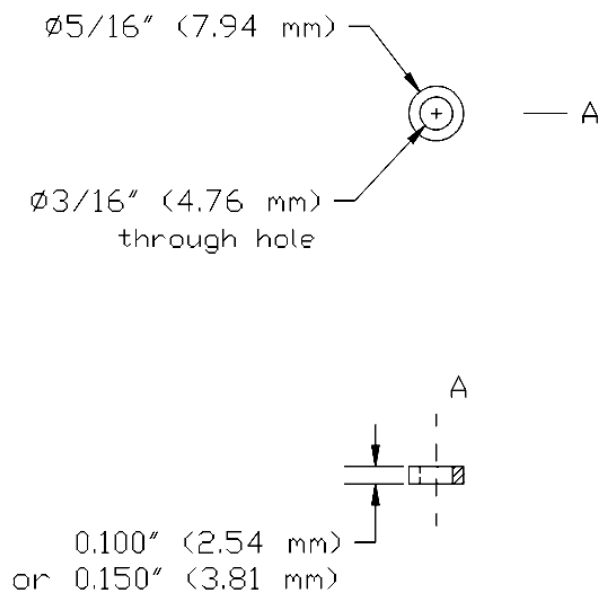


Figure B.6: Electrode inserts for screw insulation.

Screw Washer

Material: Teflon

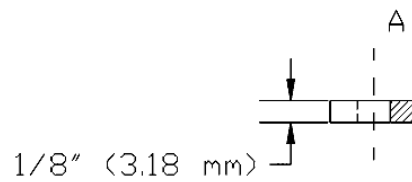
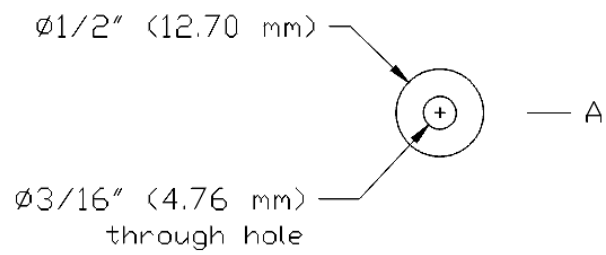


Figure B.7: Screw washer for insulation form outside electrode.

B.1.2 Pulsed Discharge Cluster Source

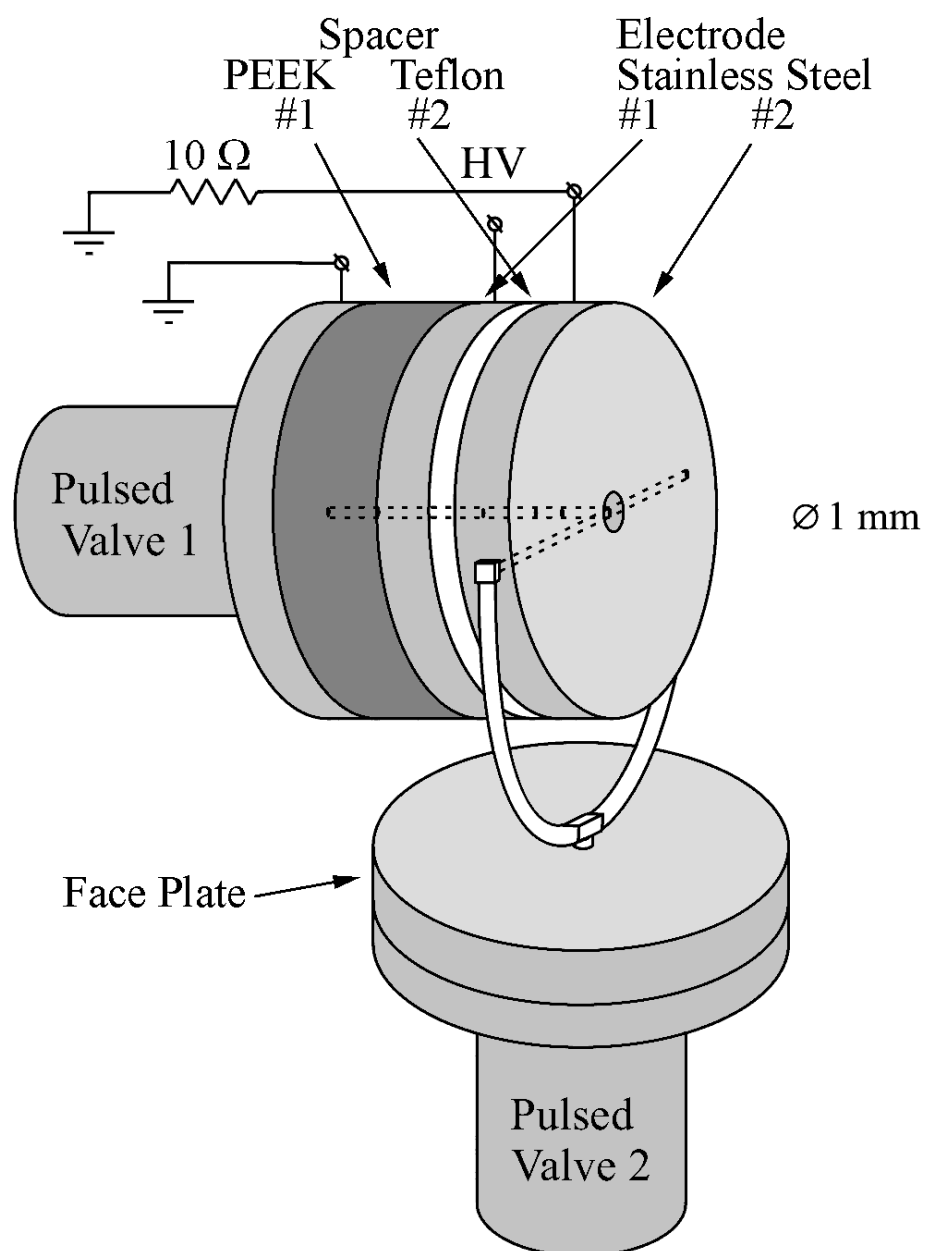


Figure B.8: Pulsed discharge cluster source with two pulsed valves.

Electrode #2 (GND)

Material: Stainless Steel

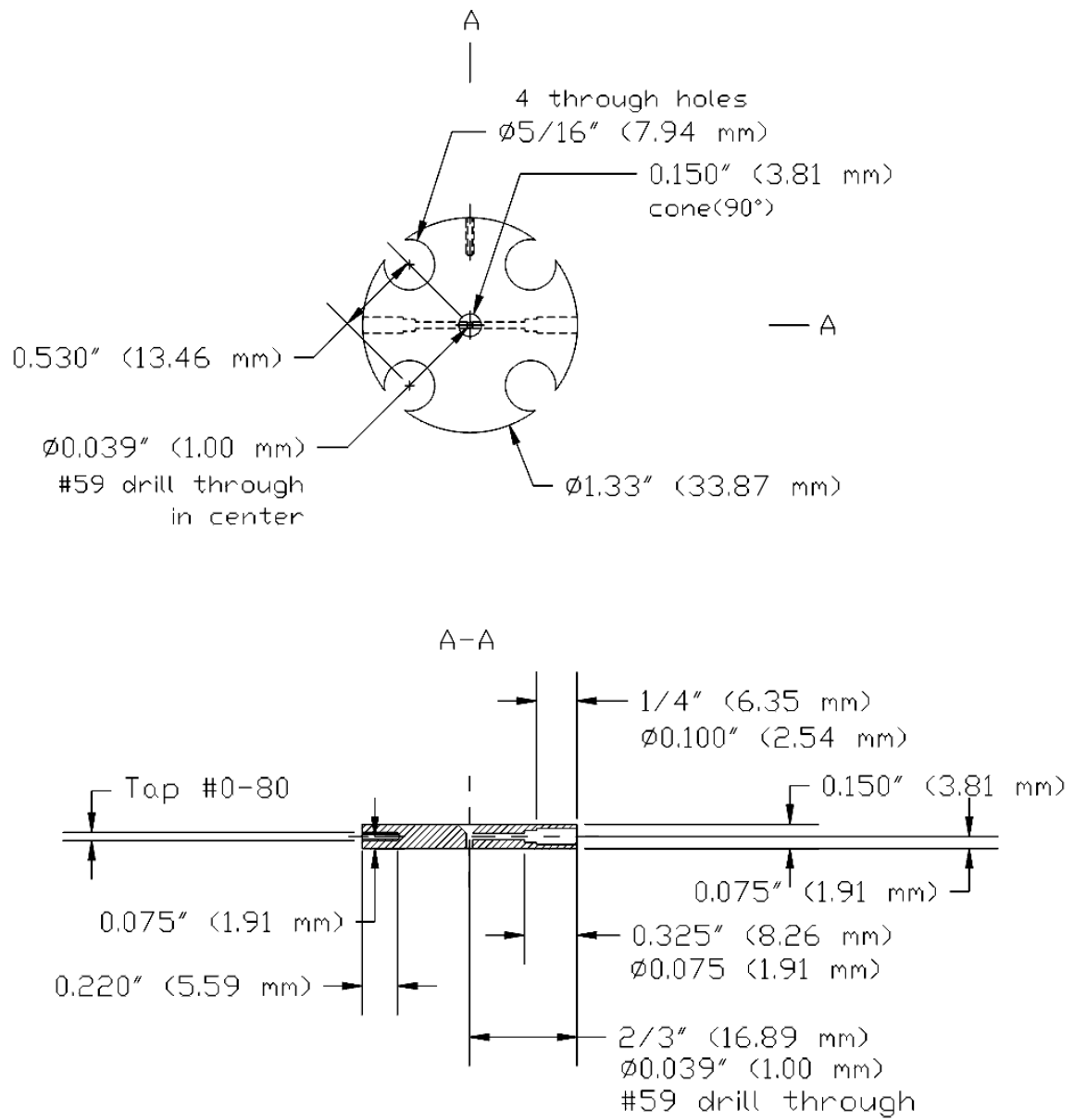


Figure B.9: Ground (outside) discharge electrode for cluster production.

Nozzle Face Plate

Material: Stainless Steel

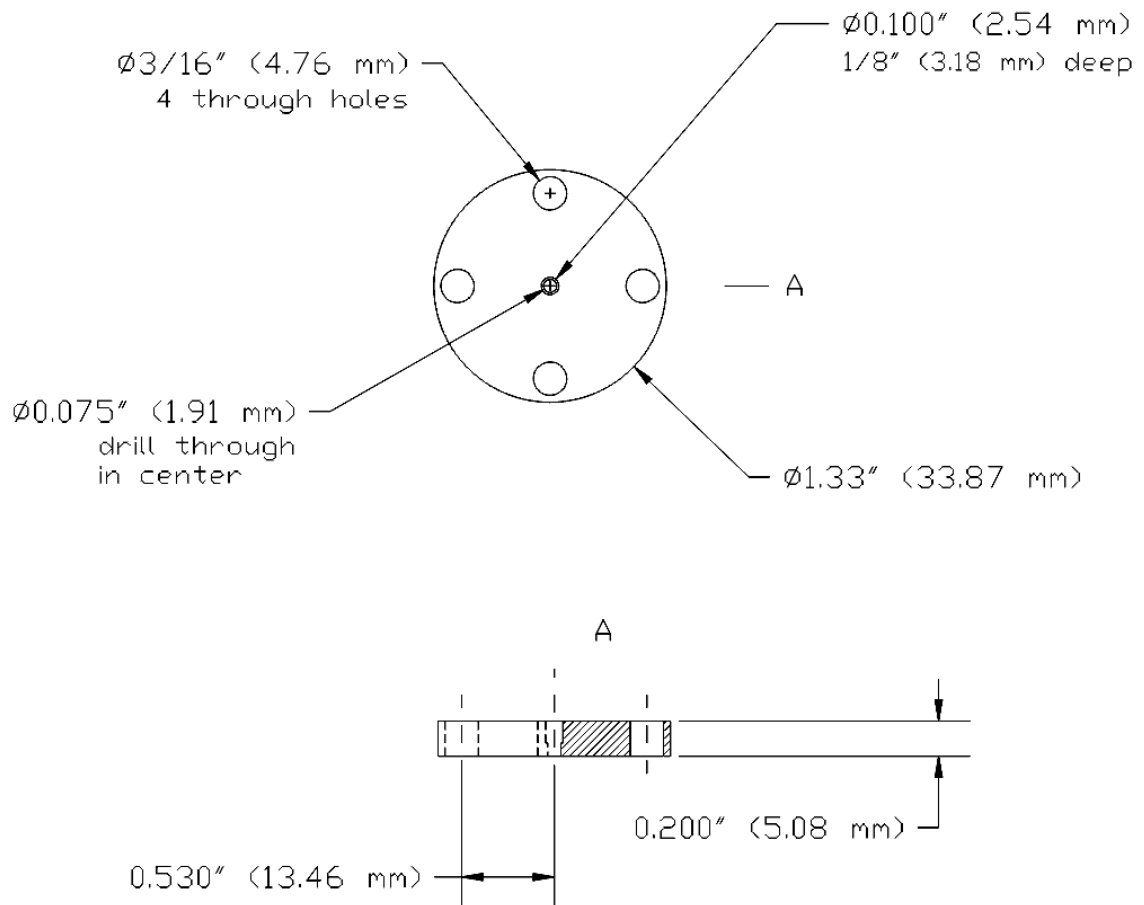


Figure B.10: Non-discharge pulsed valve faceplate flange for cluster production.

This circuit is triggered by the rising front of a TTL pulse and is used to produce a rectangular TTL pulse of desired duration (up to a few milliseconds). This helps to limit the number of triggering delay lines needed from a commonly used SRS 535 pulsed delay generator to only one. The pulse is produced by a retriggerable monostable multivibrator (74123). The pulse duration is determined by the $(R_1 + R_2)C_1$ time constant, and may be

adjusted by the R_1 trim pot. The inverter (74128) is used to invert the pulse to the proper polarity and to isolate the input (delay generator) from the output (high voltage circuit).

B.2.2 Pulsed Valve Driver

The pulsed valve driver (Figure B.12) is based on a 2N6768 power MOSFET transistor. It applies high voltage to a solenoid pulsed valve whenever the transistor is opened. High voltage (up to 400 V) was produced by charging the C_1 capacitors in a voltage doubling arrangement. The voltage was regulated by a Variac, isolated from the rest of the circuit by a transformer. The R_1 resistor is used to discharge these capacitors when the circuit is turned off. The 1 k Ω , 25 W resistor was used to limit the current through the valve solenoid coil.

The high voltage transistor was opened by the TTL pulse width selector circuit (B.2.1). The necessary +5 V should be provided by a regulated +5 V power supply (300 mA or better).

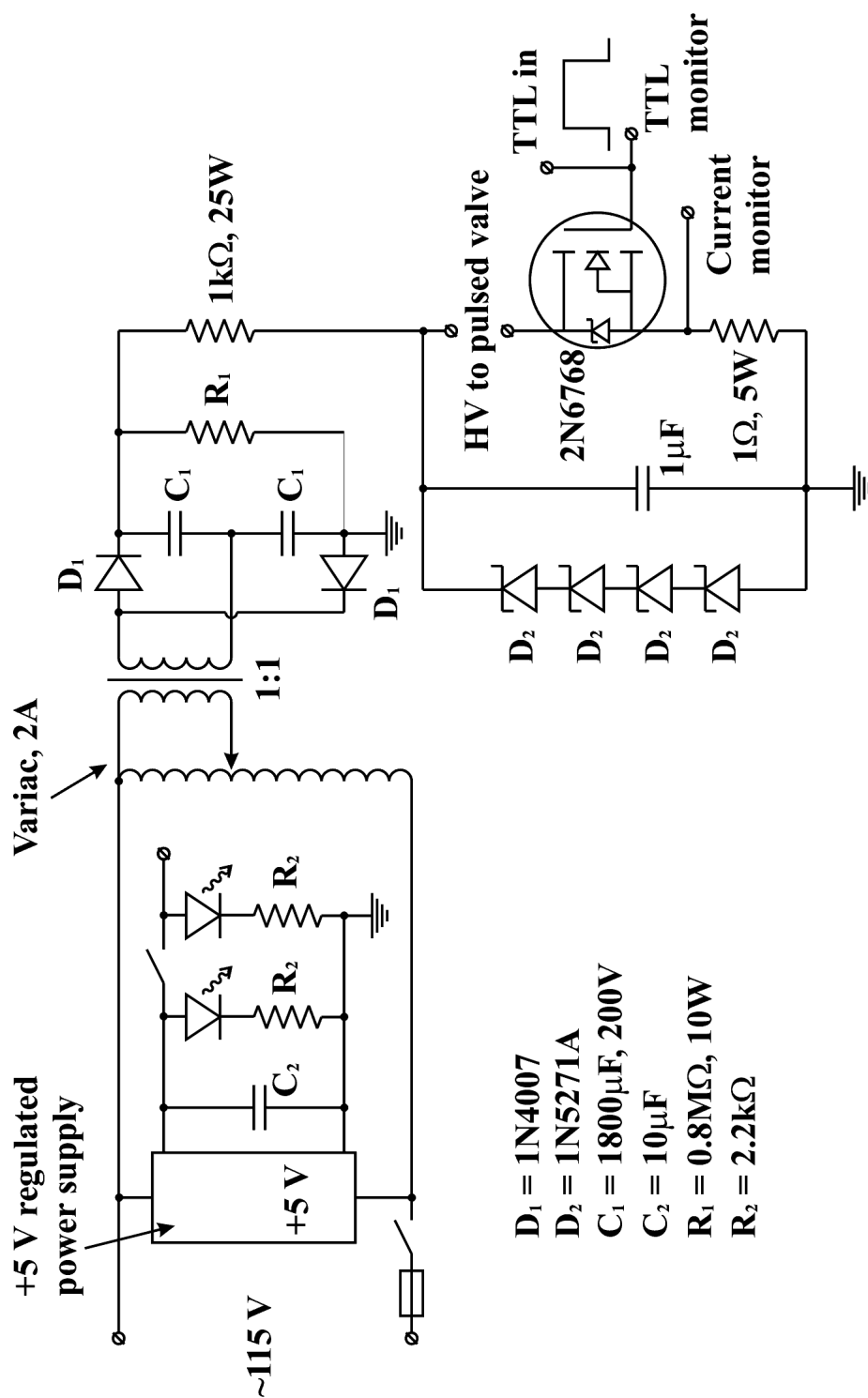


Figure B.12: Pulsed valve driver circuit.

B.2.3 TOF MS High Voltage Pulser

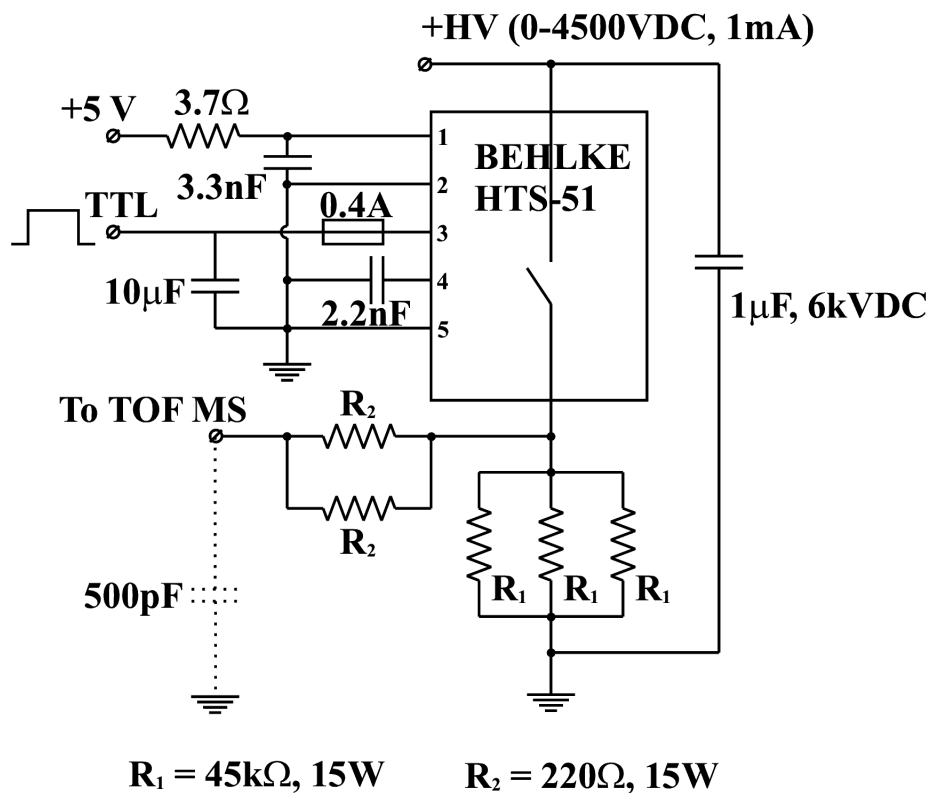


Figure B.13: One channel of the TOF MS high voltage pulser.

The pulser for high voltage ion extraction and acceleration in the time-of-flight mass spectrometer has two identical channels (Figure B.13). Each channel is based on a fast high voltage, high current switch HTS-51 (upto 5 kV, 30 A), manufactured by BEHLKE ELECTRONIC GmbH.

The high voltage capacitor was made of metalized polyester film rated up to 6 kV DC, custom made by Dearborn Electronics, Inc. It has been selected to be as large as possible to compensate for the low current from the power supply (1 mA maximum). It was therefore not possible to completely compensate for the high voltage overshoot at the beginning of

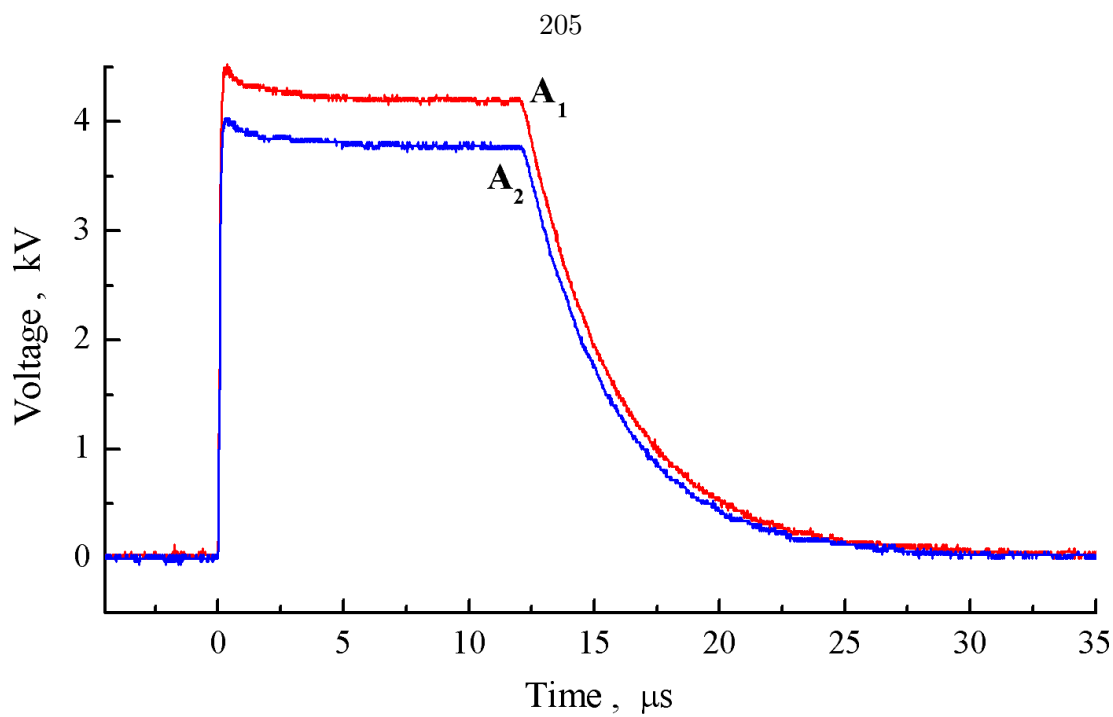


Figure B.14: TOF MS pulser high voltage pulse profile (full).

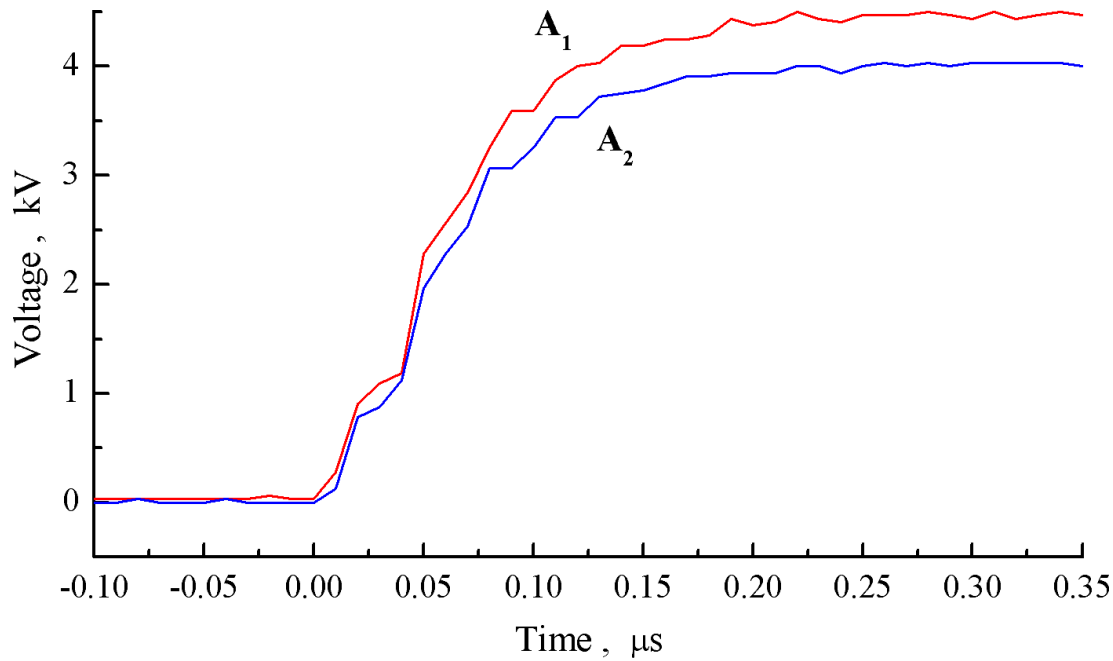


Figure B.15: TOF MS pulser high voltage pulse profile (front).

the pulse (Figures B.14, B.15; $V_{A_1} = 4200$ V, $V_{A_2} = 3800$ V).

The resistors R_1 were selected to adjust the voltage drop time constant at the pulse tail when the switch is turned off. The resistors R_2 were selected to adjust the voltage rise time constant at the pulse front after the switch is turned on, as well as to smooth out the voltage oscillations. Both R_1 and R_2 were type MS power film resistors (15 W) rated for up to 6 kV DC operation, manufactured by Caddock Electronics, Inc.

The TTL pulse width selector circuit (B.2.1) was used to adjust the duration of the high voltage pulse ($C_1 = 0.05$ μ F, $R_1 = 10$ k Ω , $R_2 = 156$ Ω , $R_3 = 1$ k Ω). An AT type computer power supply was used to provide +5 V to the TTL circuit and the low voltage side of both of the high voltage switches.

After the pulser has been turned on, the high voltage should be applied to it gradually from 0 V to the desired +HV value. This should be done simultaneously on both channels (A_1 and A_2), to avoid large voltage gradients in TOF MS ion optics. According to the switch manufacturer, instant application of high voltage may damage switch circuits. In addition, the only power supply available was not able to quickly charge a 1 μ F capacitor to the necessary few kV.

B.2.4 Frequency Divider

The TTL frequency divider (Figure B.16) is used to divide the frequency of an external source by an integer number $N = 1 - 256$. The desired divider is selected by setting the jumpers to logical 1 or 0.

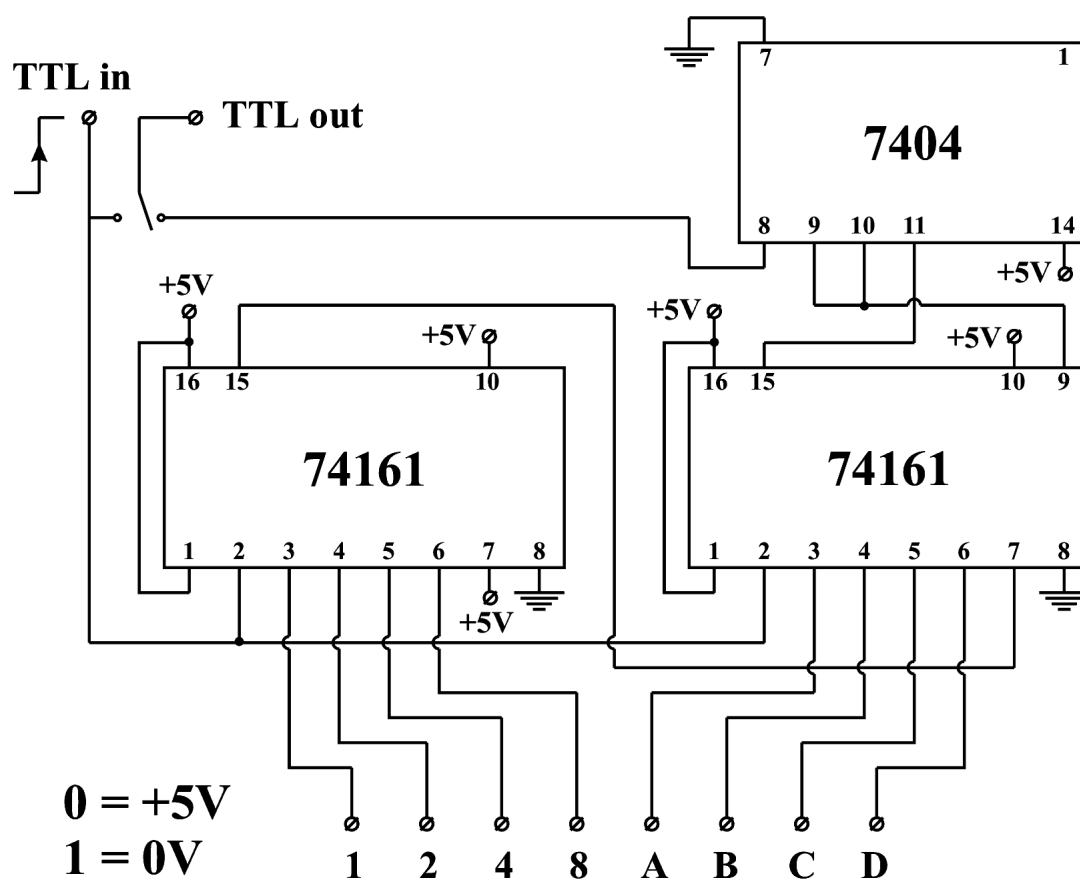


Figure B.16: TTL triggering frequency divider.

Appendix C

Blake Group Spectroscopy Tools Software

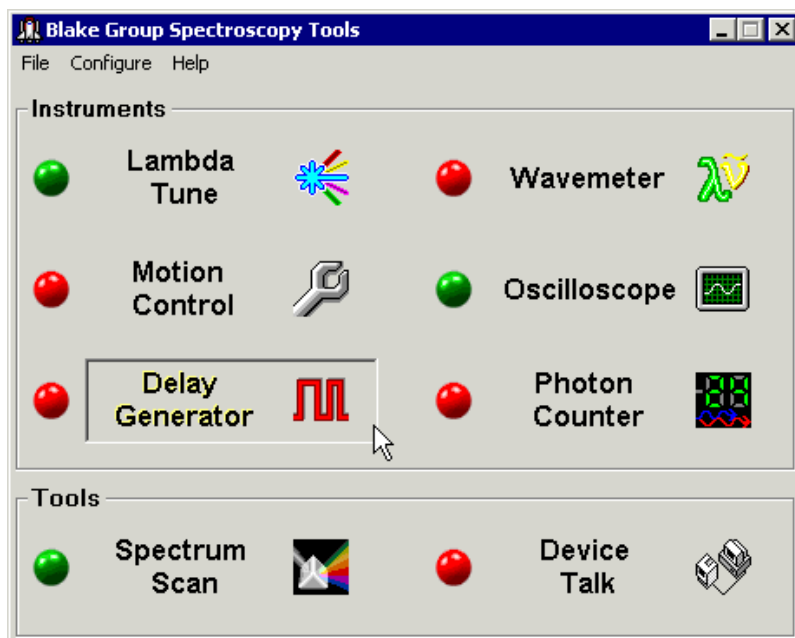
C.1 Main Panel

Blake Group Spectroscopy Tools (BGSpecT) is a set of tools for remote control of experiments and data collection. It consists of a set of modules, controlling *instruments* (C.1.1) and *tools* (C.1.2) to work with those instruments (i.e., record spectra or some other signal functions and communicate with instrument devices on low level).

Among the useful features of BGSpecT are that it:

- Simultaneously controls multiple devices of the same kind
- Controls devices via GPIB and RS232 interfaces as well as PC plug-in cards (PCI or ISA)
- Simultaneously controls multiple GPIB boards
- Incorporates smart oscilloscope waveform acquisition
- Enables wavelength source wavelength conversions
- Can Master/Slave lock delay lines from pulse/delay generator
- Has a huge number of supported oscilloscopes
- Easily enables acquisition of spectra

- Can be flexibly configured
- Provides a user friendly interface, with partial Windows XP themes support



The BGSpect panel itself is a switch board. It is used to turn On/Off the instrument and tool sub-panels which can only be accessed through the switch board. These sub-panels may be opened by pressing a corresponding button on the BGSpect panel.

C.1.1 Instruments

Instrument sub-panels communicate with miscellaneous devices and control them. Instrument panels are:

- Lambda Tune (C.2) – controls multiple multi-axis lasers via a Motion Control sub-panel and diode lasers via GPIB and RS232
- Wavemeter (C.3) – controls multiple wavemeters via GPIB and RS232
- Motion Control (C.4) – handles precision motion control micropositioners via PC plug-in cards (ISA)

- Oscilloscope (C.5) – controls multiple oscilloscopes via GPIB, RS232 and PC plug-in cards (PCI or ISA)

- Delay Generator (C.6) – controls multiple pulsed delay generators via GPIB

- Photon Counter (C.7) – controls multiple photon counters via GPIB and RS232

C.1.2 Tools

The tool sub-panels use either Instrument sub-panels to acquire data and perform data analysis, or are used as a general tool for Instrument panel devices. Tool panels are:

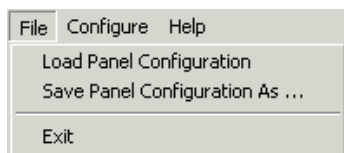
- Spectrum Scan (C.8) – records spectra using lambda tune sources, motion control micropositioners and delay generators as sources and oscilloscopes, photon counters and wavemeters as detectors

- Device Talk (C.9) – configures COM port settings for RS232 communication. Can talk to GPIB and RS232 devices using individual device commands

C.1.3 Menus

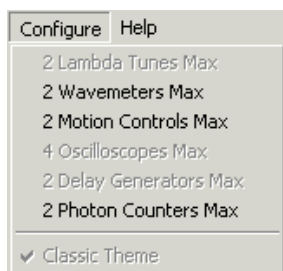
The program menus are:

- File



The “Save Window Configuration” menu saves the current On/Off status for sub-panels. The “Load Window Configuration” menu loads the above configuration. When exiting, the program saves the configuration and then loads it automatically the next time it is started.

- Configure



Here, one can change the maximum number of allowed devices in the Instrument panels. Its instrument submenus are disabled if either the corresponding panel or the Spectrum Scan panel is currently open. The valid number of devices is between 1 and 64. Keeping this number small (no larger than needed) helps to speed up multi-device tasks such as reading oscilloscope traces.

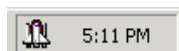
The “Classic Theme” menu is enabled only in Windows XP. It switches between the classic look of the program controls (like that in previous Windows versions) and the partial XP themes look (when the menu is not checked).

- Help

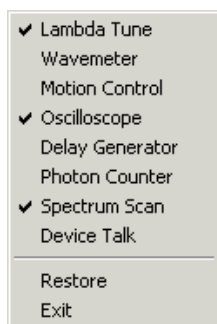
This provides help for BGSpect program. A web browser must be installed to view help files.

C.1.4 System Tray Icon

When the BGSpect panel is minimized, its icon is placed in a system tray.



It can be restored by double-clicking the icon in the system tray. Right-clicking on the icon will bring up the following menu that can be used to open/close instrument and tool panels, restore BGSpect panel to its normal state, or exit the program.



C.1.5 Other

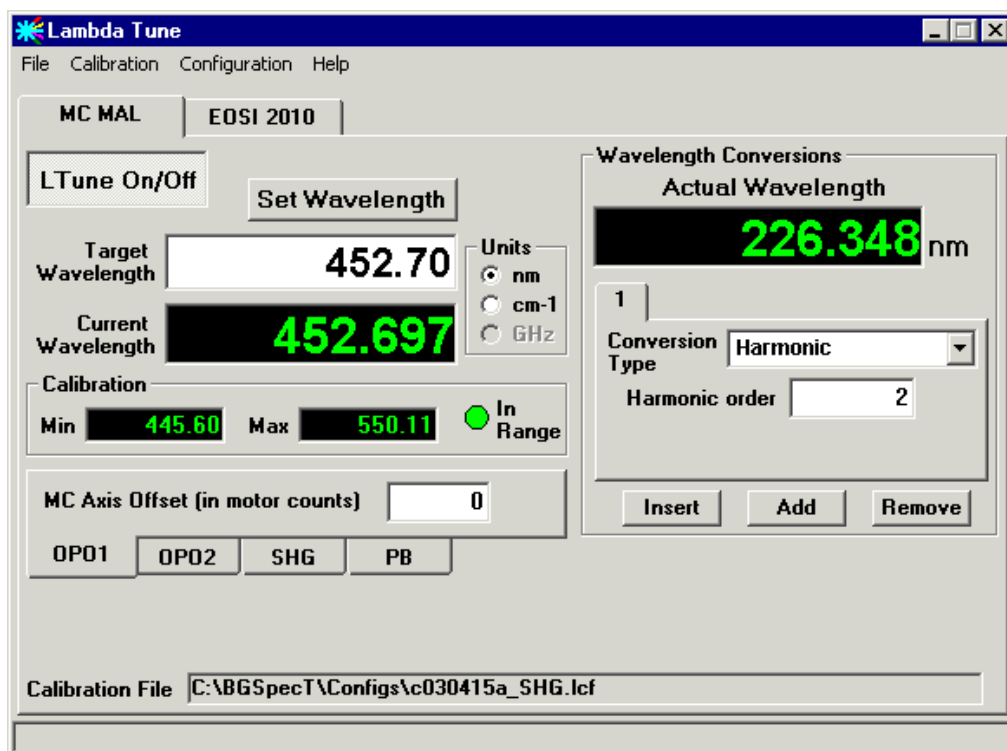
The BGSpecT main directory has 2 sub-directories: *Help* (where all the help files are stored) and *Configs*. The latter is used to store all configuration files that were created automatically. All these files are in ASCII format and all parameters have descriptions. If necessary, they may be modified in any text editor. In general, it is not advised to alter these files.

C.2 Lambda Tune Panel

The Lambda Tune sub-panel is a part of BGSpecT (C.1) that can simultaneously perform remote control of multiple, independent wavelength sources (lasers, monochromators, frequency generators).

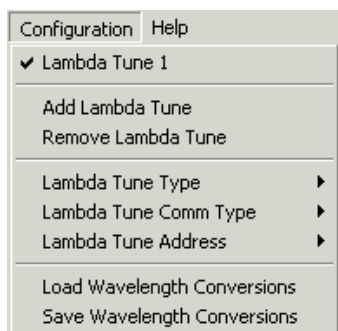
The following procedures are available that one can/should perform with the lambda tune sources:

1. Setup communication parameters before establishing remote communication (C.2.1)
2. Setup lambda tune parameters after remote communication has been established (C.2.2)
3. Change the wavelength (C.2.3)



C.2.1 Remote Parameters Setup

To prepare the panel and start communication with a lambda tune device, one first needs to perform some setup through the “Configuration” menu. Please follow the general instructions on how to setup device communications (C.11), substituting the word Device with Lambda Tune where applicable.

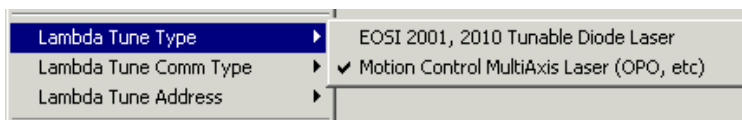


Supported devices are:

- Environmental Optical Sensors Inc. (EOSI, Newport) 2001, 2010 tunable diode lasers

(via GPIB or RS232)

- MultiAxis Laser (OPO, etc.) (via Motion Control panel)



If a few lambda tune sources have been selected, one can switch between them either by clicking the lambda tune tab (the one at the very top) or by choosing the “Configuration → Lambda Tune *N*” menu.

Once the remote communication with the lambda tune device has been established (by clicking “**LTune On/Off**” button), one can change lambda tune settings and change wavelength.

C.2.2 Lambda Tune Parameters

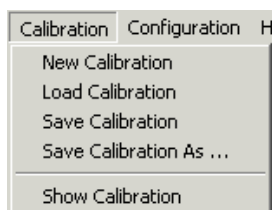
Once the lambda tune is turned On, the following parameters can be changed:

1. Calibration table – required for proper wavelength determination
2. Wavelength conversions – to show actual wavelength if any manipulations with light were performed (harmonic generation, etc.)
3. Other parameters, some of which are device-specific

C.2.2.1 Calibration File

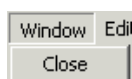
For the lambda tune to operate properly, it needs a calibration table. If the selected lambda tune has not been turned on before, you will be prompted for a file name. At that point, one can either select an existing calibration or type in a name for a new calibration file.

To perform manipulations with the calibration file, click one of “Calibration” sub-menus.



Here, one can create a new calibration, load an existing calibration or save the current calibration. The calibration file name is displayed in the bottom part of the Lambda Tune panel. The “*” (star) symbol after it means that calibration has been changed but not saved.

To access the actual calibration table, one needs to check the “Calibration → Show Calibration” menu. If this option is chosen, the Lambda Tune Calibration panel window will be open. It can be closed by either clicking the same menu again or selecting the “Window → Close” menu in the Lambda Tune Calibration panel.

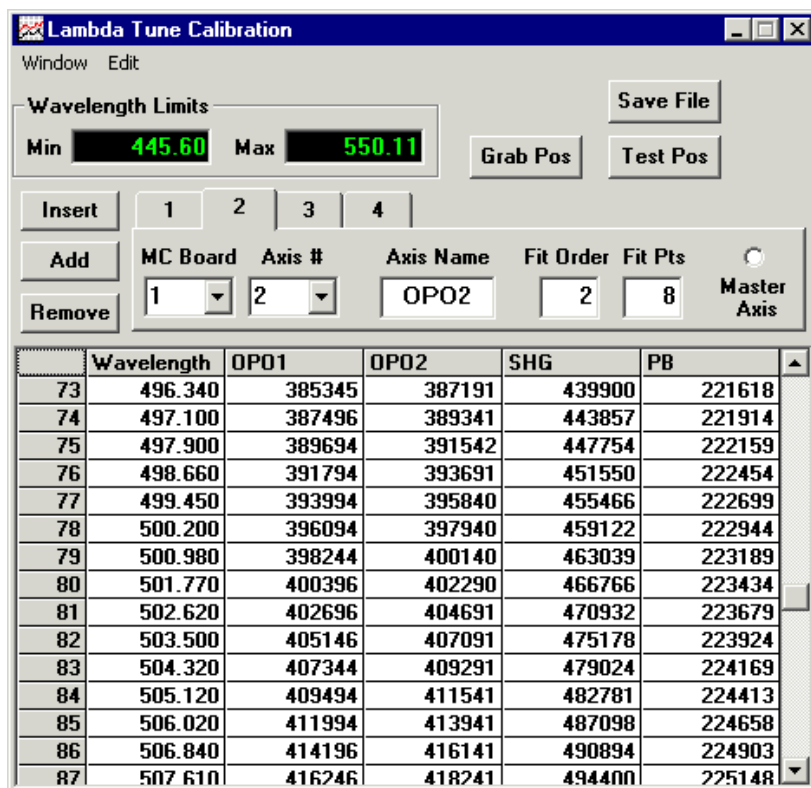
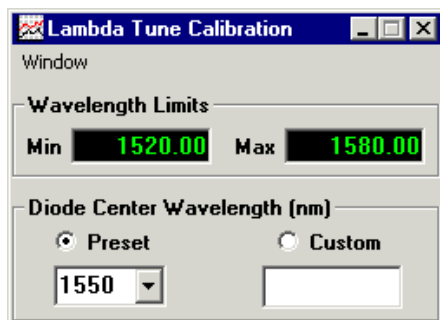


The calibration table will be different for each lambda tune type. The valid calibration range is displayed in the upper left corner of Lambda Tune Calibration panel and under the **Current Wavelength** box on the Lambda Tune panel. Depending on whether the Current Wavelength is within or outside the valid calibration wavelength range, the LED will become green or red, respectively.

The EOSI 2001 and 2010 lasers one can swap diode modules. Each of those modules has a certain tuning range and center wavelength. One can either choose the **Diode Center Wavelength** from the list or type in a custom value if the diode is not in the list. Depending on that value, the diode tuning range will be set automatically.

The MultiAxis laser uses motion axes from the Motion Control panel (C.4) to change the

wavelength of a laser or OPO. Hence, one needs to create a table where certain wavelengths correspond to some specific MC axis positions.



One can change the number of used axes by clicking the “**Insert**”, “**Add**” or “**Remove**” buttons. The parameters for each axis must then be configured:

1. **MC Board** – the number of a motion control board which the axis is connected to

This is the same as N in the Motion Control panel “Configuration \rightarrow Motion Control N ” menu.

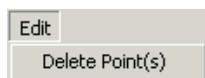
2. **Axis #** – the number of the desired axis
3. **Axis Name** – this will be displayed on the Motion Control panel Use distinct names to avoid confusion with the axis assignment
4. **Fit Order** – the order of polynomial used to fit the calibration table for wavelength or axis position interpolation

Such a fit is performed to find new axis positions for a selected wavelength and to find the wavelength for the current axis position.

5. **Fit Pts** - the number of points used in the above fit
6. **Master Axis** - indicates if the axis has been chosen as the master axis

Only the master axis column is used in Wavelength \longleftrightarrow Axis position conversions. Positions of all other axes are calculated based on the master axis position. If a position of a non-master axis has been changed (i.e. manually or through the Motion Control panel) without changing master axis position, the calculated current lambda tune wavelength will not change.

The values of the calibration point wavelength and axis positions can be edited directly in table cells. To add a new point, one can simply start editing an empty line in the end of the table or press the “**Grab Pos**” button. The latter will copy the current positions of all axes used in the calibration table. To remove points from the table, select the proper row and click the “Edit \longrightarrow Delete Point(s)” menu. Multiple row selection is allowed.



Clicking the “**Test Pos**” button will put the axis positions of a selected calibration point to Target absolute positions of those axes in the Motion Control panel. It will also set the destination to “Absolute”. However, it will not move the axes. That must be done

manually.

“**Save File**” performs the same function as the “Calibration → Save Calibration” menu in the Lambda Tune panel.

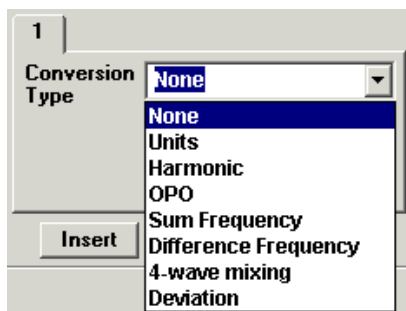
In addition to saving the calibration file manually, a temporary calibration is saved to a file “\$__\$lcfN.\$lc” whenever any calibration parameter has been changed. This feature was designed for one step manual Undo and to secure calibration from computer crashes.

C.2.2.2 Wavelength Conversions

If any wavelength conversions are performed with the lambda tune light, the actual wavelength after such conversions can be calculated in the Wavelength Conversions part of the Lambda Tune panel. One can change the number of conversions by clicking “**Insert**”, “**Add**” or “**Remove**” buttons, after which the parameters of each wavelength conversion should be set. These conversions will be applied to the initial lambda tune wavelength in order of their appearance. The calculated **Actual Wavelength** is then displayed.

There are a few wavelength conversions available:

1. **None** – does not do anything; this is the default value, and can also be used to disable some of the conversions
2. **Units** – changes actual wavelength units
3. **Harmonic** – higher order harmonics



4. **OPO** – complimentary OPO wavelength (signal/idler)

5. **Sum Frequency**

6. **Difference Frequency**

7. **4-wave mixing** – calculates the result of a four-wave mixing of the lambda tune with two other light sources

8. **Deviation** – from a fixed wavelength

Units conversion switches between **nm** (nanometers), **cm⁻¹** (wavenumbers) and **GHz** (gigahertz).

1 2

Conversion Type Units

☒ nm

☐ cm-1

☐ GHz

OPO calculates a complimentary signal/idler wavelength if the Current Wavelength is one of them. This conversion requires the wavelength of the pump laser.

1 2

Conversion Type OPO

Pump laser 355.00 nm

Sum Frequency conversion calculates the sum wavelength of the current wavelength with another one from a Second source.

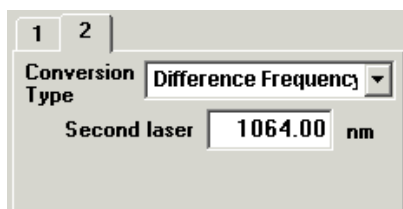
1 2

Conversion Type Sum Frequency

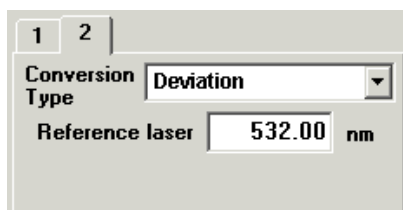
Second laser 1064.00 nm

Difference Frequency conversion calculates the difference wavelength of the current

lambda tune and another Second source. It always returns a positive value, no matter which of the two wavelengths is larger.



The **Deviation** conversion calculates the deviation wavelength of the current wavelength from a reference wavelength.



It is possible to Save/Load wavelength conversions for a lambda tune set up by clicking the “Configuration → Save/Load Wavelength Conversions” menu.

C.2.2.3 Other Lambda Tune Parameters

One can change lambda tune **wavelength units** on the right side of Target and Current Wavelength boxes.

There are also some parameters specific to a particular lambda tune type.

For the EOSI 2001 and 2010 lasers, one can change the diode **current** and/or **temperature**, switch between **User** and **Factory** settings, and change the **calibration center wavelength** (the one in the hardware, not in the software calibration table). It is also possible to perform fine wavelength tuning by changing the **Piezo Tune voltage**.

For a MC Multi-Axis laser, it is possible to set a fixed **offset** for any motion control axis. Such an offset might be needed, for example, to compensate for a gradual backlash

| | | | | |
|------------------------|-------|------------------------|------|--|
| Current (mA) | | Temperature (C) | | Wavelength |
| Diode | 0.2 | Diode | 23.1 | <input type="radio"/> User |
| Limit | 100.0 | Base | 30.0 | <input checked="" type="radio"/> Factory |
| Piezo Tune Voltage (V) | | 70.00 | | Calibration |
| | | | | 1578.853 |

accumulation without re-assigning the axis position value. This helps to avoid laser re-calibration.

C.2.3 Changing Lambda Tune Wavelength

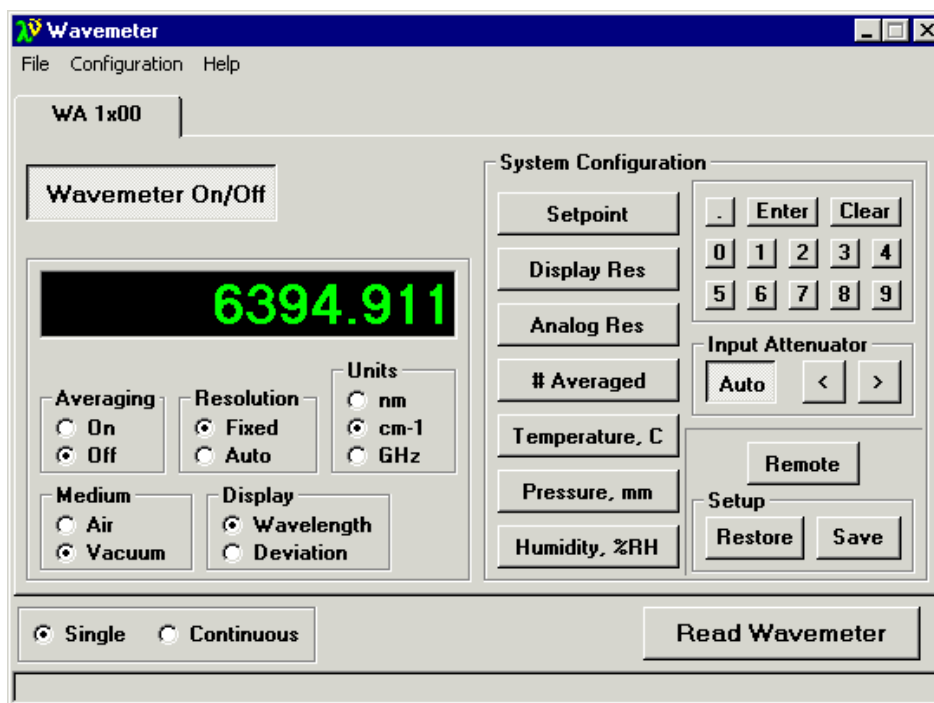
To change the lambda tune wavelength, type the desired value in the **Target Wavelength** box. If the chosen lambda tune target position is outside the valid calibration range, it will be corrected to be within that range. After entering the desired wavelength, simply click the “**Set Wavelength**” button and the wavelength will be changed. If there are a few lambda tune sources in the panel, the above procedure will apply only to the laser whose parameters are displayed on the panel.

C.3 Wavemeter Panel

The Wavemeter sub-panel is part of BGSpecT (C.1) that can simultaneously perform remote control of multiple independent wavemeters.

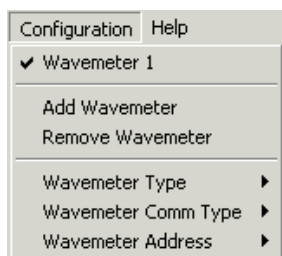
The following are procedures that one can/should perform with the wavemeters:

1. Setup communication parameters before establishing remote communication (C.3.1)
2. Setup wavemeter parameters after remote communication has been established (C.3.2)
3. Read wavelength (C.3.3)



C.3.1 Remote Parameters Setup

To prepare the panel and start communication with wavemeter(s), one first needs to perform some setup through the “Configuration” menu. Please follow the general instructions on how to setup device communications (C.11), substituting the word Device with Wavemeter where applicable.



The presently supported wavemeters are:

- Burleigh WA-1000 and WA-1500 (via GPIB and RS232)



If a few wavemeters have been selected, one can switch between them either by clicking

the wavemeter tab or by choosing the “Configuration \rightarrow Wavemeter N ” menu.

Once the remote communication with the wavemeter has been established (by clicking “**Wavemeter On/Off**” button), one can change wavemeter settings and read the wavelength.

C.3.2 Wavemeter Parameters

The wavemeter panel for Burleigh WA-1000 and 1500 is designed to mimic the front panel on the hardware wavemeters. Just choose the necessary options.

In addition, one can choose the way in which the wavelength is read from the wavemeter: once or continuously. This is done by selecting “**Single**” or “**Continuous**” mode in the bottom of the panel.

C.3.3 Reading Wavelength

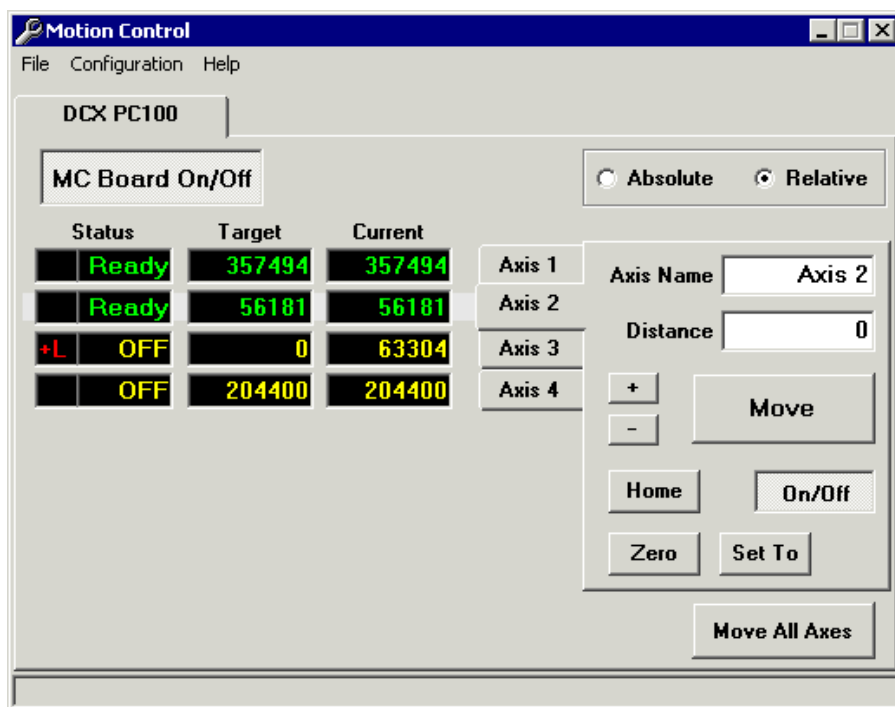
To read the wavemeters, click the “**Read Wavemeter**” button in the bottom of the panel. If a few wavemeters are turned On, wavelengths will be read from all of them. Acquired wavelength and any wavemeter messages are displayed on the panel.

C.4 Motion Control Panel

The Motion Control sub-panel is that part of BGSpecT (C.1) that can simultaneously perform remote control of multiple independent Motion Control boards with up to **8** axes (micro-positioner stepping motors) each.

The following are procedures that one can/should perform with motion control:

1. Setup communication parameters before establishing remote communication (C.4.1)
2. Setup axis parameters after remote communication has been established (C.4.2)

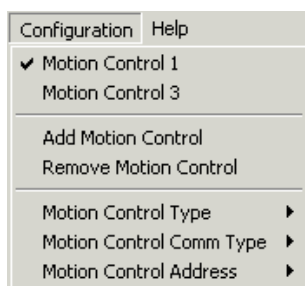


3. Move axes (C.4.3)

4. Positions file (C.4.4)

C.4.1 Remote Parameters Setup

To prepare the panel and start communication with the Motion Control board(s), one first needs to perform some setup through the “Configuration” menu. Please follow the general instructions on how to setup device communications (C.11), substituting the word Device with Motion Control where applicable.



Supported Motion Control boards are:

- Precision MicroControl:
 - DC2-PC100, DCX-PC100, DCX-AT100, DCX-AT200, DCX-AT300 series ISA cards
 - DCX-PCI100, DCX-PCI300, MFX-PCI1000 series PCI cards



If a few motion control boards have been selected, one can switch between them either by clicking the Motion Control tab (one on the very top) or by choosing the “Configuration → Motion Control *N*” menu.

Once the remote communication with the motion control board has been established (by clicking “**MC Board On/Off**” button), one can change axes settings and move axes. If the computer has been restarted, the board will not remember its axis positions. You will be prompted to confirm those when turning the board On for the first time.

C.4.2 Motion Axes Parameters

The left half of the panel is for monitoring purposes, and is where the axis position and status are displayed. Note, the **Current** and **Target** positions will be different when the axis is moving.

Switching between different axes is done through the tabs in the middle of the panel. The active axis tab will be right against the corresponding axis status and positions row.

Motion axes can be turned On/Off by clicking the “**On/Off**” button in the bottom of the axis panel.

It is possible to assign a **name** to an axis, which is handy when having to deal with too many of them.

Assigning the value (in motor counts) for the current axis position can be done by clicking the “**Zero**” or “**Set To**” buttons. The former will set the axis position to “0”. The

latter will set it to the value typed in the **Distance box**. You will be asked to confirm the new axis position assignment.

C.4.3 Moving Axes

The final (**Target**) position of the axis is determined by the number in the **Distance** box. There are two possible destination types: **Absolute** (final motor counts) and **Relative** (the Current axis position is changed by that value). To move one axis, click the “**Move**” button below the Distance box. To move all board axes, click the “**Move All Axes**” button in the lower right corner of the panel. This is equivalent to clicking “Move” buttons for each axis simultaneously. To move an axis to absolute count “0”, click “**Home**” button. “+” and “-” buttons will move an axis to an increase/decrease in its position by the relative value from the Distance box. It is always relative and independent from the Absolute/Relative setting.

While the axis is moving, its position will be tracked and displayed in the **Current** position box.

It is possible to **stop** the axis from moving by clicking a depressed “Move” button. For **emergency stops**, click the depressed “On/Off” buttons.

The current status for all axes is displayed in the **Status** boxes. “OFF” means that the axis is currently turned Off. “Ready” and “Moving” mean that the axis is turned On and is either at rest or moving to a new target position. If there is a red message at the very left, something is not right with the axis operation. “+L” or “-L” means that the stepper motor has reached positive or negative limit, “Err” means all other errors.

C.4.4 Positions File

If the position of any axis has been changed, positions for all axes will be saved in the *Configs* directory in a file with the name:

“MC”+“_t”+BoardType+“_a”+BoardAddress+“.mc1”.

As new backups are made, the extensions for the previous two backups become “.mc2” and “.mc3”. These files are created to remember last axes positions between program startups and computer crashes. The latter two files are saved in case the first one becomes corrupt.

C.5 Oscilloscope Panel

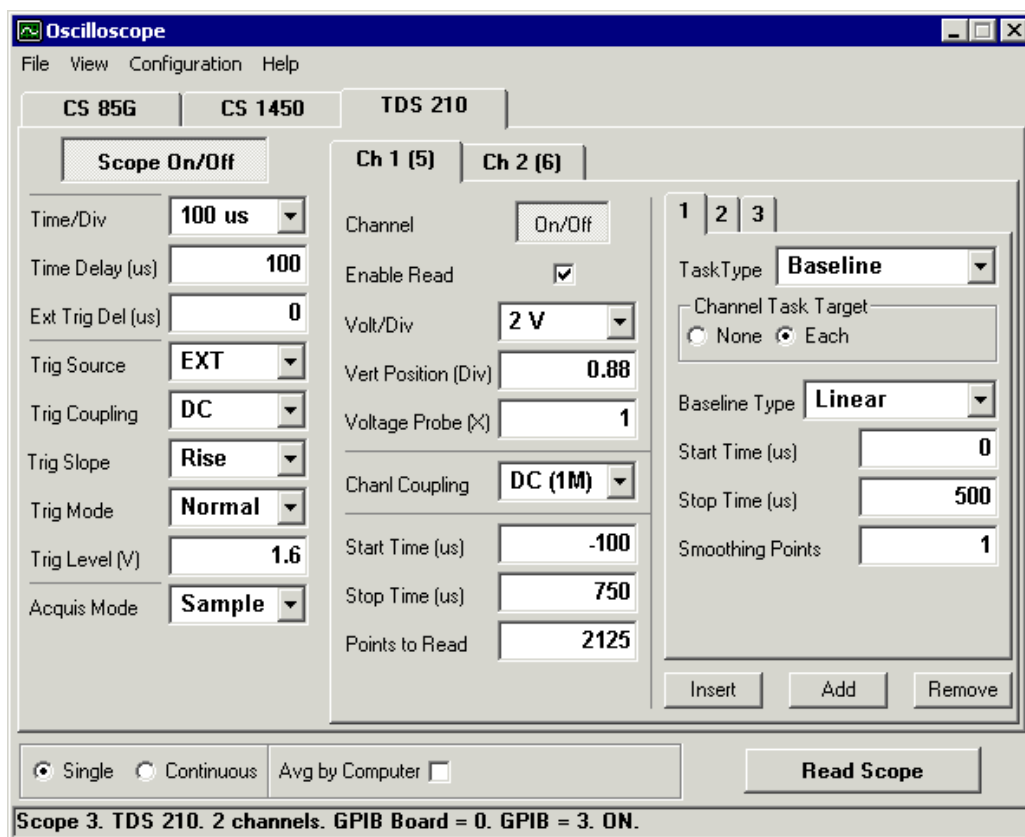
The Oscilloscope sub-panel can simultaneously and remotely control multiple independent oscilloscopes with a total number of channels up to double the number of oscilloscopes. Due to the large number of supported scope models (over 100), this software does not control all possible scope functions, but rather, accesses major common features to acquire waveforms. All waveform manipulations (math, etc) are performed on the PC during post-processing.

The following are procedures that one can/should perform with the scopes:

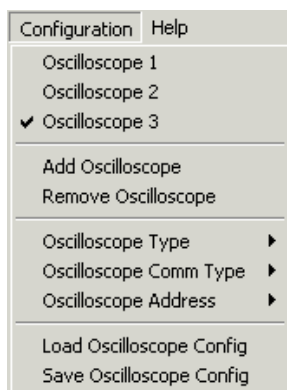
1. Setup communication parameters before establishing remote communication (C.5.1)
2. Setup scope parameters after remote communication has been established (C.5.3)
3. Acquire and manipulate waveforms (C.5.2)

C.5.1 Remote Parameters Setup

To prepare the panel and start communication with the oscilloscope(s), one first needs to perform some setup through the “Configuration” menu. Please follow the general instructions on how to setup device communications (C.11), substituting the word Device with



Oscilloscope where applicable.

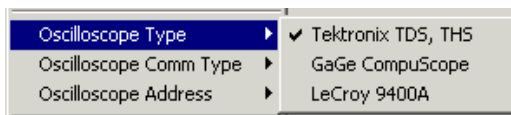


Supported oscilloscopes are:

- Tektronix TDS via GPIB and RS232:
 - series 200: 210, 220, 224
 - series 300: 310, 320, 340A, 350, 360, 380
 - series 1000: 1002, 1012

- series 2000: 2002, 2012, 2014, 2022, 2024
- series 3000: 3012, 3012B, 3014, 3014B, 3032, 3032B, 3034, 3034B, 3052, 3052B, 3054, 3054B
- Tektronix TDS via GPIB:
 - series 400: 410, 410A, 420, 420A, 430, 460, 460A
 - series 500: 510A, 520A, 520B, 520C, 520D, 524A, 540A, 540B, 540C, 540D, 544A, 580C, 580D
 - series 600: 620A, 620B, 620C, 640A, 644A, 644B, 654C, 680B, 680C, 684A, 684B, 684C, 694C
 - series 700: 714D, 714L, 724A, 724C, 724D, 744A, 754A, 754C, 754D, 782A, 784A, 784C, 784D, 794D
 - series 5000: 5032, 5032B, 5034, 5034B, 5052, 5052B, 5054, 5054B, 5054BE, 5104, 5104B
 - series 6000: 6404, 6504, 6604
 - series 7000: 7054, 7104, 7154, 7154B, 7254, 7254B, 7304, 7404, 7404B, 7704B
- Tektronix THS via RS232:
 - series 700: 710, 710A, 720, 720A, 720P, 730A
- GaGe CompuScope PC plug-in cards (PCI, CompactPCI or ISA):
 - 85G, 82G, 8500, 12100, 1250, 1220, 14200, 14100, 1450, 1610, 1602, (6012/PCI) via PCI
 - 85GC, 82GC, 14100C, 1610C via CompactPCI
 - (8012, 6012, 1012, 512, 2125, 250, 225, LITE via ISA)
- LeCroy 9400A via GPIB and RS232

If a few scopes have been selected, one can switch between them, either by clicking the



scope tab (the one on the very top) or by choosing the “Configuration → Scope N ” menu.

Once remote communication with the scope has been established (by clicking “**Scope On/Off**” button), one can change scope settings and acquire waveforms.

When turning On remote communication with the scope, the current scope configuration will be retrieved from the scope for GPIB and RS232 scopes. For GaGe CompuScopes, the last used configuration will be restored.

C.5.2 Waveform Acquisition and Manipulation

1. Read
2. View
3. Save

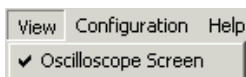
C.5.2.1 Reading Waveforms

To acquire waveforms on the scope and transfer them to the PC, one just needs to click the “Read Scope” button in the lower right corner of the Oscilloscope panel. It becomes active if at least one scope channel is turned On. When multiple scopes are On, their channels are considered by the software as channels of one scope. When acquiring waveforms, all scopes are reset to be triggered at the same time. In case of multiple acquisitions (while “Averaging by Computer” or in “Continuous” mode), scopes are not re-triggered again until all waveforms are transferred to the PC.

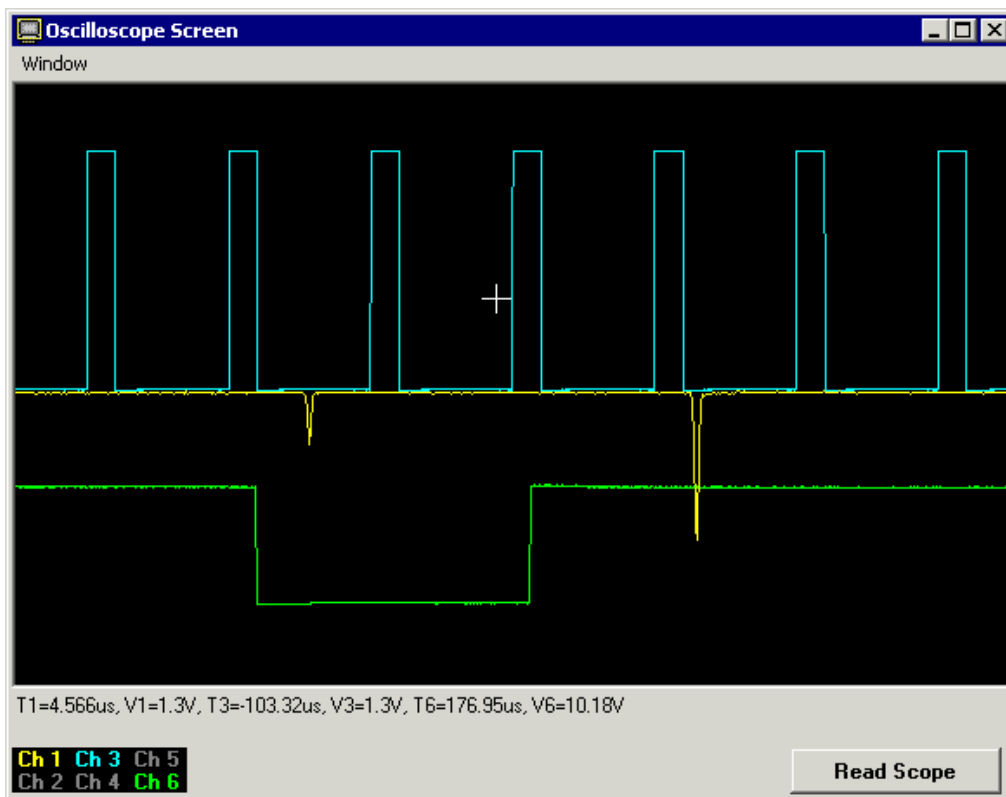
Once the waveforms are acquired, they are put through post-processing procedures that are defined for each channel individually under Channel Task tabs.

C.5.2.2 Viewing Waveforms

All new waveforms are displayed in the Oscilloscope Screen panel. One can access it through the “View → Scope Screen” menu.



Here, each channel has its own horizontal scale - waveform start/stop times define record limits and the whole record fits into the screen window. One can view time and voltage values for each channel by moving the mouse over the channel traces. These values will be displayed right below the screen part, as well as in a tool tip. There are no time/voltage grids on this panel because each channel may have its own scales.



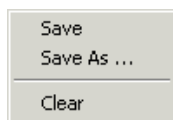
Channel numbers on the **labels** are the same as numbers in parenthesis in the channel tabs on the Oscilloscope panel. One can change a default **color** for the channel by double-

clicking the channel label in the bottom of the scope screen. A single click on the channel label will bring the trace for that channel on top of others.

If the Oscilloscope Screen panel is closed and reopened, the traces will still be displayed. However, if one clears waveform traces by double clicking on the black area, they will no longer be available. One would have to acquire new traces. The same thing happens if one changes scope or channel critical parameters (time scale, delay time, channel voltage scale, start/stop times, etc.).

The “Read Scope” button on the bottom of the Oscilloscope Screen window performs the same function as the same button in Oscilloscope panel and was put there for user convenience.

Right-clicking the mouse on the screen (black area) will bring up the menu that will allow the user to save channel waveforms into data files (same as described below). Selecting “Clear” from this menu (same as double-clicking on the screen) will remove waveform traces from the screen. Those traces will not be re-displayed until new traces are acquired.

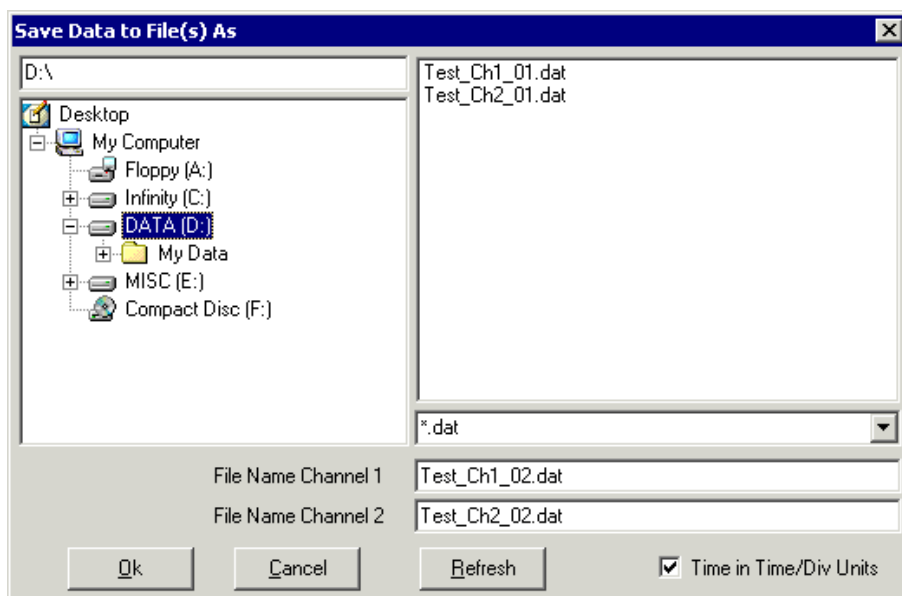
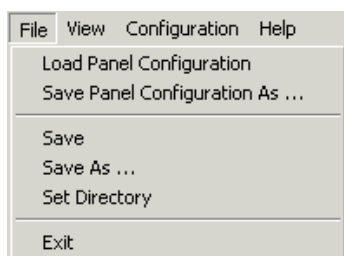


C.5.2.3 Saving Waveforms

If needed, the waveforms can be saved into data files by selecting the “File → Save” or “File → Save As” menus in Oscilloscope panel. The “Save As” menu will prompt for file names for each channel. The “Save” menu will save files with automatically generated names into the current scope directory. This directory may be changed through the “File → Set Directory” menu. If one needs to save waveforms repeatedly, it is advised to use the Autosave option under Channel Tasks.

Depending on whether the box “Time in Time/Div Units” is checked or not, time will be saved either in Time/Div units or in seconds. That value in the checkbox is also used when saving files automatically – via the “File → Save” menu, Autosave channel task or via the “Other → Dump Raw Data to File” menu in Spectrum Scan panel (C.8).

Each saved file will have two columns separated by a Tab symbol. The first column is time and the second column is voltage value in volts.



C.5.3 Oscilloscope Parameters Setup

The oscilloscope panel options span over:

1. Panel (all scopes) – software acquisition and averaging modes
2. One scope (all scope channels) – time scale, delay, triggering and scope acquisition

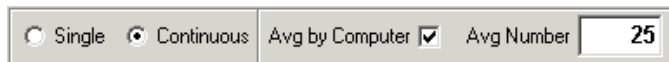
options

3. One scope channel – voltage scale, vertical position, coupling, start/stop times
4. Channel tasks – waveform post processing (baseline, smooth, autosave, voltage dynamic range)

One can also Save and Load such oscilloscope configurations to and from a file.

C.5.3.1 Panel Parameters

Panel-wide parameters are software acquisition and averaging modes. Acquisition mode can be “**Single**” or “**Continuous**” (see the bottom of the Oscilloscope panel). In “Single” mode, the waveforms are acquired only once, which is the same as “Single” triggering mode on stand alone oscilloscopes. In “Continuous” mode, the waveforms are acquired until “Read Scope” button is pressed again, which is similar to “Normal” triggering mode on stand alone oscilloscopes. The reason for having it this way is to make one software oscilloscope out of a few hardware units.



For averaging, there is a possibility of “**Averaging by Computer**” for acquired waveforms. When this option is enabled, the waveforms are acquired by scopes according to their acquisition mode settings and then are transferred to a PC and averaged by the software. This permits higher levels of synchronization and some post processing before the traces are averaged.

C.5.3.2 Common Scope Parameters

For each scope that is turned ON, one can change a few sets of parameters common to the whole scope:

1. **Time scale** and trigger **delays**

2. **Triggering** options

3. **Acquisition** options

All of these are located on the left side of the Oscilloscope panel.

For stand alone hardware oscilloscopes, one can select **Time/Division**, which is the same as Time/Div or the Horizontal scale on the scope. For GaGe scopes, this will be replaced by the **Sampling Rate** which is inverse of the time interval between two adjacent points in the record. If one of the scopes Time/Div values is not standard (not on the list, but close to another “wrong” value), one should choose that “wrong” setting. The difference adjustment will be done automatically.

Time Delay is the delay time between the trigger position and the first point on the oscilloscope screen, which is not necessarily the first point in the data record. It is positive when the trigger is displayed on the scope screen and negative when the trigger is to the left of the screen. Note that for Tektronix scopes, when such a delay is set to zero the trigger point is on the left of the screen and not in the middle. For oscilloscopes with multiple record lengths, a minimal record length is usually chosen and the delay time is adjusted accordingly. That is why it may be disabled.

External Trigger Delay is used to offset waveforms to “true zero” times in cases when the oscilloscope is being triggered by some delayed signal, but the oscilloscope does not know about the delay.

Currently, the software supports only one **trigger** (no second/delayed trigger) for a scope. All triggering is done only from the “Edge” (e.g. the rise/fall front of the waveform).

In the triggering part of the panel, one can change the **Trigger Source** (one of the channels, External, etc.), **Trigger Coupling** (AC, DC), **Trigger Slope** (Rise, Fall or

both), **Trigger Mode** (Single, Normal, Auto, etc.) and **Trigger Level**. For GaGe scopes, the Trigger Mode is replaced by **Channel Mode** (Single, Dual) which shows how many scope channels can be used.

When a scope is acquiring waveforms, the Trigger Mode is set to Single. After all waveforms are transferred to a PC, it is returned to the previous state. For repetitive waveform acquisitions when data acquisition speed is important, it is advised to switch the Trigger Mode to Single.

Acquisition Mode switches between Sample, Average, PeakDetect, Envelope, etc., when applicable. For some of these modes, such as Average or Envelope, one may be able to change the Averaging Number. **Time to Average** is an estimated time that it takes the scope to finish averaging waveforms after it was reset. A computer will wait that long before trying to download the averaged waveform. This is used to minimize communication traffic between the hardware and a PC.

C.5.3.3 Channel Parameters

The user can set up parameters for individual channels. Switching between the channels is done through the channel tab. The **name** of the channel tab is the name of the channel on the scope (Ch 1, Ch A, Aux 1, etc.). The number in parenthesis is the **channel number** in the software, and is the number that goes into the channel label in the Oscilloscope Screen panel. It is also used to identify oscilloscope channels in the Spectrum Scan panel (C.8). The number of channels on the scope is determined by the software automatically. If the software runs out of the maximum allowed number of channels (double the maximum number of devices in the Oscilloscope panel), it may cut off some of the channels that do not fit in.

The “**On/Off**” button turns the channel On and Off, reflecting all changes on the hardware as well (it (dis)appears from the hardware scope screen). For GaGe scopes, this does not change the Channel Mode between Single and Dual. The “**Enable Read**” check does not remove the channel trace from the hardware scope screen. When it is unchecked, the software will not download the waveform to a PC.

One can change a few **voltage** parameters: **Voltage/Division** (vertical scale), **Vertical Position** of the waveform trace and **Voltage Probe** (when applicable). For GaGe scopes, Volt/Div will be replaced by **Voltage Range** – the allowed voltage range for the chosen scale. The full range is 10 divisions for Tektronix scopes and 8 divisions for LeCroy 9400A. The Volt/Div scale may affect the Trigger Level when using this channel as the Trigger Source.

Channel Coupling may be AC, DC, or Ground. The number in parenthesis is input impedance (50 Ohm or 1 MOhm). Channel Coupling may affect allowed Volt/Div scales. If the oscilloscope is triggered from one of its channels, both Volt/Div and channel coupling may affect allowed triggering settings.

The entire waveform does not need to be transferred to a PC. It is possible to choose the time range (**Start** and **Stop** times) that will be downloaded, and only points from this time interval will be plotted in the Oscilloscope Screen panel. Note that the Start/Stop times are in the same units as Time/Div (s, ms, μ s, etc.). From the Start/Stop times, the software will calculate the number of **Points to Read** which cannot be changed and is there for information purposes only. Depending on these times, the minimum record length and delay times may be adjusted accordingly. For the LeCroy 9400A, one can **Read 1 Point Out of N** - each N th point of the record. This approach can be useful when the signal on one channel does not need to have as high a time resolution as another.

| | |
|-----------------|------------------|
| Acquis Mode | Average ▼ |
| Averaging Num | 16 |
| Time To Avg (s) | 1 |

C.5.3.4 Channel Task Parameters

On the right side of the channel panel, one can define **Channel Tasks** - a set of manipulations to be done with the acquired waveform. One can change their number by clicking “**Insert**”, “**Add**” and “**Remove**” buttons. There are a few types of channel tasks:

1. **None** – default value
2. **Dynamic Range**
3. **Baseline**
4. **Autosave**
5. **Smooth**
6. **Scale Up/Down**

All **Start/Stop** times must be within the selected time range for the channel.

Channel tasks can be applied in several ways: **None** (same as choosing **None** task), **Each** (applied to each downloaded waveform), **Avg** (when Averaging by Computer, applied to the averaged waveform only, not the individual ones), and **All** (same as **Each** and **Avg** together).

All tasks are performed in the order of their appearance and according to their selected time range.

Dynamic Range is the difference between the minimum 5% and maximum 5% points of the waveform in a selected time range. This difference is expressed in % of the whole voltage dynamic range at the selected Volt/Div scale. If the **Dynamic Range** value does not fit into the **Minimum/Maximum** brackets, all waveforms from this acquisition will be discarded and the acquisition will start again. This task may be very useful when trying

to average some fluctuating signal to improve signal contrast and the overall quality of the acquired waveforms. When **Adjust Volt/Div** is checked and the Dynamic Range is below Minimum or above Maximum values, the Volt/Div scale will be increased/decreased before the next acquisition attempt. It is therefore useful for establishing a dynamic voltage scale adjustment during scans.

In the **Baseline** channel task, one can choose among the following baseline subtraction types:

None – default

Linear – subtracts a straight line that goes through Start/Stop points

Vertical – moves the waveform Up/Down to bring the selected Start point to 0 V

Waveform – subtracts a “baseline” waveform that has been obtained by pressing “**Acquire Baseline**” button

In the Linear and Vertical cases, one can choose the **Smoothing Points** number that is used to average this number of points to find better voltage values for baseline Start/Stop points. This may be handy for baselining noisy waveforms.

The **Autosave** channel task will save the selected part of the waveform automatically into a file defined by the **File Mask**. The “*” symbol in it will be substituted by an

1 2 3 4

TaskType **Baseline**

Channel Task Target
☐ None ☐ Each ☒ Avg ☐ All

Baseline Type **Linear**

Start Time (us) **8.07**

Stop Time (us) **34.2**

Smoothing Points **1**

increasing integer number.

1 2 3 4

TaskType **Autosave**

Channel Task Target
☐ None ☐ Each ☒ Avg ☐ All

Start Time (us) **0**

Stop Time (us) **40**

File Mask **CH1_4_*.dat**

The **Smooth** task will average the waveform over a **Smoothing Points** window with a “moving box” method.

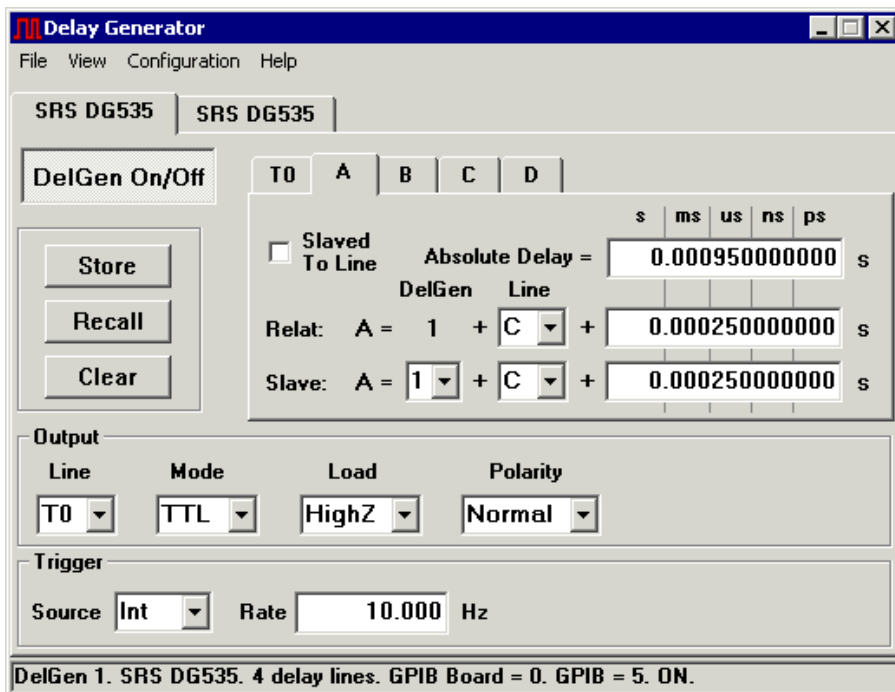
The **Scale Up/Down** channel task scales the waveform vertically via multiplying it by the **Scale Factor**. Negative numbers can be used to invert the waveform.

C.5.3.5 Save and Load Configuration

All of the above scope-specific settings may be saved to a file or loaded from a file. To do that, choose the “Configuration → Save/Load Oscilloscope Config” menu. You will be prompted for a file name.

C.6 Delay Generator Panel

The Delay Generator sub-panel is part of BGSpecT (C.1) that can simultaneously perform remote control of multiple independent delay generators.



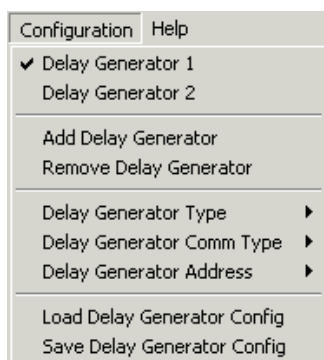
The following are procedures that one can/should perform with the delay generators:

1. Setup communication parameters before establishing remote communication (C.6.1)
2. Setup delay generator parameters after remote communication has been established (C.6.2)
3. Visualize output pulses (C.6.3)

C.6.1 Remote Parameters Setup

To prepare the panel and start communication with delay generator(s), one first needs to perform some setup through the “Configuration” menu. Please follow the general instructions on how to setup device communications (C.11), substituting the word Device with

Delay Generator where applicable.



Supported delay generators are:

- Stanford Research Systems (SRS) DG535 (via GPIB)



If a few delay generators have been selected, one can switch between them either by clicking the delay generator tab (that at the very top) or by choosing the “Configuration → Delay Generator *N*” menu.

Once remote communication with the delay generator has been established (by clicking “DelGen On/Off” button), one can change delay generator settings and adjust delays.

Caution! When remote communication is established with the SRS DG535, all device parameters are set to factory default settings. It is advised to store delay generator settings in the device’s memory **before** clicking the “DelGen On/Off” button.

C.6.2 Delay Generator Parameters

It is possible to change the following values:

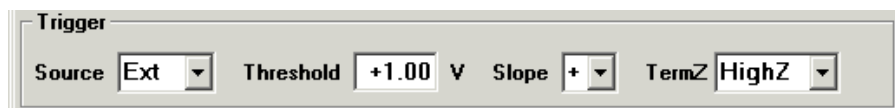
1. Trigger parameters
2. Output line parameters

3. Delay line parameters
4. Save and Load above settings

C.6.2.1 Trigger Parameters

The trigger part of the panel (at the bottom) is responsible for the delay generator triggering mode parameters. Triggering mode is selected from the **Source** list. There are four different modes for the SRS DG535:

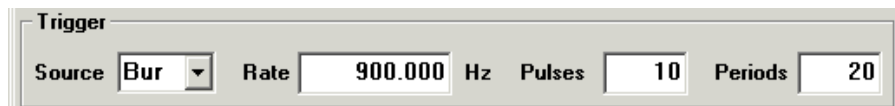
1. **Int** – Internal. One can change the **repetition rate**.
2. **Ext** – External (via Ext input). One can set the **threshold** voltage, **slope** and input **impedance**.



3. **Ss** – Single Shot. Triggering is performed by clicking the “**Single Shot**” button.



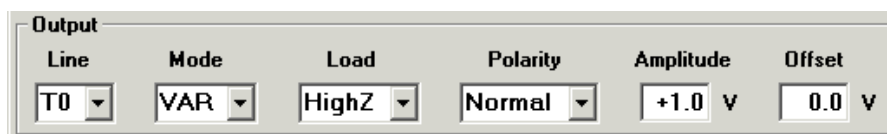
4. **Bur** – Burst mode. It is possible to change the burst **rate**, number of burst **pulses** and their **periods**.



C.6.2.2 Output Line Parameters

There are 7 output lines that can be configured in the SRS DG535: T0, A, B, $\pm AB$, C, D, $\pm CD$. They are selected from the **Line** list. For each, one can change the **mode**

(TTL, NIM, ECL and VAR), **load** impedance, and **polarity** (except $\pm AB$ and $\pm CD$). In the Variable mode, it is possible to change the **amplitude** and **offset** voltages.



| Line | Mode | Load | Polarity | Amplitude | Offset |
|------|------|-------|----------|-----------|--------|
| T0 | VAR | HighZ | Normal | +1.0 V | 0.0 V |

C.6.2.3 Delay Line Parameters

For the SRS DG535 delay generator, the number of **delay lines** (A, B, C and D) is different from the number of output lines mentioned above. For each delay line, one can change the **delay time** by changing the number in the **Relative delay** box. The **reference line** for a delay line may be selected from the “**Line**” list. The format of the Relative delay line will then be as follows:

Delay line name = Delay Generator N + Reference line name + Relative delay time (in seconds)

The absolute delay time will be displayed in the **Absolute Delay** box and cannot be changed by typing in that box.

When there are a few delay generators controlled by the software and one of them controls the others through external triggering, it is possible to **synchronize** delay lines from different devices by checking the “**Slaved To Line**” box. Prior to that the following must be done:

1. Click on T0 delay line.
2. From the **Slave DelGel** list, choose the number of the master device that triggers the current device.
3. In the **Slave Line**, choose the delay line on the master device. It must be this line that triggers the current device.

4. Type the delay in the **Slave delay** box. This is the delay generator’s lag time between the External and T0 pulses. It is not zero.

5. Click “**Slaved To Line**” box.

6. Perform same operations for the desired line, choosing the desired slave delay time.

Now the Absolute Delay will be shown with respect to the T0 line of the **master** delay generator. Changing the relative delay time for the master delay line will automatically change delay for the slave delay line.

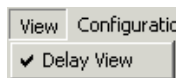
C.6.2.4 Save and Load Settings

All the device-specific settings described above may be **saved** to a file or **loaded** from a file. To do this, choose the “Configuration → Save/Load Delay Generator Config” menu. You will be prompted for a file name.

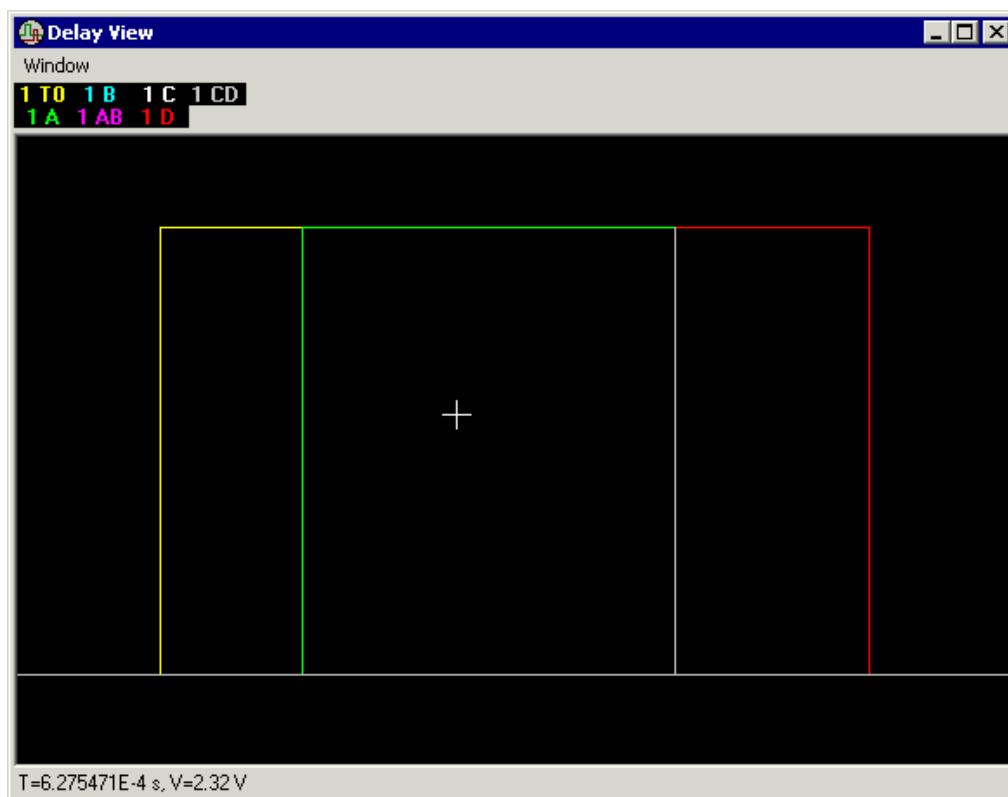
For the SRS DG535, it is possible to Store and Recall delay generator settings in devices designated memory locations 1 – 9 by clicking the “**Store**” and “**Recall**” buttons. The “**Clear**” button will set all device parameters to their factory default values.

C.6.3 Visualize Output Delay Pulses

Checking the “View → Delay View” menu will open the **Delay View** panel.



In this panel, output pulses from all delay generator output lines will be plotted as they would be seen with an oscilloscope. Current time and voltage values can be seen by moving the cursor over the black part of the panel. One can bring a trace for a selected line to the top by clicking its label. Double-clicking a label will allow the user to change the color for



that line. The label name is a combination of the device number in the Delay Generator panel and the output line name.

C.7 Photon Counter Panel

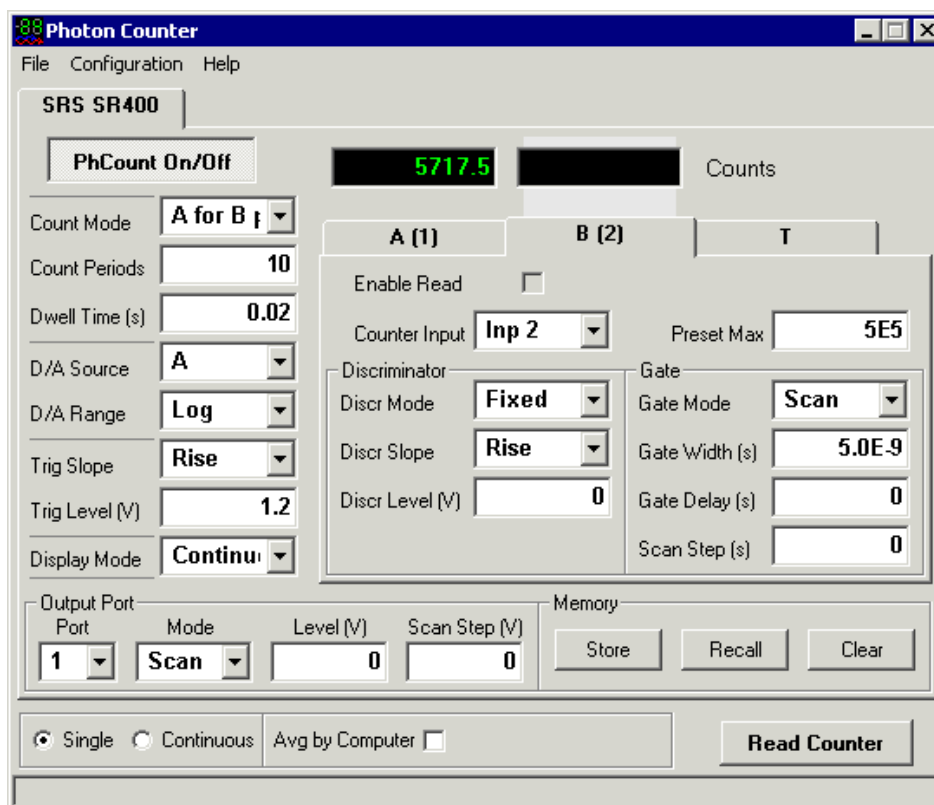
The Photon Counter sub-panel is the part of BGSpecT (C.1) that can simultaneously remotely control multiple independent photon counters.

The following are procedures that one can/should perform with the photon counters:

1. Setup communication parameters before establishing remote communication (C.7.1)
2. Setup photon counter parameters after remote communication has been established

(C.7.2)

3. Read counts (C.7.3)



C.7.1 Remote Parameters Setup

To prepare the panel and start communication with photon counter(s), one first needs to perform some setup through the “Configuration” menu. Please follow the general instructions on how to setup device communications (C.11), substituting the word Device with Photon Counter where applicable.



Supported photon counters are:

- Stanford Research Systems (SRS) SR400 (via GPIB and RS232)



If a few photon counters have been selected, one can switch between them either by clicking the photon counter tab or by choosing the “Configuration → Photon Counter N ” menu.

Once remote communication with the photon counter has been established (by clicking “PhCount On/Off” button), one can change photon counter settings and read counts.

C.7.2 Photon Counter Parameters

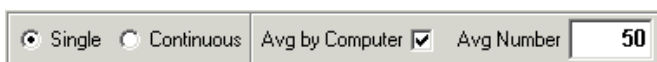
Photon Counter panel options span over:

1. Panel (all photon counters) – software acquisition and averaging modes
2. One photon counter (all device counter channels) – counting and display modes, triggering options, output ports
3. One counter channel – counter input, discriminator and gate options

One can also Save and Load a photon counter configuration to and from a file.

C.7.2.1 Panel Parameters

Panel-wide parameters are the software acquisition and averaging modes. Acquisition mode can be “Single” or “Continuous” (buttons are at the bottom of the Photon Counter panel). In “Single” mode, the counts are acquired only once. In “Continuous” mode, the counts are acquired until the “Read Counter” button is pressed again. This is done so that the software can effectively combine a few hardware photon counters into one software instrument.



For averaging, there is the option of “**Averaging by Computer**” for acquired counts. When this option is enabled, the counts are acquired by photon counters according to their settings and are then transferred to a PC and averaged by the software.

C.7.2.2 Common Photon Counter Parameters

Count Mode determines how the counting is performed (A,B, A–B, A+B for T preset, A for B preset). **Count Periods** determines the number of times the counters perform their job. The counts from each of these periods are then averaged into one number. That is why, sometimes, the final number of counts contains extra digits after the decimal point. If, in addition, the Averaging by Computer is performed, the data will be averaged twice. **Dwell Time** is the counter inactive time between two count periods.

D/A Source (A, B, A-B, A+B) and **D/A Range** (Log or Linear) set the front panel D/A output source and the scale range for it.

Trigger Slope (Rise or Fall) and **Trigger Level** determine these parameters for the external trigger input.

Display Mode switches between Continuous and Hold modes.

Output Port parameters determine the properties of Port1 and Port2 outputs on the back panel of the SRS SR400. For each **Port**, one can choose **Mode** (Fixed or Scan) and **Level**. In the Scan mode, **Scan Step** may be changed.

C.7.2.3 Counter Channel Parameters

The user can set up parameters for individual counter channels. Switching between the counters is done through the channel tab. The **name** of the channel tab is the name of the channel on the device (A, B, T). The number in parenthesis is the absolute **channel**

number in the software, and is used to identify counter channels in the Spectrum Scan panel (C.8). The number of channels on the photon counter is determined by the software automatically. If the software runs out of the maximum allowed number of channels (double the maximum number of devices in the Photon Counter panel), it may cut off some of the channels that do not fit.

The “**Enable Read**” check enables/disables downloading counts data from a photon counter to a PC.

Counter Input selects among allowed input channels for each counter (10 MHz, Input 1, Input 2, External Trigger). For a preset counter (usually T, but may be B in A for B preset count mode), one can change the counter preset maximum number (in 10 MHz clock cycles). If this number is reached during the counting, the experiment is ceased.

For each counter **Discriminator**, it is possible to change the **Discriminator Mode** (Fixed or Scan), **Discriminator Slope** (Rise or Fall) and **Discriminator Level**. In the Scan mode, **Scan Step** will also be available.

For counters A and B, one can select **Gate** parameters: **Gate Mode** (CW, Fixed or Scan), **Gate Width** and **Gate Delay**. In Scan mode, **Scan Step** will also be available.

C.7.2.4 Save and Load Settings

All of the above device-specific settings may be **saved** to a file or **loaded** from a file. To do this, choose the “Configuration → Save/Load Photon Counter Config” menu. You will be prompted for a file name.

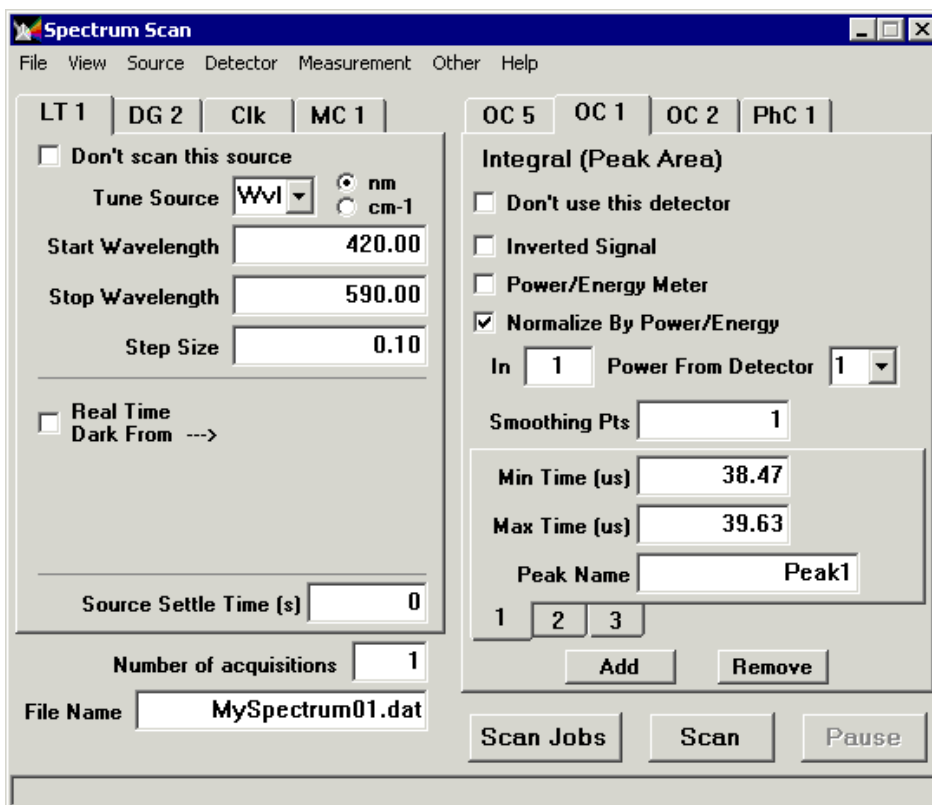
For the SRS SR400, it is possible to Store and Recall photon counter settings in devices designated memory locations 1 – 9 by clicking the “**Store**” and “**Recall**” buttons. The “**Clear**” button will set all device parameters to their factory default values.

C.7.3 Reading Counts

To read photon counter counts, click the “**Read Counter**” button in the bottom of the panel. If a few photon counters are turned On, counts will be read from all of them. Acquired counts are displayed at the top of the panel.

C.8 Spectrum Scan Panel

The Spectrum Scan sub-panel is part of BGSpecT (C.1) that uses instrument panels to record spectra. This powerful tool has many fine tuning settings that allow the user to perform more efficient and fast scans. It requires some time to set up, but then the scan can be completely automated and does not require human intervention.



To perform a successful scan, the following needs to be done:

1. Decide on your sources and detectors (C.8.1)
2. Setup sources (C.8.2)
3. Setup detectors (C.8.3)
4. Use Spectrum View (C.8.4)
5. Setup other features (C.8.5)
6. Perform the actual scan (C.8.6)

C.8.1 Sources and Detectors

In Spectrum Scan, the instruments are divided into sources and detectors.

Sources are instruments that are used to change some scan parameters such as wavelength, delay, etc. Hence, devices from Lambda Tune (C.2), Motion Control (C.4) and Delay Generator (C.6) panels may be used as scan sources. In addition, there is a built-in four-channel timer in Spectrum Scan that may be used as a source.

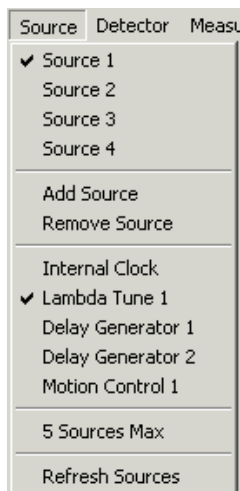
Detectors are instruments that are used to record data (e.g., waveforms, wavelengths). Hence, devices from Oscilloscope (C.5), Wavemeter (C.3) and Photon Counter (C.7) panels may be used as scan detectors.

It is advised to turn on all necessary source and detector devices using their panels before starting the Spectrum Scan panel. Doing so may save some confusion about device availability.

C.8.2 Sources Setup

The sources are located on the left side of the Spectrum Scan panel. The principle of working with sources is similar to that for devices in instrument panels. To access sources, one should first go to the “Source” menu and create a sufficient number by clicking the

“Source → Add Source” and the “Source → Remove Source” menus. Switching between different sources can be done either by clicking on the ‘Sources’ tab or by selecting the appropriate “Source → Source N ” menu. The maximum allowed number of sources (up to 128) can be changed by clicking “Source → N Sources Max” menu.



The user should next **assign** some device to each source. The order in which the sources are arranged is very important. When recording a spectrum, the sources are scanned in a nested loop order with the first source on the outermost (that is, the largest) loop and the last source on the inside (the smallest and therefore the most frequently repeated) loop.

Currently available source devices will be displayed under the “Source” menu. They will be in the form of menus with the device name and its number in the instrument panel. Only those devices that have been turned “On” (remote communication successfully established) will be shown. The Internal Clock will always be displayed, since it is built into the Spectrum Scan panel. It is possible to **refresh** the list of currently available source devices by clicking the “Source → Refresh Sources” menu.

To assign sources, first select the desired source and then choose an appropriate source device. Since many of the source devices have multiple channels, the same device may be

assigned to *multiple* sources, but each channel may be assigned to only *one* source. Upon successful assignment, the abbreviated name of the source will be displayed in the source tab.

After the sources have been assigned, each of them should be **configured**. First, a **channel** to scan should be selected for a source. For a lambda tune source, it will be a “Tune source” list; for a delay generator, “Delay Line”; for Motion Control, “MC Axis”; and for Internal Clock, “Clock Channel”. Only unassigned channels are displayed in this list.

In the case of the **wavelength**, the user can choose between nanometers and wavenumbers as units.

Now one should choose the desired **Start**, **Stop** and **Step** for the scan. In the case of the wavelength, only values within the lambda tune calibration range will be allowed. The Step Size may be larger than the difference between Stop and Start. In such a cases, only one source position will be used during the scan – Start.

If the menu “Other \longrightarrow Real Time Dark (Baseline)” is checked, one can collect the **baseline** signal in “real time.” In this case, at each source position before recording signal **all** sources, all except Internal Clocks will be moved to their “Dark” positions, that is where the signal consists only of noise, some reference value, or is “off-resonance,” etc. “Dark” signal collection happens inside the most enclosed loop, and so acquiring “dark” data doubles the scan time.

To configure **Real Time Dark**, first check the “Real Time Dark from” box. Then select a source and a channel. Only assigned source devices will be available here, but there is no limit on channel numbers. After that, type in the desired value for the “dark” position of that source.

| | | | |
|---|----------|---------|------|
| LT 1 | DG 2 | Clk | MC 1 |
| <input type="checkbox"/> Don't scan this source | | | |
| Delay Line | | B | |
| Start Delay (us) | | 400.000 | |
| Stop Delay (us) | | 600.000 | |
| Step Size (us) | | 10.000 | |
| <input checked="" type="checkbox"/> Real Time | Source | Chanl | |
| Dark From ---> | DG 2 | C | |
| "Dark" Position | 1000.000 | | |

If a delay generator was chosen as a scan source, it may be used to trigger the full data acquisition cycle (all necessary devices) from a computer. To do this, one should enable the **Master Trigger** mode by checking the “Other → Master Trigger” menu. Then, check the “Trig Master” box. Only one delay generator can be used for the Master Trigger, and it must be set to Single Shot triggering mode. The “Trig Rate” is the desired rate of triggering by computer. This is the maximum value. In case the whole data collection is slower than one triggering period, the actual triggering rate will be smaller. This is done to ensure that no data are lost.

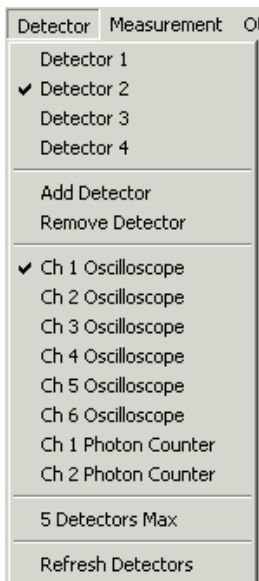
| | | |
|---|----------------|----|
| Trig Master <input checked="" type="checkbox"/> | Trig Rate (Hz) | 10 |
|---|----------------|----|

Source Settle Time is the amount of time between the end of moving the source to a new position and resetting the detectors to start data acquisition. This provides a waiting period for the system under study to adjust to the new conditions. In most cases this time is set to zero.

If for some reason the user does not wish to scan a certain source, it is possible to **disable** it for the scan by checking the “Don’t scan this source” box.

C.8.3 Detectors Setup

The detectors are located on the right side of the Spectrum Scan panel. The principle of working with detectors is similar to that used for sources. To access detectors, one should first go to the “Detector” menu and make enough boxes by clicking the “Detector → Add Detector” and the “Detector → Remove Detector” menus. Switching between different detectors can be done either by clicking on the ‘Detectors’ tab or by selecting the appropriate “Detector → Detector N ” menu. The maximum allowed number of detectors (up to 128) can be changed by clicking the “Detector → N Detectors Max” menu.

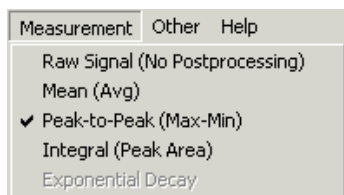


Then, detector should be **assigned** to a device. Currently available detector channels will be displayed under the “Detector” menu. They will be in the form of menus with the device name in the instrument panel and channel number. Only those device channels that have been turned “On” (remote communication successfully established) will be displayed. It is possible to **refresh** the list of currently available detector channels by clicking the “Detector → Refresh Detectors” menu.

To assign detectors, first select the desired detector and then choose an appropriate

device channel. The same device channel may be assigned to multiple detectors in order to be able to perform different post-processing mathematics. Upon successful assignment, the abbreviated name of the detector will be displayed in the detector tab.

After the detectors have been assigned, each of them should be **configured**. First, an available **measurement** type should be selected for a detector. This measurement will be used to find the final number that will be saved in the spectrum file.



There are a few possible measurement types:

1. **Raw Signal** – no post-processing is done

This is the only type available for the wavemeter and photon counter. For oscilloscopes, no number will be calculated or saved into the spectrum.

2. **Mean** – calculates the average value (mean) for all waveform points

3. **Peak-to-Peak** – finds the difference between the maximum and the minimum in the waveform

4. **Integral** – calculates the area under the curve

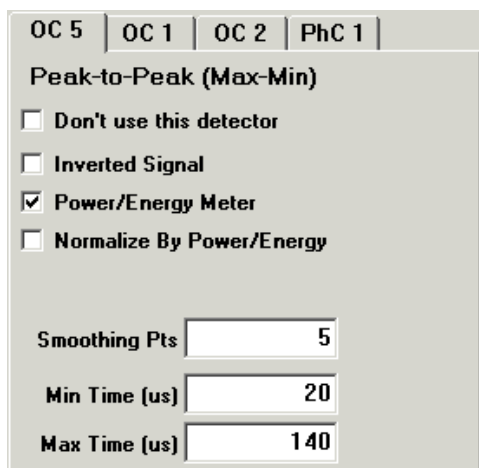
5. **Exponential Decay** – calculates the time constant for exponential decay

The user can decide if the original data from detector device should be **inverted** by checking “Inverted Signal” box. The “Power/Energy” meter box can be checked to indicate that the current detector is measuring something like laser **power** or **pulse** energy. This value might be used to normalize data from other detectors, for example.

In Integral measurements, one should make there are an appropriate number of “**peaks**”

– that is, ranges for curve integration. This is done by clicking the “Add” and “Remove” buttons in the bottom of the detector panel. Each of the peaks will then need Min/Max times assigned as well as the peak name.

In the case of an oscilloscope channel as a detector, one should choose the desired **Minimum** and **Maximum** times. They will determine the time interval over which to post-process the measurement. **Smoothing Points** are used in case there is a need to do intermediate data smoothing when performing measurement math.



OC 5 | OC 1 | OC 2 | PhC 1 |

Peak-to-Peak (Max-Min)

☐ Don't use this detector

☐ Inverted Signal

☒ Power/Energy Meter

☐ Normalize By Power/Energy

Smoothing Pts

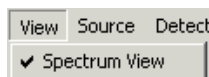
Min Time (us)

Max Time (us)

If for some reason, the user does not wish to use a certain detector, it is possible to **disable** it for the scan by checking the “Don’t use this detector” box.

C.8.4 Spectrum View

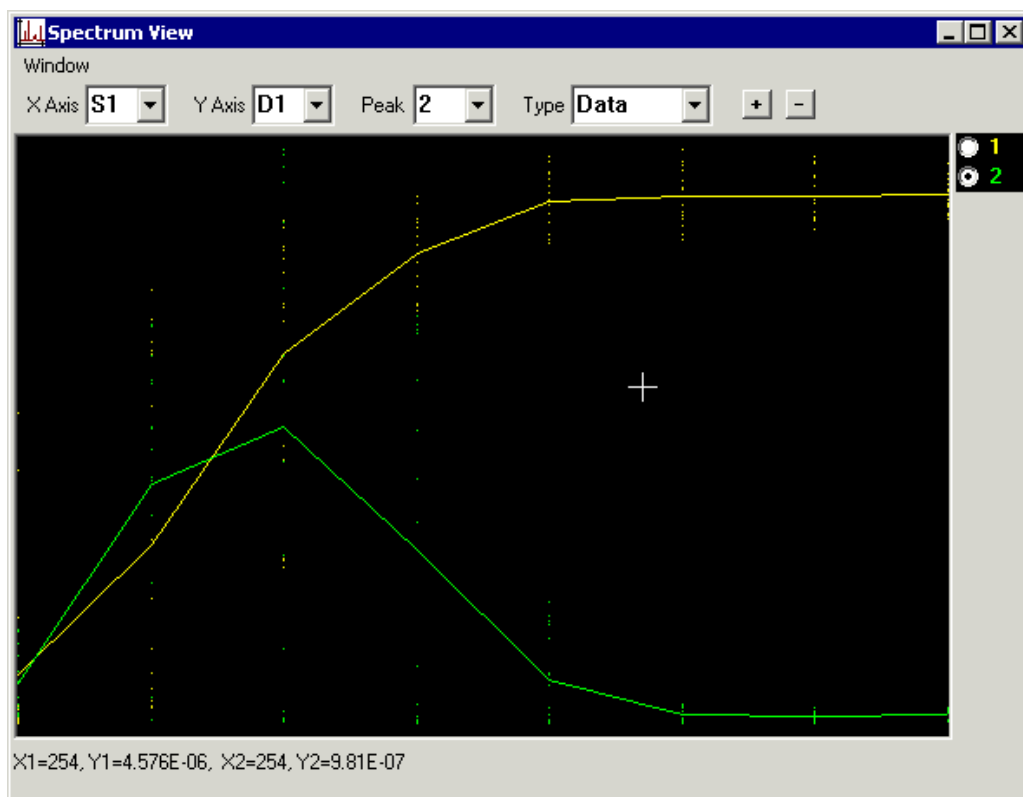
Acquired spectra can be viewed in the Spectrum View panel, accessed via the “View → Spectrum View” menu.



View | Source | Detect

✓ Spectrum View

In order to view spectral plots (traces) in Spectrum View, all parameters in that panel must be set before the beginning of the scan.



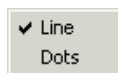
To **add** and **remove** traces, use the “+” and “-” buttons. Switching between different traces is done by clicking a trace’s label on the right side of the panel. Parameters of that trace will be displayed in boxes above the plot area.

For each trace, select references for the X and Y axes of the plot. For the **X** axis, it may be one of the **sources** or detectors (if detector is a wavemeter). For the **Y** axis, only **detectors** are allowed. If the measurement type for a detector is Integral, then the **Peak** box will appear, offering a selection of the peaks whose area is calculated in this detector measurement.

Then choose the plot **type**. It will usually be Data. If Real Time Dark baselining is enabled for some of the sources, Baseline may also be selected to plot the baseline only or Data-Bsl for a difference between normal and dark (baseline) data.

It is possible to change the trace **color** by double-clicking the trace label. Right-click

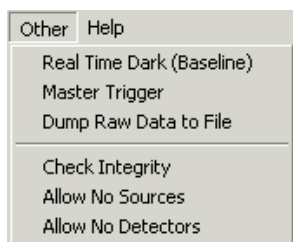
on the label to bring up a menu to choose the trace plotting style: **Line** or **Dots**. If Line is selected, the trace will be plotted as dots connected by lines. If there are a few dots with the same X and different Y, the average Y will be used to plot a line. This usually occurs for multi-dimensional scans (when using a few sources).



The scale on the plot is adjusted to fit the screen for each trace as new points are acquired. To view (X,Y) values, move the mouse over the plot. Current values will be displayed below the plot and in the tool tip.

C.8.5 Other Features

There are a few more things that may be adjusted. For example, the check “Other → Dump Raw Data to File” menu can be used to **save** all acquired waveforms for oscilloscope channel detectors. The files will be located in the directory with the same name as the spectrum file name and with the extension “.dir.” Individual file names will be made from source positions and detector channels. Waveforms acquired for normal source positions will have the extension “*.dat” and those for the “dark” source positions in Real Time Dark mode will have extensions “*.dat.bsl.”



The “Other → Check Integrity” menu will do a **self-test** to see if all settings are consistent with source and detector device settings. Such a test is always performed in the

beginning of each scan. If the test has been passed, the “Scan” button will be enabled, otherwise an error message will be displayed in the bottom of the Spectrum Scan panel. If you are sure that all settings are correct but you still get an error message in the status bar, or “Scan” button is disabled, click that menu to perform the integrity test again.

Usually, if there were no sources or detectors assigned, the integrity test will not allow the scan to be conducted. To override that, the user can check either the “Other → Allow No Sources” or “Other → Allow No Detectors” menus.

The “**Number of acquisitions**” button under the source panel determines how many times detector readings are performed at each source position. They are performed one after another at all source positions fixed (inside the most frequent source loop).

The **file name** to store the scan results may be chosen under the number of acquisitions. If a file with that name already exists, it will not be overwritten. Instead, another file with the same name and prefix “N_” will be created, where N is a positive number (1, 2, ...).

The **directory** for the scan file may be changed by clicking the “File → Set Spectrum Directory” menu.

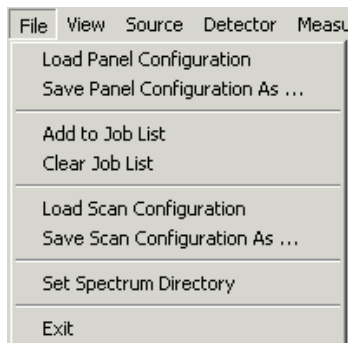
One can **Save** and **Load** the above settings into a series of files by clicking the “File → Save Scan Configuration As” and “File → Load Scan Configuration” menus. When the scan configuration is being loaded, the software will try to establish remote communication with all necessary devices if it has not been done.

Note that when using the delay generator as a source, its parameters are stored in and recalled from its memory location 9 and is therefore reserved.

If a few scans are to be performed without human intervention, it is possible to place a **few scan jobs** in a queue by clicking the “File → Add to Job List” menu. The list of such queued jobs may be **purged** by clicking the “File → Clear Job List” menu. The

scan jobs from this list are transferrable between program sessions. The list is **not** purged upon completion of all jobs in it. This should be done manually by clicking the “File → Clear Job List” menu.

Panel settings can be Saved and Loaded via the “File → Save Panel Configuration As” and “File → Load Panel Configuration” menus.



C.8.6 Performing the Scan

If everything was configured properly, the “**Scan**” button will be enabled. Click it to start the **scan**. If the scan needs to be aborted, click the “Scan” button again. This may be done both during the scan and when it was paused.

If there are any scan jobs queued in a **job list**, the “**Scan Jobs**” button will be enabled. By clicking it, one can perform scans from the list. In the case where no prior panel setup is required, scan job configurations will be loaded automatically and scans will be performed in the order of their appearance in the list. Pre-scan panel settings will be discarded if they were not added to the job list.

Clicking the “Scan Jobs” button again will abort all scans in the queue. Clicking the “Scan” button will stop only the current scan job. If there are more scans to be done, the program will proceed with them.

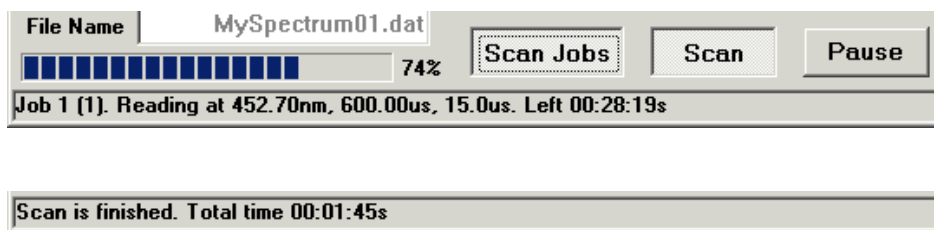
The scan may be **paused** by clicking the “**Pause**” button. This will not allow the user

to change scan parameters; however, it would be possible to adjust device parameters at their owner panels. To resume the scan, click the “Pause” button again. Please note that pausing the scan does not halt all operations immediately. Waiting to resume the scan is done after the current detector read cycle is finished.

The scan **results** are saved as lines with numbers separated by the *tab* symbol. The very first line of the file will have source and detector names for easier data identification. At the same time, selected traces are displayed in a Spectrum View (C.8.4) window (if opened).

The acquired data are added to the scan file. If something unexpected happens (computer or equipment crash), the data should not be lost.

During the scan, current job number, source positions and estimated time left will be displayed in the status bar at the bottom of the panel. There, Bsl stands for the “dark” source positions. The percentage of the scan performed will be displayed in a progress bar in the bottom left corner of the panel. When the scan is finished, the total scan time will be displayed.



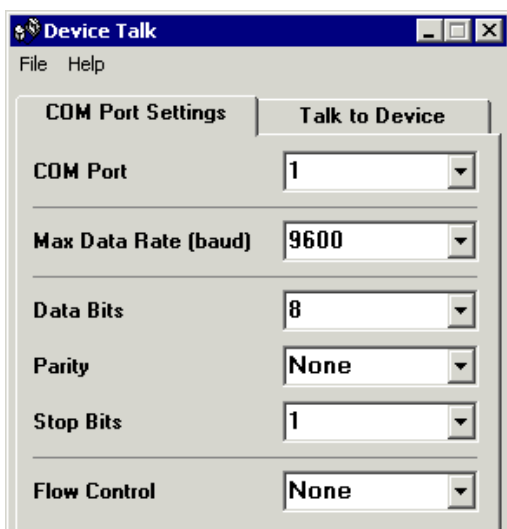
C.9 Device Talk Panel

Device Talk sub-panel is part of BGSpectT (C.1). It serves two purposes:

1. RS232 (COM) port parameter configuration (C.9.1)
2. Talking to GPIB and RS232 devices (C.9.2)

C.9.1 COM Port Settings

Before the connection between a PC and external device can be established via a serial port (COM, RS232), one should set up its parameters to match the hardware device settings. This can be done by selecting appropriate values in the boxes of the “COM Port Settings” tab. These settings may be changed as long as there is no connection with an external device. Once such communication is started, all boxes except the address (COM Port) will not be available for change, but will still show current parameters. All port settings from this tab are saved in configuration files “RS232__port__*N*.cps” in *Configs* directory, where *N* is the port number.



C.9.2 Talking to Devices

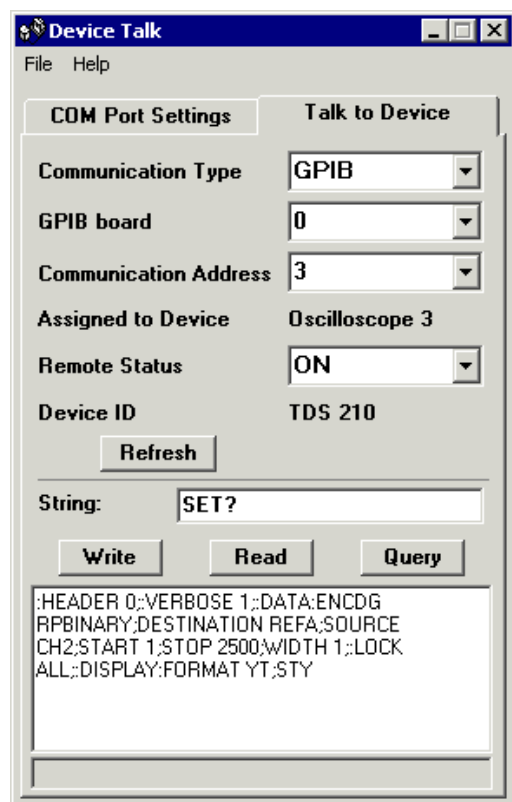
The “Talk to Device” tab allows the software to establish communication with devices, as well as send commands and receive device responses. It is useful if one needs to send a quick command to a remote device. It is also good for testing purposes.

Both GPIB and RS232 devices are supported in this tab. To be able to talk to a device, one should select its communication **Type** and **Address** (and **GPIB board** for GPIB

devices). In the case where these parameters were assigned to some device in one of the BGSpecT sub-panels, such information will be displayed.

One can Start/Stop communication with the device by selecting **Remote Status**. For assigned devices, this will also turn them On/Off in their owner panels. If an assigned device is turned On, its Device ID (as stored in the program) will be displayed. If the devices' remote status was changed via its owner panel, such information may be renewed by clicking the **“Refresh”** button.

It is possible to send a string (command) to a device by clicking the **“Write”** button. The response string from the device may be received by clicking the **“Read”** button. **“Query”** will do both Write and Read. The response from the device is displayed in the window below the buttons.



C.10 Devices

Devices are individual pieces of equipment. They usually have the same names as instruments, although many different devices may be the same kind of instrument. Device types are:

- Lambda Tune
- Wavemeter
- Motion Control
- Oscilloscope
- Delay Generator
- Photon Counter

C.11 Device Setup

After choosing some Instrument sub-panel from BGSpecT, the panel needs to be setup before communication takes place. There are some common guidelines on how to do this, independent of the instrument type.

Each Instrument panel can simultaneously control multiple devices. For example, the Oscilloscope panel can read waveforms from a few independent digital oscilloscopes without having to switch between them, i.e., turning one Off and another one On. Each of the oscilloscopes (or other type of instruments) are referred to as devices (C.10). To setup each device, one needs to follow a few steps by selecting a number of “Configuration” sub-menus:

1. Create device in the panel (C.11.1)
2. Choose device type (C.11.2)
3. Choose device communication type (C.11.3)

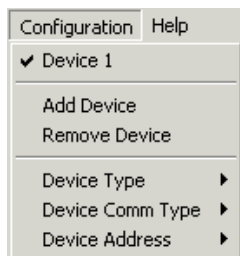
4. Choose device communication address (C.11.4)
5. Start communication (C.11.5)
- 6 (optional). Backup panel configuration (through “File” menu) (C.11.6)
7. Getting help (C.11.7)

C.11.1 Create Device

First, there should be a new device tab created for each device. This is done by clicking “Configuration → Add Device”. Each time another device is created, in addition to the new tab, a related “Configuration → Device N ” menu will appear where N is a number. One can create only a certain maximum number of devices that is specified for each instrument panel separately.

Switching between different devices is performed by choosing the respective tab or the “Configuration → Device N ” menu.

To remove unnecessary device tabs, one can use the “Configuration → Remove Device” menu. Each time it is clicked, it will remove the active (selected) device.



C.11.2 Device Type

Each device should be assigned a type, a communication address, and when applicable, a communication type.

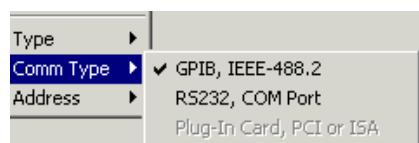
Usually, each instrument panel supports a few different device types. The device type

may be chosen through selecting one of the “Configuration → Device Type” sub-menus. This has to be done even if only one device type is supported by the current software version.

C.11.3 Device Communication Type

In most cases, each device has only one communication type. Physical equipment, represented by a device, may be either a PC plug-in card (PCI or ISA) or a stand alone unit with GPIB (IEEE-488.2) or RS232 (COM port on a PC) communication capabilities. Some stand alone units may have both GPIB and RS232 ports. In this case, if supported by the current version of software, the user can change that communication type through the the “Configuration → Device Comm Type” sub-menus. Otherwise, an appropriate menu will be selected automatically. In addition to this, for communication to take place one may need to carry out some additional steps.

For GPIB devices, a GPIB plug-in card must be installed in the computer along with the GPIB drivers. Both GPIB and RS232 equipment must be connected to a PC by appropriate cables. For RS232 devices, appropriate COM port parameters should be adjusted through the Device Talk (C.9) panel to match the settings on the device itself.



C.11.4 Device Communication Address

Next a communication address should be assigned to the device through one of the “Configuration → Device Address” sub-menus.

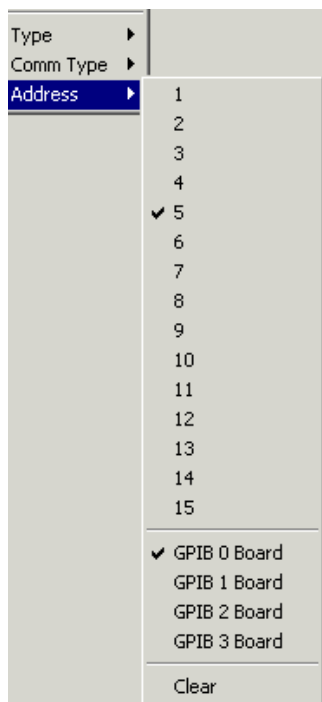
In the case of GPIB devices, it is a GPIB address selected on the physical equipment. It can be a number between 1 and 15. Also, for GPIB devices, one can select what GPIB

board the device is connected to by choosing one of the “Configuration → Device Address → GPIB *N* Board” sub-menus.

For RS232 devices, it is an address of a COM port on the PC through which communication is supposed to occur. Only addresses of installed COM ports are available.

For PC plug-in cards, the address is a card number or index. Usually, the card manufacturer will supply configuration software for their cards. In such cases, the device address is a card number or index in that configuration software. For example, GaGe CompuScope card numbering starts with 1; if there are 2 cards installed, one of them will have address 1 and another will have address 2. For PMC motion control cards, the numbering starts with 0.

For devices of the same communication type, the same address may be assigned only once. If the address needs to be re-assigned to another device, the user should free that address first by choosing the “Configuration → Device Address → Clear” menu.



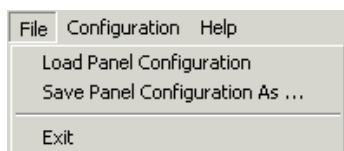
C.11.5 Turning Device On/Off

If all the above has been done correctly, the “Device On/Off” button (in the upper left corner of the panel) will become enabled. To start communication with the physical equipment, simply press this button. In most cases, the software will read device parameters from the equipment, i.e., time and voltage scales from the oscilloscope. In other cases, additional information will need to be supplied, i.e. a calibration file for Lambda Tune. In some stand alone units, when communication is started the panel with knobs on the equipment becomes locked and all control is performed through software only. This is why some functions *must* be set up manually prior to starting communication, in case they are not accessible with software. Remember that the actual equipment should have its power turned on. To gain access to the locked knobs, remote communication must be stopped by pressing the “Device On/Off” button again.

C.11.6 Panel Configuration Backup

Steps 1 through 4 do not have to be repeated every time the instrument panel is started. When closing the panel, information about tabs and devices will be saved in the .ini file. The next time the panel is opened, this information will be retrieved from the file, repeating steps 1-4, but communication will not be started automatically. Step 5 (C.11.5) should be done for each device again.

In addition to the .ini file, one can also save the necessary information to, and load it from, a file through the “File” sub-menus.



C.11.7 Help

A web browser must be installed to read the Help files. Pressing F1 will bring up help for the active device panel. It can also be selected from the “Help → Device Help” menu. “Help → BGSpecT Help” will bring up to the starting help page. “Help → About ...” menus will give a brief summary for the panel.



C.12 Readme

About Blake Group Spectroscopy Tools, version 3.2:

Blake Group Spectroscopy Tools is a set of tools for the remote control of the experiment and data collection. It consists of the following integrated modules:

Lambda Tune – controls multiple multi-axis lasers via Motion Control sub-panel and diode lasers via GPIB

Wavemeter – controls multiple wavemeters via GPIB and RS232

Motion Control – handles precision motion control micropositioners via PC plug-in cards (PCI or ISA)

Oscilloscope – controls multiple oscilloscopes via GPIB, RS232 and PC plug-in cards (PCI or ISA)

Delay Generator – controls multiple pulse delay generators via GPIB

Photon Counter – controls multiple photon counters via GPIB and RS232

Spectrum Scan – uses the above modules to acquire data (scan spectrum or any other

kind of signal dependence)

Device Talk – configures COM ports and talks to individual GPIB and RS232 devices

Useful features:

- Simultaneously controls multiple devices of the same kind
- Controls devices via GPIB and RS232 interfaces as well as PC plug-in cards (PCI or

ISA)

- Simultaneously controls multiple GPIB boards
- Smart oscilloscope waveform acquisition
- Wavelength source wavelength conversions
- Master/Slave locking of delay lines from pulse/delay generator
- Huge number of supported oscilloscopes
- Easy spectrum acquisition
- Flexible to configure
- User friendly interface. Partial Windows XP themes support

Installation.

To install the program, copy an executable BGSpecT.exe, along with the *Help* directory into your destination directory. You will also need to put the files from the *sys* directory into your Windows system directory (something like C:\Windows\System or C:\WINNT\system32 – the one that has many DLL files in it). If you are prompted to overwrite your existing files, choose No.

To uninstall this software from your system, just delete the executable and all unnecessary configuration files. No records are made in Windows registry during installation and

subsequent use of the program.

Hardware requirements:

Minimum

- CPU - Pentium or better
- RAM - 16 MB

Comfortable

- CPU - Pentium III, Athlon or better, 500 MHz or better
- RAM - 256 MB or larger

All necessary plug-in cards should be installed with the drivers supplied by the manufacturer.

Software requirements:

1. Microsoft Windows 95, 98, ME, NT (3.5+), 2000 or XP
2. Visual Basic 6 runtime files (can be downloaded from the Microsoft website)
3. All necessary drivers for hardware in use, i.e. drivers for GPIB cards (National Instruments only), GaGe CompuScope drivers (version 3.50 and higher), PMC motion control drivers (version 1.3 or higher)

All necessary drivers can be obtained from the hardware manufacturers, and must be installed and properly configured. To communicate with RS232 devices, COM ports should be physically present and enabled (installed) in Windows.

Known incompatibilities and limitations:

1. Hardware drivers. Sometimes plug-in card manufacturers will stop supporting old

hardware in their new driver releases, but the old drivers do not support new hardware. Precision MicroControl driver version 3.0+ supports only new PCI cards; for old ISA cards, use driver versions 2.23 and lower. GaGe CompuScope driver version 3.50 supports only new PCI cards (class CP500); for old ISA and class X012/PCI cards, use driver versions 3.46.02 and lower. However, the older drivers may be incompatible with a currently used SDK based on the 3.50.00 driver.

2. Some legacy devices support only IEEE-488.1 and not the IEEE-488.2 GPIB standard. They may be used with only 1 GPIB board in a system. Among currently supported by this software devices are: LeCroy 9400 oscilloscopes, SRS DG535 delay generators, Burleigh 1000 and 1500 wavemeters, and SRS SR400 photon counters.

3. When turning Off a GPIB device, some devices do not turn off from remote mode because of the above. This happens because these GPIB devices require sending a GPIB command that stops all GPIB communications with all GPIB devices on the bus. Such a command would also disconnect all other GPIB devices in use, and therefore, is sent only when turning Off the last device connected to the board.

4. For Tektronix oscilloscopes, extra options are not supported (such as extra memory, voltage probes, etc.). For GaGe oscilloscopes, some extra options are not supported (such as master/slave, multiple records).

C.13 License Agreement

Blake Group Spectroscopy Tools (BGSpect) software, California Institute of Technology.

End-User License Agreement.

PLEASE READ THIS DOCUMENT CAREFULLY BEFORE USING THE ENCLOSED

SOFTWARE. THIS AGREEMENT LICENSES THE USE OF THE ENCLOSED SOFTWARE TO YOU AND CONTAINS WARRANTY AND LIABILITY DISCLAIMERS. USING ANY PART OF THE SOFTWARE INDICATES THAT YOU ACCEPT THESE TERMS AND INDICATE YOUR ACCEPTANCE OF THIS LICENSE AGREEMENT AND WARRANTY. IF YOU DO NOT AGREE TO THE TERMS AND CONDITIONS OF THIS AGREEMENT, DO NOT USE THE SOFTWARE.

License:

This Agreement allows you to:

(a) Use the BGSpecT software on a single computer or a single System at a time. The BGSpecT software is licensed only for use on an Approved System.

(b) Make one copy of the BGSpecT software in machine-readable form solely for backup purposes. You must reproduce on any such copy all copyright notices and any other proprietary legends on the original copy of the BGSpecT software.

Restrictions:

You may not make or distribute any copy of BGSpecT software, or electronically transfer the BGSpecT software from one computer to another, or over a network, or from one System to another. You may not decompile, reverse engineer, disassemble, or otherwise reduce the BGSpecT software to a human-perceivable form. You may not modify, rent, lease, lend, resell for profit, distribute or create derivative works based upon the BGSpecT software or any part thereof.

Ownership and Distribution:

The foregoing license grants you limited rights to use the BGSpecT software. Although you own the disk or CD-ROM on which the BGSpecT software is recorded, you do not become the owner of, and California Institute of Technology (and its licensors) retains title to, the BGSpecT software, and all copies thereof, and all associated patent rights, copyrights, trade secret rights and other intellectual property rights therein and thereto. All rights not specifically granted in this Agreement are reserved by California Institute of Technology.

Warranty:

The BGSpecT software and information is provided “as is” without warranty of any kind, either expressed or implied, including but not limited to the implied warranties of merchantability and/or fitness for a particular purpose. The author takes no responsibility for any kind of damage caused by the BGSpecT software. Use this program at your own risk.

Bibliography

- [1] P. Jenniskens. “DIB Catalogue.” (2001). <http://www-space.arc.nasa.gov/~leonid/DIBcatalog.html>.
- [2] B.J. McCall (2004). <http://dib.uiuc.edu/~bjmccall/>.
- [3] N. Solcà and O. Dopfer. “Protonated benzene: IR spectrum and structure of C_6H_7^+ .” *Angew. Chem. Int. Ed.*, **41**, 3628–3631 (2002).
- [4] E. Anders and M. Ebihara. “Solar-system abundances of the elements.” *Geochim. Cosmochim. Acta*, **46**, 2363–2380 (1982).
- [5] P. Ehrenfreund and S.B. Charnley. “Organic molecules in the interstellar medium, comets, and meteorites: A voyage from dark clouds to the early earth.” *Annu. Rev. Astron. Astrophys.*, **38**, 427–483 (2000).
- [6] “Identified Interstellar and Circumstellar Molecules.” (2004). <http://www-691.gsfc.nasa.gov/cosmic.ice.lab/interste.htm>.
- [7] J. Cernicharo, A.M. Heras, A.G.G.M. Tielens, J.R. Pardo, F. Herpin, M. Guélin and L.B.F.M. Waters. “Infrared Space Observatorys discovery of C_4H_2 , C_6H_2 , and benzene in CRL 618.” *Astrophys. J.*, **546**, L123-L126 (2001).
- [8] F.C. Gillett, W.J. Forrest and K.M. Merrill. “8–13-micron spectra of NGC-7027, BD+30°3639, and NGC-6572.” *Astrophys. J.*, **183**, 87–93 (1973).

- [9] R.W. Russell, B.T. Soifer and S.P. Willner. “4 to 8 micron spectrum of NGC-7027.” *Astrophys. J.*, **217**, L149–L153 (1977).
- [10] M.M. Phillips, D.K. Aitken and P.F. Roche. “8–13- μ m spectrophotometry of galaxies. 1. Galaxies with giant H–II region nuclei.” *Mon. Not. R. Astron. Soc.*, **207**, 25–33 (1984).
- [11] S.P. Willner, R.C. Puetter, R.W. Russell and B.T. Soifer. “Unidentified infrared spectral features.” *Astrophys. Space Sci.*, **65**, 95–101 (1979).
- [12] D.K. Aitken. C.G. Wynn-Williams, D.P. Cruikshank, eds., “*Infrared astronomy*.” 207, Reidel, Dordrecht (1981).
- [13] S.P. Willner. M.F. Kessler, J.P. Phillips, eds., “*Galactic and extragalactic infrared spectroscopy*.” 37, Reidel, Dordrecht (1984).
- [14] K. Sellgren. “Spatial observations of the Orion nebula in the unidentified 3.28 micron feature.” *Astrophys. J.*, **245**, 138–147 (1981).
- [15] A. Léger and J.L. Puget. “Identification of the “unidentified” IR emission features of interstellar dust?”, *Astron. Astrophys.*, **137**, L5–L8 (1984).
- [16] L.J. Allamandola and A.G.G.M. Tielens, and J.R. Barker. “Polycyclic aromatic hydrocarbons and the Unidentified Infrared Emission bands: Auto exhaust along the Milky Way.” *Astrophys. J.*, **299**, L93–L97 (1985).
- [17] W.W. Duley, D.A. Williams. “The infrared spectrum of interstellar dust: Surface functional groups on carbon.” *Mon. Not. R. Astron. Soc.*, **196**, 269–274 (1981).

- [18] M. Cohen, A.G.G.M. Tielens and L.J. Allamandola. “A new emission feature in *IRAS* spectra and the polycyclic aromatic hydrocarbon spectrum.” *Astrophys. J.*, **299**, L93–L97 (1985).
- [19] L.J. Allamandola, A.G.G.M. Tielens and J.R. Barker. “Interstellar polycyclic aromatic hydrocarbons: The infrared emission bands, the excitation/emission mechanism, and the astrophysical implications.” *Astrophys. J. Suppl. Ser.*, **71**, 733–775 (1989).
- [20] L.J. Allamandola, S.A. Sandford, D.M. Hudgins, F.C. Witteborn. “Airborne and laboratory studies of interstellar PAHs.” In “*Airborne astronomy symposium on the galactic ecosystem.*” M.R. Haas, J.A. Davidson, E.F. Erickson, eds., no. 73, 23–32, San Francisco (1995). Astronomical Society of the Pacific.
- [21] A.G.G.M. Tielens, E. Peeters, S. Palfner, C. Kramer, C. Straubmeier, A. Heithausen, eds., “*The dense interstellar medium in galaxies.*” 497–506, Springer-Verlag, Berlin (2004).
- [22] J. Szczepanski and M. Vala. “Laboratory evidence for ionized polycyclic aromatic hydrocarbons in the interstellar medium.” *Nature*, **363**, 699–701 (1993).
- [23] D.M. Hudgins, C.W. Bauschlicher, Jr, L.J. Allamandola. “Closed-shell polycyclic aromatic hydrocarbon cations: a new category of interstellar polycyclic aromatic hydrocarbons.” *Spectrochim. Acta A*, **57**, 907–930 (2001).
- [24] D.M. Hudgins and L.J. Allamandola. “Interstellar PAH emission in the 11-14 micron region: New insights from laboratory data and a tracer of ionized PAHs.” *Astrophys. J.*, **516**, L41–L44 (1999).

- [25] E. Dwek, R.G. Arendt, D.J. Fixsen, T.J. Sodroski, N. Odegard, J.L. Weiland, W.T. Reach, M.G. Hauser, T. Kelsall, S.H. Moseley, R.F. Silverberg, R.A. Shafer, J. Ballester, D. Bazell, and R. Isaacman. “Detection and characterization of cold interstellar dust and polycyclic aromatic hydrocarbon emission, from *COBE* observations.” *Astrophys. J.*, **475**, 565–579 (1997).
- [26] A.G.G.M. Tielens and T.P. Snow, eds. “*The Diffuse Interstellar Bands.*” Kluwer Academic Press, Dordrecht (1994).
- [27] M.L. Heger. *Lick Obs. Bull.*, **10**, 146 (1922).
- [28] P.W. Merrill. *Publs. Astr. Soc. Pacific*, **46**, 206 (1934).
- [29] P.W. Merrill. *Publs. Astr. Soc. Pacific*, **48**, 179 (1936).
- [30] G.H. Herbig. “The diffuse interstellar bands. IV. The region 4400–6850 Å.” *Astrophys. J.*, **196**, 129–162 (1975).
- [31] P. Jenniskens and F.-X. Desert. “A survey of diffuse interstellar bands (3800 – 8680 Å).” *Astron. Astrophys. Suppl. Ser.*, **106**, 39–78 (1994).
- [32] J. Krelowski, C. Sneden, D. Hiltgen. “A survey of weak diffuse interstellar bands in selected ranges between 5600 and 7000 Å.” *Planet. Space Sci.*, **43**, 1195–1203 (1995).
- [33] P. Jenniskens, I. Porceddu, P. Benvenuti, and F.-X. Desert. “Diffuse interstellar bands: Resolved rotational band structure at 5850 Å.” *Astron. Astrophys.*, **313**, 649–656 (1996).
- [34] L.J. Allamandola. “Laboratory studies of DIB carriers.” A.G.G.M. Tielens and T.P. Snow, eds., “*The Diffuse Interstellar Bands.*” Kluwer Academic Press, Dordrecht (1994).

- [35] S. Leach. "Spectroscopy and photophysics of possible large molecule carriers of the diffuse interstellar bands." A.G.G.M. Tielens and T.P. Snow, eds., *"The Diffuse Interstellar Bands."* Kluwer Academic Press, Dordrecht (1994).
- [36] A.E. Douglas. "Origin of diffuse interstellar lines." *Nature*, **269**, 130-132 (1977).
- [37] P. Thaddeus. "Carbon chains and the diffuse interstellar bands." A.G.G.M. Tielens and T.P. Snow, eds., *"The Diffuse Interstellar Bands."* Kluwer Academic Press, Dordrecht (1994).
- [38] M.B. Bell, P.A. Feldman, M.J. Travers, M.C. McCarthy, C.A. Gottlieb and P. Thaddeus. "Detection of HC₁₁N in the cold dust cloud TMC-1." *Astrophys. J.*, **483**, L61–L64 (1997).
- [39] M.B. Bell, P.A. Feldman, J.K.G. Watson, M.C. McCarthy, M.J. Travers, C.A. Gottlieb and P. Thaddeus. "Observations of long C_nH molecules in the dust cloud TMC-1." *Astrophys. J.*, **518**, 740–747 (1999).
- [40] M.C. McCarthy, M.J. Travers, A. Kovács, C.A. Gottlieb and P. Thaddeus. "Eight new carbon chain molecules." *Astrophys. J. Suppl. Ser.*, **113**, 105–120 (1997).
- [41] P. Thaddeus, M.C. McCarthy, M.J. Travers, C.A. Gottlieb and W. Chen. "New carbon chains in the laboratory and in interstellar space." *Faraday Discuss.*, **109**, 121–135 (1998).
- [42] M.C. McCarthy and P. Thaddeus. "Microwave and laser spectroscopy of carbon chains and rings." *Chem. Soc. Rev.*, **30**, 177–185 (2001).
- [43] J.P. Maier. "Electronic spectroscopy of carbon chains." *Chem. Soc. Rev.*, **26**, 21–28 (1997).

- [44] J.P. Maier. “Electronic spectroscopy of carbon chains.” *J. Phys. Chem. A*, **102**, 3462–3469 (1998).
- [45] D.A. Kirkwood, M. Tulej, M.V. Pachkov, M. Schnaiter, F. Guthe, M. Grutter, M. Wyss and J.P. Maier, G. Fischer. “Electronic spectra of carbon chain anions: $C_{2n}H^-$ ($n=5-12$).” *J. Chem. Phys.*, **111**, 9280–9286 (1999).
- [46] T. Piño, H.B. Ding, F. Guthe and J.P. Maier. “Electronic spectra of the chains $HC_{2n}H$ ($n=8-13$) in the gas phase.” *J. Chem. Phys.*, **114**, 2208–2212 (2001).
- [47] H. Ding, T.W. Schmidt, T. Piño, A.E. Boguslavskiy, F. Guthe and J.P. Maier. “Gas phase electronic spectra of the linear carbon chains $HC_{2n+1}H$ ($n = 3-6, 9$).” *J. Chem. Phys.*, **119**, 814–819 (2003).
- [48] M. Tulej, D.A. Kirkwood, G. Maccaferri, O. Dopfer and J.P. Maier. “Electronic spectra of linear carbon anions.” *Chem. Phys.*, **228**, 293–299 (1998).
- [49] M. Tulej, D.A. Kirkwood, M. Pachkov and J.P. Maier. “Gas-phase electronic transitions of carbon chain anions coinciding with diffuse interstellar bands.” *Astrophys. J.*, **506**, L69–L73 (1998).
- [50] G.A. Galazutdinov, J. Krelowski and F.A. Musaev. “On bare carbon chain anions as possible carriers of the diffuse interstellar features.” *Mon. Not. R. Astron. Soc.*, **310**, 1017–1022 (1999).
- [51] B.J. McCall, J. Thorburn, L.M. Hobbs, T. Oka and D.G. York. “Rejection of the C_7^- diffuse interstellar band hypothesis.” *Astrophys. J.*, **559**, L49–L53 (2001).
- [52] T. Motylewski, H. Linnartz, O. Vaizert and J.P. Maier, G.A. Galazutdinov and F.A. Musaev, J. Krelowski, G.A.H. Walker and D.A. Bohlender. “Gas-phase electronic

spectra of carbon-chain radicals compared with diffuse interstellar band observations.”

Astrophys. J., **531**, 312–320 (2000).

- [53] J.P. Maier, G.A.H. Walker and D.A. Bohlender. “On the possible role of carbon chains as carriers of diffuse interstellar bands.” *Astrophys. J.*, **602**, 286–290 (2004).
- [54] F. Salama, G.A. Galazutdinov, J. Krelowski, L.J. Allamandola and F.A. Musaev. “Polycyclic aromatic hydrocarbons and the diffuse interstellar bands: A survey.” *Astrophys. J.*, **526**, 265–273 (1999).
- [55] J. Krelowski, G.A. Galazutdinov, F.A. Musaev and J. Nirski. “Identification of naphthalene cation in space?”, *Mon. Not. R. Astron. Soc.*, **328**, 810–814 (2001).
- [56] R. Ruiterkamp, T. Halasinski, F. Salama, B.H. Foing, L.J. Allamandola, W. Schmidt and P. Ehrenfreund. “Spectroscopy of large PAHs. Laboratory studies and comparison to the Diffuse Interstellar Bands.” *Astron. Astrophys.*, **390**, 1153–1170 (2002).
- [57] T.M. Halasinski, D.M. Hudgins, F. Salama, L.J. Allamandola, T. Bally. “Electronic absorption spectra of neutral pentacene ($C_{22}H_{14}$) and its positive and negative ions in Ne, Ar, and Kr matrices.” *J. Phys. Chem. A*, **104**, 7484–7491 (2000).
- [58] C. Joblin, F. Salama, L. Allamandola. “Absorption and emission spectroscopy of perylene ($C_{20}H_{12}$) isolated in Ne, Ar, and N_2 matrices.” *J. Chem. Phys.*, **110**, 7287–7297 (1999).
- [59] F. Salama, C. Joblin and L.J. Allamandola. “Electronic absorption spectroscopy of matrix-isolated polycyclic aromatic hydrocarbon cations. II. The phenanthrene cation ($C_{14}H_{10}^+$) and its 1-methyl derivative.” *J. Chem. Phys.*, **101**, 10252–10262 (1994).

- [60] M. Hartmann, A. Lindinger, J.P. Toennies and A.F. Vilesov. “The phonon wings in the $S_1 \leftarrow S_0$ spectra of tetracene, pentacene, porphin and phthalocyanine in liquid helium droplets.” *Phys. Chem. Chem. Phys.*, **4**, 4839–4844 (2002).
- [61] G. Rouillé, S. Krasnokutski, F. Huisken, and T. Henning, O. Sukhorukov and A. Staicu. “Ultraviolet spectroscopy of pyrene in a supersonic jet and in liquid helium droplets.” *J. Chem. Phys.*, **120**, 6028–6034 (2004).
- [62] D. Romanini, L. Biennier, F. Salama, A. Kachanov, L.J. Allamandola, F. Stoeckel. “Jet-discharge cavity ring-down spectroscopy of ionized polycyclic aromatic hydrocarbons: Progress in testing the PAH hypothesis for the diffuse interstellar band problem.” *Chem. Phys. Lett.*, **303**, 165–170 (1999).
- [63] L. Biennier, F. Salama and L.J. Allamandola, J.J. Scherer. “Pulsed discharge nozzle cavity ringdown spectroscopy of cold polycyclic aromatic hydrocarbon ions.” *J. Chem. Phys.*, **118**, 7863–7872 (2003).
- [64] L. Biennier, F. Salama and M. Gupta, A. O’Keefe. “Multiplex integrated cavity output spectroscopy of cold PAH cations.” *Chem. Phys. Lett.*, **387**, 287–294 (2004).
- [65] L.A. Chewter, M. Sander, K. Müller–Dethlefs and E.W. Schlag. “High resolution zero kinetic energy photoelectron spectroscopy of benzene and determination of the ionization potential.” *J. Chem. Phys.*, **86**, 7763–7772 (1987).
- [66] G.I. Nemeth, H.L. Selzle and E.W. Schlag. “Magnetic ZEKE experiments with mass analysis.” *Chem. Phys. Lett.*, **215**, 151–155 (1993).
- [67] J.A. Syage and J.E. Wessel. “Resonance ion dissociation spectroscopy of naphthalene ions prepared in a supersonic expansion.” *J. Chem. Phys.*, **87**, 3313–3320 (1987).

- [68] M.C.R. Cockett, H. Ozeki, K. Okuyama and K. Kimura. "Vibronic coupling in the ground cationic state of naphthalene: A laser threshold photoelectron [zero kinetic energy (ZEKE)-photoelectron] spectroscopic study." *J. Chem. Phys.*, **98**, 7763–7772 (1993).
- [69] M.C.R. Cockett and K. Kimura. "A study of anthracene-Ar_n ($n = 0-5$) in the ground cationic state by laser threshold photoelectron spectroscopy: Selective ionization of complex isomers formed in the free jet expansion." *J. Chem. Phys.*, **100**, 3429–3441 (1994).
- [70] T. Vondrak, S. Sato and K. Kimura. "Zero kinetic energy photoelectron study of the naphthalene-Ar van der Waals complex." *Chem. Phys. Lett.*, **261**, 481–485 (1996).
- [71] T. Pino, N. Boudin and P. Bréchnignac. "Electronic absorption spectrum of cold naphthalene cation in the gas phase by photodissociation of its van der Waals complexes." *J. Chem. Phys.*, **111**, 7337–7347 (1999).
- [72] P. Bréchnignac and T. Pino. "Electronic spectra of cold gas phase PAH cations: Towards the identification of the Diffuse Interstellar Bands carriers." *Astron. Astrophys.*, **343**, L49-L52 (1999).
- [73] P. Bréchnignac, T. Pino, N. Boudin. "Laboratory spectra of cold gas phase polycyclic aromatic hydrocarbon cations, and their possible relation to the diffuse interstellar bands." *Spectrochim. Acta A*, **57**, 745–756 (2001).
- [74] N. Boudin, T. Pino and P. Bréchnignac. "Visible spectroscopy of polycyclic aromatic hydrocarbons ionic derivatives: Application to astrophysics." *J. Mol. Struct.*, **563**, 209–214 (2001).

- [75] T.P. Snow, V. Le Page, Y. Keheyian and V.M. Bierbaum. “The interstellar chemistry of PAH cations.” *Nature*, **391**, 259–260 (1998).
- [76] E. Herbst and V. Le Page. “Do H atoms stick to PAH cations in the interstellar medium?”, *Astron. Astrophys.*, **344**, 310–316 (1999).
- [77] T.R. Geballe and T. Oka. “Detection of H_3^+ in interstellar space.” *Nature*, **384**, 334–335 (1996).
- [78] B.J. McCall, K.H. Hinkle, T.R. Geballe and T. Oka. “ H_3^+ in dense and diffuse clouds.” *Faraday Discuss.*, **109**, 267–280 (1998).
- [79] P.J. Huggins, T.G. Phillips, G. Neugebauer, M.W. Werner, P.G. Wannier and D. Ennis. “Detection of the $J = 3-2$ lines of HCN, HNC, and HCO^+ in the Orion molecular cloud.” *Astrophys. J.*, **227**, 441–445 (1979).
- [80] A. Wootten, J.G. Mangum, B.E. Turner, M. Bogey, F. Boulanger, F. Combes, P.J. Encrenaz and M. Gerin. “Detection of interstellar H_3O^+ : A confirming line.” *Astrophys. J.*, **380**, L79–L83 (1991).
- [81] T.G. Phillips, E.F. van Dishoeck and J. Keene. “Interstellar H_3O^+ and its relation to the O_2 and H_2O abundances.” *Astrophys. J.*, **399**, 533–550 (1992).
- [82] D.B. Milligan, P.F. Wilson, C.G. Freeman, M. Meot-Ner (Mautner) and M.J. McEwan. “Dissociative proton transfer reactions of H_3^+ , N_2H^+ , and H_3O^+ with acyclic, cyclic, and aromatic hydrocarbons and nitrogen compounds, and astrochemical implications.” *J. Phys. Chem. A*, **106**, 9745–9755 (2002).

- [83] V. Le Page, T.P. Snow and V.M. Bierbaum. "Hydrogenation and charge states of PAHs in diffuse clouds. I. Development of a model." *Astrophys. J. Suppl. Ser.*, **132**, 233–251 (2001).
- [84] V. Le Page, T.P. Snow and V.M. Bierbaum. "Hydrogenation and charge states of PAHs in diffuse clouds. II. Results." *Astrophys. J.*, **584**, 316–330 (2003).
- [85] G.A. Olah. "Aromatic substitution. XXVIII. Mechanism of electrophilic aromatic substitutions." *Acc. Chem. Res.*, **4**, 240–248 (1971).
- [86] C. Reid. "The aromatic carbonium ions." *J. Am. Chem. Soc.*, **76**, 3264–3268 (1954).
- [87] von H. Luther and G. Pockels. "Molekülverbindungen mit ansolvosäuren. 1. Ultraviolettspektren von systemen aromat–aluminiumhalogenid–(halogenwasserstoff)." *Z. Elektrochem.*, **59**, 159–168 (1955).
- [88] H.-H. Perkampus and E. Baumgarten. "Proton-addition complexes of aromatic hydrocarbons." *Angew. Chem. Int. Ed.*, **3**, 776–783 (1964).
- [89] B.S. Freiser and J.L. Beauchamp. "Photochemistry of organic ions in the gas phase. Comparison of the gas phase photodissociation and solution absorption spectra of benzoyl cation, protonated benzene and protonated mesitylene." *J. Am. Chem. Soc.*, **98**, 3136–3139 (1976).
- [90] B.S. Freiser and J.L. Beauchamp. "Acid-base properties of molecules in excited electronic states utilizing ion cyclotron resonance spectroscopy." *J. Am. Chem. Soc.*, **99**, 3214–3225 (1977).
- [91] J.L. Beauchamp. Private communication.

- [92] H.-J. Köhler and H. Lischka. "Theoretical investigations on carbocations. Structure and stability of $C_3H_5^+$, $C_4H_9^+$ (2-butyl cation), $C_5H_5^+$, $C_6H_7^+$ (protonated benzene) and $C_7H_{11}^+$ (2-norbornyl cation)." *J. Am. Chem. Soc.*, **101**, 3479–3486 (1979).
- [93] M. Eckert-Maksić, Z.B. Maksić and M. Klessinger. "Protonation of fused aromatic systems – ab-initio study of some model Wheland intermediates." *Int. J. Quantum Chem.*, **49**, 383–396 (1994).
- [94] M.N. Glukhovtsev, A. Pross, A. Nicolaides and L. Radom. "Is the most stable gas-phase isomer of the benzenium cation a face-protonated π -complex?" *J. Chem. Soc. Chem. Commun.*, **1**, 2347–2348 (1995).
- [95] R. Sumathy and E.S. Kryachko. "Multiprotonation of benzene: a theoretical study." *J. Phys. Chem. A*, **106**, 510–519 (2002).
- [96] N. Solcà and O. Dopfer. "Interaction of the benzenium ion with inert ligands: IR spectra of $C_6H_7^+-L_n$ cluster cations ($L = Ar, N_2, CH_4, H_2O$)." *Chem. Eur. J.*, **9**, 3154–3163 (2003).
- [97] W. Jones, P. Boissel, B. Chiavarino, M.E. Crestoni, S. Fornarini, J. Lemaire and P. Maitre. "Infrared fingerprint of protonated benzene in the gas phase." *Angew. Chem. Int. Ed.*, **42**, 2057–2059 (2003).
- [98] M.J. Frisch, G.W. Trucks, H.B. Schlegel, G.E. Scuseria, M.A. Robb, J.R. Cheeseman, V.G. Zakrzewski, J.A. Montgomery, Jr, R.E. Stratmann, J.C. Burant, S. Dapprich, J.M. Millam, A.D. Daniels, K.N. Kudin, M.C. Strain, O. Farkas, J. Tomasi, V. Barone, M. Cossi, R. Cammi, B. Mennucci, C. Pomelli, C. Adamo, S. Clifford, J. Ochterski, G.A. Petersson, P.Y. Ayala, Q. Cui, K. Morokuma, D.K. Malick, A.D. Rabuck, K.

- Raghavachari, J.B. Foresman, J. Cioslowski, J.V. Ortiz, A.G. Baboul, B.B. Stefanov, G. Liu, A. Liashenko, P. Piskorz, I. Komaromi, R. Gomperts, R.L. Martin, D.J. Fox, T. Keith, M.A. Al-Laham, C. Y. Peng, A. Nanayakkara, M. Challacombe, P.M.W. Gill, B. Johnson, W. Chen, M.W. Wong, J.L. Andres, C. Gonzalez, M. Head-Gordon, E.S. Replogle and J.A. Pople. “*GAUSSIAN 98, Revision A.9.*” Gaussian, Inc., Pittsburgh, PA (1998).
- [99] P. Hohenberg and W. Kohn. “Inhomogeneous electron gas.” *Phys. Rev.*, **136**, B864–B871 (1964).
- [100] W. Kohn and L.J. Sham. “Self-consistent equations including exchange and correlation effects.” *Phys. Rev.*, **140**, A1133–A1138 (1965).
- [101] A.D. Becke. “Density-functional thermochemistry. III. The role of exact exchange.” *J. Chem. Phys.*, **98**, 5648–5652 (1993).
- [102] C. Lee, W. Yang and R.G. Parr. “Development of the Colle-Salvetti correlation-energy formula into a functional of the electron density.” *Phys. Rev. B*, **37**, 785–789 (1988).
- [103] A.D. McLean and G.S. Chandler. “Contracted Gaussian basis sets for molecular calculations. I. Second row atoms, Z=11–18.” *J. Chem. Phys.*, **72**, 5639–5648 (1980).
- [104] R. Krishnan, J.S. Binkley, R. Seeger and J.A. Pople. “Self-consistent molecular orbital methods. XX. A basis set for correlated wave functions.” *J. Chem. Phys.*, **72**, 650–654 (1980).
- [105] M.J. Frisch, J.A. Pople and J.S. Binkley. “Self-consistent molecular orbital methods. 25. Supplementary functions for Gaussian basis sets.” *J. Chem. Phys.*, **80**, 3265–3269 (1984).

- [106] T. Clark, J. Chandrasekhar, G.W. Spitznagel and P.v.R. Schleyer. "Efficient diffuse function-augmented basis-sets for anion calculations. 3. The 3-21+G basis set for 1st-row elements, LI-F." *J. Comp. Chem.*, **4**, 294–301 (1983).
- [107] "*GaussView, ver. 2.1.*" Gaussian, Inc., Pittsburgh, PA (2000).
- [108] A.P. Scott and L. Radom. "Harmonic vibrational frequencies: An evaluation of Hartree-Fock, Møller-Plesset, quadratic configuration interaction, density functional theory, and semiempirical scale factors." *J. Phys. Chem.*, **100**, 16502–16513 (1996).
- [109] J.M.L. Martin, J. El-Yazal and J.-P. François. "Structure and vibrational spectrum of some polycyclic aromatic compounds studied by density functional theory. 1. Naphthalene, azulene, phenanthrene and anthracene." *J. Phys. Chem.*, **100**, 15358–15367 (1996).
- [110] M.W. Wong. "Vibrational frequency prediction using density functional theory." *Chem. Phys. Lett.*, **256**, 391–399 (1996).
- [111] A. Miani, E. Cané, P. Palmieri and A. Trombetti, N.C. Handy. "Experimental and theoretical anharmonicity for benzene using density functional theory." *J. Chem. Phys.*, **112**, 248–259 (2000).
- [112] E. Cané, A. Miani, P. Palmieri, R. Tarroni and A. Trombetti. "The gas-phase infrared spectra of anthracene- h_{10} and anthracene- d_{10} ." *J. Chem. Phys.*, **106**, 9004–9012 (1997).
- [113] "NIST Chemistry WebBook." (2003). <http://webbook.nist.gov/chemistry/>.
- [114] E.P. Hunter, S.G. Lias. "Evaluated gas phase basicities and proton affinities of molecules: An update." *J. Phys. Chem. Ref. Data*, **27**, 413–656 (1998).

- [115] J.W. Hager, S.C. Wallace. "Two-laser photoionization supersonic jet mass spectrometry of aromatic molecules." *Anal. Chem.*, **60**, 5–10 (1988).
- [116] C.W. Bauschlicher, Jr and S.R. Langhoff. "Bond dissociation energies for substituted polycyclic aromatic hydrocarbons and their cations." *Mol. Phys.*, **96**, 471–476 (1999).
- [117] C.W. Bauschlicher, Jr. "The reaction of polycyclic aromatic hydrocarbon cations with hydrogen atoms: the astrophysical implications." *Astrophys. J.*, **509**, L125–L127 (1998).
- [118] R.J. McMahon, M.C. McCarthy, C.A. Gottlieb, J.B. Dudek, J.F. Stanton and P. Thaddeus. "The radio spectrum of the phenyl radical." *Astrophys. J.*, **590**, L61–L64 (2003).
- [119] D.J. DeFrees, A.D. McLean and E. Herbst. "Theoretical investigation of the interstellar $\text{CH}_3\text{NC}/\text{CH}_3\text{CN}$ ratio." *Astrophys. J.*, **293**, 236–242 (1985).
- [120] C. Joblin, C. Masselon, P. Boissel, P. de Parseval, S. Martinovic and J.F. Muller. "Simulation of interstellar aromatic hydrocarbons using ion cyclotron resonance. Preliminary results." *Rapid Comm. Mass Spectrom.*, **11**, 1619–1623 (1997).
- [121] M. Hirama, T. Ishida, J.-I. Aihara. "Possible molecular hydrogen formation mediated by the radical cations of anthracene and pyrene." *J. Comp. Chem.*, **24**, 1378–1382 (2003).
- [122] J.B. Foresman, M. Head-Gordon, J.A. Pople and M.J. Frisch. "Toward a systematic molecular orbital theory for excited states." *J. Phys. Chem.*, **96**, 135–149 (1992).

- [123] J.M.O. Matos, B. Roos and P.-Å. Malmqvist. “A CASSCF–CCI study of the valence and lower excited states of the benzene molecule.” *J. Chem. Phys.*, **86**, 1458–1466 (1987).
- [124] J.V. Goodpaster, J.F. Harrison and V.L. McGuffin. “*Ab Initio* Study of Polycyclic Aromatic Hydrocarbons in Their Ground and Excited States.” *J. Phys. Chem. A*, **102**, 3372–3381 (1998).
- [125] R. González-Luque, L. Serrano-Andrés, M. Merchán, M.P. Fülscher. “Theoretical characterization of the absorption spectra of phenanthrene and its radical cation.” *Theor. Chem. Acc.*, **110**, 224–232 (2003).
- [126] J.L. Weisman, T.J. Lee and M. Head-Gordon. “Electronic spectra and ionization potentials of a stable class of closed shell polycyclic aromatic hydrocarbon cations.” *Spectrochim. Acta A*, **57**, 931–945 (2001).
- [127] T. Hashimoto, H. Nakano and K. Hirao. “Theoretical study of the valence $\pi \rightarrow \pi^*$ excited states of polyacenes: Benzene and naphthalene.” *J. Chem. Phys.*, **104**, 6244–6258 (1996).
- [128] J.B. Foresman and Æ. Frisch. “*Exploring Chemistry with Electronic Structure Methods*.” second ed., Gaussian, Inc., Pittsburgh, PA (1996).
- [129] G. Müller, J.Y. Fan, J.L. Lyman, W.E. Schmid and K.L. Kompa. “Two-laser resonance-enhanced photoionization spectrum of benzene.” *J. Chem. Phys.*, **90**, 3490–3497 (1989).
- [130] T. Troxler, R. Knochenmuss and S. Leutwyler. “Isomer-specific spectra and ionization potentials of van der Waals clusters.” *Chem. Phys. Lett*, **159**, 554–558 (1989).

- [131] J.W. Hager and S.C. Wallace. "Two-laser photoionization supersonic jet mass spectrometry of aromatic molecules." *Anal. Chem.*, **60**, 5–10 (1988).
- [132] E.A. Mangle and M.R. Topp. "Excited-state dynamics of jet-cooled pyrene and some molecular complexes." *J. Phys. Chem.*, **90**, 802–807 (1986).
- [133] "*ChemOffice 2000: ChemDraw, Chem3D, ChemFinder.*" CambridgeSoft Corp., Cambridge, MA (2000).
- [134] D.C. Harris and M.D. Bertolucci. "*Symmetry and Spectroscopy. An introduction to vibrational and electronic spectroscopy.*" Dover Publications, Inc., New York (1989).
- [135] Y. Ohshima and Y. Endo. "Structure of C₃S studied by pulsed-discharge-nozzle Fourier-transform microwave spectroscopy." *J. Mol. Spectr.*, **153**, 627–634 (1992).
- [136] M. Tulej, D.A. Kirkwood, G. Maccaferri, O. Dopfer and J.P. Maier. "Electronic spectra of linear carbon anions." *Chem. Phys.*, **228**, 293–299 (1998).
- [137] S. Davis, D.T. Anderson, G. Duxbury and D.J. Nesbitt. "Jet-cooled molecular radicals in slit supersonic discharges: Sub-Doppler infrared studies of methyl radical." *J. Chem. Phys.*, **107**, 5661–5675 (1997).
- [138] D. Rolland, A.A. Specht, M.W. Blades, J.W. Hepburn. "Resonance enhanced multiphoton dissociation of polycyclic aromatic hydrocarbons cations in an RF ion trap." *Chem. Phys. Lett.*, **373**, 292–298 (2003).
- [139] W.H. Robertson, J.A. Kelley and M.A. Johnson. "A pulsed supersonic entrainment reactor for the rational preparation of cold ionic complexes." *Rev. Sci. Instr.*, **71**, 4431–4434 (2000).

- [140] W.C. Wiley, I.H. McLaren. “Time-of-flight mass spectrometer with improved resolution.” *Rev. Sci. Instr.*, **26**, 1150–1157 (1955).
- [141] V.I. Karataev, B.A. Mamyrin and D.V. Shmikk. “New method for focusing ion bunches in time-of-flight mass spectrometers.” *Sov. Phys. – Tech. Phys. USSR*, **16**, 1177 (1972).
- [142] B.A. Mamyrin, V.I. Karataev, D.V. Shmikk and V.A. Zagulin. “Mass-reflectron: A new nonmagnetic time-of-flight high-resolution mass-spectrometer.” *Sov. Phys. – JETP*, **64**, 82–89 (1973).
- [143] D.A. Rodham. “Spectroscopic studies of the gas phase complexes benzene–ammonia, sodium–water, and sodium–ammonia.” Ph.D. thesis, *California Institute of Technology* (1997).
- [144] S. Wu. “Development of broadly tunable parametric light sources and their application to alkali metal – small molecule cluster spectroscopy.” Ph.D. thesis, *California Institute of Technology* (1999).
- [145] H. Zhang. “Spectroscopic studies of N_2O and HNO_4 : A window into the global biogeochemistry of nitrogen.” Ph.D. thesis, *California Institute of Technology* (2001).
- [146] S. Wu, G.A. Blake, Z.Y. Sun and J.W. Ling. “Simple, high-performance type II β - BaB_2O_4 optical parametric oscillator.” *Appl. Optics*, **36**, 5898–5901 (1997).
- [147] G. Anstett, G. Göritz, R. Urschel, R. Wallenstein, A. Borsutzky. “Reduction of the spectral width and beam divergence of a BBO–OPO by using collinear type-II phase matching and back reflection of the pump beam.” *Appl. Phys. B*, **72**, 583–589 (2001).

- [148] D.J. Armstrong and A.V. Smith. "Demonstration of improved beam quality in an image-rotating optical parametric oscillator." *Optics Lett.*, **27**, 40–42 (2002).
- [149] B.S. Freiser and J.L. Beauchamp. "Laser photodissociation of benzene radical cations. Evidence for a two photon process involving a long lived intermediate." *Chem. Phys. Lett.*, **35**, 35–40 (1975).
- [150] O. Dopfer, R.V. Olkhov and J.P. Maier. "Infrared photodissociation spectra of the CH stretch vibrations of $\text{C}_6\text{H}_6^+-\text{Ar}$, $\text{C}_6\text{H}_6^+-\text{N}_2$, and $\text{C}_6\text{H}_6^+(\text{CH}_4)_{1-4}$." *J. Chem. Phys.*, **111**, 10754–10757 (1999).
- [151] R.G. Satink, H. Piest, G. von Helden and G. Meijer. "The infrared spectrum of the benzene-Ar cation." *J. Chem. Phys.*, **111**, 10750–10753 (1999).
- [152] J.M. Bakker, R.G. Satink, G. von Helden and G. Meijer. "Infrared photodissociation spectroscopy of benzene–Ne,Ar complex cations." *Phys. Chem. Chem. Phys.*, **4**, 24–33 (2002).
- [153] H. Piest, G. von Helden and G. Meijer. "Infrared spectroscopy of jet-cooled cationic polyaromatic hydrocarbons: Naphthalene." *Astrophys. J.*, **520**, L75–L78 (1999).
- [154] J.A. Piest, J. Oomens, J. Bakker, G. von Helden and G. Meijer. "Vibrational spectroscopy of gas-phase neutral and cationic phenanthrene in their electronic ground-states." *Spectrochim. Acta A*, **57**, 717–735 (2001).
- [155] S. Suzuki, P.G. Green, R.E. Bumgarner, S. Dasgupta, W.A. Goddard, G.A. Blake. "Benzene forms hydrogen-bonds with water." *Science*, **257**, 942–944 (1992).
- [156] E.S. Kryachko and M.T. Nguyen. "Low energy barrier proton transfer in protonated benzene–water complex." *J. Phys. Chem. A*, **105**, 153–155 (2001).

- [157] P.M. Palmer, M.R. Topp. “Electronic spectroscopy of jet-cooled anthracene(H_2O) $_n$ clusters ($n = 1 - 16$): comparisons of inhomogeneous structure.” *Chem. Phys.*, **239**, 65–81 (1998).
- [158] P.M. Palmer, M.R. Topp. “Spectroscopic properties of jet-cooled methanol clusters ($n = 1 - 6$) attached to anthracene.” *Chem. Phys. Lett.*, **292**, 307–316 (1998).